Aristotle University of Thessaloniki

Faculty of Sciences

School of Geology

Maria Chara Karypidou

Estimating errors and uncertainties of precipitation in regional climate simulations over southern Africa: investigation of physical processes

Doctoral Thesis

Thessaloniki

2022

Αριστοτέλειο Πανεπιστήμιο Θεσσαλονίκης

Σχολή Θετικών Επιστημών

Τμήμα Γεωλογίας

Μαρία Χαρά Καρυπίδου

Εκτίμηση των σφαλμάτων και της αβεβαιότητας του υετού στη νότια Αφρική σε περιοχικές κλιματικές προσομοιώσεις: διερεύνηση των φυσικών διεργασιών

Διδακτορική Διατριβή

Θεσσαλονίκη

2022

Maria Chara Karypidou

Estimating errors and uncertainties of precipitation in regional climate simulations over southern Africa: investigation of physical processes

Submitted to the School of Geology A.U.Th.
Department of Meteorology and Climatology
Date of Oral Defense: July 12, 2022

Annex Number of the Scientific Annals of the School of Geology No. 231

Supervisory committee:

Dr. Eleni Katragkou, Associate Professor, Department of Meteorology and Climatology, School of Geology, Aristotle University of Thessaloniki, Thessaloniki, Greece (Supervisor)

Dr. Prodromos Zanis, Professor, Department of Meteorology and Climatology, School of Geology, Aristotle University of Thessaloniki, Thessaloniki, Greece

Dr. Stefan Pieter Sobolowski, Research Professor, NORCE Norwegian Research Centre, Bjerknes Centre for Climate Research, Bergen, Norway

Examination committee:

1. Dr. Eleni Katragkou, Associate Professor, Department of Meteorology and Climatology, School of Geology, Aristotle University of Thessaloniki, Thessaloniki, Greece (Supervisor)
2. Dr. Prodromos Zanis, Professor, Department of Meteorology and Climatology, School of Geology, Aristotle University of Thessaloniki, Thessaloniki, Greece
3. Dr. Stefan Pieter Sobolowski, Research Professor, NORCE Norwegian Research Centre, Bjerknes Centre for Climate Research, Bergen, Norway
4. Dr. Ioannis Pytharoulis, Associate Professor, Department of Meteorology and Climatology, School of Geology, Aristotle University of Thessaloniki, Thessaloniki, Greece
5. Dr. Petros Katsafados, Associate Professor, Department of Geography, Harokopio University, Athens, Greece
6. Dr. Evangelos Tyrlis, Assistant Professor, Department of Physics, National and Kapodistrian University of Athens, Athens, Greece
7. Dr. Priscilla Mooney, Research Professor, NORCE Norwegian Research Centre, Bjerknes Centre for Climate Research, Bergen, Norway

Εκτίμηση των σφαλμάτων και της αβεβαιότητας του υετού στη νότια Αφρική σε περιοχικές κλιματικές προσομοιώσεις: διερεύνηση των φυσικών διεργασιών.

Citation:
Καρυπίδου Μ. Χ., 2022, Εκτίμηση των σφαλμάτων και της αβεβαιότητας του υετού στη νότια Αφρική σε περιοχικές κλιματικές προσομοιώσεις: διερεύνηση των φυσικών διεργασιών. Διδακτορική Διατριβή, Τμήμα Γεωλογίας, Αριστοτέλειο Πανεπιστήμιο Θεσσαλονίκης, Αριθμός Παραρτήματος Επιστημονικής Επετηρίδας Τμ. Γεωλογίας No. 231, 214 σελ.

[page intentionally left blank]

Estimating errors and uncertainties of precipitation in regional climate simulations over southern Africa: investigation of physical processes

Citation:
Karypidou M. C., 2022, Estimating errors and uncertainties of precipitation in regional climate simulations over southern Africa: investigation of physical processes, Doctoral Thesis, School of Geology, Aristotle University of Thessaloniki, Annex Number of Scientific Annals of the School of Geology No. 231, 214 pg.

[page intentionally left blank]

Χρηματοδότηση

Η παρούσα Διδακτορική Διατριβή χρηματοδοτήθηκε από το Ελληνικό Ίδρυμα Έρευνας και Καινοτομίας (ΕΛΙΔΕΚ), στο πλαίσιο της δράσης "2η Προκήρυξη Υποτροφιών ΕΛΙΔΕΚ για Υποψήφιους Διδάκτορες". Αριθμός αίτησης: 1323

[page intentionally left blank]

Funding

The present Doctoral Thesis was funded by the Hellenic Foundation for Research & Innovation (HFRI), in the context of the "2nd Call for PhD Candidates". Application number: 1323

H.F.R.I.
Hellenic Foundation for
Research & Innovation

[page intentionally left blank]

Περίληψη Διατριβής

Το κλίμα της νότιας Αφρικής χαρακτηρίζεται από μια πληθώρα μόνιμων και ημιμόνιμων ατμοσφαιρικών χαρακτηριστικών που συνδέονται μεταξύ τους σε διάφορα επίπεδα πολυπλοκότητας, τόσο στην ξηρά όσο και στους δύο γειτνιάζοντες ωκεανούς. Η παρούσα Διατριβή στοχεύει στο να προσφέρει μια ολοκληρωμένη επισκόπηση της μοντελοποιημένης και παρατηρούμενης κλιματολογίας βροχοπτώσεων στη νότια Αφρική, αξιοποιώντας όλα τα εργαλεία που είναι επί του παρόντος διαθέσιμα στην κλιματική κοινότητα. Επιπλέον, στοχεύει στη διερεύνηση της επίδρασης που ασκούν οι πλευρικές οριακές συνθήκες στις προσομοιώσεις Περιοχικών Κλιματικών Μοντέλων που πραγματοποιούνται στο πλαίσιο του CORDEX-Africa. Επιπρόσθετα, αποσκοπεί στη διερεύνηση των δυναμικών διεργασιών στην περιοχή μελέτης που είναι υπεύθυνες για τη δημιουργία βροχόπτωσης στο σύνολο του σμήνους προσομοιώσεων του CORDEX-Africa. Τέλος, πραγματοποιείται μια σειρά προσομοιώσεων με χρήση του Weather Research and Forecasting μοντέλου (WRF), με σκοπό να εξεταστεί ο αντίκτυπος των σχημάτων παραμετροποίησης της ανωμεταφοράς στις διαδικασίες της βροχόπτωσης στη νότια Αφρική.

Συμπεραίνεται πως οι περιοχικές κλιματικές προσομοιώσεις βελτιώνουν σημαντικά τα μηνιαία ποσά βροχοπτώσεων στην περιοχή της νότιας Αφρικής (CORDEX-0.44), σε σχέση με τα Παγκόσμια Κλιματικά Μοντέλα από τα οποία λαμβάνουν πλευρικές οριακές συνθήκες (CMIP5). Επιπλέον, η υψηλότερη χωρική ανάλυση του συνόλου του σμήνους προσομοιώσεων CORDEX-Africa επιτρέπει την ακριβέστερη αναπαράσταση της τοπογραφίας, σε σύγκριση με αυτή που πραγματοποιείται από τα Παγκόσμια Κλιματικά Μοντέλα αδρής χωρικής ανάλυσης. Αυτό έχει ως αποτέλεσμα η εισροή υγρασίας στα χαμηλά ύψη της τροπόσφαιρας προερχόμενη από τον τροπικό Ινδικό Ωκεανό να εμποδίζεται ορθώς από τα βουνά στην περιοχή της Τανζανίας και να μην της επιτρέπεται να προχωρήσει προς την περιοχή της κεντρικής νότιας Αφρικής, όπως λανθασμένα συμβαίνει στο σμήνος προσομοιώσεων CMIP5. Σε όλους τους μήνες, και για τις διάφορες υποπεριοχές που εξετάζονται, τα Περιοχικά Κλιματικά Μοντέλα μειώνουν συστηματικά το σφάλμα της βροχόπτωσης, σε σχέση με τα Παγκόσμια Κλιματικά Μοντέλα που τα οδηγούν.

Τα πειράματα ευαισθησίας πραγματοποιήθηκαν χρησιμοποιώντας το μοντέλο WRF, εξετάζοντας την επίδραση του σχήματος παραμετροποίησης που ελέγχει τις διαδικασίες ανωμεταφοράς σε διάφορα χαρακτηριστικά που αφορούν τη βροχόπτωση στη νότια Αφρική. Οι προσομοιώσεις έδειξαν ότι η βροχόπτωση επηρεάζεται σημαντικά από το σχήμα παραμετροποίησης της ανωμεταφοράς και τα αποτελέσματα ήταν συνεπή ανεξάρτητα από την περίοδο μελέτης. Πιο συγκεκριμένα, τα σχήματα Betts - Miller - Janjic και New - Tiedtke παρήγαγαν τα πιο ρεαλιστικά αποτελέσματα (σε σύγκριση με τα χρησιμοποιούμενα δορυφορικά προϊόντα βροχόπτωσης και τα δεδομένα επανάλυσης ERA5) για ολόκληρη την περίοδο μελέτης. Το σχήμα Kain - Fritsch εμφάνισε συστηματική υπερεκτίμηση της βροχόπτωσης καθ' όλη την περίοδο μελέτης.

[page intentionally left blank]

Abstract

The climate of southern Africa is characterized by a plethora of distinct permanent and semi permanent atmospheric features that are interconnected at various levels of complexity, both over land and over the two adjacent oceans. The current Thesis aims to provide a comprehensive overview of the modeled and observed precipitation climatology over southern Africa, in all tools that are currently available in the climate community. Additionally, it aims to investigate the impact that the lateral boundary conditions exert on Regional Climate Model (RCM) simulations performed in the context of CORDEX-Africa, and to further investigate the dynamical processes over the study region that are responsible for precipitation in the CORDEX-Africa ensemble. Lastly, a series of RCM simulations using the Weather Research and Forecasting (WRF) model is used, with the purpose to examine the impact of cumulus parameterization schemes on precipitation over southern Africa.

It is concluded that RCM simulations significantly improve monthly precipitation amounts in the southern African region (CORDEX-0.44), relative to Global Climate Models (GCMs) from which they receive lateral boundary conditions (CMIP5). Moreover, the higher spatial resolution of the CORDEX-Africa ensemble allows the more accurate representation of topography, compared to that in the coarse resolution GCMs. This results to the low-tropospheric moisture inflow from the tropical Indian Ocean being correctly blocked by the mountains over the Tanzania region and hindering it from progressing towards the central southern African region, as is erroneously the case in the CMIP5 ensemble. In all months and for the various subregions considered, the regional models systematically reduce the precipitation bias, relative to the driving global models.

Sensitivity experiments were performed using the WRF model, examining the impact of the cumulus parameterization scheme on several aspects of the southern Africa precipitation regime. The simulations showed that precipitation is significantly affected by the cumulus parameterization scheme and the results were consistent regardless of the study period. More specifically, the Betts - Miller - Janjic and New - Tiedtke schemes produced the more realistic results (compared to satellite precipitation products and the ERA5 reanalysis dataset) for the entire study period (rainy season 2012-2013), but also for the intense precipitation event examined during January 2013, over south-eastern South Africa. The Kain - Fritsch scheme displayed an overestimation of precipitation throughout the study period.

[page intentionally left blank]

Ευχαριστίες

«Περπατώ, όπως όλοι μας, σε μιαν έρημο απόλυτη.
Εάν μου φανεί ότι άκουσα κελαηδισμό πουλιού,
ας μου λέει η λογική ότι παραφέρομαι,
εγώ, νιώθω υποχρεωμένη
να ετοιμάσω σ' αυτό το πουλί ένα δέντρο.»

Κική Δημουλά, *Ο Φιλοπαίγμων Μύθος*

Η Διατριβή αυτή είναι η δική μου απόπειρα να φυτέψω ένα δέντρο, χάριν κάποιων κελαηδισμάτων που άκουσα. Σε καμιά περίπτωση, όμως, αυτό δε θα μπορούσα να το κάνω μόνη μου. Ίσως εδώ, τολμώ να διαφωνήσω με την αγαπημένη ποιήτρια. Δεν περπατώ σε μιαν «έρημο απόλυτη». Έχω σπουδαίους συνοδοιπόρους τους οποίους ευγνωμονώ. Ευγνωμονώ όμως και την ποιήτρια καθώς ο στίχος της με βοηθά να καταλάβω πως αυτό δεν είναι δεδομένο. Είναι μια ευλογία, ένα προνόμιο. Έτσι λοιπόν, θέλω να ευχαριστήσω τους ανθρώπους που ανέτρεψαν την έρημό μου.

Θέλω να ευχαριστήσω εκ βαθέων τον άνθρωπο που μου έμαθε να σκάβω στο χωράφι της γνώσης. Να μη φοβάμαι να λερώσω τα χέρια μου με το χώμα, αλλά αντίθετα, να βλέπω την τέχνη αυτή ως κομμάτι απαραίτητο ενός έργου ωραίου. Μου έμαθε να χαίρομαι τις ημέρες της ποθητής βροχής και να ανέχομαι τις ημέρες της ξηρασίας. Να σέβομαι τους χρόνους και τις διαδικασίες των πραγμάτων, άσχετα με το πόσο βιαστική ήμουν πολλές φορές για τον ερχομό της Άνοιξης. Αναφέρομαι στην Επιβλέπουσα Καθηγήτριά μου, Δρ. Ελένη Κατράγκου. Της είμαι βαθιά ευγνωμονούσα που με βοήθησε να φυτέψω το δικό μου δέντρο.

Ευχαριστώ από καρδιάς, τους δύο υπέροχους ανθρώπους που φύτεψαν και αυτοί το δικό τους δέντρο, κάτω από το οποίο βρήκα άφθονη σκιά, δροσιά και αγάπη. Χωρίς αυτούς, δε θα είχα ακούσει καν το κελάηδισμα των πουλιών. Αναφέρομαι στους αγαπημένους μου γονείς, Ιωάννη και Ανατολή.

Ευχαριστώ θερμά τους συναδέλφους μου, Δρ. Βασίλειο Παυλίδη, Δρ. Στέργιο Κάρτσιο και κο Ιωάννη Σοφιάδη, για την επιστημονική βοήθεια, τις όμορφες συζητήσεις μας και το άφθονο γέλιο στο Γραφείο 4.6β.

Ευχαριστώ θερμά τον Δρ. Stefan Sobolowski για τη βοήθεια και καθοδήγησή του καθ' όλη τη διάρκεια του διδακτορικού, καθώς και για τη φιλοξενία του στο NORCE Climate το 2020 στο όμορφο Bergen, στο πλαίσιο του προγράμματος ERASMUS-Placement. Ευχαριστώ τον Δρ. Πρόδρομο Ζάνη, τη Δρ. Priscilla Mooney, τον Δρ. Ιωάννη Πυθαρούλη, τον Δρ. Ευάγγελο Τυρλή και τον Δρ. Πέτρο Κατσαφάδο για τις χρήσιμες συμβουλές τους, τις διορθώσεις και τα εποικοδομητικά σχόλιά τους στο κείμενο της διατριβής.

Πάνω από όλους και πάνω από όλα, θα ήθελα να ευχαριστήσω Εκείνον που *κάνει δρόμο μέσα στην έρημο, ποταμούς μέσα στην άνυδρη γη* (Ησαΐας 43:19), στον Οποίον είναι *κρυμμένοι όλοι οι θησαυροί της σοφίας και της γνώσης* (Επιστολή προς Κολοσσαείς 2:3), Αυτόν που *φωτίζει το σκοτάδι μου* (Β' Σαμουήλ 22:29), Αυτόν, που το *έξοχο της γνώσης Του* (Επιστολή προς Φιλιππησίους 3:8) είναι απείρως πολυτιμότερο από κάθε Διατριβή. Αυτόν που είναι *το τέλος της υποθέσεως* (Εκκλησιαστής 12:13), τον Κύριό μου, *Ιησού Χριστό*.

Μαρία Χαρά Καρυπίδου
Θεσσαλονίκη 2022

[page intentionally left blank]

Acknowledgements

«I walk, as everyone, in an absolute desert.
If I have the impression that I heard the song of a bird,
even though my logic may say that I misbehave,
I am obliged to prepare a tree for that bird.»

Kiki Dimoula, *The Playful Myth*

This Thesis is my attempt to plant a tree, for the sake of some bird chirping I heard. However, by no means do I dare think that I could have done it on my own. Perhaps here, I would like to express my objection to the dear poet. I do not walk in an "absolute desert". I have great fellow travelers, to whom I am grateful. However, I am also grateful to the dear poet because her words make me realize that this should not be taken for granted. It is a blessing, a privilege. For this reason, I would like to express my gratitude towards the people who challenged my desert.

I would like to thank, from the depths of my heart, the person who taught me how to plough the field of knowledge. Not to be afraid to mar my hands with dust, but instead to view it as a beautiful craft, necessary for the creation of a beautiful work. She taught me to rejoice for the days of the longed-for rain and to tolerate the seasons of drought. She taught me to be respectful of times and season and of the necessary procedure of things, regardless of how impatient I was for the arrival of Spring. I refer to my Supervisor, Dr. Eleni Katragkou. I am deeply grateful to her for helping me plant my own tree.

I would like to thank from the depths of my heart the two wonderful people that also planted their tree, under which I found abundant shade, peace, and love. Without them, I would not have even heard the song of the birds. I refer to my beloved parents, Ioannis and Anatoli.

I thank my dear colleagues Dr. Vassileios Pavlidis, Dr. Stergios Kartsios, and Mr. Ioannis Sofiadis, for their scientific help, our delightful discussions, and the times of laughter in Office 4.6b.

I thank Dr. Stefan Sobolowski for his help and guidance during the course of the PhD project, and for his hospitality at NORCE Climate in beautiful Bergen, in the context of the ERASMUS–Placement project. I thank Dr. Prodromos Zanis, Dr. Priscilla Mooney, Dr. Ioannis Pytharoulis, Dr. Evangelos Tyrlis, and Dr. Petros Katsafados for their useful advice, corrections, and constructive comments on the Thesis.

Above everyone and everything, I would like to thank Him, who *makes a way in the wilderness, and rivers in the desert* (Isaiah 43:19), *in whom are hid all the treasures of wisdom and knowledge* (Epistle to the Colossians 2:3), He who *lightens my darkness* (2 Samuel 22:29), Him whose *excellency of knowledge* (Epistle to the Philippians 3:8) is infinitely more precious than any Thesis. Him who is the *conclusion of the whole matter* (Ecclesiastes 12:13), my Lord, *Jesus Christ*.

Maria Chara Karypidou
Thessaloniki 2022

[page intentionally left blank]

Στην υπέροχή μου Μητέρα, Ανατολή,
που έζησε στο ενθάδε
μια ζωή
λουσμένη με το Ανέσπερο Φως του Επέκεινα,
η οποία πλέον "κατέλαβε, ἐφ᾽ ᾧ καὶ κατελήφθη".

[page intentionally left blank]

To my wonderful Mother, Anatoli,
who lived her life in the Light of Eternity,
and has now "apprehended that for which also she was apprehended".

[page intentionally left blank]

Contents

List of Figures

List of Tables

[page intentionally left blank]

1 Introduction

A panoramic view of the Thesis is provided in this Chapter. First, the main climatological features over southern Africa during the rainy season are briefly discussed. Secondly, the main research aims of the Thesis are presented and lastly, the structure of the Thesis is delineated.

1.1 Basic Climatological Features over southern Africa

The climate of southern Africa is characterized by a plethora of distinct permanent and semi-permanent atmospheric features that are interconnected at various levels of complexity, both over land and over the two adjacent oceans. The main features that are discussed in the context of this Thesis are briefly described below and refer to the main atmospheric processes that are at play during the rainy season. A descriptive schematic is shown in Fig. 1.1.1. The rainy season over southern Africa begins approximately in October and extends until March, with October and November being described as the early rainy season and the period during December-January-February being described as the core rainy season. March usually heralds the cessation of the rainy season and the retreat of the rainband equatorwards.

During the rainy season, southern Africa is characterized by severe thunderstorm activity which moves southwards in October, reaches its southernmost location during January and begins its northward retreat after February. The seasonal migration of the rainband reflects the seasonal movement of the Sun's maximum heating. For convective activity to occur, there are two main necessary components that must co-occur, namely the existence of warm moist air, and the adequate heating of the Earth's surface from the Sun. During the summer of the southern hemisphere (Dec-Jan-Feb: DJF), the heating from the Sun is maximized over southern Africa due to the tilt of the Earth's axis. During DJF, maximum heating moves southwards, causing the southward migration of the rainband. However, the necessary fuel for the development of convection is moisture, which over southern Africa is provided by three main sources. These sources are the warm south Atlantic and south Indian Oceans, and moisture originating from the Congo Basin. Air following the synoptic circulation over these regions moves towards the subcontinent, supplying the atmosphere with the necessary moisture to fuel the wet season rainfall.

Another important feature responsible for precipitation over southern Africa, is the elongated band of deep convective clouds, the tropical temperate troughs (TTTs) (Hart et al. (2010)), that extend from the central part of the subcontinent towards its southeast coast, and functions as a conveyor belt of

latent heat and momentum, moving from the tropics towards the extra-tropics. An additional, very important feature over southern Africa is the Angola Low pressure system, which is a semi-permanent low, identified over the greater Angola region and is responsible for redistributing low-level moisture that enters southern Africa from different directions. The Angola Low pressure system has solely heat low characteristics during the early rainy season (Oct-Nov: ON), while during DJF it is expressed as the climatological mean of transient low-pressure systems (Howard and Washington (2018)). The Angola Low pressure system has been found to exert a significant impact on the severity of ENSO events over southern Africa (Reason and Jagadheesha (2005)). Usually, the Angola Low events precede the formation of TTTs and hence, they can be considered as their precursor in the "climate process chain" controlling precipitation over southern Africa (Daron et al. (2019)). As stated in Howard and Washington (2018), it is common that Angola Low events precede TTT events.

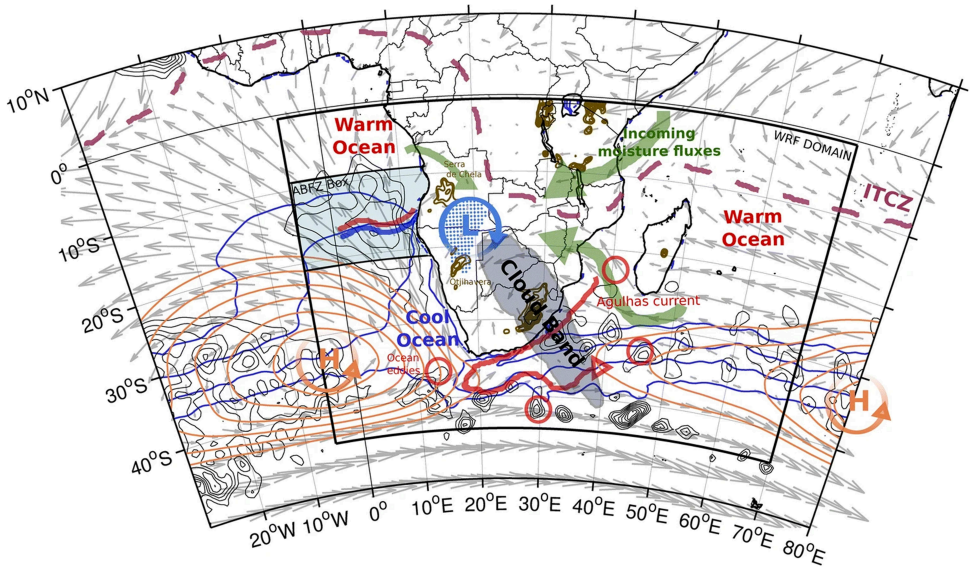

Figure 1.1.1: Schematic of the main climatological features over southern Africa during the rainy season. Figure taken from Desbiolles et al. (2020).

1.2 Aims of the Thesis

Compared to other parts of Africa, southern Africa has been relatively understudied. Several endeavors from various modeling consortia have been performed during the last decade, however, a synthetic work integrating all data from both modeling and precipitation observation efforts was missing. Nikulin et al. (2012) was the first to present an overview of the CORDEX-Africa ensemble and to analyze the spatiotemporal patterns of precipitation. They showed that during the rainy season (Jan-Mar as used in Nikulin et al. (2012)) there is a weak wet bias over southern Africa, and that the use of the ensemble mean was able to outperform individual models, highlighting the importance of ensemble-based approaches. The Nikulin et al. (2012) analysis was conducted on a pan-African scale. Similarly, Kalognomou et al. (2013) analyzed the same ensemble of CORDEX-Africa simulations, focusing over southern Africa and reported similar findings to Nikulin et al. (2012). In Shongwe et al. (2014) a particular empha-

sis was put on the onset and retreat of the rainy season, especially over the eastern part of southern Africa. Nonetheless, as stated in Shongwe et al. (2014) "No attempt is made in this paper to identify the model physics and dynamics responsible for the differences in RCM performance." All the aforementioned studies employed the evaluation (hindcast) simulations performed within CORDEX-Africa, driven by ERA-Interim; the analyzed ensemble was comprised of 10 RCMs. It is also worth mentioning that the Regional Climate Model (RCM) versions used in the studies listed above, refer to previous versions of the respective RCMs, which have now been replaced by newer versions in more recent studies.

In Meque and Abiodun (2015) the same ensemble of 10 hindcast simulations was again used, but it was also compared to a set of CMIP5 GCM simulations, with the purpose to identify a causal association between ENSO and drought events over southern Africa. Meque and Abiodun (2015) stated that RCMs were able to provide added value, compared to their driving GCMs. The issue of the added value of the CORDEX-Africa ensemble was clearly stated in Dosio et al. (2015), where one RCM participating in CORDEX-Africa (CCLM) was compared against four different driving GCMs. In Favre et al. (2016) a special focus was given on the annual cycle of precipitation over South Africa, using the same ensemble of 10 CORDEX-Africa hindcast simulations and in Abba Omar and Abiodun (2017), although the same hindcast ensemble was used, there was an effort to associate extreme precipitation events with dynamical processes such as the Tropical Temperate Troughs.

A comprehensive assessment of the added value between historical CORDEX-Africa RCM simulations and of their driving CMIP5 GCMs on a seasonal timescale over the whole of Africa, was performed in Dosio et al. (2019). The CORDEX-Africa ensemble over southern Africa was compared to an extensive set of observational and satellite products in Abiodun et al. (2020), while the first time that CORDEX Africa simulations available at 0.44° and at 0.22° was analyzed compared to both CMIP5 and CMIP6 ensembles is presented in Dosio et al. (2021). More specifically, in Dosio et al. (2021) the analysis is performed on a seasonal timestep and on pan-African scale and its particular emphasis is placed on the projected changes of future precipitation, although a part of the analysis is dedicated to the period 1981-2010.

The current Thesis aims to provide a comprehensive overview of the modeled and observed precipitation climatology over southern Africa, in all tools that are currently available in the climate community. Additionally, it aims at investigating the impact that the lateral boundary conditions exert on Regional Climate Model simulations performed in the context of CORDEX-Africa, and to further investigate the dynamical processes over the study region that are responsible for precipitation in the CORDEX-Africa ensemble. Lastly, a series of RCM simulations using the Weather Research and Forecasting (WRF) is used, with the purpose to examine the impact of cumulus parameterization schemes on precipitation over southern Africa

1.3 Structure of the Thesis

In Chapter 2, monthly precipitation climatologies during the rainy season (Oct-Mar) are examined, across various modeling and observational ensembles, for the period 1986-2005. The modeling ensembles examined are the Regional Climate Model simulations performed in the context of the Coordinated Regional Climate Downscaling Experiment (CORDEX) – Africa domain (Giorgi and Gutowski (2015)) at 0.44° horizontal spatial resolution (CORDEX-0.44), and the RCM simulations performed within CORDEX-

CORE, at 0.22° horizontal spatial resolution (CORDEX-0.22). In addition, Global Climate Model (GCM) simulations are analyzed. The examined GCMs belong to the Coupled Model Intercomparison Project Phase 5 (CMIP5). he GCMs selected are those that provided the lateral boundary conditions for the CORDEX-Africa RCM simulations (CORDEX-0.44). Furthermore, the next generation of the same GCMs that participate in the CMIP6 ensemble are also analyzed. Besides the climate model simulations, a series of gauge-based gridded rainfall products, along with a set of satellite rainfall products and a reanalysis product are exploited.

An intercomparison study is performed, with the purpose to address the question of whether there is consensus among GCMs, RCMs and observational data, concerning monthly precipitation climatologies during the rainy season (Oct-Mar), for the period 1986-2005 over southern Africa. This is achieved through the use of total monthly precipitation amounts, standard deviation of monthly precipitation across all various ensembles, calculation of precipitation-related indices and the calculation of monthly precipitation trends. Finally, the investigation of improvement of monthly precipitation in RCM simulations (CORDEX-0.44), relative to their driving GCMs (CMIP5) is performed through the assessment of a dynamical process responsible for moisture transport from the tropical Indian Ocean towards mainland southern Africa. The analysis of all RCM and GCM simulations is performed using ensemble means. The analysis of individual RCM and GCM simulations is performed in the following chapter.

In Chapter 3, the RCM-GCM matrix is analyzed. All CORDEX-0.44 simulations are examined individually, relative to the CMIP5 GCMs from which they receive their lateral boundary conditions. One of the main points of interest with regards to the available RCM-GCM matrix is whether the monthly precipitation signal is dominated by the RCMs or their driving GCMs and whether the impact of the lateral boundary conditions displays variability depending on the examined month. The choice of a monthly timestep for the analysis, instead to that of a seasonal timestep, for all months of the rainy season (Oct-Mar), is selected as a proxy for certain atmospheric processes that are dominant during specific months. The analysis is performed for historical simulations (1985-2005) and for future projections under the Representative Concentration Pathway (RCP) 8.5, for the period 2065-2095. The whole of southern Africa is examined, along with three subregions, namely the greater Angola region, the greater Mozambique region, and the greater South Africa region.

The impact of lateral boundary forcing in the CORDEX-Africa ensemble over southern Africa is assessed. This is achieved by analyzing monthly precipitation climatologies during the rainy season, monthly precipitation biases and monthly precipitation climate change signal for the end of the 21st century (2065-2095). In addition, the increment of each RCM is examined relative to the GCM that provided the lateral boundary conditions, with the purpose to identify whether RCMs systematically increase or decrease the monthly precipitation bias. Lastly, the amount of monthly precipitation variability is examined through the analysis of variance across all RCMs that were driven by the same GCM, and across all GCMs driving the same RCM. The conclusions drawn are related to whether precipitation is caused by local scale processes or by the large-scale synoptic circulation. The large-scale atmospheric circulation over the whole southern hemisphere, with a special emphasis on the upper troposphere, is examined in the following chapter.

In Chapter 4, the jet stream over the whole of southern hemisphere is examined, using the ERA5 reanalysis dataset (Hersbach et al. (2020)) for the period 1950-2021. The analysis in Chapter 2 and Chap-

ter 3 is constrained to the land grid points available within the CORDEX-Africa domain, south of 10° latitude. In Chapter 4, the endeavor is to obtain a semi-hemispheric view of the large-scale processes related to the jet stream at the top of the troposphere (250 hPa). The jet stream provides an upper-level large scale forcing to the region of southern Africa, however its comprehensive study within the CORDEX-Africa set of simulations is implausible, due to the spatial extent of the CORDEX-Africa domain. Therefore, the ERA5 dataset is employed instead, with the purpose to obtain an understanding of the large-scale processes occurring outside of the CORDEX-Africa domain, during the observed period. In this way, Chapter 4 introduces the dynamical large-scale forcing affecting severely the climate of southern Africa and moreover, paves the way for the dynamical analysis of the CORDEX-Africa ensemble (CORDEX-0.44) that is performed in Chapter 5, for the CORDEX-Africa domain located to the south of the Equator.

The two primary aspects of the jet stream examined in Chapter 4, are the mean annual zonal wind speed, and its vertical wind shear at 250 hPa. A further emphasis is given on the vertical wind shear, which is calculated by means of exploiting zonal wind speed fields at 200 and 300 hPa and by employing the thermal wind balance equation, using temperature fields at 250 hPa. Employing the thermal wind balance for the calculation of the vertical wind shear of the jet stream aims to investigate the degree to which the vertical wind shear is caused by the planetary scale differential warming between the tropics and the South Pole. Annual trends of wind speed and vertical wind shear are calculated for the whole of the southern hemisphere and for selected subregions. Areas displaying increasing wind shear trends are of special concern, due to the impact that upper-level convergence/divergence exerts on surface atmospheric conditions. Due to mass continuity, regions of the jet stream over which strong convergence (divergence) is observed, results in divergence (convergence) in the lower troposphere.

In Chapter 5, the dynamical analysis of the CORDEX-Africa ensemble (CORDEX-0.44) is performed for the historical period (1986-2005), over the southern hemisphere counterpart of the CORDEX-Africa domain. The analysis is performed for the early rainy season (Oct-Nov) and the core rainy season (Dec-Jan-Feb) and aims to exploit all available variables within CORDEX-Africa at the three available pressure levels, namely 850, 500 and 200 hPa. Variable availability is an enormous constrain to the analysis, however, exploiting both u and v wind components at 850, 500 and 200 hPa allows for the assessment of specific kinematic properties of the atmosphere within all available CORDEX-Africa (CORDEX-0.44) simulations. The examined fields involve vorticity and vorticity advection (relative and absolute) and low-level (850 hPa) moisture flux divergence. In addition, zonal wind speed at 200 hPa is used as a proxy for the Subtropical Jet Stream, while zonal wind speed at 500 hPa is used as a proxy for the southern branch of African Easterly Waves. The aim of Chapter 5 is to analyze specific atmospheric dynamical processes in the CORDEX-Africa (CORDEX-0.44) ensemble, that have not been discussed before in the scientific literature, and to investigate their impact on regional precipitation.

In Chapter 6, the Weather Research and Forecasting (WRF) model is used for a series of cumulus parameterization sensitivity experiments over southern Africa. The simulation period extends from October the 1st 2012 until February the 28th 2013. A three-month spinup time is used from July the 1st until September the 30th. The horizontal spatial resolution of all experiments is 15 x 15 km. The cumulus schemes examined are the Betts-Miller-Janjic scheme, the New-Tiedtke scheme, the Kain-Fritsch scheme, and the Grell-Freitas scheme. Chapter 6 aims at investigating the sensitivity of precipitation

and specific precipitation-bearing processes to parameterized cumulus schemes. A particular emphasis is also given to an intense rain event that occurred during the 15-20 January 2013 period, to the southeast part of southern Africa.

Finally, concluding remarks and potential pathways for future research topics are presented in the last Chapter, "Conclusions".

2 Precipitation over southern Africa: An introduction

This chapter investigates the monthly precipitation climatology during the rainy season over southern Africa for the period 1986-2005 in multiple modeling and observational ensembles, quantifies their consensus (or the lack thereof). This chapter was published in Geoscientific Model Development (GMD):

Karypidou, M. C., *Katragkou, E., and Sobolowski, S. P.: Precipitation over southern Africa: is there consensus among global climate models (GCMs), regional climate models (RCMs) and observational data?, Geosci. Model Dev., 15, 3387–3404,* `https://doi.org/10.5194/gmd-15-3387-2022`

2.1 Introduction

The region of Sub-Saharan Africa has been characterized as one of the most vulnerable regions to climate change (Kula et al. (2013); Serdeczny et al. (2017)) and more specifically, the region of southern Africa (SAF) has been identified as a climate change hotspot (Diffenbaugh and Giorgi (2012)). Taking into consideration that the majority of the population living in SAF (70%) is dependent on rainfed agriculture (Mabhaudhi et al. (2018)), any climate change induced alteration of the spatiotemporal patterns of precipitation will require a rapid adaptation of the agricultural sector. Concurrently, SAF is also characterized by low adaptive capacity to changes in climatic conditions Davis and Vincent (2017), hence, it emerges as a high risk region. In addition, approximately 26% of the SAF population is undernourished (AFDB (2019)). This figure is expected to increase significantly by 2050 Tirado et al. (2015). Apart from the impacts on the agricultural sector though, climatic changes are expected to alter the spatiotemporal patterns of vector-borne disease occurrence (Rocklöv and Dubrow (2020)), cause severe damage to infrastructure and road networks (Chinowsky et al. (2015)) and exacerbate poverty (Azzarri and Signorelli (2020)). Due to these impacts it is critical that the current spatiotemporal patterns of precipitation are accurately reproduced by our modelling systems and observations (whether in-situ, reanalysis or satellite) over SAF. Only then can we credibly assess future climate change impacts and inform strategies aiming to mitigate their effects on local communities.

Towards this end, satellite, gauge-based and reanalysis products are extensively used, in order to monitor current spatial and temporal precipitation patterns and to further characterize precipitation variability and change during recent decades. For future projections however, climate models able to simulate the (thermo)dynamical processes of the atmosphere are employed. Such an endeavor has been

performed in the context of the Coupled Model Intercomparison Project Phase 5 (CMIP5) Taylor et al. (2012) using General Circulation Models (GCMs) and in the context of the Coordinated Regional Climate Downscaling Experiment (CORDEX) – Africa domain (Giorgi and Gutowski (2015)) using Regional Climate Models (RCMs). The latest advancement in the climate modelling community involves GCMs and earth system models (ESMs), participating in the CMIP6 ensemble, providing input for the 6th Assessment Report of the Intergovernmental Panel on Climate Change (IPCC) (Eyring et al. (2016)). However, the confidence with which one can claim future climate projections produced by GCMs, ESMs or RCMs are fit for purpose, is usually assessed based on their ability to simulate current climatic conditions. For instance, Munday and Washington (2017) showed that the CMIP5 ensemble displayed a systematic wet bias over the SAF region that was caused by the misrepresentation of orographic features located over the area of Tanzania. A wet bias caused by structural model errors was also identified in the dynamically downscaled and higher-resolution CORDEX-Africa ensemble (Kim et al. (2014)). Therefore, a valid question arises as to what the most suitable dataset is, with which climate impact studies can be fed with when the SAF region is concerned. In addition, before the task of characterizing future precipitation trends is addressed, it is imperative to diagnose the degree to which observed precipitation trends over the recent decades are reproduced by GCMs and RCMs.

A comprehensive analysis of the performance of the CORDEX-Africa ensemble over Africa was first presented in Nikulin et al. (2012). They showed that during the rainy season (Jan-Mar as used in Nikulin et al. (2012)) there is a weak wet bias over southern Africa, and that the use of the ensemble mean was able to outperform individual models, highlighting the importance of ensemble-based approaches. The Nikulin et al. (2012) analysis was conducted on a pan-African scale. Similarly, Kalognomou et al. (2013) analyzed the same ensemble of CORDEX-Africa simulations, focusing over southern Africa and reported similar findings. In Meque and Abiodun (2015) the same ensemble of 10 evaluation simulations was again used, but it was also compared with a set of CMIP5 GCM simulations, with the purpose to identify a causal association between ENSO and drought events over southern Africa. In Meque and Abiodun (2015) it was stated that RCMs were able to provide added value, compared to their driving GCMs. A comprehensive assessment of the added value between historical CORDEX-Africa RCMs simulations and of their driving CMIP5 GCMs on a seasonal timescale over the whole of Africa, was performed in Dosio et al. (2019). The first time the CORDEX-Africa ensemble is compared to both CMIP5 and CMIP6 ensembles is presented in Dosio et al. (2021). More specifically, in Dosio et al. (2021) the analysis is performed on a seasonal timestep and on pan-African scale and its particular emphasis is placed on the projected changes of future precipitation, although a part of the analysis is dedicated to the period 1981-2010.

Satellite and gauge-based datasets display increasing trends during the historical period for annual precipitation over SAF (32-41 mm year-1 per decade), an observation that is also identifiable in the Atmospheric Model Intercomparison Project (AMIP), but not in CMIP5 (Maidment et al. (2015)). During DJF, precipitation trends over SAF display a remarkably robust signal in gauge-based, satellite and AMIP datasets (Maidment et al. (2015)). In addition, Onyutha (2018) also reported on the increasing precipitation trends over SAF during DJF, especially after the 1960's. However, according to CMIP5, precipitation is projected to decrease over SAF in the 21st century (IPCC and Stocker (2013)). This estimate also holds for simulations performed using RCMs forced with CMIP5 (Pinto et al. (2016); Dosio et al. (2019)). The

increase of the observed precipitation trends over SAF has been attributed to the recent strengthening of the Pacific Walker Circulation (Maidment et al. (2015)), which is captured in observational datasets and in AMIP simulations, but not in CMIP5 (L'Heureux et al. (2013); Yim et al. (2016)). CMIP6 displays an even more robust future decline in precipitation and increase of drought events over SAF, relative to its predecessor (Ukkola et al. (2020)). However, although the CMIP6 ensemble exhibits multiple improvements on various levels (Wyser et al. (2020)), certain biases and challenges identified in CMIP5 during the historical period persist in CMIP6 (Kim et al. (2020)).

RCMs are known to add value to climate simulations over regional scales, mainly because the spatial resolution increases, resolving atmospheric waves in a more detailed manner and also, because surface characteristics interacting with the atmosphere are represented more accurately (Denis et al. (2003); Giorgi et al. (2014)). Considering the aforementioned challenges displayed in the CMIP5 simulations to accurately capture precipitation amounts under current climatic conditions and recent precipitation trends, we investigate the degree to which this observation holds also for RCMs, forced with GCMs participating in the CMIP5 ensemble. Theory tells us that RCMs develop their own physics. However, often times the impact of the driving GCMs is evident on the RCM simulations (Denis et al. (2003); Laprise et al. (2008); Di Luca et al. (2013); Di Luca et al. (2013)).

Therefore, in this chapter we expand on previous research to investigate how monthly precipitation during the rainy season over southern Africa is simulated by different modelling systems, by analyzing the monthly precipitation climatologies, the interannual variability, specific precipitation indices and monthly precipitation trends during the period 1986-2005, in four different modeling systems (CORDEX 0.220/0.440, CMIP5/6) and observational ensembles (satellite, reanalysis and gridded datasets). Our main goal is to provide a comprehensive overview with regards to precipitation climatology over SAF as simulated by the state-of-the-art tools used by climate scientists. In addition, we investigate whether higher resolution models are able to provide an improved representation of precipitation over southern Africa and we investigate how a particularly important atmospheric feature, the Angola Low (AL) pressure system, is simulated in the RCM and GCM ensembles.

2.2 Data

We analyse daily and monthly precipitation from 5 types of datasets, namely observational datasets (OBS), GCMs and ESMs that comprise the CMIP5 and CMIP6 ensembles and regional climate models (RCMs) that comprise the CORDEX-Africa ensemble at 0.44° of spatial resolution (CORDEX0.44) and at 0.22° of spatial resolution (CORDEX0.22). The analysis is concerned with the SAF region, which is defined as the area between 10 °E to 42 °E and 10 °S to 35 °S. The analysed period is 1986-2005. Although satellite and reanalysis products cannot be termed as purely "observational", in the context of the current work they are classified as such, in order to differentiate them from climate model datasets (CORDEX0.44, CORDEX0.22, CMIP5, CMIP6). Hereafter "OBS" refers to satellite, gauge-based and reanalysis products.

2.2.1 Observational data

The OBS data used are based on the analysis of Le Coz and van de Giesen (2020) and are comprised of five gauge-based products (datasets that are derived by spatial interpolation of rain gauges and station data: CRU.v4.01, UDEL.v7, PREC/L.v0.5, GPCC.v7, CPC-Global.v1), six satellite products and one reanalysis product, ERA5. The datasets have a temporal coverage that extends through the analysed period (1986-2005). The gauge-based products are chosen so that they have a spatial resolution less than or equal to 0.5° x 0.5° and the satellite products have a spatial resolution less or equal to 0.25° x 0.25°. For satellite products however, there is an exception for two products (CMAP.v19.11and GPCP.v2.2) with a resolution equal to 2.5° x 2.5° that are also included in the analysis due to their wide use in the literature. The OBS ensemble is made of 12 products. More details concerning the OBS datasets are provided in Table 2.2.1. In certain parts of the following analysis, the OBS products are either used collectively or they are split into sub-ensembles, based on the methods used for their production. More specifically, these sub-ensembles are the mean of all gauge-based precipitation products (Gauge-Based), the ensemble mean of satellite products that merge with rain gauges (Satellite-Merge) (ARC.v2, CMAP.v19.11, GPCP.v2.2) and the ensemble mean of satellite products that do not merge directly with rain gauges (Satellite-NoMerge) (CHIRPS.v2, TAMSAT.v3, PERSIANN-CDR), but use alternative methods such as calibration, bias adjustment or artificial neural network techniques (Le Coz and van de Giesen (2020)).

Table 2.2.1: Observational datasets used.

Dataset	Resolution	Frequency	Type	Period	Reference
ARC.v2	0.1°	Daily total	Satellite	1983-present	Novella and Thiaw (2013)
PERSIANN-CDR	0.25°	Daily total	Satellite	1983-present	Ashouri et al. (2015)
CMAP	2.5°	Monthly mean	Satellite	1979-present	Xie and Arkin (1997)
TAMSAT.v3	0.0375°	Daily total	Satellite	1983-present	Tarnavsky et al. (2014)
GPCP.v2	2.5°	Monthly mean	Satellite	1979-2015	Adler et al. (2012)
CRU TS4.01	0.5°	Monthly total	Gauge-Based	1901-2016	Harris et al. (2014)
GPCC.v7	0.5°	Monthly total	Gauge-Based	1901-2013	Schneider et al. (2015)
PREC/L	0.5°	Monthly mean	Gauge-Based	1948-2012	Chen et al. (2002)
UDEL.v4.01	0.5°	Monthly total	Gauge-Based	1900-2014	Willmott and Matsuura (2001)
CPC-Unified	0.5°	Daily total	Gauge-Based	1979-present	Chen et al. (2008)
CHIRPS.v2	0.5°	Daily total	Satellite	1981-present	Funk et al. (2015)
ERA5	0.25°	Hourly	Reanalysis	1979-present	Hersbach et al. (2020)

2.2.2 Climate model simulations

Daily precipitation for a set of 25 RCM simulations performed as part of CORDEX-Africa historical simulations at 0.44° x 0.44° (50 km) of horizontal spatial resolution are utilised, comprising the CORDEX0.44 ensemble, shown in Table 2.2.2. In addition, a set of 10 RCM simulations performed also within CORDEX-Africa, as part of the CORDEX-CORE project (Coppola et al. (2021)), available at 0.22° x 0.22° (25 km) of horizontal spatial resolution (CORDEX0.22) are also retrieved, shown in Table 2.2.3.

Table 2.2.2: CORDEX-Africa historical simulations participating in the Coordinated Regional Climate Downscaling Experiment (CORDEX) Africa ensemble used in the current analysis, with a horizontal spatial resolution equal to 0.44° (CORDEX0.44). Data are retrieved from the Earth System Grid Federation (`https://esgf-data.dkrz.de/projects/esgf-dkrz/`).

RCM	Institute	LBC	Realization	Reference
CCLM4-8-17.v1	CLMcom	CNRM-CM5	r1i1p1	COSMO (2020)
		EC-EARTH	r12i1p1	
		HadGEM2-ES	r1i1p1	
		MPI-ESM-LR	r1i1p1	
HIRHAM5.v2	DMI	EC-EARTH	r3i1p1	Christensen et al. (2007)
RACMO22T.v1	KNMI	EC-EARTH	r1i1p1	van Meijgaard et al. (2008)
		EC-EARTH	r12i1p1	
		HadGEM2-ES	r1i1p1	
RCA4.v1	SHMI	CanESM2	r1i1p1	Samuelsson et al. (2015)
		CNRM-CM5	r1i1p1	
		CSIRO-Mk3-6-0	r1i1p1	
		EC-EARTH	r12i1p1	
		IPSL-CM5A-MR	r1i1p1	
		HadGEM2-ES	r1i1p1	
		MPI-ESM-LR	r1i1p1	
		NorESM1-M	r1i1p1	
		GFDL-ESM2M	r1i1p1	
REMO2009.v1	MPI - CSC	EC-EARTH	r12i1p1	Jacob et al. (2012)
	MPI - CSC	MPI-ESM-LR	r1i1p1	
	GERICS	IPSL-CM5A-MR	r12i1p1	
	GERICS	MIROC5	r1i1p1	
	GERICS	HadGEM2-ES	r1i1p1	
	GERICS	GFDL-ESM2G	r1i1p1	
CRCM5.v1	CCCma	CanESM2	r1i1p1	Scinocca et al. (2016)
		MPI-ESM-LR	r1i1p1	

SHMI: Swedish Meteorological and Hydrological Institute, CLMcom: Climate Limited-area Modelling Community, DMI: Danish Meteorological Institute, KNMI: Royal Netherlands Meteorological Institute, MPI-CSC: Max Planck Institut and Climate Service Center Germany, Helmholtz-Zentrum Geesthacht, GERICS: Climate Service Center Germany, CCCma: Canadian Centre for Climate Modelling and Analysis

Table 2.2.3: CORDEX-Africa historical simulations participating in the Coordinated Regional Climate Downscaling Experiment (CORDEX) Africa ensemble used in the current analysis, with a horizontal spatial resolution equal to 0.22° (CORDEX0.22). Data were retrieved from the Earth System Grid Federation (`https://esgf-data.dkrz.de/projects/esgf-dkrz/`).

RCM	LBC	Realization	Variables available
CanRCM4	CanESM2	r1i1p1	pr
CCLM5-0-15	HadGEM2-ES	r1i1p1	pr, hus850, ua850, va850, ta850
REMO2015		r1i1p1	
RegCM4-7		r1i1p1	
CCLM5-0-15	MPI-ESM-LR	r1i1p1	pr, hus850, ua850, va850, ta850
REMO2015		r1i1p1	
RegCM4-7		r1i1p1	
CCLM5-0-15	NorESM1-M	r1i1p1	pr, hus850, ua850, va850, ta850
REMO2015		r1i1p1	
RegCM4-7		r1i1p1	

In addition, daily precipitation was retrieved for a set of 10 CMIP5 GCMs, with 3 additional simulations with variations in the GCM's resolution (IPSL-LR/IPSL-MR), the ocean model (GFDL-ESM2M/GFDL-ESM2G) and Realization/Initialization/Physics (ICHCE-EC-EARTH-r1i1p1/ ICHCE-EC-EARTH-r12i1p1). The CMIP5 models selected, were the ones used as forcing in the CORDEX0.44 historical simulations. In total, precipitation from a set of 13 CMIP5 simulations was used. Additionally, daily precipitation from a set of 8 CMIP6 GCM and ESM simulations was used. The CMIP6 simulations selected, were performed with the updated versions of the same models that were part of the CMIP5 ensemble. This selection served to construct CMIP5 and CMIP6 ensembles that were comparable. Precipitation data for all simulations were retrieved from the Earth System Grid Federation (ESGF). In addition, temperature at 850 hPa for both CORDEX0.44/0.22 was retrieved. For the CMIP5 and CMIP6 simulations, temperature and geopotential height at 850 hPa was retrieved from the Climate Data Store (CDS). Geopotential height at 850 hPa was not available for CORDEX-Africa simulations. Lastly, elevation data for CORDEX-Africa and CMIP5 were obtained from ESGF, while the Shuttle Radar Topography Mission (SRTM) (Farr et al. (2007)) Digital Elevation Model was used as the observed elevation in the topography transects for a selected latitude over SAF. Details about the models used are provided in Table 2.2.4 (for CMIP5) and in Table 2.2.5 (for CMIP6).

Table 2.2.4: General circulation models participating in the Coupled Model Intercomparison Project Phase 5 (CMIP5) that were used as forcing fields in the Coordinated Regional Climate Downscaling Experiment (CORDEX) Africa historical simulations. Data for precipitation were retrieved from the Earth System Grid Federation (`https://esgf-data.dkrz.de/projects/esgf-dkrz/`). Data for temperature at 850 hPa were retrieved from the Climate Data Store (`https://cds.climate.copernicus.eu`).

GCM	Institute	Ensemble	Latitude Res.	Longitude Res.	References
CanESM2	CCCma	r1i1p1	2.7906	2.8125	CCCma (2017)
CNRM-CM5	CERFACS	r1i1p1	1.40008	1.4062	Voldoire et al. (2013)
CSIRO-MK3-6-0	CSIRO	r1i1p1	1.8653	1.875	Jeffrey et al. (2013)
EC-EARTH	DMI	r1i1p1 r12i1p1	1.1215	1.125	Hazeleger et al. (2010)
GFDL-ESM2M GFDL-ESM2G	NOAA	r1i1p1	2.0225	2.5	Dunne et al. (2012)
HadGEM2-ES	Met Office	r1i1p1	1.25	1.875	Collins et al. (2011)
IPSL-CM5A-MR IPSL-CM5A-LR	IPSL	r1i1p1	1.2676	2.5	Dufresne et al. (2013)
MIROC5	AORI	r1i1p1	1.4008	1.40625	Watanabe et al. (2010)
MPI-ESM-LR MPI-ESM-MR	MPI	r1i1p1	1.8653	1.875	
NORESM1-M	EarthClim	r1i1p1	1.8947	2.5	Bentsen et al. (2013)

CCCma: Canadian Centre for Climate Modelling and Analysis, CERFACS: Centre Européen de Recherche et de Formation Avancée en Calcul Scientifique, CSIRO: Commonwealth Scientific and Industrial Research Organisation, DMI: Danish Meteorological Institute, NOAA: National Oceanic and Atmospheric Administration, IPSL: Institute Pierre Simon Laplace, AORI: Atmosphere and Ocean Research Institute, MPI: Max Planck Institut

Table 2.2.5: General circulation models participating in the Coupled Model Intercomparison Project Phase 6 (CMIP6). Data were retrieved from the Earth System Grid Federation (`https://esgf-data.dkrz.de/projects/esgf-dkrz/`). The CMIP6 models used were selected in accordance to their predeseccor CMIP5, so that the 2 ensembles (CMIP5 and CMIP6) would be comparable.

GCM	Institute	Ensemble	Latitude Res.	Longitude Res.	References
CanESM5	CCCma	r1i1p1f1	2.7906	2.8125	Swart et al. (2019)
CNRM-CM6-1	CERFACS	r1i1p1f1	1.40008	1.4062	Voldoire et al. (2019)
EC-EARTH3	DMI	r1i1p1f1	1.1215	1.125	Massonnet et al. (2020)
GFDL-ESM4	NOAA	r1i1p1f1	2.0225	2.5	Held et al. (2019)
IPSL-CM6A-LR	IPSL	r1i1p1f1	1.2676	2.5	
MIROC6	AORI	r1i1p1f1	1.4008	1.40625	Tatebe et al. (2019)
MPI-ESM-2-LR	MPI	r1i1p1f1	1.8653	1.875	Mauritsen et al. (2019)
NorESM2-LM	EarthClim	r1i1p1f1	1.8947	2.5	Seland et al. (2020)

CCCma: Canadian Centre for Climate Modelling and Analysis, CERFACS: Centre Européen de Recherche et de Formation Avancée en Calcul Scientifique, CSIRO: Commonwealth Scientific and Industrial Research Organisation, DMI: Danish Meteorological Institute, NOAA: National Oceanic and Atmospheric Administration, IPSL: Institute Pierre Simon Laplace, AORI: Atmosphere and Ocean Research Institute, MPI: Max Planck Institut

2.3 Methodology

Precipitation climatologies are investigated on a monthly basis, due to the fact that precipitation over SAF arises as the result of atmospheric mechanisms that display high variability during the rainy season. The aggregation of precipitation to seasonal means might often obscure certain spatial characteristics that are better identified on a monthly basis. The within-ensemble agreement is investigated using the sample standard deviation (SD), which is calculated using monthly mean values over the period 1986-2005 for each model (or observational dataset) separately. Also, four precipitation indices are constructed in the context of the Expert Team on Climate Change Detection and Indices (ETCCDI) (Peterson and Manton (2008)), utilising daily precipitation amounts for the period 1986-2005. The four ETCCDI indices are used to describe total annual precipitation (PRCPTOT), annual maximum daily precipitation (Rx1Day), annual number of days with daily precipitation >10 mm (R10mm) and annual number of days with daily precipitation >20 mm (R20mm). These indices are calculated for each individual simulation of each ensemble (CMIP5, CMIP6, CORDEX0.44 and CORDEX0.22), and OBS products, separately and yield a value for every year (Jan-Dec) during the period 1986-2005. The calculation of indices required data having a daily temporal resolution, hence, observational datasets that provided monthly aggregates are excluded. The spatial averages calculated over SAF for the annual cycle and the ETCCDI indices consider land grid points only. For the construction of ensemble means, either in observational or model

ensembles, datasets are remapped to the coarser grid using conservative remapping for precipitation, and bilinear interpolation for temperature and geopotential height at 850 hPa.

In order to investigate some basic thermodynamical aspects that may differentiate precipitation in the CMIP5/6 and the CORDEX0.44/0.22 ensembles, the seasonal representation of the Angola Low (AL) pressure system over SAF is examined. The AL pressure system is a semi-permanent synoptic scale system, that plays a strong role in modulating precipitation over SAF (Reason and Jagadheesha (2005); Lyon and Mason (2009); Crétat et al. (2019); Munday and Washington (2017); Howard and Washington (2018)). More specifically, the reason why the AL pressure system is emphasized in the current work, is because it redistributes low-tropospheric moisture entering SAF from the southern Atlantic and the southern Indian Oceans and also, moisture transport originating from the Congo Basin. In addition, AL events precede the formation of Tropical Temperate Troughs (TTTs) and hence, they can be considered as their precursor in the "climate process chain" (Daron et al. (2019)). As stated in Howard and Washington (2018), it is common that AL events precede TTT events, since the AL pressure system functions as a key process necessary for the transport of water vapor from the tropics towards the extratropics (Hart et al. (2010)).

In Munday and Washington (2017) AL events are identified using geopotential height at 850 hPa. However, since geopotential height at 850 hPa is not available for CORDEX0.44/0.22 simulations, this method can not be employed here. Hence, based on the variables that are already available within both CORDEX and CMIP5/6 ensembles, potential temperature at 850 hPa (theta850) is used instead as an alternative "proxy" variable that provides thermodynamical information. In order to ensure that theta850 can be used instead of zg850, the relationship between theta850 and zg850 over the study region is examined in ERA5, for each month of the rainy season (Oct-Mar), using the climatological mean monthly values for the period 1986-2005 (2.3.1). As shown in Fig. 2.3.1a, during October over the south-eastern part of Angola, there is a region of low geopotential heights. Moving towards the core of the rainy season, the low-pressure system deepens, while there seems to be a weak extension of low geopotential heights towards the south. Also, as shown in Fig. 2.3.1b, during October there is an area of high theta850 values located over south-eastern Angola, coinciding with the region of low zg850 values. As stated in Munday and Washington (2017), this is indicative of the dry convection processes that are at play during the beginning of the rainy season over the region. Moving towards DJF, the high theta850 values move southwards, indicating that during the core rainy season, convection over the greater Angola region is not thermally induced, but there is a rather dynamical large-scale driver.

In Fig. 2.3.2 the scatterplots between zg850 (x-axis) and theta850 (y-axis) for each month of the rainy season are shown, over the whole southern Africa region (land grid points only). The same plot, but with grid points only from the greater Angola region (14 °E to 25 °E and from 11 °S to 19 °S) is displayed in Fig. 2.3.3. Although the relationship between the two variables is not linear, they display a considerable association, especially over the greater Angola region.

In Howard and Washington (2018) AL events are identified using daily relative vorticity (ζ) at 800 hPa. Since u and v wind components are not available at 800 hPa (but at 850 hPa) for the CORDEX ensembles, it is imperative to investigate whether the 850 hPa pressure level can be used instead. In addition, it is examined whether the ζ threshold as used in Howard and Washington (2018) has to be adjusted. In Howard and Washington (2018), AL events are identified within the region ranging from 14 °E to 25 °E

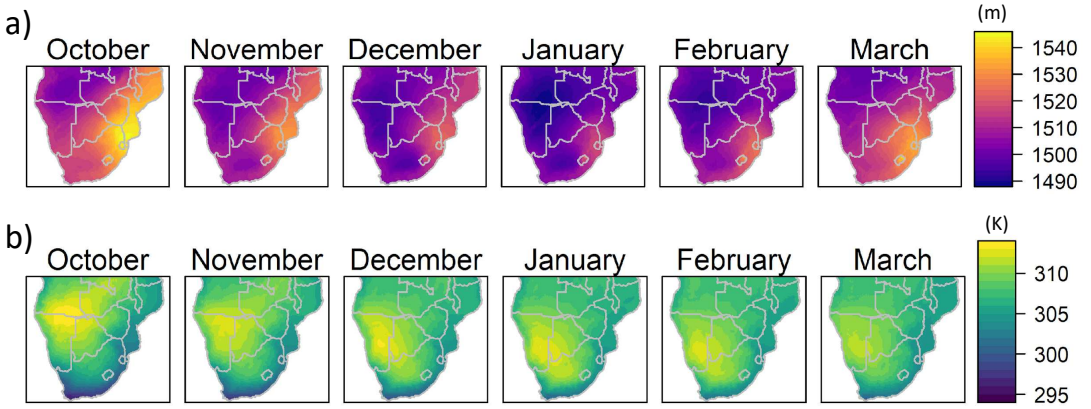

Figure 2.3.1: a) Mean monthly geopotential height at 850 hPa in ERA5 for the period 1986-2005 (in meters), b) Mean monthly potential temperature at 850 hPa in ERA5 for the period 1986-2005 (in Kelvin).

and from 11 °S to 19 °S for mean daily ζ values less than $< -4 \times 10^5\ s^1$. An additional issue that is taken into account, is that u and v wind components are not available on a daily timestep for CMIP6, but only on a monthly timestep. Hence, for consistency reasons monthly files in all ensembles are used (both CMIP, CORDEX) and in ERA5.

With regards to the question of whether the 850 hPa pressure level can be used instead of 800 hPa, monthly relative vorticity in ERA5 is examined in both pressure levels, within the region from 14 °E to 25 °E and from 11 °S to 19 °S (Fig. 2.3.4a and Fig. 2.3.4b). Both distributions are very similar in shape, maxima and spread, although the distribution of ζ values at 800 hPa (Fig. 2.3.4a) appear to have a shorter tail. On both panels, both the Howard and Washington (2018) and the (Desbiolles et al., 2020) thresholds are indicated. Therefore it is concluded that the 850 hPa pressure level can be used instead of 800 hPa. With regards to the fact that u and v wind components are available only on a monthly timestep in CMIP6, daily and monthly relative vorticity values at 800 hPa are compared for all the months of the rainy season (Oct-Mar) (Fig. 2.3.4c and Fig. 2.3.4d).

The difference in the y-axis results from the fact that when ζ is calculated using a daily timestep, the histogram is drawn using 5,421,825 values, while when ζ is calculated using monthly u and v values, it is drawn using 178,200 values (for the period 1986-2005). As shown, the distribution of the monthly values has a much shorter tail and the Howard and Washington (2018) threshold appears to be a very strict criterion for the identification of AL events. Concerning the question of what the optimal threshold for the identification of AL events in all datasets is, the statistical distribution of mean monthly cyclonic vorticity in all ensembles is investigated, for the 850 hPa pressure level (Fig. 2.3.5).

Moreover, it is concluded that the threshold used in Desbiolles et al. (2020) (ζ values $< -1.5 \times 10^5\ s^1$) is reasonable, considering the shape of the distributions examined. However, when the Desbiolles et al. (2020) threshold is applied to the data, it is also found to be too strict, especially for CMIP5/6. Hence, AL events are identified having ζ <-0.00001 s^1. Lastly, geopotential height at 850 hPa is used for visual inspection only in the ERA5 and CMIP5/6 ensembles. Lastly, the Theil-Sen's slope (Theil (1992);Sen (1968)) for monthly precipitation during the period 1986-2005 is calculated for each dataset. This is

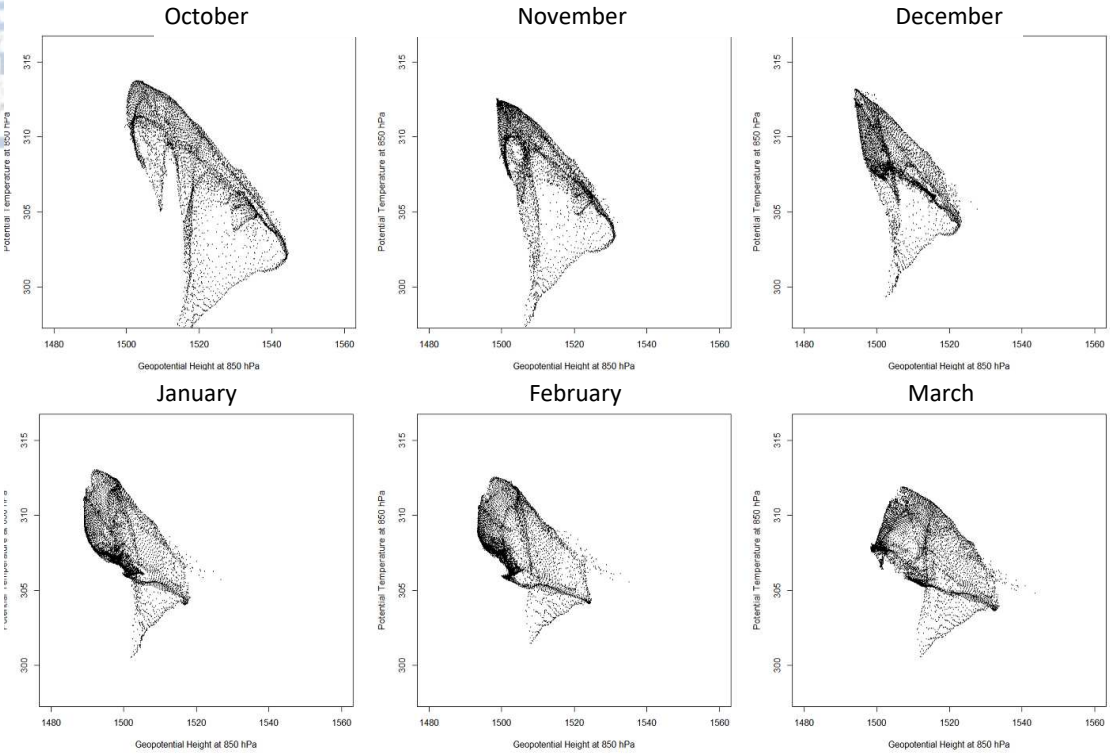

Figure 2.3.2: Geopotential height at 850 hPa in meters (x-axis) plotted against potential temperature at 850 hPa in Kelvin (y-axis). Values refer to climatological monthly means for the period 1986-2005. Each dot in the scatterplot represents a grid point of the ERA5 dataset over the whole southern Africa region from 10 °E to 42 °E and from 10 °S to 35 °S.

a non-parametric approach to estimate trends, that is insensitive to outliers. Statistical significance is assessed using the Mann-Kendall test (Mann (1945); Kendall (1948)).

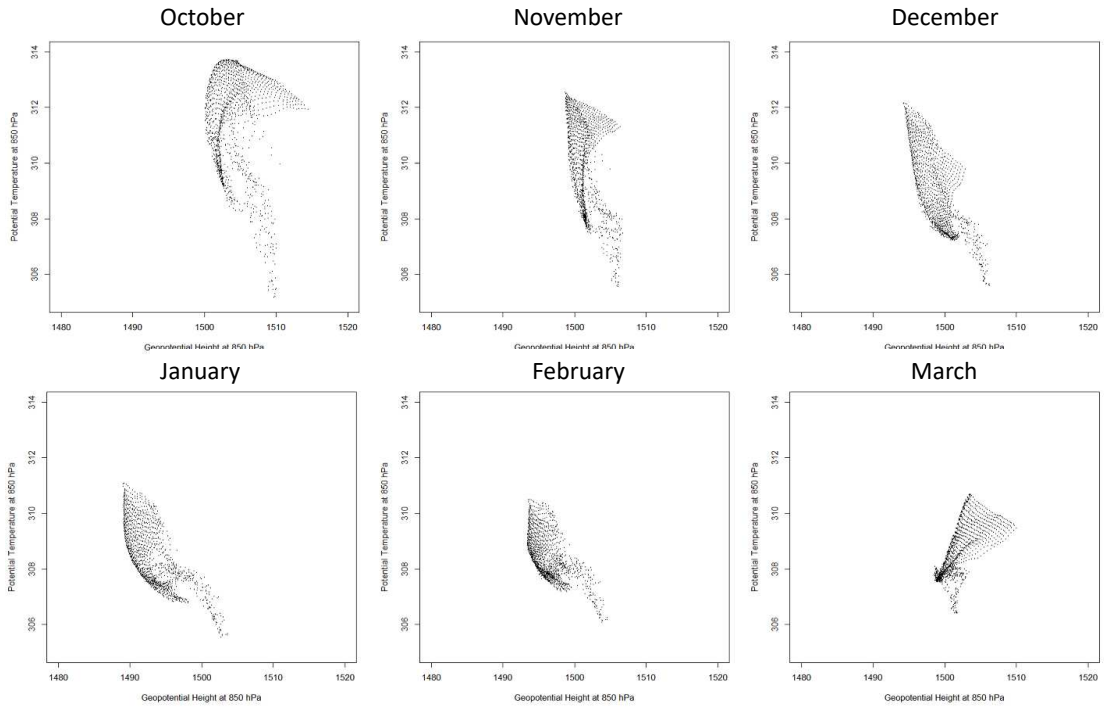

Figure 2.3.3: Geopotential height at 850 hPa in meters (x-axis) plotted against potential temperature at 850 hPa in Kelvin (y-axis). Values refer to climatological monthly means for the period 1986-2005. Each dot in the scatterplot represents a grid point of the ERA5 dataset over the greater Angola region, from 14 °E to 25 °E and from 11 °S to 19 °S.

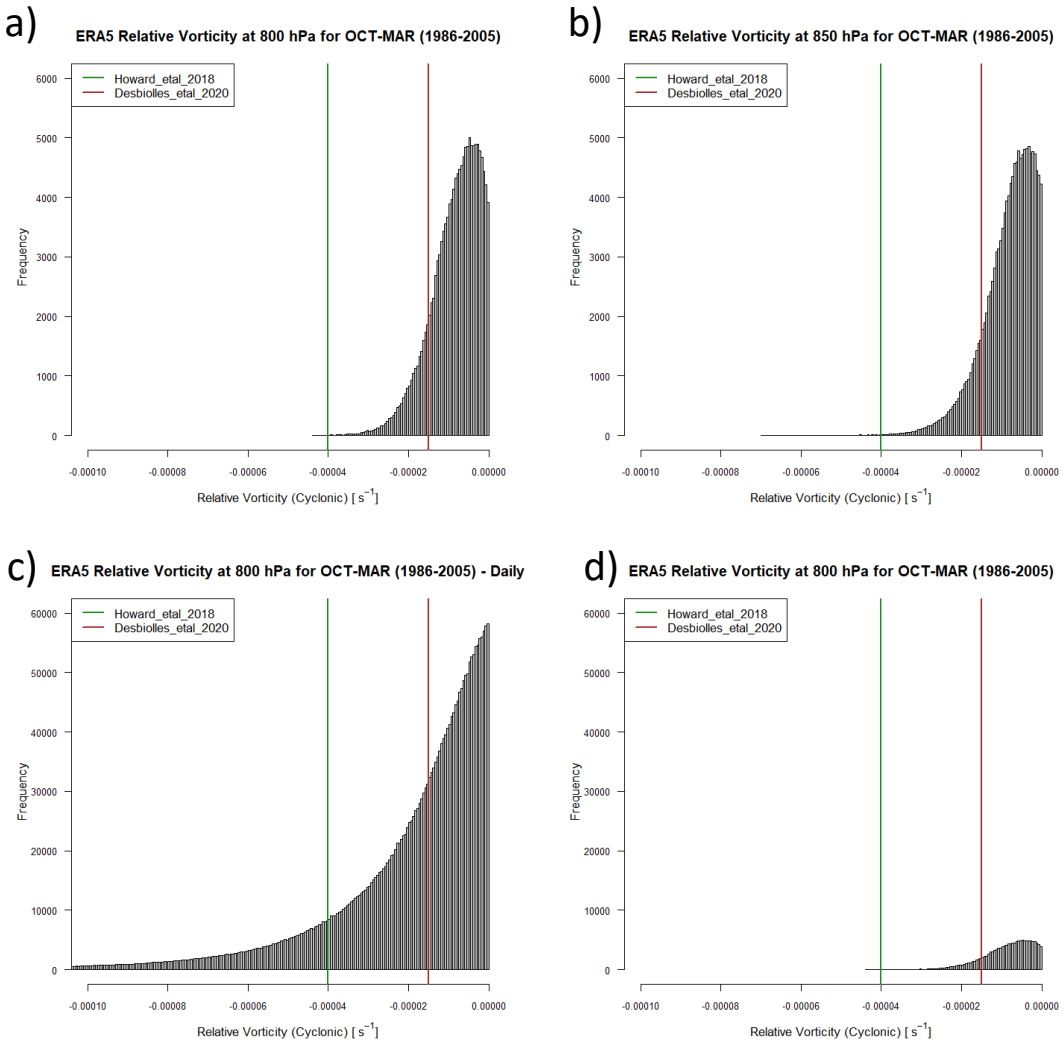

Figure 2.3.4: Histogram of relative vorticity for months Oct-Mar during 1986-2005 in ERA5 using u and v values at 800 hPa (a) and at 850 hPa (b). Grid points used are enclosed within the region from 14 °E to 25 °E and from 11 °S to 19 °S. For both histograms mean monthly u and v values are used. Histogram of relative vorticity for months Oct-Mar during 1986-2005 in ERA5 using daily u and v values (c) and using monthly u and v values (d).

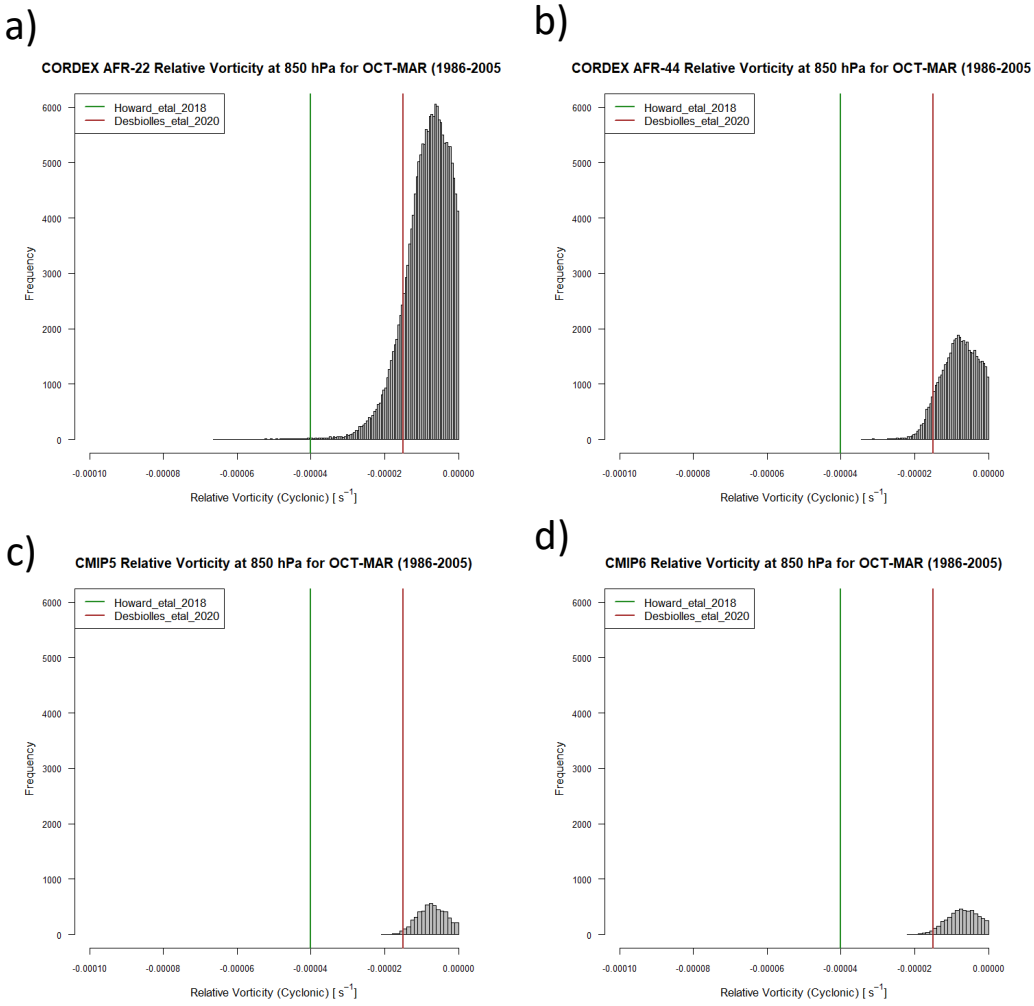

Figure 2.3.5: Histogram of relative vorticity for months Oct-Mar during 1986-2005 at 850 hPa for CORDEX-Africa at 0.22° (a), for CORDEX-Africa at 0.44° (b), for CMIP5 (c), and for CMIP6 (d). Grid points used are enclosed within the region from 14 °E to 25 °E and from 11 °S to 19 °S. For all histograms mean monthly u and v values are used.

2.4 Results

2.4.1 Climatology

Figure 2.4.1 displays monthly precipitation climatologies during Oct-Mar (rainy season over the study region) for ERA5 and for the ensemble means of 7 additional types of datasets. At the beginning of the rainy season (Oct) all products display precipitation maxima at the north-western part of the study region. Another region of precipitation maxima is observed at eastern South Africa. For both regions, there is a slight tendency for gauge-based products to yield approximately 1 mm d^{-1} less precipitation than reanalysis and satellite products. The CMIP5, CMIP6, CORDEX0.44 and CORDEX0.22 ensembles are also in agreement with regards to the location and amounts, however, CORDEX0.44 displays approximately 2 mm d^{-1} more precipitation over Angola. During November, the rainband extends southwards and the region over South Africa experiencing high precipitation enlarges.

Moving towards the core of the rainy season (DJF), precipitation maxima extend southwards following the collapse of the Congo air boundary (CAB) (Howard and Washington (2019)) and high precipitation amounts are also observed over the eastern part of the study region. More specifically during January, high precipitation amounts (>10 mm d^{-1}) are observed over an extended region in northern Mozambique for non-merging satellite products (Satellite-NoMerge). This area is also identified as a region of high precipitation in gauge-based products and in merging satellite products, however, with a smaller magnitude. In ERA5, the spatial pattern of precipitation is patchier and exhibits higher than observed precipitation amounts in the wider region of lake Malawi, reaching extremely high values (34 mm d^{-1}). As is also indicated in the known precipitation issues of ERA5 over Africa (Hersbach et al. (2020)), this is possibly caused by a deficiency in the convection scheme that erroneously yields "explicit-convection" over isolated grid-points. During DJF, both CORDEX0.44 and CORDEX0.22 ensembles display precipitation values >3 mm d^{-1} over almost all of the SAF region. This observation is also consistent in CMIP5 and CMIP6, however, maximum precipitation amounts in CMIP5 and CMIP6 are approximately >3 mm d^{-1} larger than in the CORDEX ensembles. It is noteworthy, that in CORDEX0.22 during DJF, there are parts over northern SAF experiencing precipitation amounts >10 mm d^{-1}, a feature that is not seen in any of the observational products. After investigating the individual ensemble members used in the CORDEX0.22 ensemble, it is concluded that the excess amount of precipitation is removed from the CORDEX0.22 ensemble mean when RegCM4-7 simulations are not included (Fig. 2.4.2). In March, the rainband starts its northward shift, nevertheless, high precipitation amounts are still observed over the eastern parts of the study region and over the coastal region of Angola. The retreat of the rainband is evident in both CORDEX0.44 and CORDEX0.22 however, CMIP5 and CMIP6 still exhibit extended regions of high precipitation.

In Fig. 2.4.3, SD values for the seven ensembles are presented during months Oct-Mar for the period 1986-2005 expressed as mm d^{-1}. SD is used as a measure of the within-ensemble agreement. As it is shown for gauge-based products, during October and November high SD values are observed primarily over Angola. For months Dec-Mar Angola remains a high SD region, however, increased SD values are also observed over the eastern parts of SAF and especially over northern Mozambique. An important aspect influencing gauge-based products is the spatiotemporal coverage of the rain gauges used

(Le Coz and van de Giesen (2020)), which is highly variable between regions and reporting periods. More specifically, after the 1970's the rain gauge coverage over Africa has decreased significantly (Janowiak (1988)) and the gauge network has been particularly sparse over the SAF region (Lorenz and Kunstmann (2012); Giesen et al. (2014)), which further implies that gauge-based products depend on extrapolating values from surrounding gauges.

A similar spatiotemporal pattern of SD is also observed in satellite-based products (Sat-Merge) which employ algorithms that merge rain gauges with thermal-infrared (TIR) images. This is indicative of the strong impact that the location and number of rain gauges exert on satellite algorithms that employ merging techniques (Maidment et al. (2014); Maidment et al. (2015)). The spatiotemporal pattern of SD for satellite-based products that do not merge with gauges (Sat-NoMerge) displays low SD values for October and November, however, during DJF localized areas of high SD appear over Angola, Zambia, Malawi and Mozambique. The satellite products used in this ensemble are based on TIR images and precipitation is indirectly assessed through cloud top temperature (Tarnavsky et al. (2014); Ashouri et al. (2015); Funk et al. (2015)). Hence, the occurrence and severity of precipitation is calculated based on a temperature threshold. In cases that the threshold is set to very low cloud top temperature values, the algorithm has high skill at identifying deep convection, however, warm rain events are not adequately captured (Toté et al. (2015)). As it is shown in Fig. 2.4.3, high SD values in non-merging satellite products are primarily observed over coastal regions and over regions where the elevation increases rapidly. These type of regions can be associated with orographic or frontal lifting of air masses (Houze Jr. (2012)), resulting in precipitation, without the threshold temperature of the cloud top being reached.

In the CORDEX0.44 ensemble SD values are >0.8 mm d^{-1} over almost all of the SAF region, however, very high SD values (3-9.8 mm d^{-1}) are observed in the coastal part of Angola and over the lake Malawi region during Nov-Mar. SD values in CORDEX0.22 are considerably larger throughout the greater part of SAF, especially during DJF. In the CMIP5 ensemble the spatiotemporal pattern of SD values exceeds 2 mm d^{-1} during Nov-Mar throughout the whole SAF region. CMIP6 displays a similar SD pattern. During March however, CMIP6 displays a substantial improvement in the agreement between its ensemble members. Overall, for the whole extent of SAF, the CORDEX-Africa ensembles display greater agreement among ensemble members, however SD values become large over specific localized regions, mainly at western Angola and in the Malawi region. The CMIP5 and CMIP6 ensembles although not displaying the localized extreme SD values as CORDEX-Africa, display generally high SD values throughout the whole extent of SAF.

Therefore, station density and the interpolation method employed are key factors in determining the accuracy of the final product (Le Coz and van de Giesen (2020)). The high SD values over Angola, are mainly due to the scarcity of available rain gauges used in the interpolation method (Fig. Fig. 2.4.4). After 1995, there is a noticeable reduction of the station/rain gauge data used over the SAF region (Fig. 2.4.5)) for three of the gauge-based products.

2.4.2 Annual cycle

Figure 2.4.6 displays the annual cycle of precipitation in the CORDEX0.44, CORDEX0.22, CMIP5, CMIP6 and observational ensembles for land grid points. All datasets capture the unimodal distribution of precipitation over SAF, however considerable differences in precipitation amount and spread are ob-

served. Specifically, the CMIP5 ensemble exhibits significantly higher precipitation amounts than both CORDEX and observational ensembles. This difference becomes particularly pronounced during the rainy season, with CMIP5 yielding approximately 2 mm d^{-1} more precipitation than the observational ensemble. It is also notable that for Nov-Feb, even the driest ensemble members of CMIP5 yield approximately 1 mm d^{-1} more precipitation than the wettest ensemble members of the observational data. This is in agreement with Munday and Washington (2018) who identified a systematic wet bias over SAF in CMIP5, that was associated with an intensified north-easterly transport of moisture that erroneously reaches SAF, due to the poorly represented orography in the region of Tanzania and Malawi (which would hinder moisture originating from the Indian Ocean from reaching SAF and instead force it to recurve towards the region of Madagascar). The behaviour of CMIP6 is similar to CMIP5, with a slightly smaller ensemble spread during Jan-Mar and a considerable reduction in spread during November.

The CORDEX0.44 ensemble reduces precipitation amounts during the core of the rainy season (DJF) compared to CMIP5, however, its behavior during the rest of the months is complicated. More specifically, during Aug-Oct CORDEX0.44 displays slightly higher precipitation amounts compared to CMIP5. During November, the difference between the CORDEX0.44 and the CMIP5 ensembles becomes noticeable, with the CMIP5 ensemble median becoming 0.4 mm d^{-1} larger than the CORDEX0.44 ensemble median. During DJF the differences between the two ensembles maximize, with the CORDEX0.44 ensemble displaying good agreement with the OBS ensemble (<1 mm d^{-1} difference in the ensemble medians of CORDEX0.44 and OBS). From March until July, the difference between the CORDEX0.44 and CMIP5 ensembles starts to reduce gradually. The ensemble median of the CORDEX0.22 ensemble is similar to that of the CORDEX0.44 ensemble, however its spread during the rainy season is considerably larger. Taking into consideration that excess precipitation in the CORDEX0.22 ensemble is introduced by RegCM4-7, we observe that the ensemble spread of the CORDEX0.22 ensemble is reduced, when RegCM4-7 is not included in the CORDEX0.22 ensemble.

Since the maximum impact of the north-easterly moisture transport into SAF responsible for the wet bias in CMIP5 occurs during DJF (Munday and Washington (2018)), the impact of the CORDEX0.44 and CORDEX0.22 increase in resolution and the effect of the improved representation of topography is also more intensely identified during DJF. As it is displayed in Fig. 2.4.7, surface orography is substantially improved in the CORDEX ensembles, relative to CMIP5/6.

The improvement of orography has a further effect in blocking moisture transport entering SAF from the northeast, especially during Dec-Jan, as seen in Fig. 2.4.8.

2.4.3 Angola Low pressure system

In Fig. 2.4.9 the mean monthly climatology of the AL pressure system during the rainy season is displayed for the period 1986-2005. The AL is explored by means of relative vorticity, only within the region extending from 14 °E to 25 °E and from 11 °S to 19 °S. This region is characterized by Howard and Washington (2018) as the main region of interest for the AL. In addition, potential temperature at 850 hPa (theta850) is overlaid on relative vorticity, with the first contour set at 308 K, the last contour set at 318 K and the increment between the isotherms being set to 2 K. For ERA5 and the ensemble means of CMIP5/6 the geopotential height at 850 hPa is also available.

As shown in Fig. 2.4.9, ζ values for October are greater than >-0.000025 s^{-1} for ERA5 and CORDEX0.44/0.22

and are relatively weaker in CMIP5 and even weaker in CMIP6. The high cyclonic vorticity values overlap with the 312 K isotherm for all datasets. It is also observed that the isoheights in the ERA5 and CMIP5/6 ensembles are closely collocated with the 312 K isotherms, indicating that the low pressure system observed over the region is caused by the excess heating of the air and hence, it is indicative of a typical heat low pressure system (Munday and Washington (2017); Howard and Washington (2018)). Moving to November, the picture is similar however, the isotherms display a southward extension, while the 850 hPa isoheigths deepen 5 m in ERA5 and CMIP5/6. In December, all datasets display an increase in cyclonic vorticity, however, the maximum heating area has migrated southwards over the Kalahari region. This fact indicates that cyclonic activity over the AL region is no longer due to thermal causes. During December and January the cyclonic activity is enhanced in all datasets and the isotherms have migrated even more southwards, forming the Kalahari heat low, which is distinct from the AL. It is also observed that during January, the isoheights in ERA5 and CMIP5/6 become even deeper. It is also noted that the elongated trough during Dec-Jan can be indicative of the formation of TTTs, which account for a large proportion of rainfall over SAF (Hart et al. (2010)). February displays similar spatial patterns to January for all datasets, however slightly weakened for all variables. In March, cyclonic activity over the region has seized. Taking into consideration the distribution of the cyclonic vorticity field, it is observed that in higher resolution datasets (ERA5, CORDEX0.22), high vorticity values are more severe, on very localized regions. With respect to potential temperature, all datasets during October and November have a similar distribution of theta850 values. It is also noted that CMIP6, in general, displays higher theta850 values and lower geopotential heights, relative to CMIP5.

2.4.4 Precipitation indices

Total annual precipitation (PRCPTOT) is displayed in Fig. 2.4.10a. The mean of the CMIP6 ensemble displays the largest amounts of PRCPTOT (approximately 1000 mm year^{-1}), with CMIP5 following closely. The CORDEX0.44 and CORDEX0.22 ensembles display a very similar behaviour, systematically reducing PRCPTOT amounts seen in CMIP5/6 by approximately 200 mm year^{-1}, yielding PRCPTOT values closer to that of the observational datasets. Both CMIP5/6 and CORDEX0.22/0.44 ensembles display similar within-ensemble variability. The ensemble mean of the observational datasets is considerably lower than CORDEX ensembles and displays an interannual variability between 500-800 mm year^{-1}. Both the ensemble means of CMIP5/6 and CORDEX0.44/0.22 fail to reproduce the interannual variability of the observational ensemble. In Fig. 2.4.10b the annual maximum 1 day precipitation (Rx1Day) is displayed. For Rx1Day, the mean of the CMIP5 ensemble is in close agreement with the mean of the observational ensemble (approximately 40 mm d^{-1}). The ensemble mean of CORDEX0.44 yields larger precipitation amounts (approximately 55 mm d^{-1}) than CMIP5 and the observational ensemble. The CORDEX0.22 ensemble mean displays even higher values (approximately 75 mm d^{-1}). As it is shown in Fig. 2.4.10b, the CORDEX0.44 ensemble mean is influenced by higher Rx1Day values, originating from ensemble members that cluster within the range 65-85 mm d^{-1}. The spread of the CMIP5 ensemble is comparable to that of the observational data, however, the CORDEX0.44/0.22 ensemble spreads are still larger, ranging from 25-85 and from 55-100 mm d^{-1}, respectively. The CMIP6 ensemble falls between the CORDEX0.44 and CMIP5 ensembles, with a spread comparable to that of CMIP5. In Fig. 2.4.10c the annual number of days with daily precipitation greater than 10 mm (R10mm) is presented. It is noted

that the ensemble mean of the CORDEX0.44 ensemble is close to that of the observational datasets (25 days year^{-1} with daily precipitation greater than 10 mm), while the ensemble mean of CORDEX0.22 almost coincides with the mean of the observational datasets. The mean of the CMIP5 ensemble yields approximately 34 days of extreme precipitation annually. It is also highlighted that the CMIP5 ensemble displays a large range of R10mm values (10-55 days year^{-1}). Again, the CMIP6 ensemble mean coincides with that of CMIP5. In Fig. 2.4.10d the annual number of days with daily precipitation greater than 20 mm (R20mm) is shown. There is close agreement between the CMIP5 and CORDEX0.44 ensembles, however both datasets overestimate R20mm relative to the observational data. Again, the CMIP5 ensemble displays the largest spread and a very weak interannual variability is seen on both CMIP5 and CORDEX0.44 ensemble means. The CMIP6 ensemble mean is slightly larger than its predecessor. R20mm in CORDEX0.22 mean is almost identical to the mean of the CMIP6 ensemble.

2.4.5 Trends

In Fig. 2.4.11 the monthly precipitation trends for the rainy season of the period 1986-2005 are displayed for all three observational datasets (gauge-based, SatelliteMerge, Satellite-NoMerge) and for the CORDEX0.44, CORDEX0.22, CMIP5 and CMIP6 ensembles. Precipitation trends display considerable agreement among all three observational datasets, both concerning the signal and the magnitude of the trend. However, the CORDEX0.44/0.22 and CMIP5/6 ensembles display trends that are considerably smaller in magnitude. In addition, CORDEX0.44, CMIP5 and CMIP6 ensembles display fairly distinct spatial patterns that are not in agreement either among them, or with the spatial pattern of precipitation trends displayed by the observational datasets. In general, it is observed that the signal between CORDEX0.44 and CORDEX0.22 is consistent, with trends in CORDEX0.22 displaying a larger magnitude.

More specifically, during October, all observational products display decreasing trends for the most part of SAF that reach up to -0.1 mm d^{-1} per 20 years. During November the signal changes and SAF experiences increasing trends, with an exception for NW SAF, northern Mozambique and regions of eastern South Africa. During December increasing trends become even more spatially extended and pronounced, especially for satellite products. During January, certain areas of decreasing trends over northern SAF appear, while during February decreasing trends are observed over almost the whole extent of SAF. In March, increasing trends are observed in the region extending from southern Mozambique and stretching towards Zimbabwe and southern Zambia.

Monthly precipitation trends in the CORDEX0.44 ensemble are significantly weaker than in the observational datasets and display precipitation increase during Oct–Dec. After January certain regions of intensified decreasing trends appear over southern Angola-northern Namibia and Botswana (Jan) and over Botswana and South Africa (Feb). The pattern of trends is relatively similar in CORDEX0.22, however, the trend magnitude is more enhanced. In CMIP5 decreasing trends are observed during October, but for November increasing trends are observed over the northern part of SAF. During December, strong increasing trends (0.1 mm d^{-1} per 20 years) appear for central SAF, while, during January almost all of the SAF region (with an exception for Mozambique) experiences decreasing precipitation trends. In CMIP6 persistent drying trends are observed almost throughout the whole of SAF and are particularly strong during Jan-Feb (-0.1 mm d^{-1} per 20 years). During March however, the signal is reversed. Statistical significance assessed with the Mann-Kendall test is shown in Fig. , while the number of ensemble

members displaying increasing or decreasing trends in each ensemble is shown in Fig. .

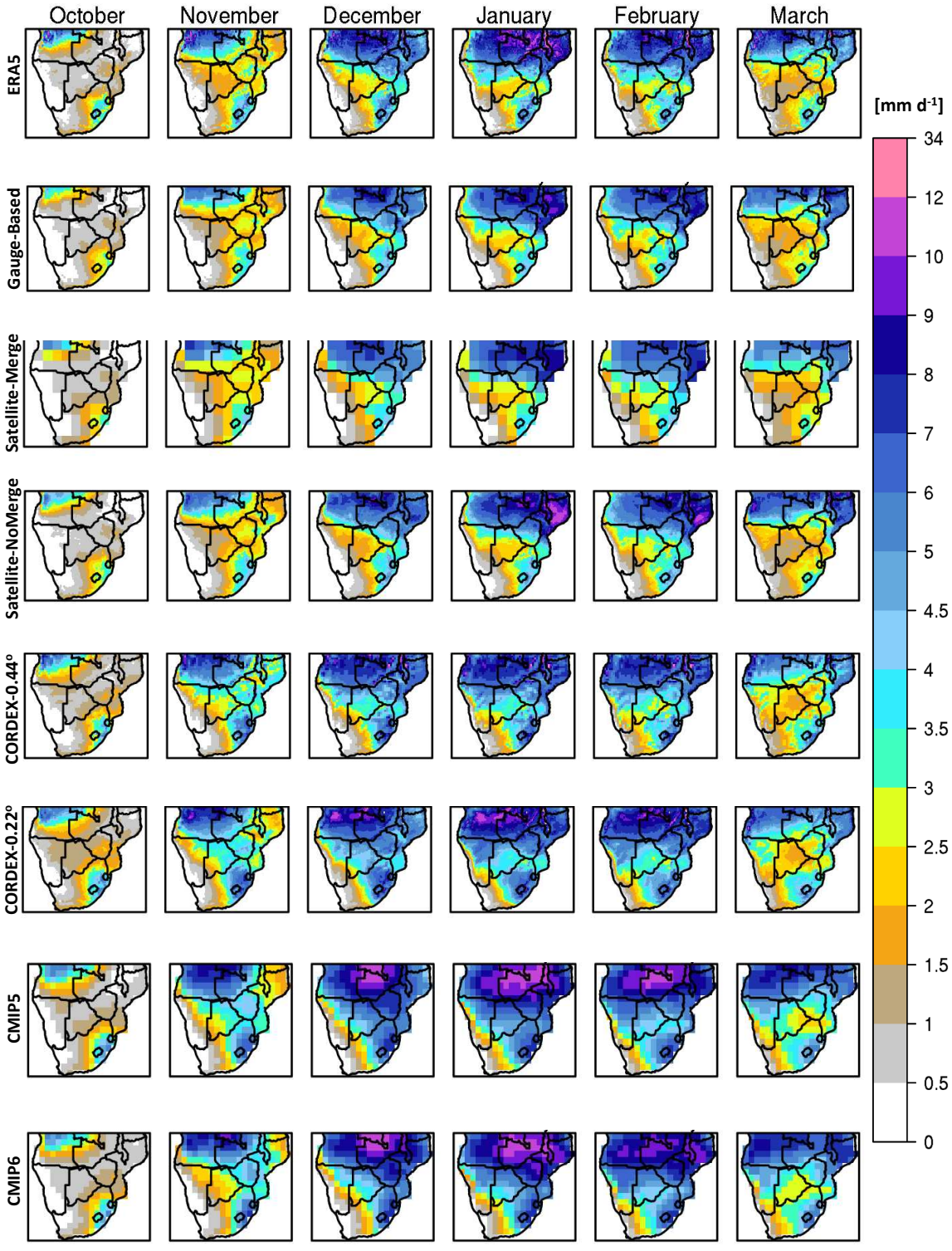

Figure 2.4.1: Monthly precipitation climatologies during the period 1986-2005 in mm d^{-1}.

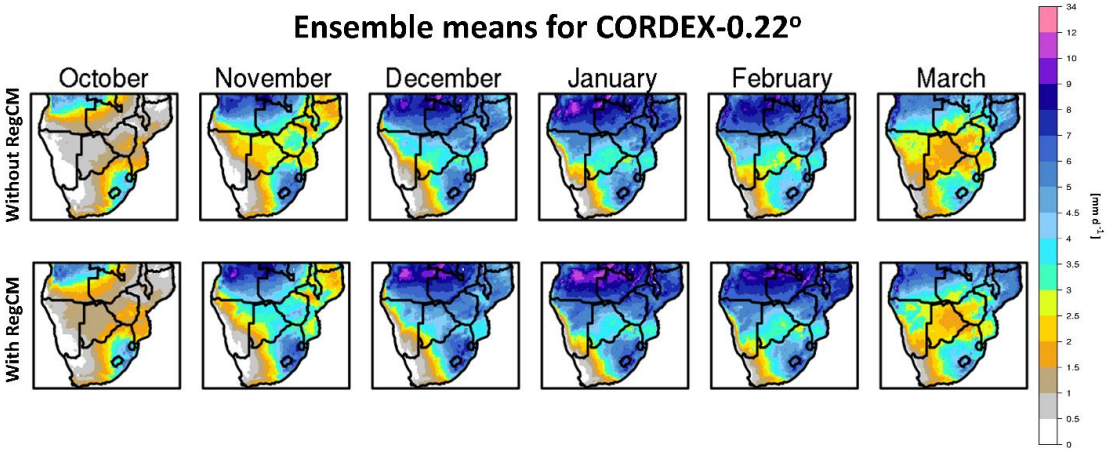

Figure 2.4.2: Ensemble mean of the CORDEX-Africa 0.22° ensemble (CORDEX0.22) by excluding the RegCM4-7 simulations (upper row) and by including all available simulations (bottom row).

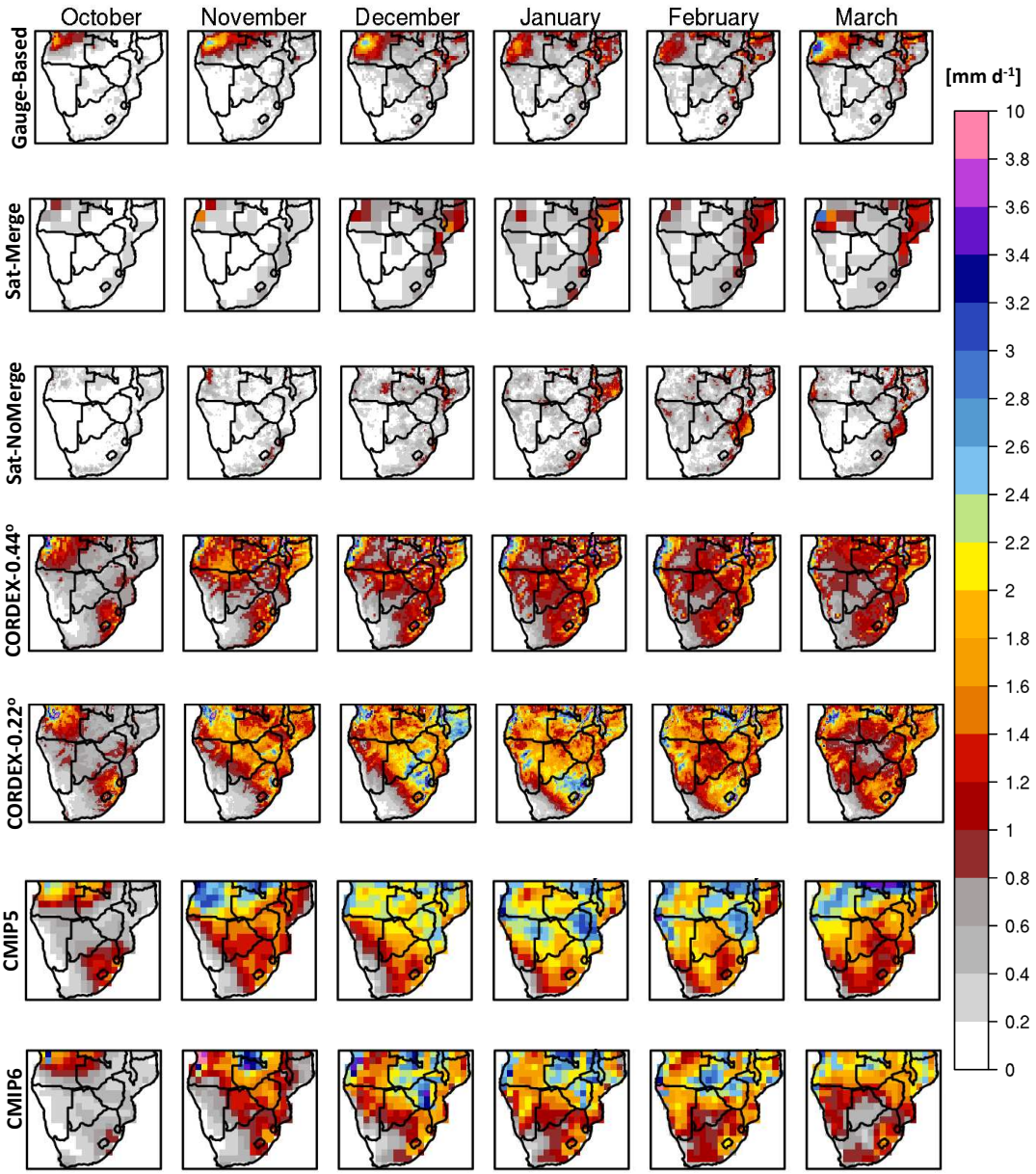

Figure 2.4.3: Standard deviation of monthly precipitation [mm d^{-1}] during the period 1986-2005. From top to bottom: Gauge-based: Ensemble mean of datasets that were produced by employing spatial interpolation methods. Satellite-Merge: Ensemble mean of satellite products that merge with rain gauges. Satellite-NoMerge: Ensemble mean of satellite products that do not merge with rain gauges. CORDEX-0.44°: Ensemble mean of RCM simulations performed within CORDEXAfrica with a spatial resolution equal to 0.44° x 0.44°. CORDEX-0.22°: CORDEX-Africa simulations with a spatial resolution equal to 0.22° x 0.22°. CMIP5: Ensemble mean of CMIP5 GCMs. CMIP6: Ensemble mean of CMIP6 GCMs.

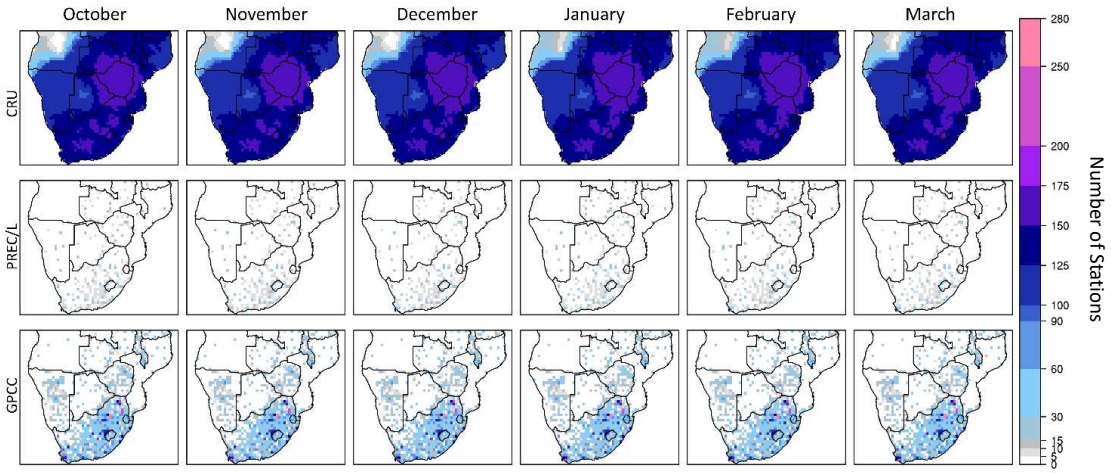

Figure 2.4.4: Total number of reporting stations/rain-gauges for each month during the period 1986-2005, used in the interpolation process of each gauge-based product (CRU, PREC/L, GPCC).

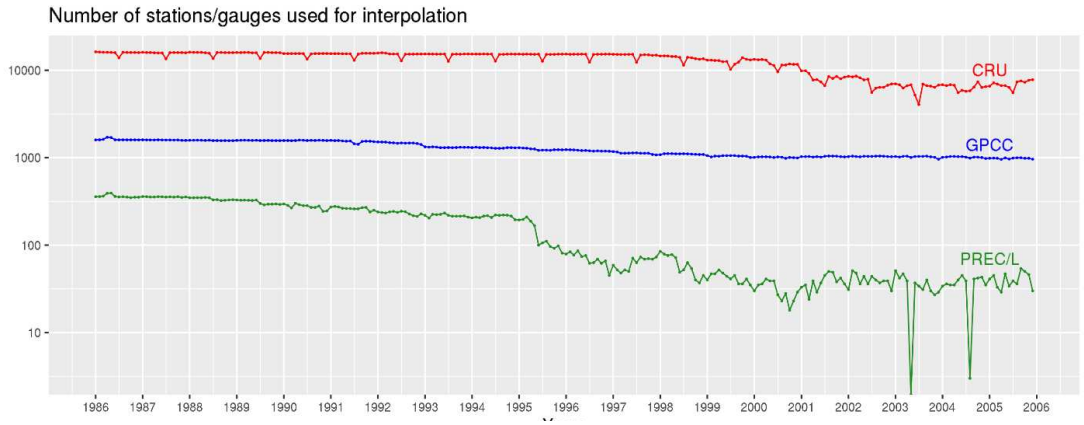

Figure 2.4.5: Timeseries of the number of stations/rain-gauges used in three gauge-based products, over the southern Africa region (10 °E to 42 °E and 10 °S to 35 °S).

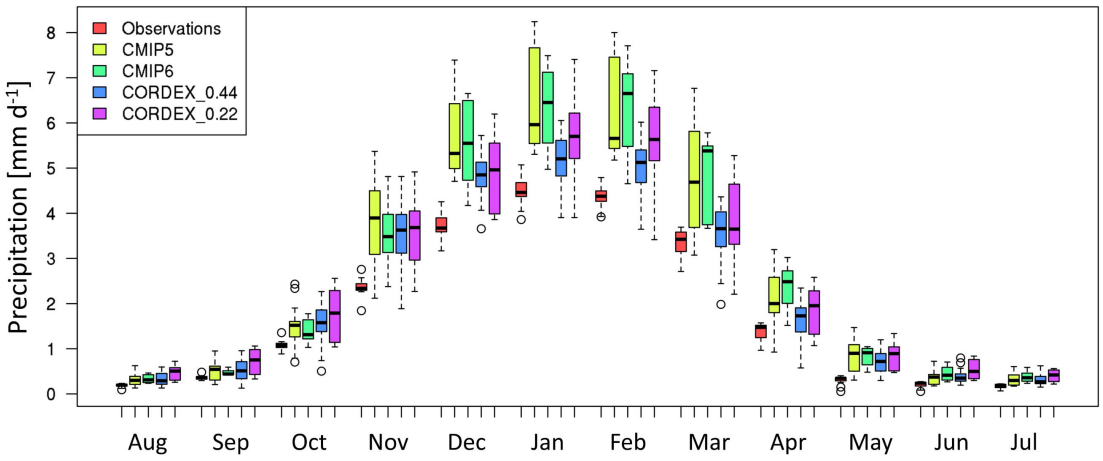

Figure 2.4.6: Annual cycle of monthly precipitation during 1986-2005 for the ensemble of observational data (gauge-based, satellite and reanalysis), CMIP5 (Coupled Model Intercomparison Project Phase 5), CMIP6 (Coupled Model Intercomparison Project Phase 6), CORDEX0.44 (Coordinated Regional Climate Downscaling Experiment Africa domain with a spatial resolution equal to 0.44° x 0.44°) and CORDEX-0.22° (CORDEX-Africa simulations with a spatial resolution equal to 0.22° x 0.22°). The thick horizontal black lines indicate the ensemble median for each month, the box encloses the interquartile range, and the tails denote the full ensemble range. Circles represent the outliers for each ensemble. Grid points only are considered.

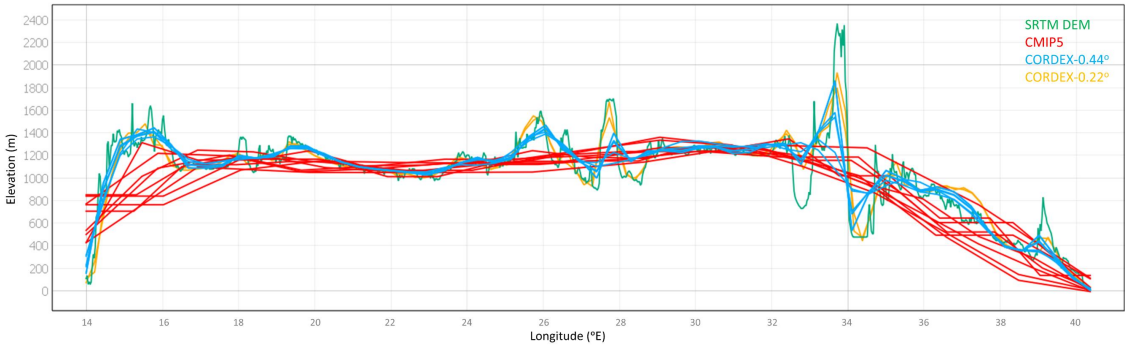

Figure 2.4.7: Cross section of surface elevation at 11°S across southern Africa for the Shuttle Radar Topography Mission (SRTM) Digital Elevation Model (in green), the surface altitude as represented in the CMIP5 (Coupled Model Intercomparison Project Phase 5) global climate models (in red), the surface altitude as represented in the CORDEX0.44 (Coordinated Regional Climate Downscaling Experiment Africa domain with a spatial resolution equal to 0.44° x 0.44°) (in blue) and the surface altitude as represented in the CORDEX-0.22° (CORDEX-Africa simulations with a spatial resolution equal to 0.22° x 0.22°) (in yellow).

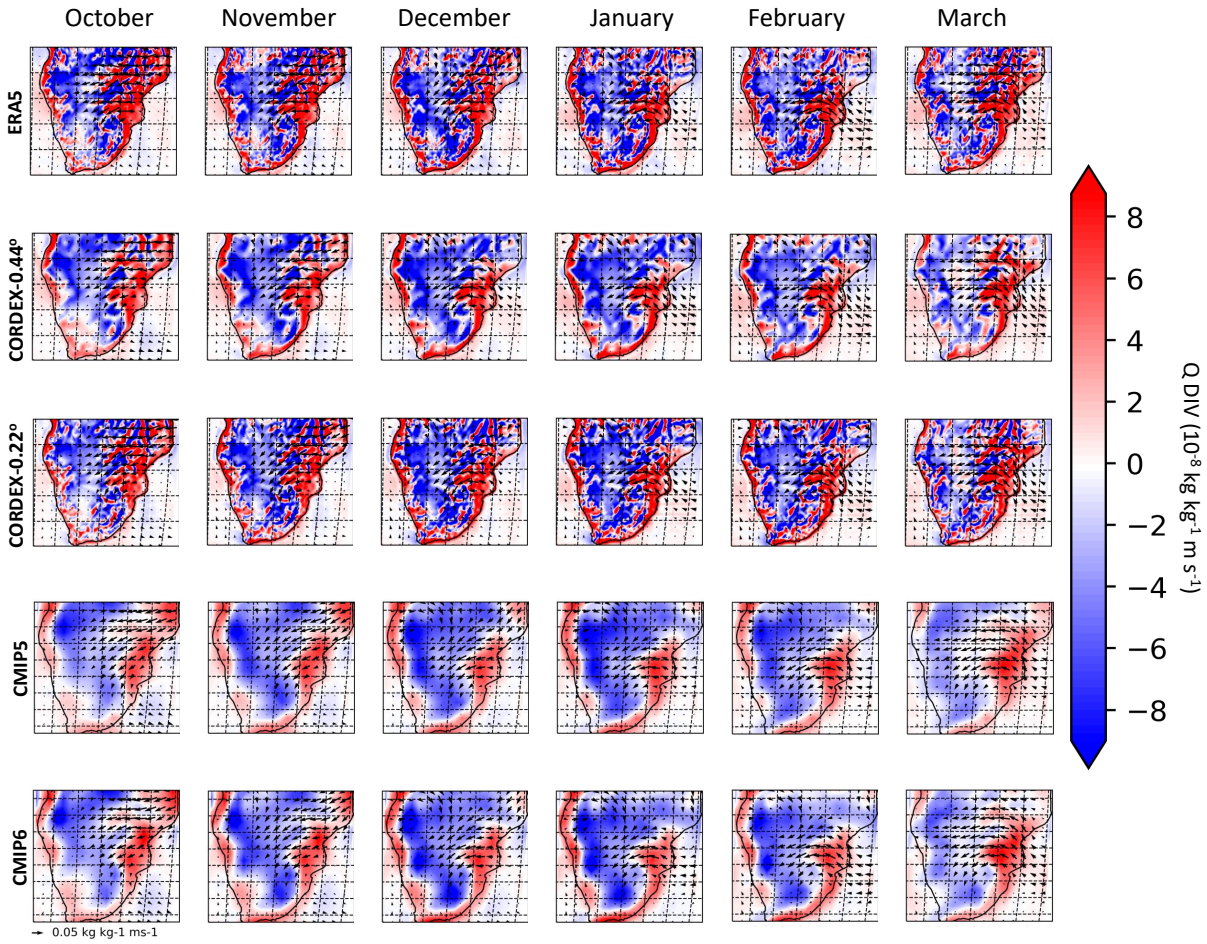

Figure 2.4.8: Mean monthly moisture flux and divergence at 850 hPa during the period 1986-2005. Rows indicate the ensemble means analyzed. From top to bottom: ERA5, ensemble mean of CORDEX0.44°, CORDEX0.22°, CMIP5 and CMIP6 simulations..

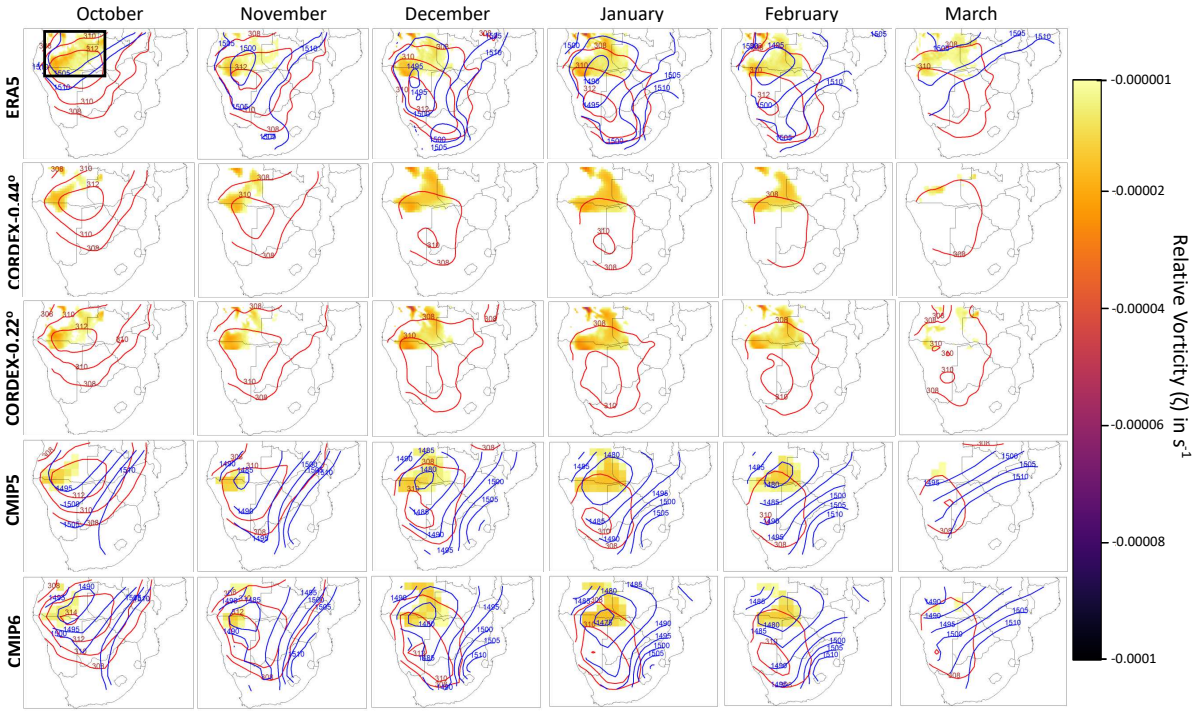

Figure 2.4.9: Monthly climatologies of the Angola Low pressure system during the rainy season for the period 1986-2005. Filled contours indicate cyclonic relative vorticity (ζ) for ζ <-0.00001 s^{-1} over the region extending from 14 °E to 25 °E and from 11 °S to 19 °S. Red lines indicate the isotherms of potential temperature at 850 hPa, having an increment of 2 K. Blue lines indicate isoheights of the geopotential height at 850 hPa, having an increment of 5 m. CORDEX0.44/0.22 are not plotted with geopotential isoheights, because this variable is not available for CORDEX simulations. From top to bottom: ERA5, ensemble mean of CORDEX0.44°, CORDEX0.22°, CMIP5 and CMIP6 simulations.

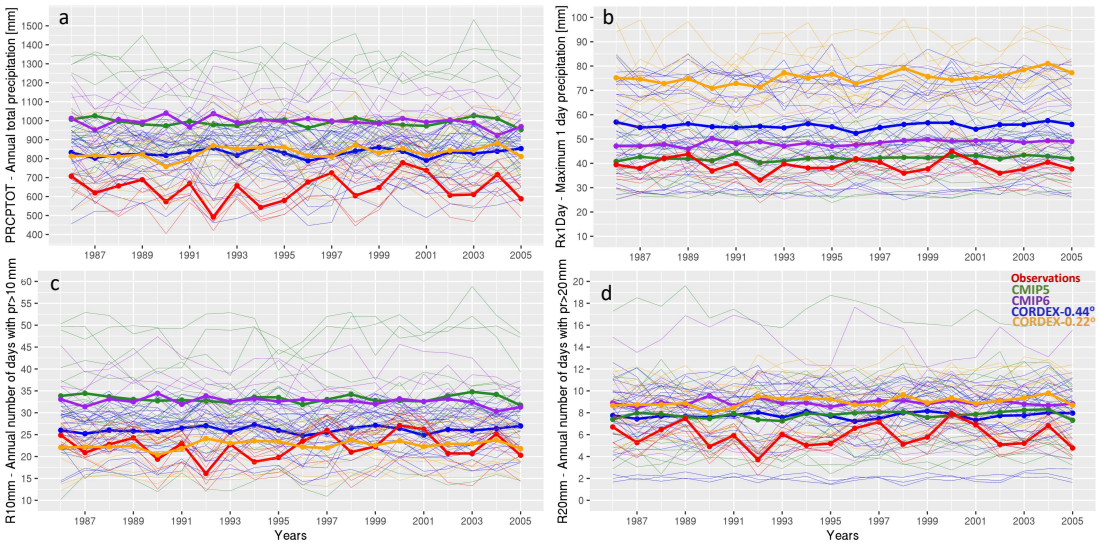

Figure 2.4.10: Timeseries of the ETCCDI indices over southern Africa (10 °E to 42 °E and 10 °S to 35 °S) for the observational ensemble in red (gauge-based, satellite and reanalysis), CMIP5 (Coupled Model Intercomparison Project Phase 5) ensemble in green, CMIP6 (Coupled Model Intercomparison Project Phase 6) ensemble in purple, CORDEX-0.44°: Ensemble mean of regional climate model simulations performed in the context of the Coordinated Regional Climate Downscaling Experiment Africa domain with a spatial resolution equal to 0.44° x 0.44° in blue and CORDEX-0.22° in orange. Thin lines display single ensemble members, thick lines display ensemble means. Y-axis on each panel depicts: (a) PRCPTOT (total annual precipitation), (b) Rx1Day (annual maximum daily precipitation), (c) R10mm (annual number of days with daily precipitation >10 mm), (d) R20mm (annual number of days with daily precipitation >20 mm).

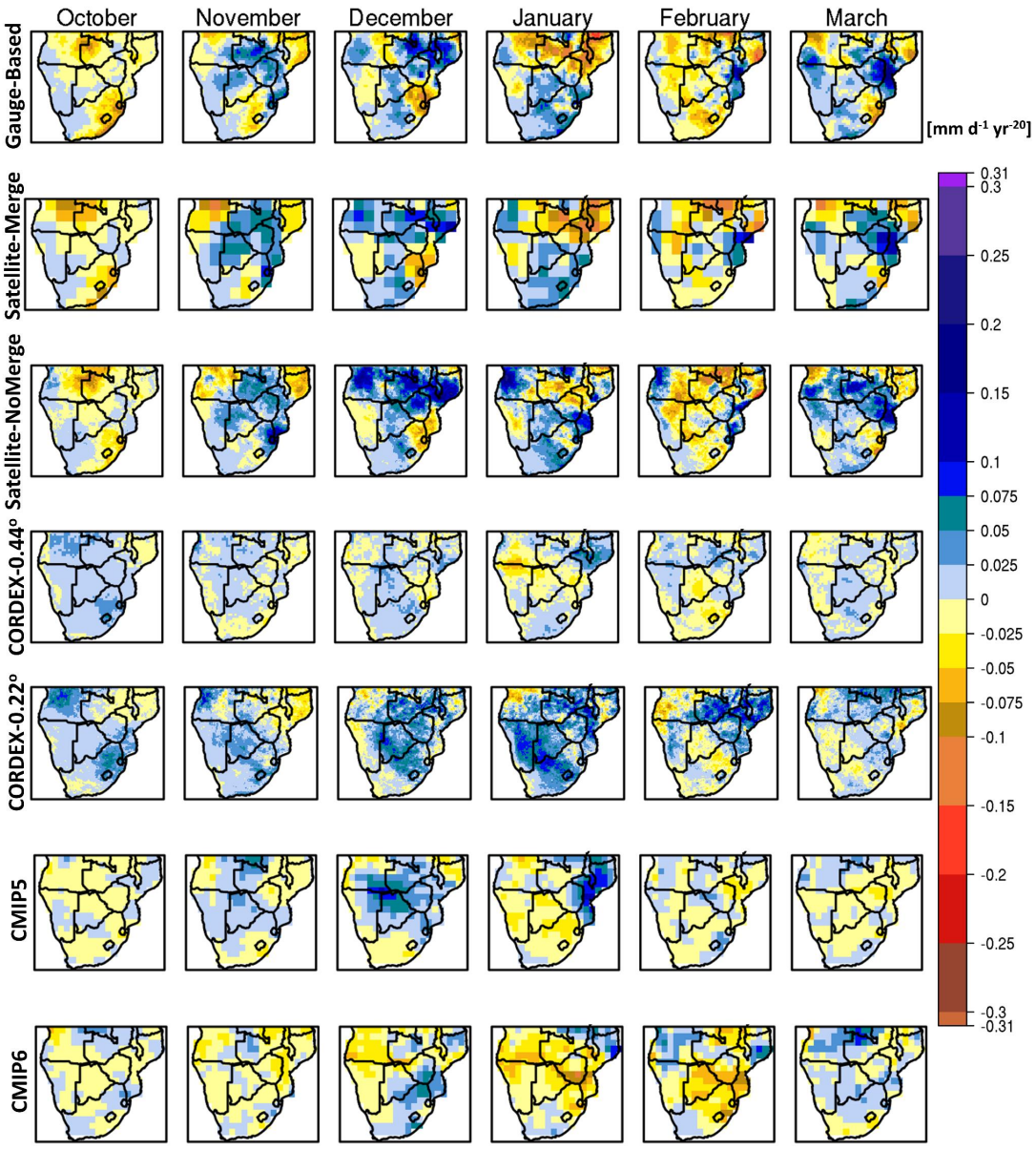

Figure 2.4.11: Trends for monthly precipitation for the period 1986-2005 [mm d^{-1} per 20 years] calculated using Sens Slope. Rows indicate the ensemble mean of trends produced by each ensemble member.

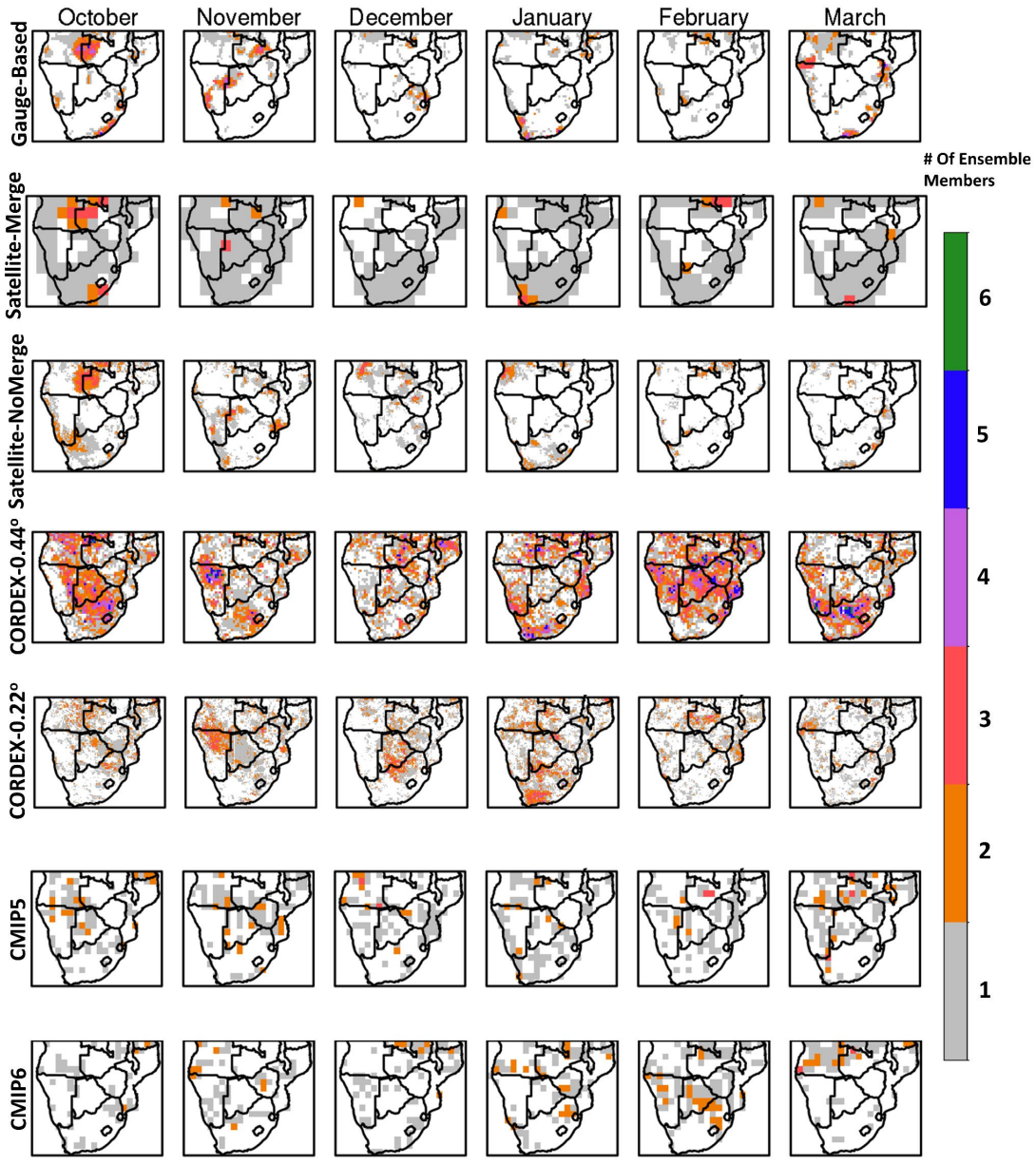

Figure 2.4.12: Number of ensemble members yielding statistically significant results for monthly precipitation trends based on the Mann-Kendall test (a=0.05).

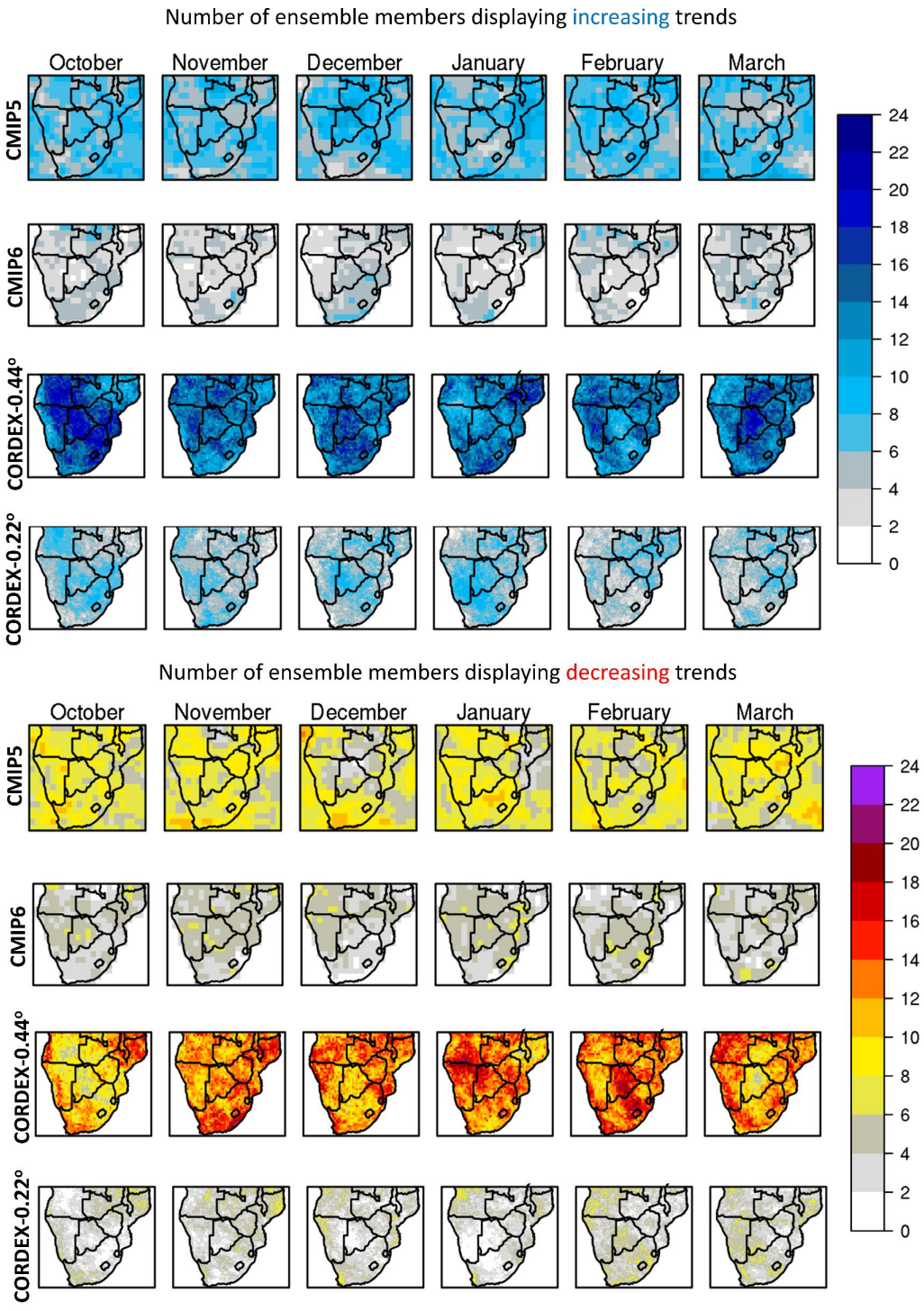

Figure 2.4.13: Number of ensemble members displaying increasing or decreasing trends for each ensemble.

2.5 Discussion and conclusions

The analysis of the SD among the different observational products highlights the fact that precipitation assessment requires consultation of multiple (gauge-based, satellite and reanalysis) products. If this is not possible, then it is highly recommended that the spatial distribution and frequency of reporting of the underlying station data is examined, for each respective precipitation product in use. This should be also regarded in cases when gauge-based or satellite products are utilized for model evaluation purposes. Moreover, satellite products that merge with rain gauges should not be considered independent from gauge-based products that exploit similar gauge-networks. In addition, it is noted that SD in the CORDEX0.44 ensemble is considerably lower than in the CMIP5/6 ensembles, supplying evidence that the CORDEX0.44 set of simulations provide more constrained results and can thus be considered to be a suitable dataset for climate impact assessment studies over SAF. However, that is not entirely the case for the CORDEX0.22 ensemble, which although it displays SD values smaller to that of CMIP5/6, it still yields SD values higher than that of CORDEX0.44.

Concerning the annual cycle of precipitation, it is noted that although the seasonality is captured reasonably by both the CMIP and CORDEX-Africa ensembles, still, there are considerable differences between them. More specifically, it is concluded that the CORDEX0.44 ensemble exhibits smaller ensemble spread for all months of the rainy season compared to the driving GCMs (CMIP5). In addition, the strong wet bias over SAF in the CMIP5 ensemble (Munday and Washington (2017)) is considerably reduced in the CORDEX0.44 ensemble. This bias is still evident in CMIP6. A plethora of references in the literature (Reason and Jagadheesha (2005); Lyon and Mason (2009); Crétat et al. (2019); Munday and Washington (2017); Howard and Washington (2018)) have highlighted the importance of the AL pressure system in modulating precipitation over SAF. It is noted that the strength of the AL as assessed in the current study was simulated to be weaker in the CORDEX0.44 than in the CORDEX0.22 ensemble. This may partly explain why precipitation in the CORDEX0.44 ensemble is reduced, relative to the CORDEX0.22 ensemble. However, there is need for a more in-depth dynamical analysis of the simulation of the AL in the CORDEX-Africa ensemble (both CORDEX0.44 and CORDEX0.22) and its impact on modulating precipitation seasonality and patterns over SAF.

The use of the four ETCCDI indices demonstrated that the CORDEX-Africa ensemble yields results that are in closer agreement to the observational data, compared to CMIP5/6 ensembles. It is, nevertheless, noticed that the improvement in the CORDEX-Africa ensemble is most evident when the ensemble mean is used. This highlights the fact that the ensemble mean performance is improved, relative to the performance of individual models (Nikulin et al. (2012)). For this reason, it is advisable that climate impact studies employ multi-model ensemble means, as a method of obtaining the consensus climatic information emanating from various models (Duan et al. (2019)). In addition, it is highlighted that in all indices the ensemble means of CMIP5/6 and CORDEX-Africa were not able to reproduce the interannual variability that was seen in the observational ensemble. This remark is in agreement with the fact that the task of reproducing precipitation variability across various time-scales by the CMIP5 ensemble is known to present challenges (Dieppois et al. (2019)), that inevitably cascade into the CORDEX-Africa simulations that are forced with CMIP5 GCMs (Dosio et al. (2015)). Lastly, even though the CORDEX-Africa ensembles reduce precipitation amounts over SAF, their use in drought-related impact studies

should take into consideration that still, they yield larger precipitation amounts than the observational data, which might eventually lead to underestimation of drought risk.

Precipitation trends during the rainy season displayed high spatial variability depending on the month. All observed (gauge-based and satellite) trends display substantial spatial agreement. The precipitation trends obtained by the CMIP5/6, and CORDEX0.44/0.22 ensembles, did not display consistency with the trends obtained from the observational datasets. This is not entirely unexpected, due to the role of internal variability compared to external forcing in recent decades (Pierce et al. (2009)), unlike temperature trends which have been shown to have a good agreement between the CORDEX-Africa (at 0.44° degrees of spatial resolution) and CMIP5 ensembles with observed temperature trends (Dosio and Panitz (2016); Warnatzsch and Reay (2019)). Nonetheless, it is noted that the trend signal between CORDEX0.44 and CORDEX0.22 is consistent, with CORDEX0.22 in general enhancing the CORDEX0.44 precipitation trends.

In conclusion, while CORDEX0.44 displays marked improvement over coarser resolution products, there are still further improvements to be made. More specifically, since the wet bias in RCM simulations persists (although considerably reduced relative to GCMs), it is necessary that precipitation over southern Africa is no longer assessed based on bulk descriptive statistics, but that there will be a shift towards process-based evaluation, where the dynamical and thermodynamical characteristics of specific atmospheric features are investigated more thoroughly in the CORDEX-Africa simulations. For this reason, it is imperative that all institutes submitting RCM simulations in data repositories such as the Earth System Grid Federation or the Copernicus Climate Data Store, provide model output data on multiple pressure levels, so that a fair comparison with the CMIP community would be possible. In addition, since the climate of southern Africa is highly coupled with the moisture transport coming from the adjacent oceans, it is necessary that the next generation of RCM simulations within CORDEX-Africa are performed coupled with ocean models. Lastly, since convection over southern Africa has a strong thermal component during specific months of the year (Oct-Nov), it is necessary that the land-atmosphere coupling processes within each RCM are examined in more detail, with coordinated efforts such as the LUCAS Flagship Pilot Study https://ms.hereon.de/cordex$_fps_lucas/index.php.en$, as performed in the Euro-CORDEX domain. In the world of regional climate modelling community, the 0.44° resolution of CORDEX-Africa is no longer state of the art and ensemble efforts are now approaching convection permitting grid-spacing (i.e., <4 km) in some parts of the world (Ban et al. (2021); Pichelli et al. (2021)). We also note, that increasing effort should be made with regards to understanding the improvements made from CORDEX0.44 simulations to CORDEX0.22. Although higher resolution is a desired target in the climate modelling community due to the more realistic representation of processes that it offers, still it should not be used as a panacea. In the current work, certain weaknesses in the CORDEX0.22 ensemble were identified, that should be addressed before the community populates further its simulation matrix. The next generation ensembles for Africa will hopefully provide insight and improvements to the challenges described here.

A key aspect in regional climate modelling is related to the impact that global climate models exert on regional simulations, when GCMs are used as lateral boundary conditions for the RCM simulations. Based on the location over which an RCM is applied and the atmospheric processes that are at play, the lateral boundary conditions may obscure the signature of an RCM, or vice versa. This topic, focusing

over southern Africa, is addressed in the next chapter.

3 The impact of lateral boundary forcing in the CORDEX-Africa ensemble over southern Africa

This chapter investigates the impact that the driving Global Circulation Models exert on Regional Climate Model simulations, performed within CORDEX-Africa for historical and future projections, concerning precipitation during the rainy season over Southern Africa. This chapter has been sumbitted to Geoscientific Model Development (GMD) Journal and is currently under review:

***Karypidou, M. C.**, Sobolowski, S. P., Katragkou, E., Sangelantoni, L., and Nikulin, G.: The impact of lateral boundary forcing in the CORDEX-Africa ensemble over southern Africa, Geosci. Model Dev. Discuss. [preprint], https://doi.org/10.5194/gmd-2021-348, in review, 2022.*

3.1 Introduction

The region of southern Africa (SAF) is among the most exposed climate change hotspots (Diffenbaugh and Giorgi (2012)), and is projected to experience severe impacts on multiple economical and societal sectors (Conway et al. (2015); Masipa (2017); Shew et al. (2020)). Poverty, food insecurity and high levels of malnutrition (Misselhorn and Hendriks (2017)) render SAF a region particularly vulnerable to the impacts of climate change (Casale et al. (2010); Luan et al. (2013); Wolski et al. (2020)). In addition, the population's reliance on rain-fed agriculture makes strategic planning necessary, as it aims to mitigate the impact of climate change on local communities.

Global climate models (GCM) participating in the Coupled Model Intercomparison Project Phase 5 (CMIP5) (Taylor et al. (2012)) project a significant decline in annual precipitation over SAF (IPCC and Stocker (2013)), with the most pronounced changes projected under representative concentration pathway 8.5 (RCP8.5) (Sillmann et al. (2013)). This reduction is also identified in the regional climate model (RCM) simulations performed in the context of the Coordinated Regional Climate Downscaling Experiment (CORDEX) – Africa domain (Nikulin et al. (2012); Giorgi and Gutowski (2015)). More specifically according to CORDEX-Africa simulations, annual precipitation is expected to decline by up to 50% by the end of the 21st century (Pinto et al. (2018)), while duration of dry spells is projected to increase (Dosio et al. (2019)). Despite this, extreme rain events are expected to increase in frequency and intensity (Pinto et al. (2016); Abiodun et al. (2019)). Nevertheless, for a global warming level of 2 °C, certain parts of SAF (northern Angola, Zambia, northern Mozambique and eastern South Africa) are projected to experience precipitation increase during specific times of the year (Maúre et al. (2018)). The question of whether or

not RCMs produce demonstrable added value relative to their driving GCMs, has often fueled debate between the RCM and GCM modelling communities (Lloyd et al. (2020)). The outcome of the debate is not binary. The literature provides ample evidence that there is indeed evidence of added value in RCMs, but it is dependent on the region examined, on the season and the climate mechanisms that are at play (Feser et al. (2011); Luca et al. (2016)). RCM ensembles such as those participating in CORDEX-Africa endeavor to provide added value, by dynamically downscaling historical and scenario simulations originating from coarse resolution GCMs (Dosio et al. (2019)). The added value in RCM simulations arises as a result of their higher horizontal resolution (<50 km), which makes it possible for atmospheric waves and synoptic scale disturbances to be represented in a more realistic manner. An additional aspect that further contributes towards this end, is the more accurate representation of land surface characteristics (topography, land use etc.) in RCMs (Di Luca et al. (2013)). Moreover, the physics of an RCM can be targeted for processes specific to the region it is being run for, giving it a local advantage over GCMs that may have had their physics developed for global applications. Nevertheless, RCMs also are accompanied by a set of model deficiencies of their own that affect the final output of the downscaled data (Boberg and Christensen (2012)). In Sørland et al. (2018) it is reported that although RCM biases are affected by the driving GCMs, these biases are not additive, a result that counters the common "cascade of uncertainty" criticism. Still, uncertainty arising from both the driving GCM and the downscaling RCM affect the final product, and it is important to diagnose the sources and causes of these errors (Déqué et al. (2012)).

Attributing this uncertainty into its respective components is key for a better assessment of the reliability of RCM simulations (Christensen and Kjellström (2020)). GCMs provide the lateral boundary conditions to the RCMs and each RCM receives, absorbs, and modulates the received atmospheric forcing in different ways, depending on the numerical formulations and parameterization schemes employed. Discerning between the signal received by the GCM and the signal produced by the RCM is critical for assessing the robustness with which different modelling systems are able to accurately reproduce observed climatologies and generate reliable estimates of the expected climate change. In addition, the manner in which an RCM responds to the atmospheric forcing provided by a GCM can be region specific (Rana et al. (2020); Wu and Gao (2020)) (e.g., regions located in close proximity to the boundaries of the RCM domain can be more severely affected by the driving GCMs, than regions at the center of the RCM domain or there can be region specific response around complex topography versus lowlands). Also, the degree to which an RCM is influenced by the driving GCM can be process specific. For instance, when there is a strong large-scale circulation signal that is introduced to an RCM domain (e.g. advective mid-latitude storms), it is quite likely that the RCM will be able to reproduce the information that is received at its lateral boundaries. If, however, the large-scale forcing is weak, then the atmospheric conditions simulated within the RCM domain are more dependent on the dynamic and thermodynamic processes employed by the RCM (e.g. convective thunderstorms).

The aim of this work is to assess whether it is the RCMs or their driving GCMs that dominate monthly precipitation climatology, monthly precipitation bias and climate change signal over SAF. The region-specific characteristics of this question are taken into account, by analyzing SAF and three subregions, namely southeastern Angola, Mozambique and South Africa. The different atmospheric processes that are in play over each region are also taken into account, by analyzing monthly climatologies. Precip-

itation over SAF results from various atmospheric processes that are highly variable during the rainy season (Oct-Mar), so by performing the analysis on a monthly basis, it is possible to indirectly study how certain processes are reproduced by GCM and RCM simulations. In order to differentiate between the signal emanating from the RCMs and their driving GCMs, the analysis of variance (ANOVA) in both the GCM and the RCM ensembles is utilized (Déqué et al. (2007); Déqué et al. (2012)).

3.2 Material and methods

3.2.1 Data

The data analyzed in the current work are displayed in Table 3.2.1 and consist of RCM simulations performed in the context of CORDEX-Africa, a set of simulations performed in the context of CMIP5, and the CHIRPS satellite rainfall product (Funk et al. (2015)). More specifically, the CORDEX-Africa simulations selected are those that were driven by more than two GCMs and for which there are runs available for both the historical and the future period under RCP8.5. The CMIP5 GCMs selected are the ones that were used to drive the CORDEX-Africa simulations. All RCM and GCM simulations were retrieved from the Earth System Grid Federation (`https://esgf-data.dkrz.de/projects/esgf-dkrz/`). The CHIRPS rainfall product is used for calculating precipitation biases in both the CORDEX-Africa and CMIP5 ensembles and was retrieved from: `https://www.chc.ucsb.edu/data/chirps`. CHIRPS is available at 5 km spatial resolution and for the calculation of biases it was remapped to the coarser resolution grid using conservative remapping. The analysis is split into two sections: the qualitative and the quantitative part. In the qualitative part, the aim is to identify if RCMs exhibit systematic behavior relative to their driving GCMs. For the quantitative part, the aim is to quantify the degree to which monthly precipitation climatologies, biases and climate change signals are affected by the downscaled RCMs or by the GCMs driving the RCM simulations. For this purpose, an ensemble of 19 RCM simulations driven by 10 GCMs is employed, along with the driving GCMs that were used to provide the lateral boundary conditions to the RCMs. For the historical simulations the period 1985-2005 is analyzed and for the projection simulations, the period 2065-2095 under RCP8.5 is selected. All CORDEX-Africa simulations are available at 50 km horizontal resolution, while the horizontal resolution for the driving GCMs is provided in Table 3.2.2.

Table 3.2.1: Input RCM and GCM simulations used. The CORDEX-Africa simulations are given in the columns. The CMIP5 GCMs used as driving fields are given in the rows.

	CCLM4-8-17.v1	RCA4.v1	REMO2009.v1
CanESM2		✓	
CNRM-CM5	✓	✓	
EC-EARTH	✓	✓	✓
HadGEM2-ES	✓	✓	✓
MIROC5		✓	✓
MPI-ESM-LR	✓	✓	✓
IPSL-CM5A-LR			✓
IPSL-CM5A-MR		✓	
CSIRO-Mk3-6-0		✓	
GFDL-ESM2M		✓	
NorESM1-M		✓	

Table 3.2.2: Horizontal resolution of the CMIP5 GCMs used as driving fields in the CORDEX-Africa simulations.

GCMs	Latitude Res.	Longitude Res.	References
CanESM2	2.7906°	2.8125°	(CCCma (2017))
CNRM-CM5	1.40008°	1.40625°	(Voldoire et al. (2013))
CSIRO-Mk3-6-0	1.8653°	1.875°	(Jeffrey et al. (2013))
EC-EARTH	1.1215°	1.125°	(Hazeleger et al. (2010))
GFDL-ESM-2M	2.0225°	2.5°	(Dunne et al. (2012))
HadGEM2-ES	1.25°	1.875°	(Collins et al. (2011))
IPSL-CM5A-MR	1.2676°	2.5°	(Dufresne et al. (2013))
IPSL-CM5A-LR	1.894737°	3.75°	
MIROC5	1.4008°	1.40625°	(Watanabe et al. (2010))
MPI-ESM-LR	1.8653°	1.875°	(Giorgetta et al. (2013))
NorESM1-M	1.894737°	2.5°	(Bentsen et al. (2013))

3.2.2 Methods

The study region and subregions considered are depicted in Fig. 3.2.1. The subregions are selected based on particular phenomena and processes that are of importance for the seasonal cycle of precipitation. More specifically, Region A encompasses the entire SAF region and is defined as the area extending from 10 °E to 42 °E and from 10 °S to 35 °S. Region B was selected to capture the main region of interest with regards to the Angola Low (AL) pressure system (Howard and Washington (2018)) and covers the area extending from 14 °E to 25 °E and from 11 °S to 19 °S. Region C covers the eastern coastline, Mozambique and surrounding countries and extends from 31 °E to 41 °E and from 10 °S to 28

°S. Lastly, Region D is selected, which covers much of South Africa and extends from 15 °E to 33 °E and from 26 °S to 35 °S.

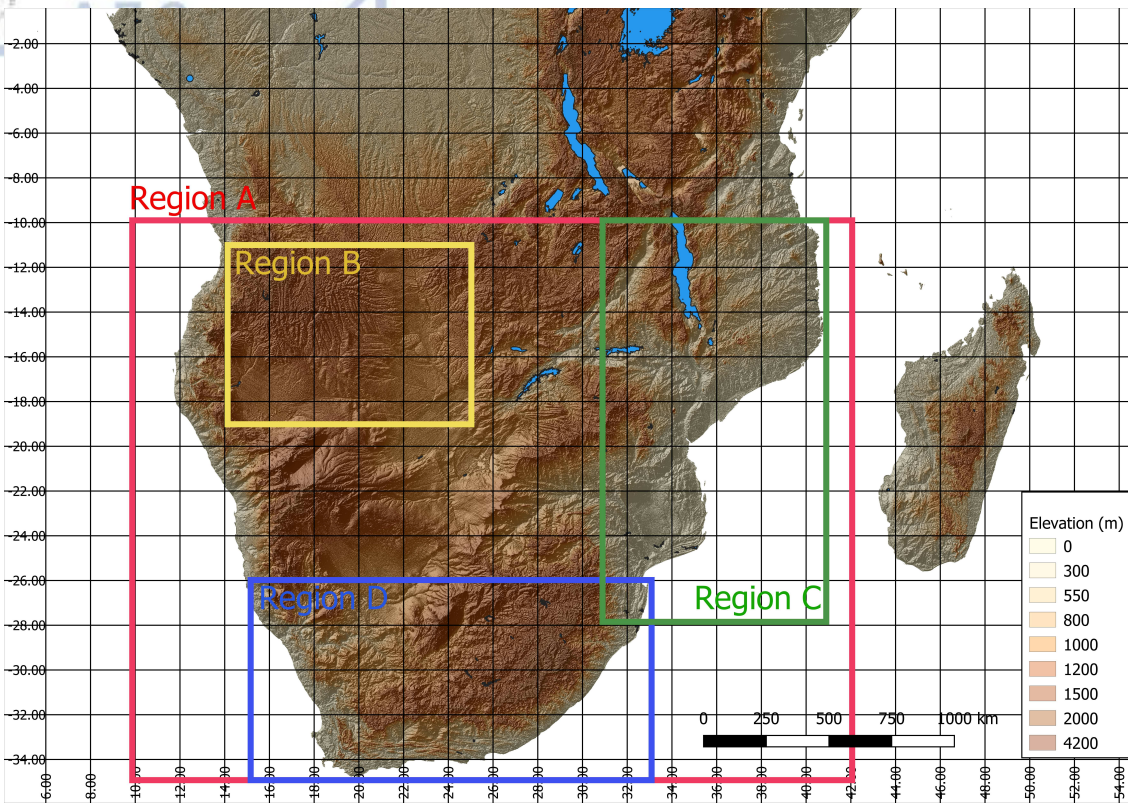

Figure 3.2.1: Study region and subregions over southern Africa.

One of the primary synoptic scale features controlling precipitation over SAF is the Angola Low (AL) pressure system (Reason and Jagadheesha (2005); Lyon and Mason (2007); Crétat et al. (2019); Munday and Washington (2017); Howard and Washington (2018)), which has a distinct seasonal cycle throughout the rainy season (Oct-Mar). This motivates its selection as a subregion for the current study. The AL exhibits heat low characteristics during Oct-Nov and tropical low characteristics during Dec-Jan-Feb (DJF) (Howard and Washington (2018)). This suggests that during Oct-Nov, since precipitation is thermally induced and thus tightly dependent on land-atmosphere interactions, it will be the RCMs that are dominant in controlling precipitation processes. As the rainy season progresses, the AL changes to a tropical low pressure system and its formation is controlled by the large-scale circulation that is characterized by easterly winds from the Indian Ocean that enter SAF via the Mozambique channel. Since precipitation during DJF is caused by transient low-pressure systems, it is hypothesized that the impact of the driving GCM fields during DJF is enhanced.

In addition, the wider area of Mozambique is a region where the majority of tropical cyclones/depressions make landfall over continental SAF. The occurrence of transient low-pressure systems is enhanced during the core of the rainy season (DJF) and thus it is imperative to identify whether the impact of the driving GCMs is dominant during DJF. Also, since according to Muthige et al. (2018), the number of landfalling tropical cyclones under RCP8.5 is expected to decline in the future, it is examined whether the impact of the driving GCMs to the RCM simulations will be altered under future conditions. Hence,

Region C is used as a region indicative of the landfalling tropical cyclones/depressions. Lastly, the area encompassing South Africa (Region D) is also investigated, due to its strong land-ocean gradients, complex topography and strong seasonal variations in rainfall zones.

3.2.2.1 Monthly precipitation climatology and bias

In order to assess whether or not the RCMs improve the monthly precipitation climatologies relative to their driving GCMs, a method initially described in Kerkhoff et al. (2015) and later employed by Sørland et al. (2018) is currently utilized, which displays in a scatterplot form the RCM increment as a function of the GCM bias. More specifically, the RCM increment is described as the difference of each RCM simulation from its driving GCM (RCM-GCM). The RCM increment is plotted against the GCM bias (GCM-OBS). This plot displays whether or not the RCM increment counteracts the GCM bias. If the RCM increment reduces the GCM bias, then points are expected to lie along the $y = -x$ line (negative correlation). On the contrary, if the RCM increment increases the GCM bias, then points are expected to lie along the $y = x$ line (positive correlation). If the RCM increment and the GCM bias are independent, then points are expected to be scattered randomly.

3.2.2.2 Climate change signal

The climate change signal (CCS) is identified as the monthly mean difference between the future period (2065-2095) minus the historical period (1985-2005). As an exploratory method of inspecting the differences between each RCM simulation from its respective driving (GCM) for monthly precipitation during both the historical and the future period, the downscaled precipitation field (RCM_{DRI}) is subtracted from its driving (DRI) GCM, as in Eq. 3.2.2.2:

$$DIFF = RCM_{DRI} - DRI$$

If DIFF>0, then we assume that the RCM enhances precipitation, relative to its driving GCM, while if DIFF<0 then we assume that the RCM reduces precipitation, relative to its driving GCM. This method is employed in the qualitative part of the analysis.

3.2.2.3 Analysis of variance

Additionally, ANOVA decomposition (Déqué et al. (2007); Déqué et al. (2012)) is employed, in order to understand whether it is the RCMs or their respective driving GCMs that are responsible for controlling precipitation during the historical (1985-2005) period and the future period (2065-2095). For this purpose, two quantities are used, namely the "inter-RCM" variance and the "inter-GCM" variance, as in (Déqué et al. (2012)). More specifically, the "inter-RCM variance" is the variance between all the RCM simulations that are driven by the same GCM. Subsequently, all variances obtained for all driving GCMs are averaged.

$$RCM_{var} = \frac{1}{N_{RCM}} \sum_{RCM_j} (P_{ij} - P_j)^2$$

The quantity P_{ij} is the monthly precipitation obtained from all RCMs (j) that were driven by the same GCM (i). The quantity P_j is the mean monthly precipitation obtained by all RCMs (j) that share a common driving GCM (i). As a final step, the average of all variances is calculated.

$$InterRCM_{var} = \frac{\sum_{GCM_I}}{N}$$

Similarly, the "inter-GCM" variance describes the variance between all the GCMs that were used to drive a single RCM and then averaged over all the variances obtained for all driven RCMs.

$$GCM_{var} = \frac{1}{N_{GCM}} \sum_{GCM_j} (P_{ij} - P_j)^2$$

Likewise, the average of all variances is calculated.

$$InterGCM_{var} = \frac{\sum_{RCM_I}}{N}$$

Both "inter-RCM" and "inter-GCM" variances are normalized by the total variance obtained for all months, as in Vautard et al. (2020), so that all values, both for historical and projection runs and RCM and GCM simulations are comparable.

3.3 Results

The October and January precipitation climatologies for the period 1985-2005 are displayed in Fig. 3.3.1 - Fig. 3.3.2 and Fig. 3.3.3 - Fig. 3.3.4, respectively. October and January climatologies are used, since these two months can be considered representative of the distinctive processes controlling precipitation over SAF. The use of seasonal means is preferred, since the temporal averaging of precipitation often obscures attributes that are better identified on a monthly basis. More specifically, October is used as it is the month that heralds the onset of the rainy season and is often associated with weak precipitation and convective processes that are mainly due to excess surface heating. Also, it is during October that the most intense formations of the heat low expression of the AL are observed. Likewise, January is used as it represents the core of the rainy season (DJF), with very strong large-scale precipitation, mainly from the southeastern (SE) part of SAF, through transient synoptic scale low pressure systems.

As displayed in Fig. 3.3.1- Fig. 3.3.2, precipitation during October occurs in the northwestern (NW) part and the SE part of SAF. Precipitation in the NW part is associated with the southward migration of the rainband (Nicholson (2018)), while precipitation over the SE part is associated with an early formation of the tropical temperate troughs (TTTs). As it is evident from Fig. 3.3.1- Fig. 3.3.2, CCLM4-8-17.v1 reduces precipitation amounts (approximately 4-5 mm/d) in both the NW and SE parts of SAF, relative to the lateral boundary forcing it receives. On the contrary, RCA4.v1 systematically enhances precipitation amounts, regardless of the driving GCM. Also, precipitation according to RCA4.v1 displays a very localized spatial pattern with very strong spatial heterogeneity. This may be attributed to the fact that the topography is not smoothed enough and leads to high precipitation values over grid boxes with high elevation (Van Vooren et al. (2019)). This is particularly evident in the mountainous region over coastal Angola. REMO2009.v1 also enhances precipitation amounts regardless of the driving GCM, however in a much more spatially homogeneous way than RCA4.v1.

As it is shown in Fig. 3.3.3- Fig. 3.3.4, high precipitation amounts during January are observed over the northern and eastern regions of SAF. During January, differences among the driving GCMs become

more pronounced, however, all models agree on the dry conditions observed over the southwestern (SW) part of SAF. With regards to the downscaled products, CCLM4-8-17.v1 produces high precipitation amounts over the central part of northern SAF but displays varying amounts of precipitation over the coastal parts, depending on the driving GCM. RCA4.v1 downscales precipitation in a very localized pattern and enhances precipitation over areas with steep terrain. Also, precipitation over the lake Malawi region is particularly enhanced, regardless of the driving GCM. REMO2009.v1 displays similar precipitation amounts to its driving GCMs, however it enhances precipitation over the coastal part of Angola and Mozambique and yields excess precipitation over lake Malawi, when it is driven by HadGEM2-ES and IPSL.

In Fig. 3.3.5-3.3.6 the monthly precipitation bias for October over SAF is shown. Biases are calculated using the CHIRPS satellite rainfall product as a reference. With the exception of IPSL-CM5A (LR/MR) and CanESM2, all other GCMs display a consistent wet bias that ranges from 0.1 – 30 mm/d (in isolated areas), with most values over SAF falling 0.1-3 mm/d. Overall, the same pattern generally holds for RCA4.v1 and REMO2009.v1, while CCLM4-7-18.v1 displays a systematic dry bias that reaches 2 mm/d, when forced with EC-EARTH, MPI-ESM-LR and HadGEM2-ES. More specifically, concerning RCA4.v1, the region where the highest wet bias is observed is over Region B (the Angola Low region) and over the NW parts of coastal Angola. The dry bias regions in RCA4.v1 are identified over the northeastern (NE) and southern parts of SAF and they rarely exceed -1.5 mm/d.

The monthly precipitation biases for January over SAF are shown in Fig. 3.3.7-3.3.8. There is a prevailing wet bias identified in almost all GCMs that typically reaches 3 - 3.5 mm/d, however, in MIROC5, NorESM and GFDL-ESM2M the biases exceed 5 mm/d over a major part of SAF. Another feature that systematically appears in GCMs is a dry bias over the NE part of SAF. This bias pattern is also identified in almost all RCMs with a systematic wet bias over central and western SAF and a region of dry bias in the NE part. More specifically, in RCA4.v1 and REMO2009.v1, there is a dry bias over the NE and the southern coast of SAF, while in CCLM4-7-18.v1 the dry bias over the eastern region extends inland to cover almost the whole of Mozambique. Another interesting feature is identified around the Angolan coast, where wet biases exceed 5 mm/d, while over an adjacent region there is a strip of dry biases that reaches 2 mm/d. Considering the abrupt increase in elevation and the steep escarpment over the coastal Angola-Namibia region, this is possibly caused by local circulation driving excess moisture transport from the Atlantic Ocean and overly aggressive orographically triggered precipitation on the windward side of the topography (wet bias strip), that leads to dry conditions in the lee side (dry bias strip) (Howard and Washington (2018)). It is noted that the wet bias over the coastal region is identified in most of the RCA4.v1 simulations and in all REM2009.v1 simulations, however, the dry bias in the lee side is seen in CCLM4-7.18.v1 only.

A more detailed look into specific subregions over SAF where certain climatological features and processes are at play, can help gain a more in-depth insight of how the precipitation biases are distributed during each month of the rainy season and whether or not the RCMs display any improvement relative to their driving GCMs. For this reason, we plot the RCM increments (RCM-GCM) as a function of the GCM biases (GCM-OBS). The results for October over SAF and the 3 subregions are displayed in Fig. 3.3.9. In general, all points are identified close to the y=-x line, hence there is a tendency that RCMs systematically counteract GCM biases. There are nonetheless substantial differences between

the four regions. For instance, over Region A (SAF region) the IPSL-MR GCM has a wet bias equal to almost 1 mm/day, which is counteracted by RCA by an increment of -0.4 mm/month. Other RCA simulations when driven by HadGEM2-ES, CNRM-CM5 or EC-EARTH, display an RCM increment similar to that of the GCM bias, hence RCMs mitigate the GCM bias. Over Region B (Angola Low region) most of the RCMs display an RCM increment that is nearly equal to the GCM bias. Similar conclusions are drawn for Regions C and D also. The RCM increments as a function of the GCM biases for January are shown in Fig. 3.3.10. For all regions except Region D (South Africa) points are lying closely to the y=-x line, hence overall, RCM increments counteract the GCM biases. In general, although precipitation in RCMs is strongly dependent on the driving GCMs, the RCM increments are anticorrelated to the GCM biases.

In Fig. 3.3.11 the mean analysis of variance of all RCMs driven by the same GCM and of all GCMs driving the same RCM is shown. Values are spatially averaged for southern Africa and the 3 subregions examined (land pixels only) and refer to the period 1985-2005. In Region A, monthly precipitation during October and November is dominated by the RCMs, while during Jan-Mar, it is the GCMs that play a dominant role in formulating precipitation over SAF. This is indicative of the impact that RCMs exert on the formulation of precipitation during Oct-Nov-Dec and the fact that the contribution from the GCMs becomes dominant during Jan-Feb-Mar. The fact that the contribution of RCMs during Oct-Nov-Dec dominates can be attributed to the fact that precipitation during these months is the result of regional processes that are largely dependent on the coupling between the surface and the atmosphere. The land-atmosphere coupling is a characteristic resolved by the RCMs, through mechanisms described in land surface models, planetary boundary layer schemes, convection schemes etc., making the contribution of the large scale drivers from the GCM less important. However, during Jan-Feb-Mar we observe that the contribution from the RCMs is reduced, and it is the GCMs that control the monthly precipitation variability. This can be attributed to the fact that during Jan-Feb-Mar it is the large-scale circulation that modulates precipitation over SAF and the GCMs control the transient synoptic scale systems that enter SAF. In Region B, the pattern is similar, however, October and November precipitation are closer to the diagonal, indicating an almost equal contribution by both RCMs and GCMs. Also, Dec-Feb move closer to the diagonal, nevertheless, precipitation during March is mainly formulated by GCMs. In Region C, October remains equally influenced by both RCMs and GCMs, however November and December are dominated by the influence of the RCMs. In Region D, precipitation for all months except October is influenced by GCMs.

In Fig. 3.3.12-3.3.13 the climate change signal for October precipitation over SAF is depicted. All GCMs agree that October precipitation will decline by approximately 2 mm/d over the regions that experience precipitation during this period, namely the NW and SE parts of SAF. In addition, some GCMs display a minor precipitation increase (0 - 0.5 mm/d) in the SW part of SAF, while some others display a slightly larger (1.5 mm/d) precipitation increase over the eastern parts of South Africa. Moreover, it is seen that the precipitation change signal is replicated by almost all the downscaling RCMs, nevertheless, there are some considerable differences between the RCMs and their driving GCM. More specifically, RCA4.v1 in almost all simulations, displays a larger reduction of the precipitation change signal relative to its driving GCM, both in magnitude and in spatial extent. Precipitation changes in CCLM4-8-17.v1 seem to follow closely the driving GCMs, with a severe exception when CNRM-CM5 is used (the NW part of SAF

experiences precipitation decline almost 4 mm/d larger than in the driving GCM). The case for when CCLM4-8-17.v1 is driven by CNRM-CM5 may be partly caused by the fact that the historical simulation had erroneously used lateral boundary conditions from a different simulation member of CNRM-CM5 (Vautard et al. (2020)). In REMO2009.v1, a precipitation decline region is identified in the NW part of SAF and a minor precipitation increase over eastern South Africa is identified. This pattern for REMO2009.v1 appears to be consistent, regardless of the driving GCM, which could be partly explained by the fact that precipitation during October is thermally driven, and thus the impact of the driving GCMs is not dominant. The precipitation increase in the SE part of SAF is seen over a localized region and could be associated with an increase in the precipitation caused by the Tropical Temperate Troughs (TTTs) (Ratna et al. (2013);Macron et al. (2014);Shongwe et al. (2014)).

In Fig. 3.3.14 - Fig. 3.3.15 the climate change signal for precipitation during January is displayed. The precipitation change displays a very strong regional heterogeneity. It is also observed that although there is a strong precipitation change signal in all driving GCMs, not all RCMs downscale the signal uniformly. It is also notable that, even among the GCMs, there are substantial differences in the spatial extent and sign of the change. Nevertheless, there are some features that appear in most of the simulations. For instance, almost all GCMs project drying conditions over the SW part of SAF, especially the coastal zone. The precipitation decline is equal to -1 mm/d. This could be explained by a consistent increase in frequency of the Benguela Coastal Low-Level Jet events (Lima et al. (2019); Reboita et al. (2019)), causing oceanic upwelling and a subsequent reduction in precipitation. In addition, there is a subset of GCMs that identify a severe precipitation decline over the Angola region that reaches -5 mm/d. Furthermore, in many GCMs a region of precipitation increase is identified, extending from central SAF towards SE SAF. This is particularly identifiable in HadGEM2-ES, and the RCM simulations forced by it.

In Fig. 3.3.16 the spatial average of the RCM_{DRI} – DRI difference (DIFF) is shown for the whole of SAF (land pixels only). If DIFF>0, it indicates that the RCMs enhance precipitation relative to their driving GCM, while if DIFF<0 then RCMs reduce precipitation relative to their driving GCM. As it is shown, DIFF values for October are symmetric around zero and do not exceed the range (-1) – 1 mm/d, either for the historical or the future period. Almost symmetric are the DIFF values for November also, however, their spread increases, reaching values that range (-2) – 2 mm/d. In both months, CCLM4-7-18.v1 always reduces precipitation amounts relative to the lateral boundary forcing it receives, regardless of the driving GCM or the period examined. During December, the precipitation reduction in all RCMs becomes more pronounced and reaches values equal to -3 mm/d. In January, only 1 RCM enhances precipitation (0.5 mm/d) with all the rest displaying precipitation reduction. During February and March, some positive DIFF values re-appear for some simulations. Overall, there is a strong linear relationship between DIFF in 1985-2005 and 2065-2095, which further implies that if an RCM is drier than its driving GCM during the historical period, then it will retain this attribute during the future period also. Nonetheless, we highlight that RCMs preserve precipitation change signal generated by the GCMs. Considering that one primary shortcoming of the GCMs over SAF is their wet bias and that RCMs systematically reduce this bias, we gain increased confidence that RCMs can be reliably used for future projections with regards to precipitation change.

In Fig. 3.3.17 the spatial average of the precipitation change signal from RCMs and their driving GCMs relative to 1985-2005 for SAF and the 3 subregions is displayed. Concerning Region A, all models

during October identify a precipitation reduction at the end of the 21st century that can reach -0.9 mm/d. The precipitation decline signal is also identified during November, indicating a later onset of the rainy season over SAF, as it has already been shown for CMIP5 (Dunning et al. (2018)). During December and January there is a variability in the spatial averages of the change signal that ranges from -0.8 to 0.8 mm/d. A similar pattern is also seen for February and March. The distribution of the ensemble members for both RCMs and GCMs in Regions B and C is similar to that of Region A, however in Regions B and C precipitation change values display a considerably larger spread. In Region D the climate change signal is symmetric around 0 for all months, except March.

The impact the RCMs and GCMs on monthly precipitation for the period 2065-2095 under RCP8.5 is shown in Fig. 3.3.18. Regions A and B show a similar behavior as in the historical period, however, in Region C, precipitation during March is more strongly dominated by GCMs. The same observation holds also for Region D. In general, regional processes continue to dominate contributions to variability during Oct-Nov, while large scale features dominate during Dec-Mar.

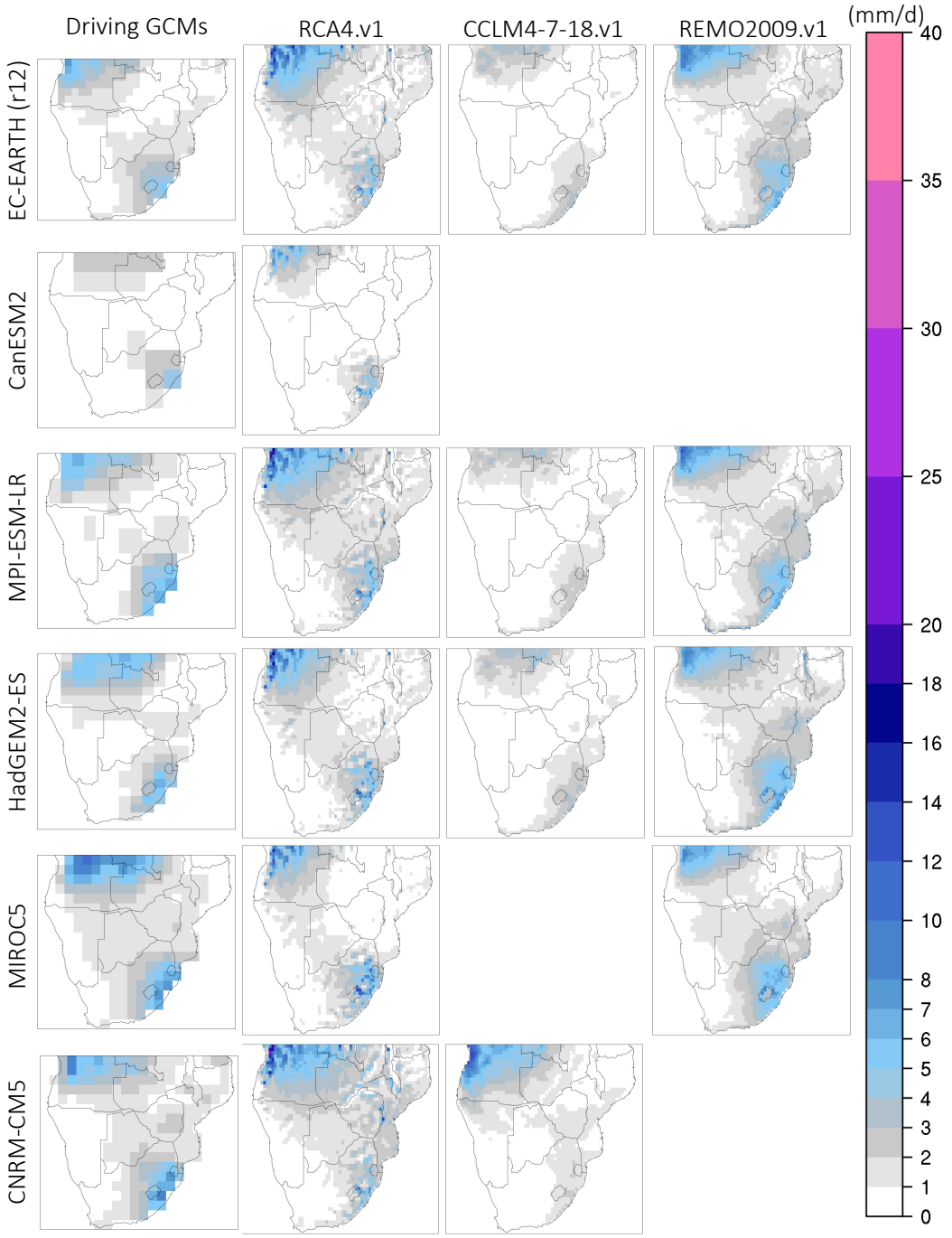

Figure 3.3.1: Monthly precipitation climatologies (mm/d) during October for the period 1985-2005. First column (from the left) displays precipitation from the driving GCMs and columns 2-4 display the downscaled precipitation output from RCA4.v1, CCLM4-8-17.v1 and REMO2009.v1.

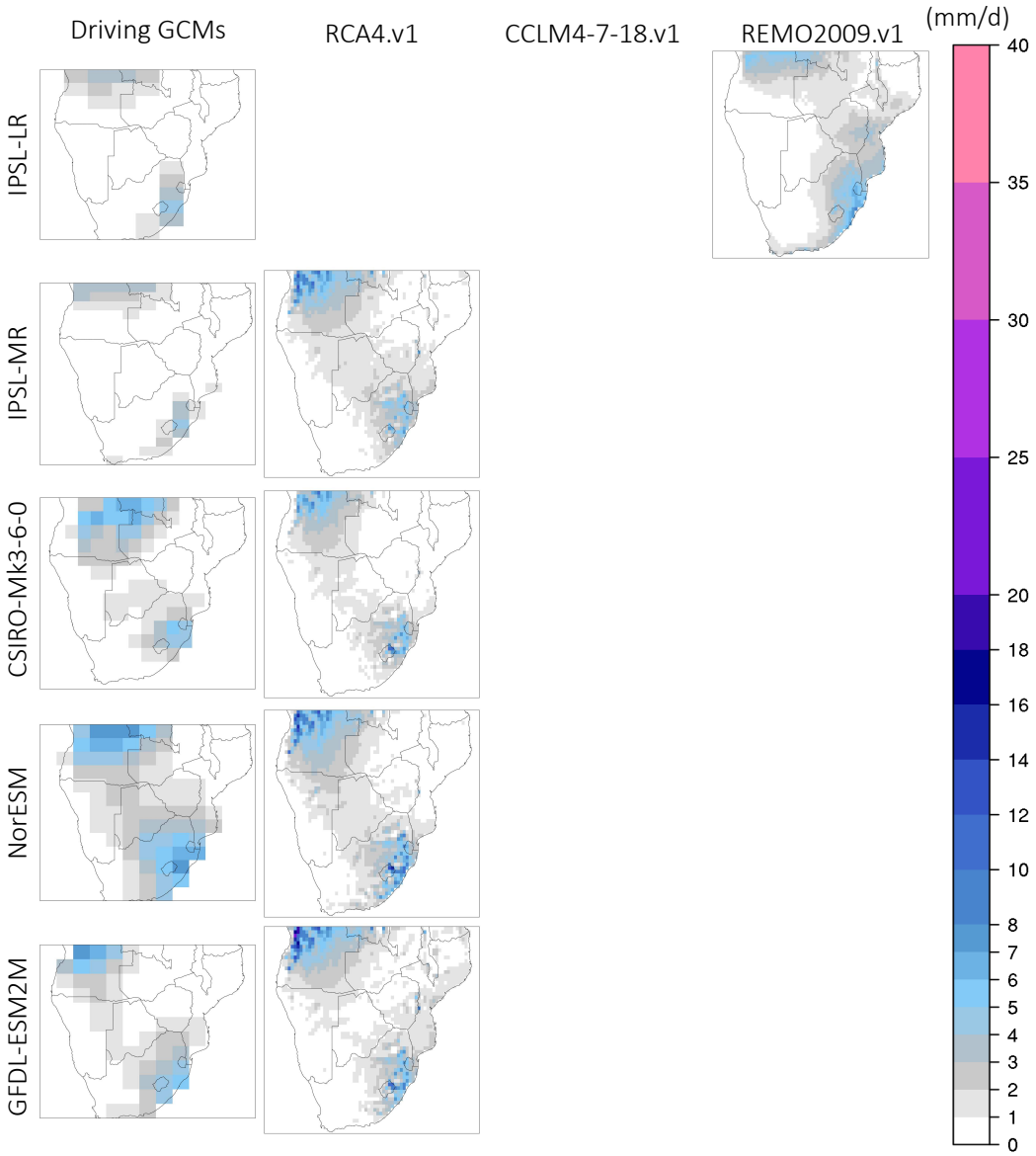

Figure 3.3.2: Continued.

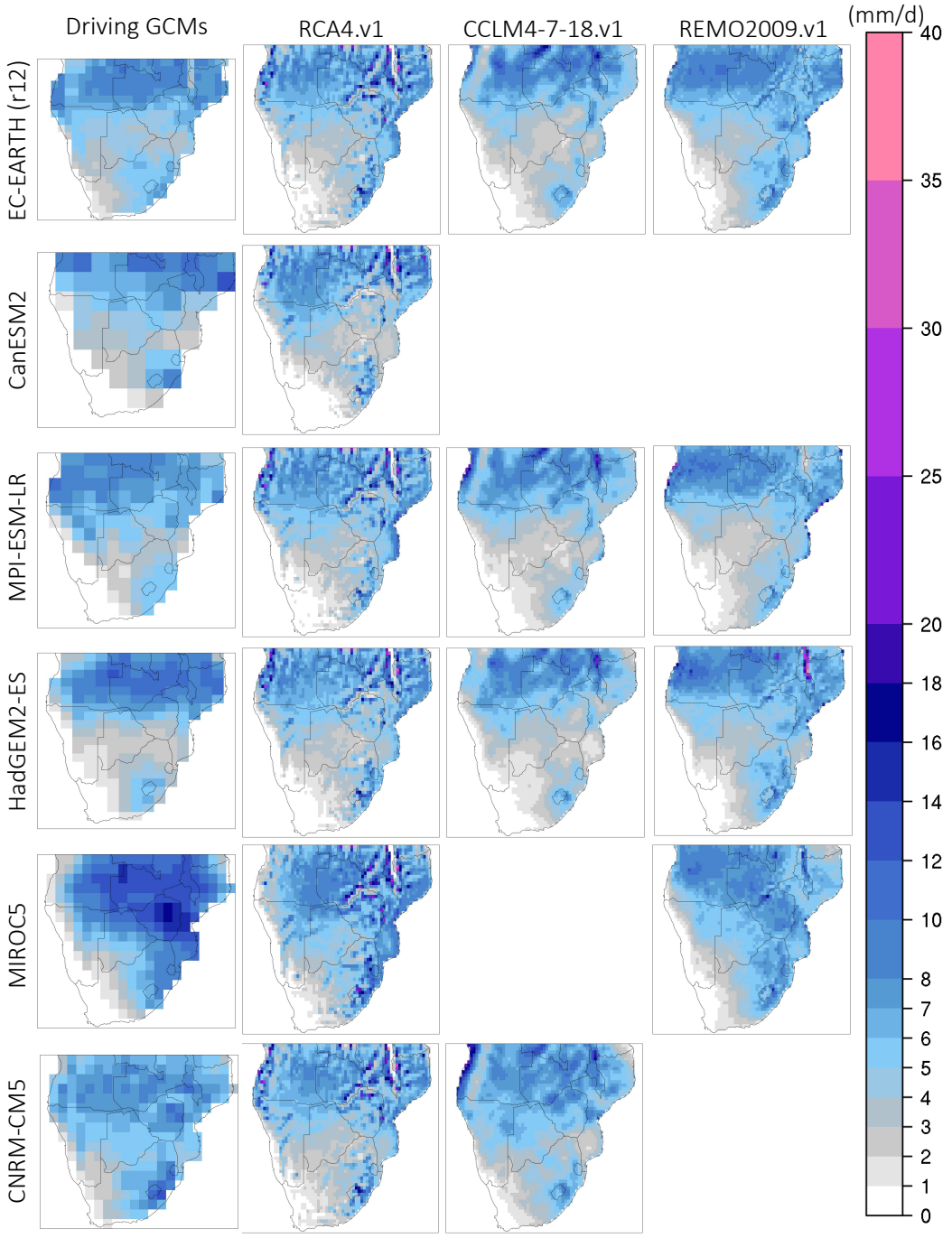

Figure 3.3.3: Monthly precipitation climatologies (mm/d) during January for the period 1985-2005. First column (from the left) displays precipitation from the driving GCMs and columns 2-4 display the downscaled precipitation output from RCA4.v1, CCLM4-8-17.v1 and REMO2009.v1.

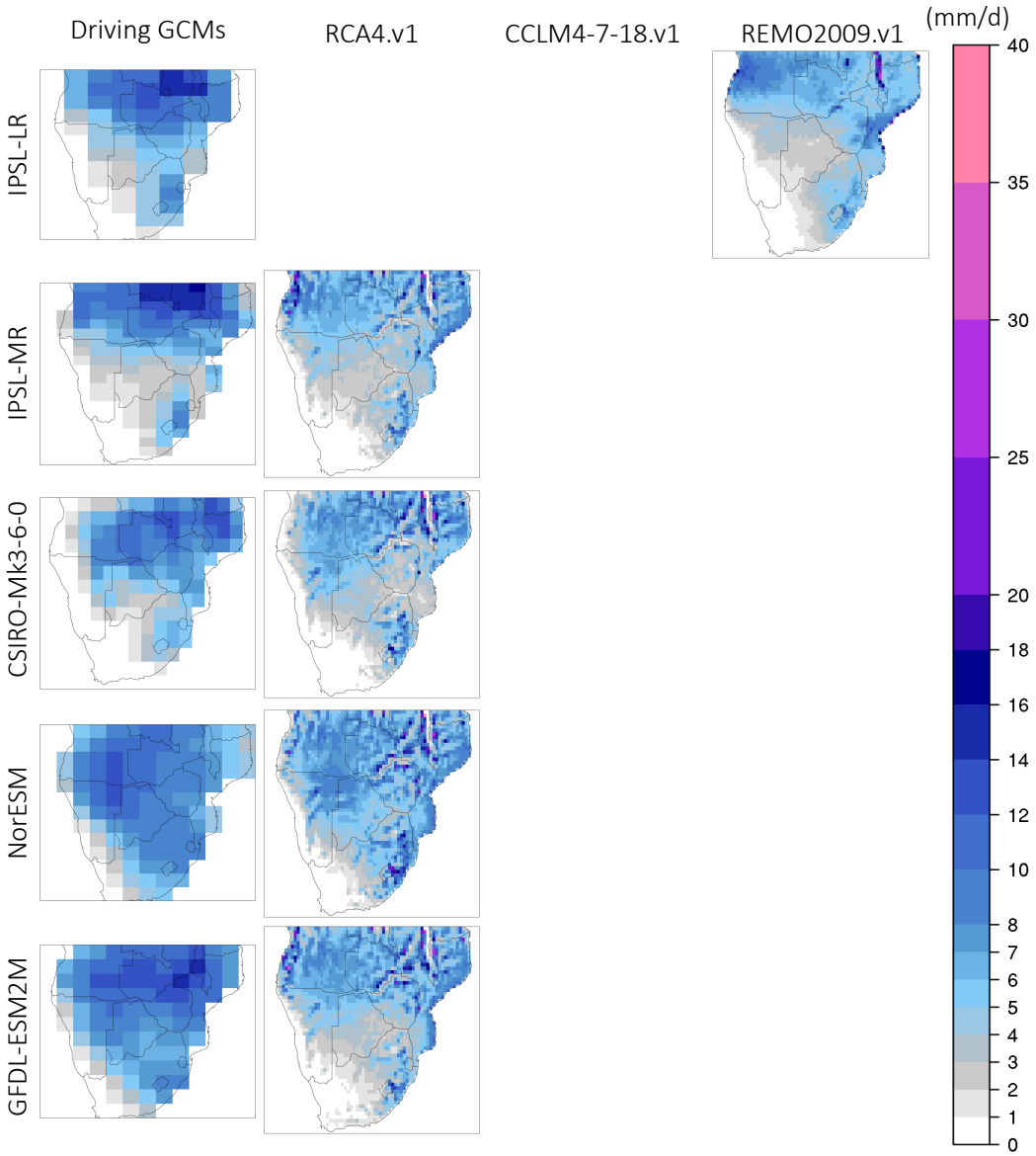

Figure 3.3.4: Continued.

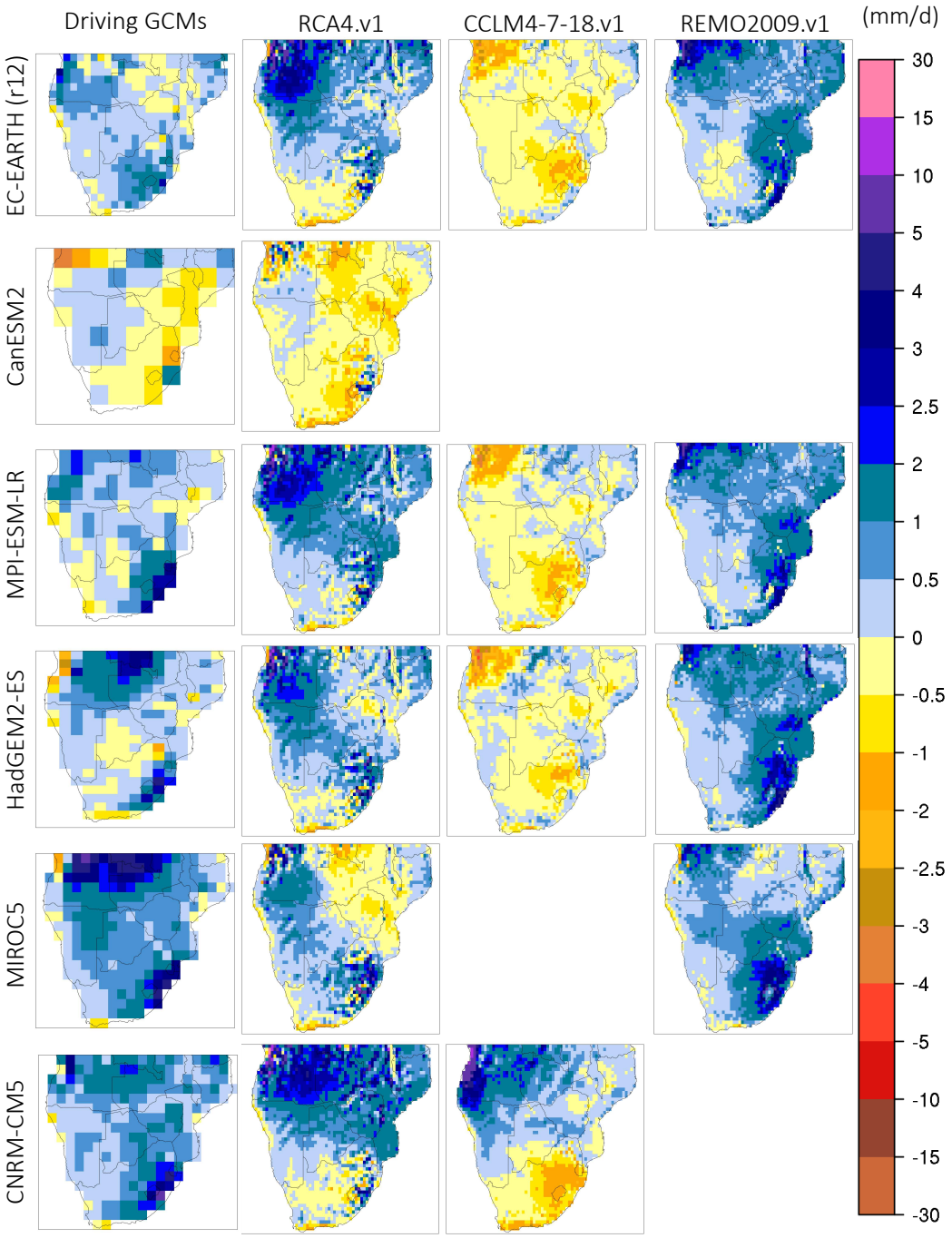

Figure 3.3.5: Monthly precipitation bias (model CHIRPS in mm/d) during October for the period 1985-2005. First column (from the left) displays the biases in the driving GCMs and columns 2-4 display the biases in the downscaled precipitation output according to RCA4.v1, CCLM4-8-17.v1 and REMO2009.v1.

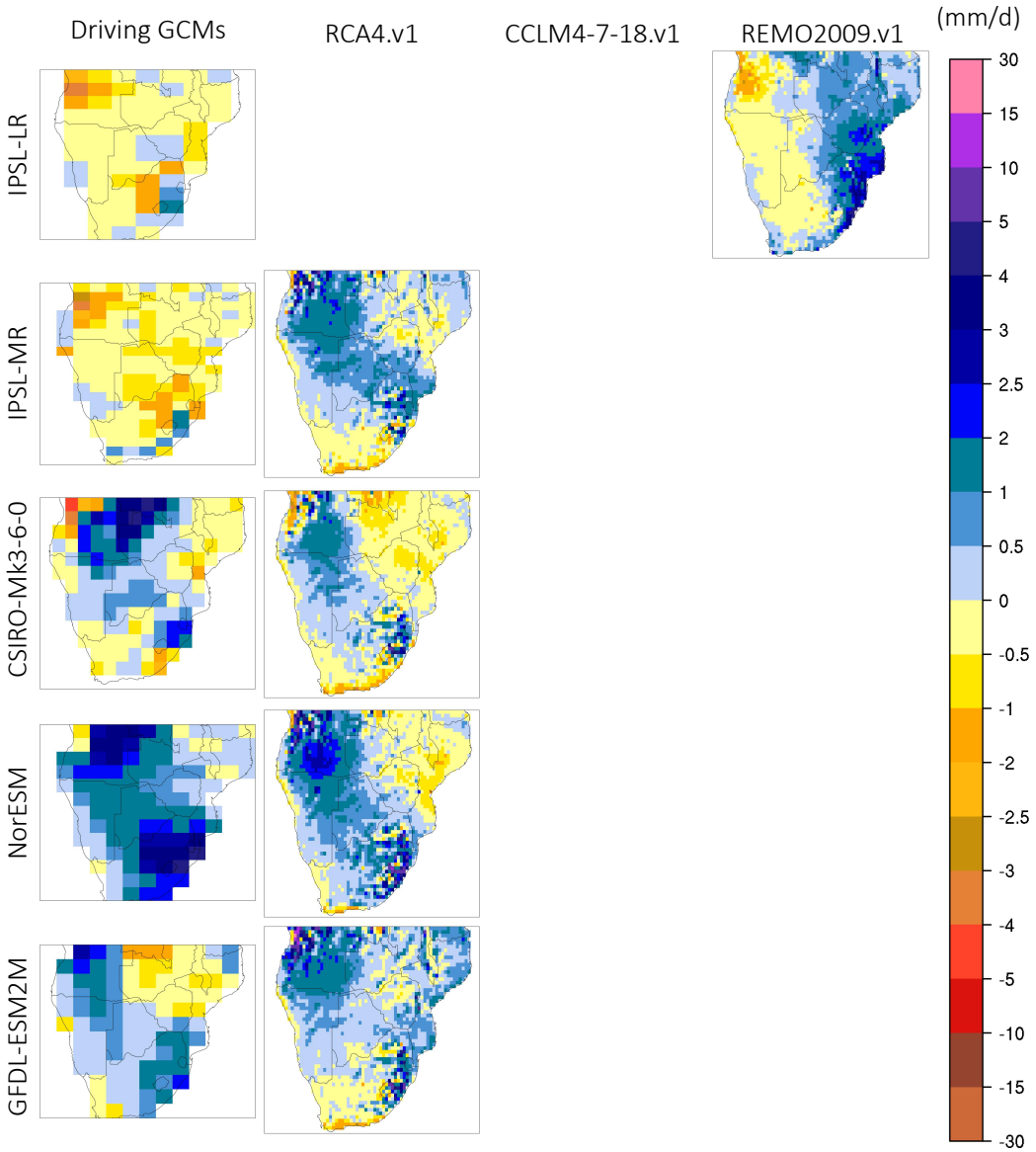

Figure 3.3.6: Continued.

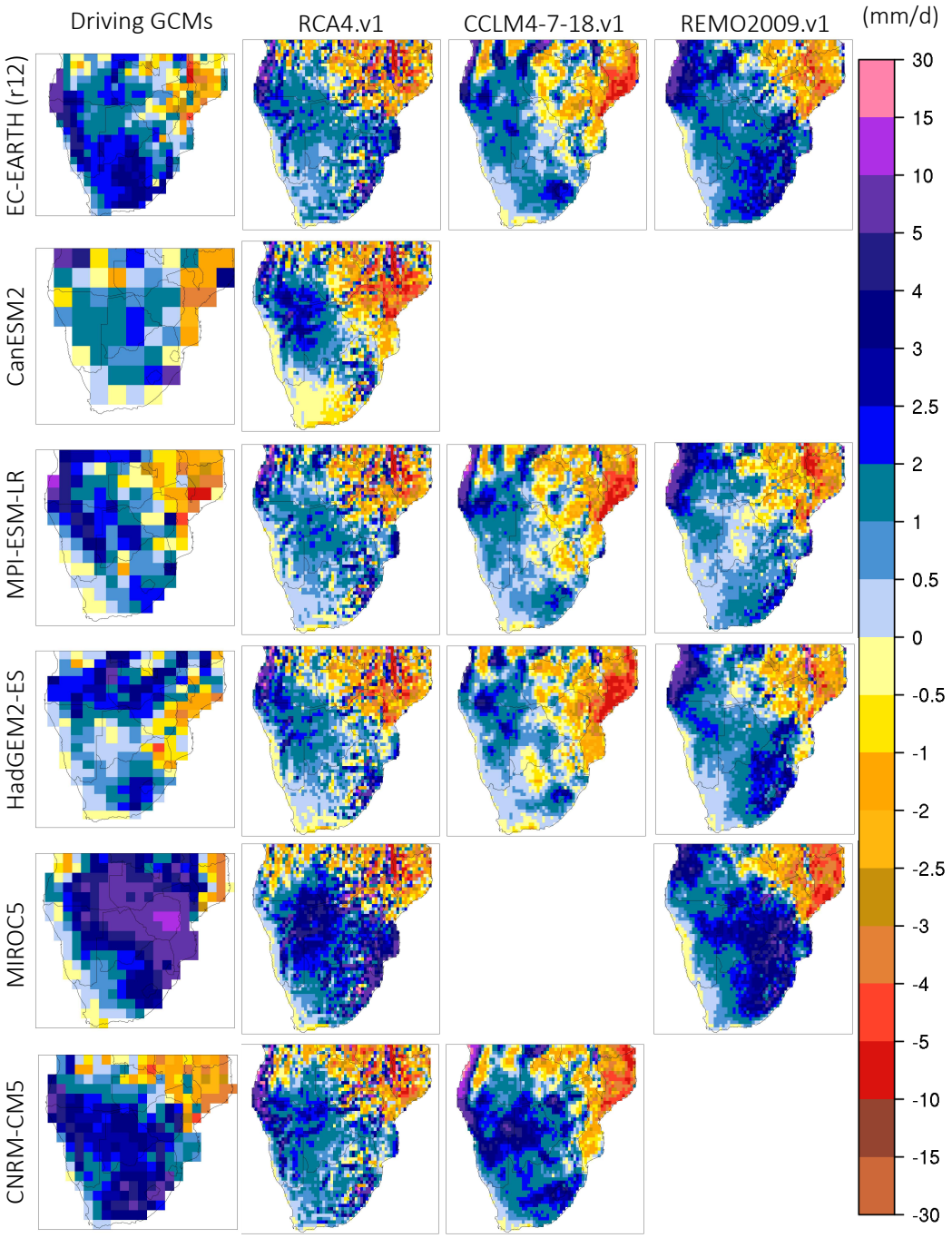

Figure 3.3.7: Monthly precipitation bias (model CHIRPS in mm/d) during January for the period 1985-2005. First column (from the left) displays the biases in the driving GCMs and columns 2-4 display the biases in the downscaled precipitation output according to RCA4.v1, CCLM4-8-17.v1 and REMO2009.v1.

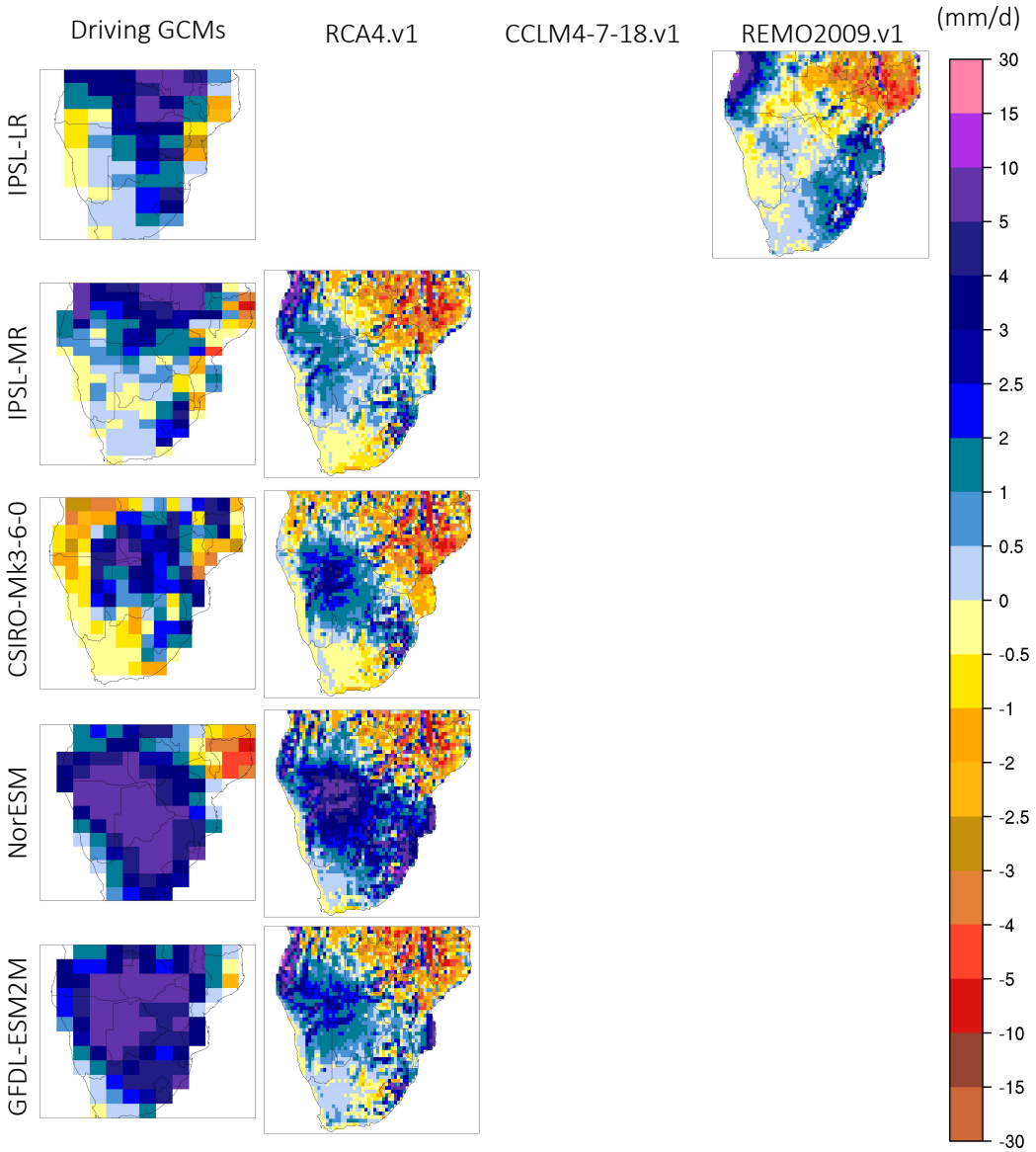

Figure 3.3.8: Continued.

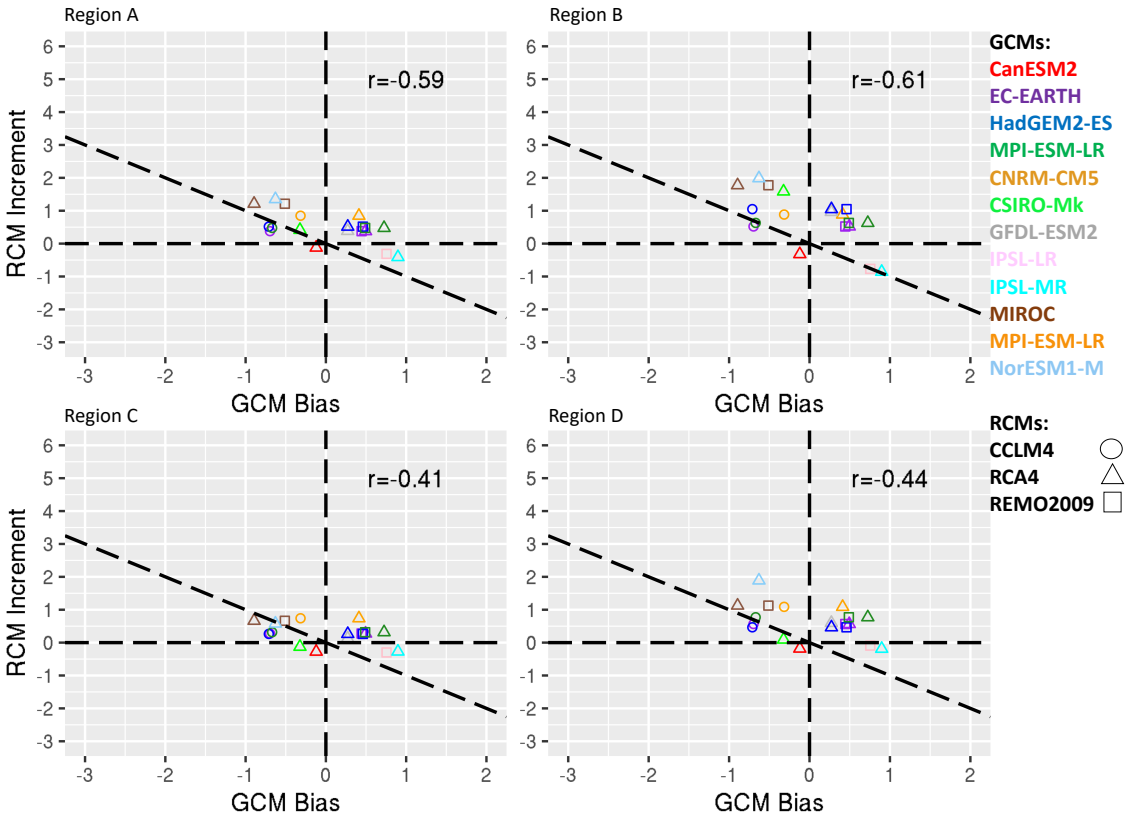

Figure 3.3.9: Scatterplots of the RCM increment (RCM-GCM) for precipitation (mm/day) as a function of the GCM bias (GCM-OBS) for October. Colors indicate the driving GCM and shapes indicate the downscaling RCMs. The four panels indicate spatial averages over southern Africa (Region A), the Angola Low region (Region B), the Mozambique region (Region C) and South Africa region (Region D).

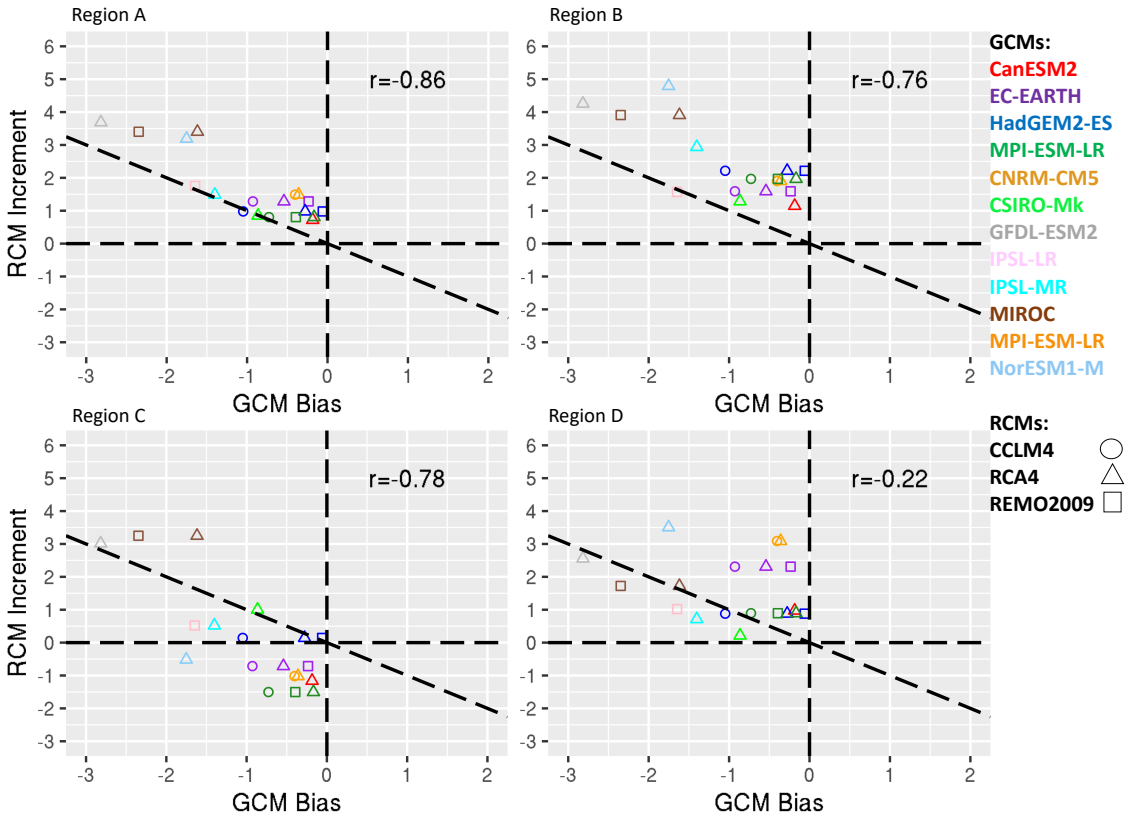

Figure 3.3.10: Scatterplots of the RCM increment (RCM-GCM) for precipitation (mm/day) as a function of the GCM bias (GCM-OBS) for January. Colors indicate the driving GCM and shapes indicate the downscaling RCMs. The four panels indicate spatial averages over southern Africa (Region A), the Angola Low region (Region B), the Mozambique region (Region C) and South Africa region (Region D).

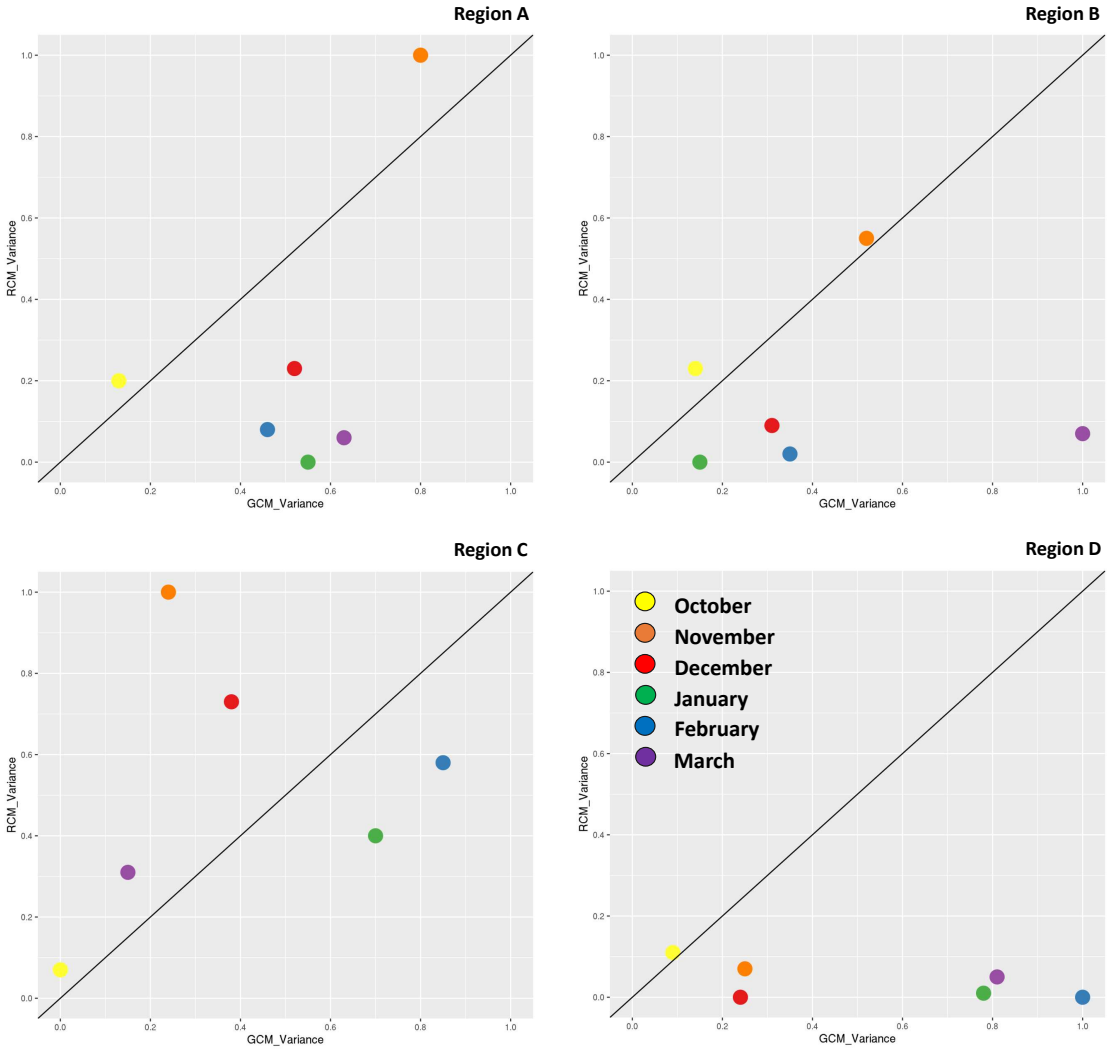

Figure 3.3.11: Analysis of variance for monthly precipitation during 1985-2005 for southern Africa (Region A) and the 3 sub-regions examined, namely Region B (Angola region), Region C (Mozambique region) and Region D (South Africa region). The x and y-axis display standardized precipitation variances.

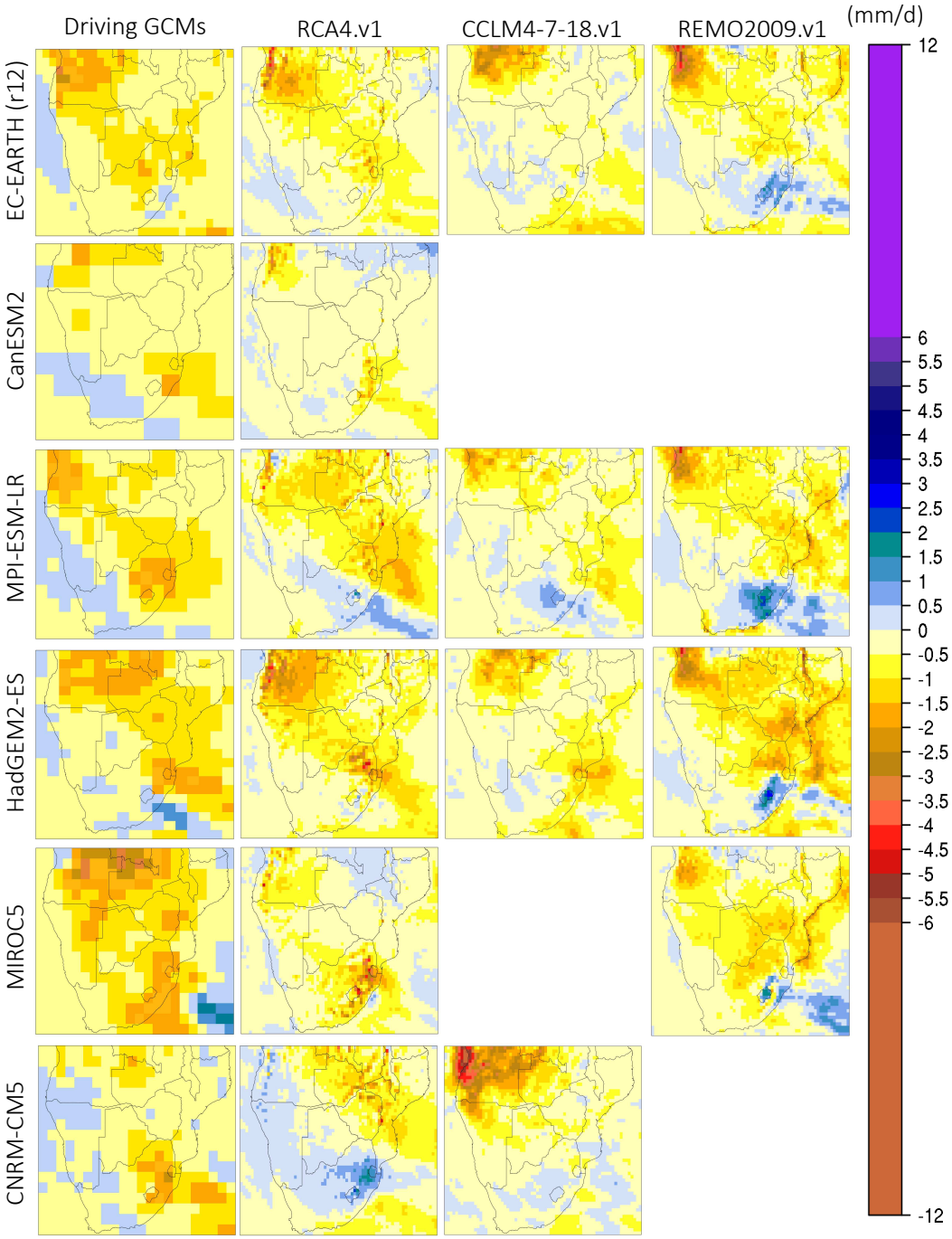

Figure 3.3.12: Monthly precipitation change (future present in mm/d) during October for the period 2065-2095 relative to 1985-2005. First column (from the left) displays precipitation change from the driving GCMs used and columns 2-4 display the downscaled products according to RCA4.v1, CCLM4-8-17.v1 and REMO2009.v1.

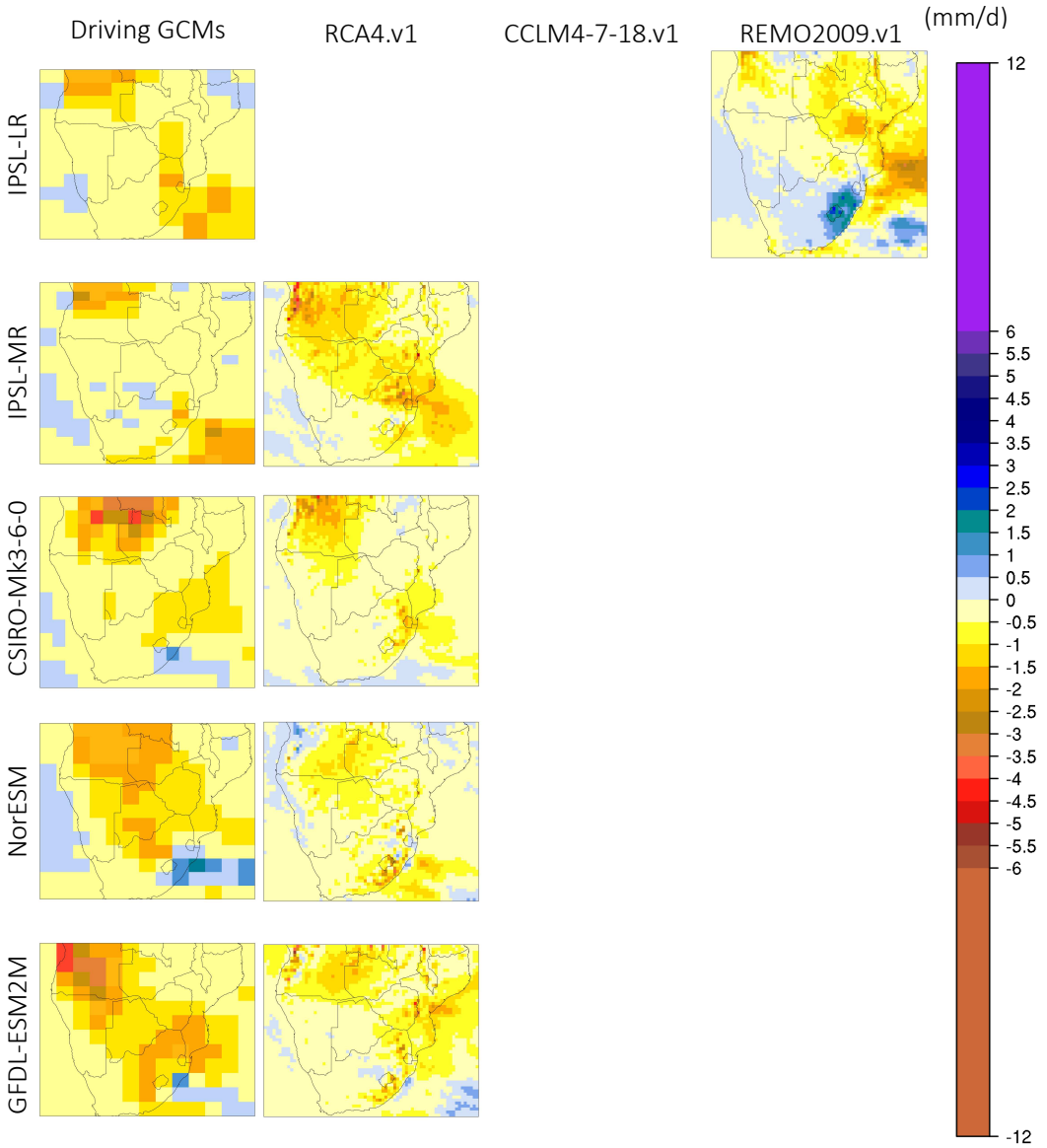

Figure 3.3.13: Continued.

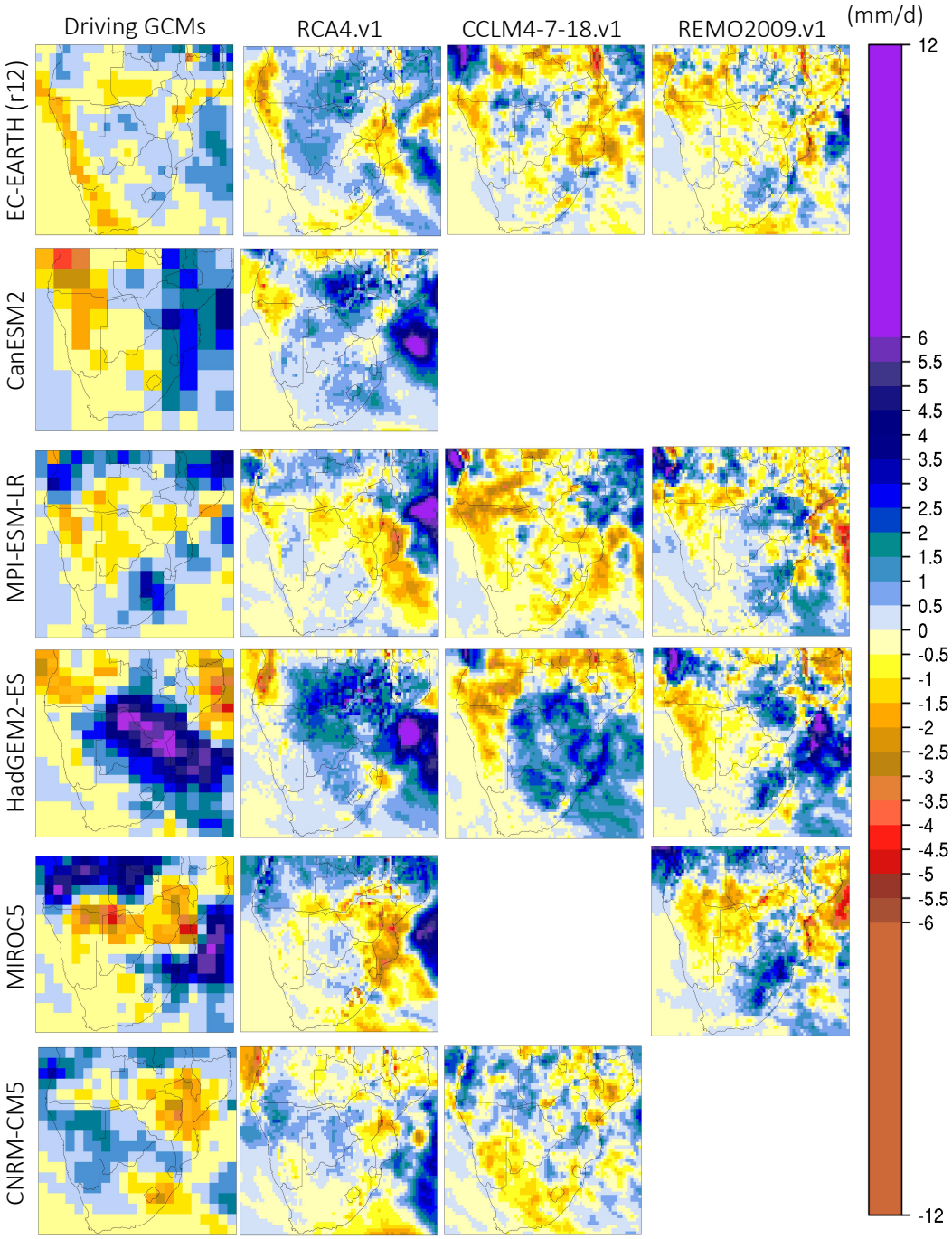

Figure 3.3.14: Monthly precipitation change (future present in mm/d) during January for the period 2065-2095 relative to 1985-2005. First column (from the left) displays precipitation change from the driving GCMs used and columns 2-4 display the downscaled products according to RCA4.v1, CCLM4-8-17.v1 and REMO2009.v1.

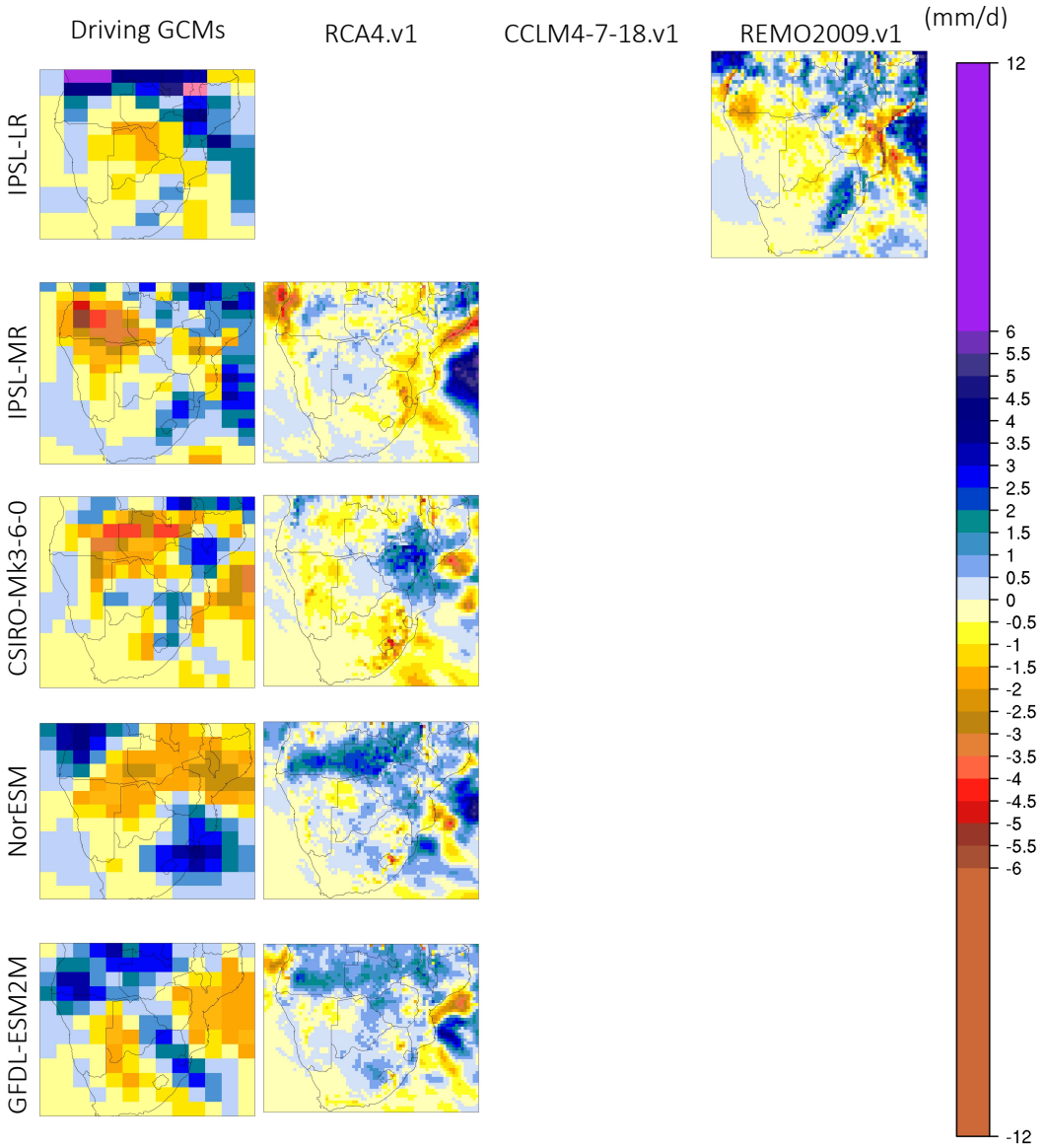

Figure 3.3.15: Continued.

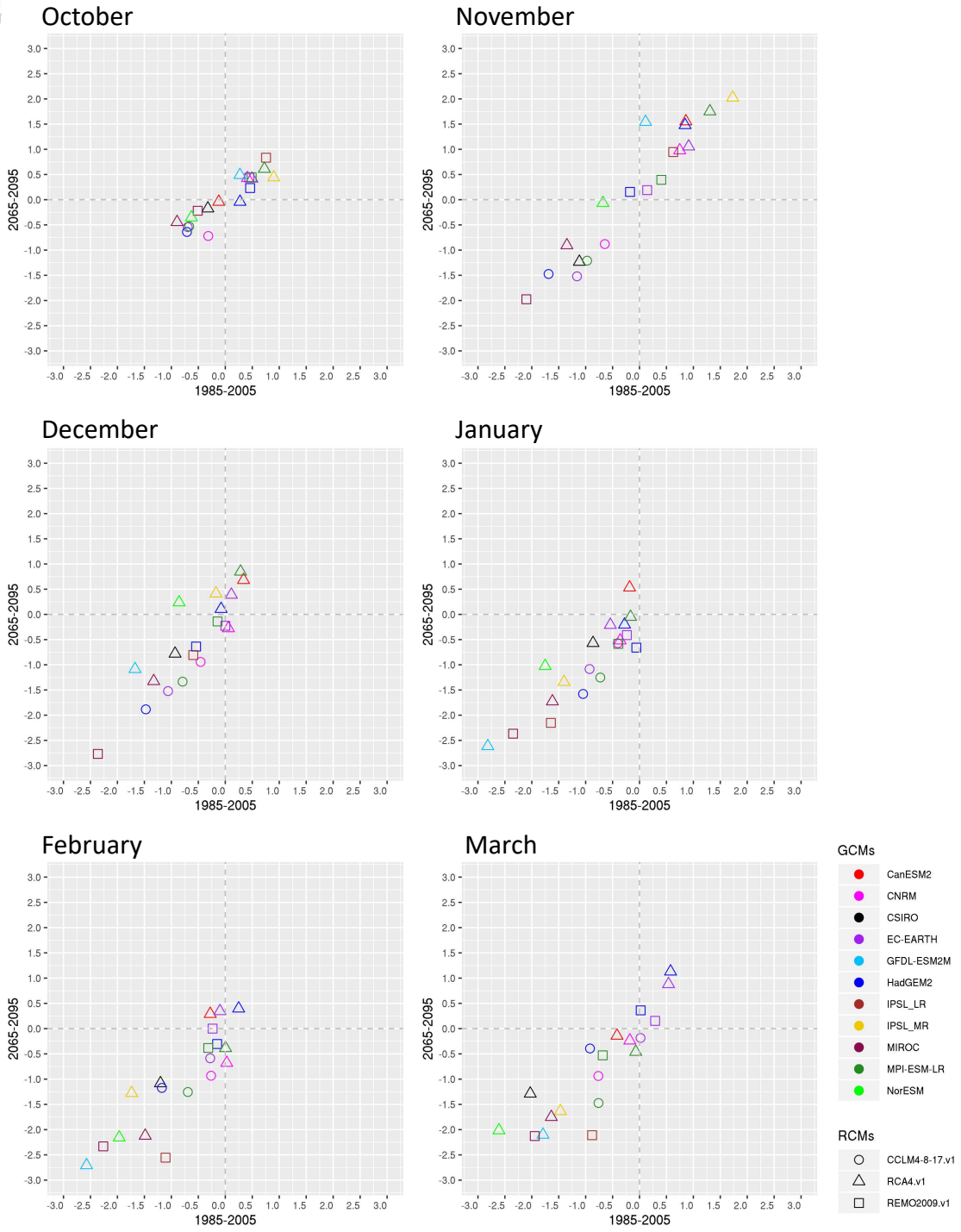

Figure 3.3.16: Monthly RCMDRI DRI spatial averages over southern Africa for the historical period (1985-2005) on the x-axis and the future period (2065-2095) under RCP8.5 on the y-axis.

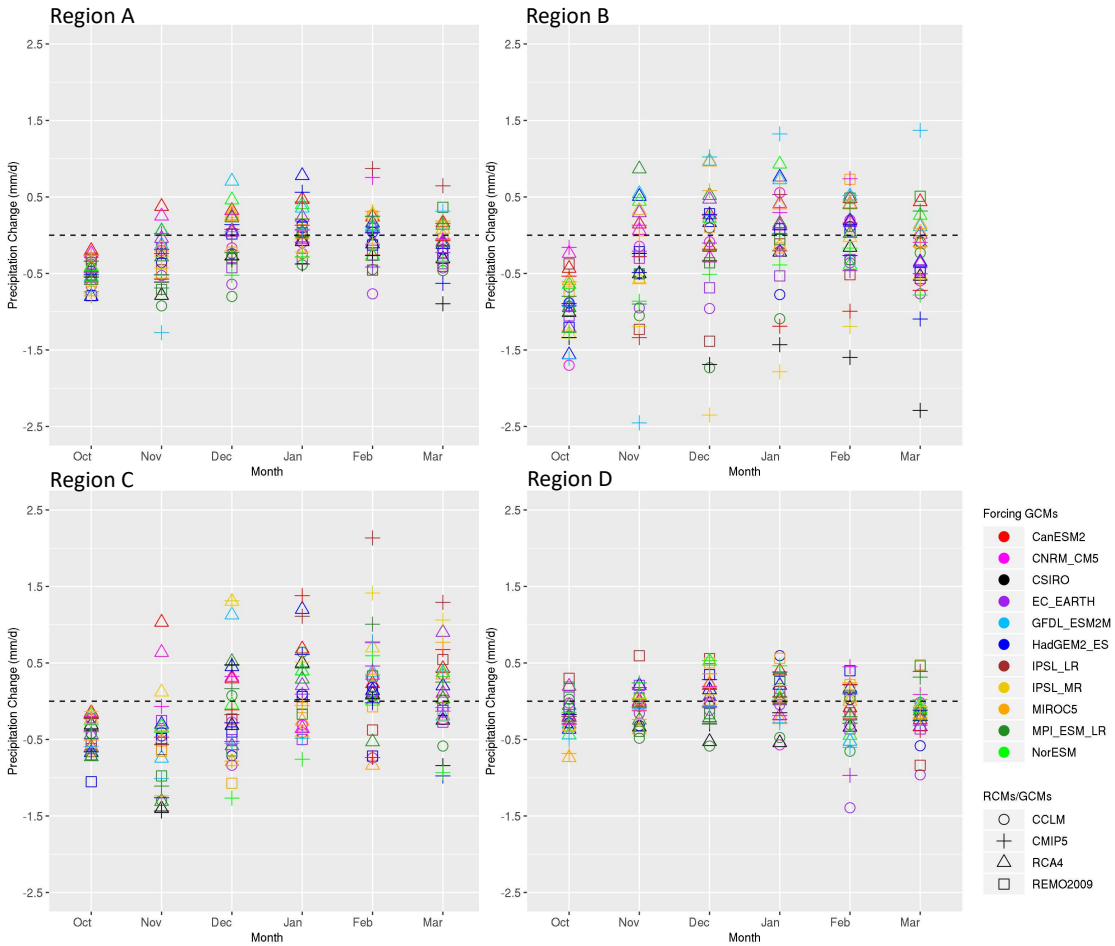

Figure 3.3.17: Spatial average of the precipitation change signal (mm/d) from RCMs and their driving GCMs relative to 1985-2005 for southern Africa and the 3 sub-regions examined.

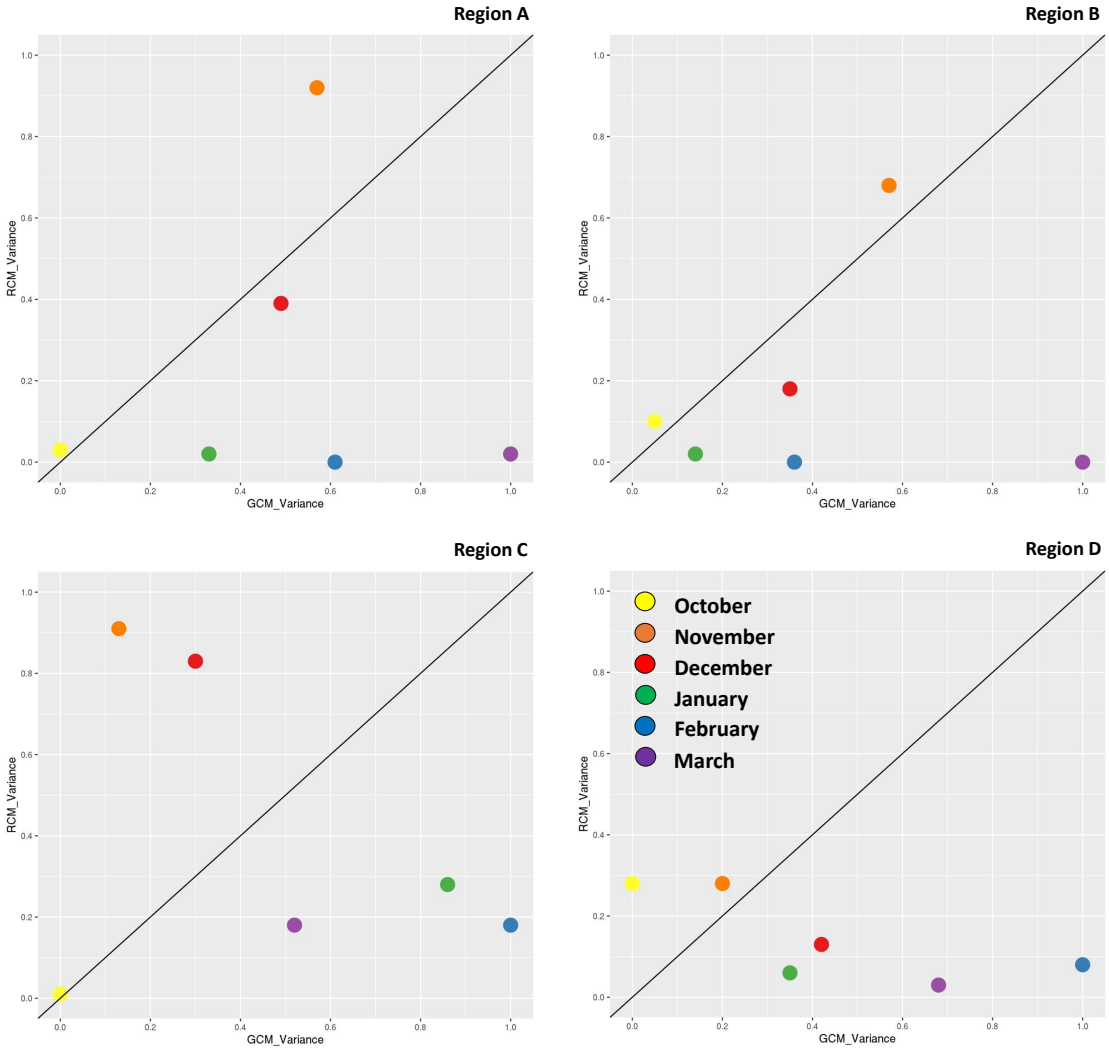

Figure 3.3.18: Analysis of variance for monthly precipitation during 2065-2095 for southern Africa (Region A) and the 3 sub-regions examined, namely Region B (Angola region), Region C (Mozambique region) and Region D (South Africa region). The x and y-axis display standardized precipitation variances.

3.4 Discussion and conclusions

In this work we investigated whether it is the RCMs or the driving GCMs that control the monthly precipitation variability, monthly precipitation biases and the climate change signal over southern Africa and how these relationships vary from month-to-month through the rainy season. Towards this end, we use an ensemble of 19 RCM simulations performed in the context of CORDEX-Africa and their driving GCMs. According to the literature (Munday and Washington (2018)), precipitation in the CMIP5 simulations is characterized by a systematic wet bias over southern Africa. In the CORDEX-Africa RCM simulations there is also a persistent wet bias, especially during the core of the rainy season (DJF), however, it is of smaller magnitude and of smaller spatial extent in the RCMs than the GCMs. It is found that all RCMs reduce monthly precipitation compared to their driving GCMs for both historical (1985-2005) and future period (2065-2095) under RCP8.5.

Over Region B, which encompasses Angola Low (AL) activity, the months with the largest biases are found to be November and March. November is the month during which there is a transition of the AL from a heat low phase to a tropical low system, and March indicates the end of the rainy season. Hence, precipitation during the transition months is challenging for both RCMs and GCMs. Over Region C, representing the wider area of Mozambique, the bias signal is reversed and after January most of the models display a dry bias. Over South Africa (Region D), the majority of models display a consistent wet bias for all months of the rainy season. All models (CMIP5 and CORDEX-Africa) display an intense dry bias in the NE part of SAF, which can be related to the misrepresentation of the moisture transport entering the region from the Indian Ocean (Munday and Washington (2018)). In general, although RCMs display an improvement of precipitation biases relative to their driving GCMs, still some bias patterns persist even in RCMs, calling for a process-based evaluation of specific climatological features such as the formulation of the Angola Low and the transport of moisture from the NE part of SAF towards central SAF.

More specifically, we found that CCLM4-7-18.v1 produces the smallest bias when the whole of SAF is examined, however, it displays a systematic dry bias over Region C (greater Mozambique region), hence, CCLM4-7-18.v1 should be used with caution over eastern SAF, especially if it is exploited within drought-related climate services. Concerning RCA4.v1, we find a very regionally heterogeneous -almost pixelated- spatial pattern for precipitation, which can be attributed to the sharp topography used (Van Vooren et al. (2019)). RCA4.v1, due to the large size of its ensemble, is optimal for analyzing its behavior under different driving GCMs. In general, we find that RCA4.v1 is more prone to follow the signal received from the driving GCMs, contrary to what is observed for CCLM4-7-18.v1. REMO2009.v1 presents a compromise between the behaviors of RCA4.v1 and CCLM4-7-18.v1.

It is highly recommended that when RCM simulations are used for the whole of SAF or a subregion thereof, the spread and statistical properties of all available RCMs and their driving GCMs should be examined and an ensemble of RCMs should be employed based on their ability to reproduce key climatic features of the region of interest. Increasing evidence is provided that not all models are fit for constructing an ensemble mean (or median) for all regions (Her et al. (2019); Raju and Kumar (2020); Tebaldi and Knutti (2007)). Lastly, a very important aspect when the calculation and characterization of biases is discussed for GCMs and RCMs, is that biases are assessed based on a satellite or gauge-based prod-

uct, which are often erroneously regarded as "the ground truth" (Harrison et al. (2019); Alexander et al. (2020)). Of course, the climate community is bound to work with the state-of-the-science products that are available, however, biases and errors in the "observational datasets" should be kept in sight when the bias of climate models is discussed. In this work we use the CHIRPS precipitation product, as it has been shown to outperform other satellite precipitation products (Toté et al. (2015); Ayehu et al. (2018); Dinku et al. (2018)).

Concerning the climate change signal, there is a strong agreement among all GCMs and RCMs that precipitation during October will decrease by (-0.1) – (-1) mm/d, a fact which is associated with a projected later onset of the rainy season, which is further associated by a northward shift of the tropical rain belt (Dunning et al. (2018)). For the rest of the months, the results are variable, indicating the need for a multi-model approach, when climate change impacts are assessed. A feature that is identified in some GCMs and is transferred to the downscaling RCMs, is a precipitation increase that extends from the central SAF region towards the southeast. This result is consistent with previous work that shows an increase in frequency of landfalling cyclones along the eastern seaboard of SAF (Muthige et al. (2018)). Since tropical cyclones are a particular cause of severe flooding events over the region of Mozambique, there is an urgent need for planning and mitigation strategies over the region.

Lastly, concerning precipitation variability and whether it is the RCMs or the driving GCMs that dominate monthly precipitation, we find that, as expected, over the whole of SAF (Region A), October and November are dominated by RCMs, while during Dec-Mar it is the GCMs that mainly formulate the precipitation climatologies. This is explained by the fact that after December there is a strong large-scale forcing, which is provided to the RCMs by the lateral boundary conditions given through the GCMs. The results for the historical period are comparable to that for future projections.

4 Southern Hemisphere upper-troposphere jet stream

4.1 Introduction

The meridional temperature gradient caused by the differential warming between the tropics and the poles is responsible for the existence of a baroclinic zone at mid-latitudes in both hemispheres (Thompson and Woodworth (2014)). The transport of momentum and energy from the tropics towards the poles, under the influence of the Coriolis force, produces fast moving atmospheric currents in the upper troposphere, the jet streams (Li and Wettstein (2012)). In light of the anthropogenic warming observed during the last decades (IPCC and Stocker (2013)) and the poleward expansion of the tropics (Staten et al. (2018); Maher et al. (2020); Yang et al. (2020)), a crucial question has emerged with regards to how this temperature gradient will change (Yang et al. (2020)) and what further implications will this have on jet streams, storm tracks and weather regimes on both hemispheres. Jet stream characteristics display variable attributes between the two hemispheres Manney and Hegglin (2018).

In the Northern Hemisphere (NH), the disentangling of the climate change signal from the internal variability noise, poses severe challenges in determining whether the jet has strengthened and whether it has shifted polewards (Barnes and Screen (2015)). The fast warming rate of the Arctic, compared to warming observed over lower latitudes has been termed as Arctic Amplification (Previdi et al. (2021); Rantanen et al. (2022)). Arctic amplification (Cohen et al. (2014)) has caused the weakening of the meridional temperature gradient between the tropics and the pole in lower troposphere. This mechanism alone would shift the jet equatorward (Woollings and Blackburn (2012); Pena-Ortiz et al. (2013)), as it has been simulated during summer by climate models (Barnes and Simpson (2017)). Nonetheless, the temperature gradient of the upper troposphere between the tropics and the Arctic has increased, a fact that would cause a poleward jet shift. Therefore, the aforementioned competing forces are in a tug-of-war and the question of which force has historically dominated the jet shift is not fully answered. However, since competing forces act on different pressure levels in the troposphere, it was found that a unique signature of the climate change impact on the NH jet is a robust increase of its wind shear (Lee et al. (2019)). More specifically, no increase of wind speed in the North Atlantic sector of the jet was identified, however, vertical wind shear increased by 15% during the last four decades (Lee et al. (2019)).

The dominant process over the Southern Hemisphere (SH) controlling the position and intensity of the jet stream is ozone depletion in the lower stratosphere – upper troposphere of Antarctica (Thompson

et al. (2011); Dhomse et al. (2019)), which is particularly evident during summer. The reported poleward shift of the jet was found to be 2° polewards during the end of the 20th century (Rivière (2011); Pena-Ortiz et al. (2013); Karpechko (2020)). In addition, the increase of long-lived greenhouse gases (LLGHGs) in the tropics that warm the middle and upper tropical troposphere have contributed significantly (Steiner et al. (2020)) in enhancing the temperature gradient between the tropics and the pole (Rotstayn et al. (2013)). This pattern (increase in LLGHGs over the tropics and ozone depletion over the Antarctica) steers the poleward migration of the jet and favors the occurrence of the positive phase of the South Annular Mode (SAM) (Thompson and Wallace (2000); Kushner et al. (2001); Swart et al. (2015)), which further causes temperature increase over Antarctica in the lower troposphere also (Clem et al. (2020)). Consequently, the wind speed of the jet has also increased during the last decades (Gallego et al. (2005); Pena-Ortiz et al. (2013)). Nonetheless, an aspect that until now has not been examined for the SH jet yet, is the change (if any) in its vertical wind shear.

The aim of this chapter is to tackle the question with regards to whether wind shear of the SH jet stream has increased during the last decades, using a reanalysis product, and to further investigate the degree to which vertical wind shear in the jet stream can be attributed to the thermal wind balance.

4.2 Data and Methods

This work is performed using the ERA5 reanalysis product Hersbach et al. (2020) on a 0.25° x 0.25° horizontal spatial resolution. Data are retrieved from the Copernicus Climate Data Store for the period 1950-2021. Mean monthly temperature is retrieved for 200, 250, 300, 400, 500, 600, 700, 850, 925 and 1000 hPa, while mean monthly zonal wind component is retrieved on 200, 250, and 300 hPa. All variables are obtained and analyzed for the SH (1 – 90 °S and 180 °W to 180 °E).

The jet stream is identified as the zonal wind component at 250 hPa, where mean annual eastward wind speed exceeds 20 m/s. Other studies have used the threshold of 30 m/s (Gallego et al. (2005); Pena-Ortiz et al. (2013)), however they considered daily wind speed fields. Here, the threshold of 20 m/s corresponds to the 90th percentile of the distribution of annual 250 hPa zonal wind values. In addition, the jet stream is identified into its subtropical jet (STJ) and polar jet (PJ) counterparts, based on the latitude on which they occur, which in general is an acceptable compromise for the SH. More specifically, when jet structures are identified between 1 °S to 40 °S then this is termed as STJ, while when they are identified from 40 °S to 90 °S, then this is considered as PJ (Gallego et al. (2005); Pena-Ortiz et al. (2013)).

Wind shear at 250 hPa is calculated using two different approaches. The first approach to calculate Wind shear is by employing centered vertical finite differences between 200 and 300 hPa, according to Eq. 4.2, using mean annual zonal wind speed, following Lee et al. (2019) and is expressed as m/s per 100 hPa.

$$WindShear = U_{200} - U_{300}$$

The second approach to calculate wind shear at 250 hPa is by using the thermal wind balance, as shown in Eq. 4.2, in accordance to Wallace and Hobbs (2006):

$$-\frac{\partial u}{\partial p} = -\frac{R}{f * p} * \frac{\partial T}{\partial y}$$

in which p is atmospheric pressure, R is the specific gas constant for dry air (R 0.286), f is the Coriolis parameter, u is the zonal wind speed and T is temperature at 250 hPa. The left side of Eq. 4.2 indicates wind shear as a function of pressure, while the right side indicates the meridional temperature gradient.

Trends are calculated using Theil-Sen's slope (Sen (1968); Theil (1992)) and statistical significance is assessed using the Mann-Kendall test (Mann (1945); Kendall (1948)).

4.3 Results

In Fig. 4.3.1 the annual temperature trends (K per decade) in ERA5 for the period 1950-2021 at each pressure level are shown. Trends are calculated using Sen's slope. It is evident that the upper troposphere (200 and 250 hPa) displays the largest warming difference between the tropics and Antarctica. Temperature trends over the tropics and part of the extra-tropics (30 °S) increase with a rate of 0.2 - 0.3 K/decade at 200 and 250 hPa, while the region from 60 °S and polewards is dominated by decreasing trends that reach -0.3 to -0.1 K/decade, for 200 and 250 hPa, respectively. Statistical significance is examined for a=0.05. At 300 hPa increasing trends are observed across the whole SH, ranging from 0.1 to 0.25 K/decade, with an exception for Antarctica where weak and not statistically significant trends are displayed. At 400 and 500 hPa increasing trends are observed throughout the whole SH, while at 600 hPa, isolated areas of temperature increase exceeding 0.3 K/decade are observed over Antarctica. These regions become more pronounced closer to the surface.

In Fig. 4.3.2 the density plots of annual temperature (K) for five climatological periods in ERA5 and for three pressure levels are shown. Spatial averages over the original ERA mesh are calculated across the tropical – extratropical region (1 - 40 °S) (Fig. 4.3.2a) and across the higher latitude region (40 °S – 80 °S) (Fig. 4.3.2b) for the upper troposphere (200, 250, and 300 hPa). For both regions and for all pressure levels there is a clear shift of the calculated densities towards higher temperature values, moving from the 1951–1980 climatology towards the most recent climatology (1991–2020). During the latter climatology there is also an observed stretching of the tails of the distributions, indicative of extreme events. There is, however, an exception for 200 hPa in Fig. 4.3.2b, where the distribution of the latter climatology displays an identifiable shrinkage and shift towards lower temperatures.

In Fig. 4.3.3a, the mean annual zonal wind speed at 250 hPa (m/s) for the period 1950–2021 is displayed. Maximum wind speeds indicative of the jet stream are observed between 20 °S and 60 °S. The STJ identified equatorward of 40 °S displays maximum speed values over Australia and the western Pacific, reaching 36 m/s. These regions are also characterized by the descending branch of the Hadley cell. Poleward of 40 °S, maxima of zonal wind speeds are identified over the southwestern Indian Ocean. As shown in Fig. 4.3.3b, statistically significant increasing trends of wind speed are identified between latitudes 40 °S to 60 °S ranging from 0.2 to 0.65 m/s per decade. Maximum increasing trends are almost collocated with the PJ jet core region. Across latitudes 20 °S there is also a secondary region of increasing trends identified, which is however of smaller magnitude. Vertical wind shear at 250 hPa calculated from the difference between 200 and 300 hPa is displayed in Fig. 4.3.3c. High wind shear values are observed between 20 °S to 40 °S, indicating that the STJ is highly sheared. Wind shear poleward

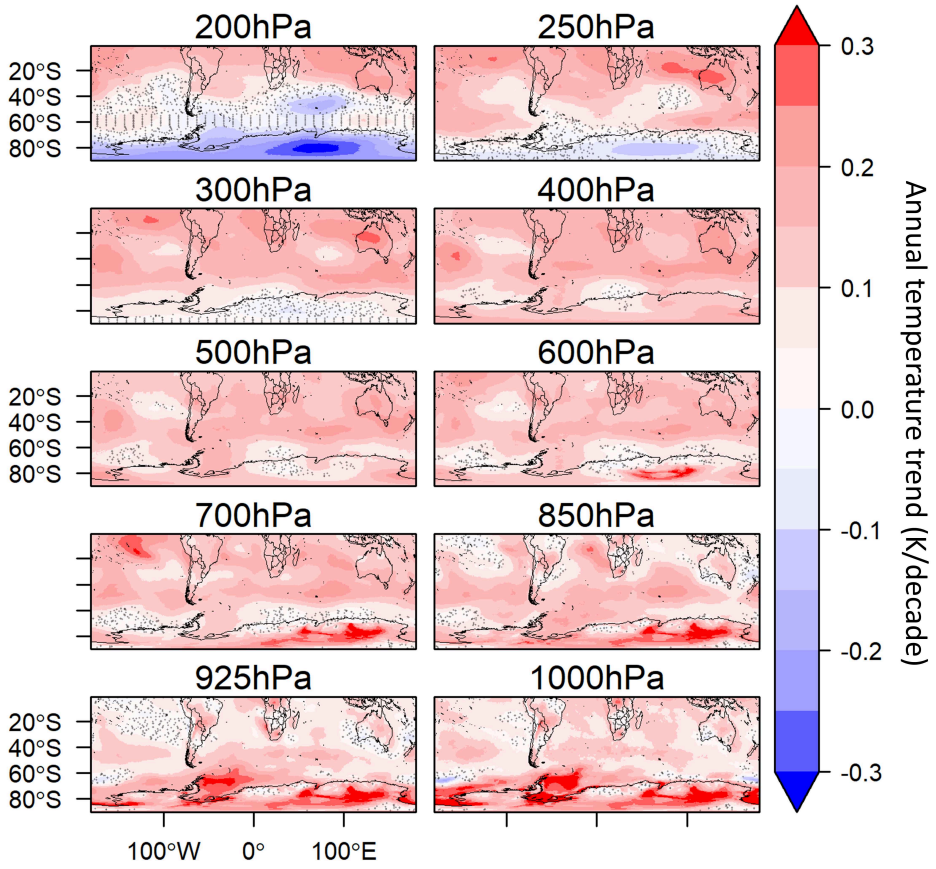

Figure 4.3.1: Annual temperature trends (K per decade) in ERA5 for the period 1950-2021 at each pressure level. Trends are calculated using Sens slope. Statistical significance is assessed using the Mann-Kendall test. Non-statistically significant trends are indicated by dots (a=0.05).

of 40 °S is considerably weaker. In Fig. 4.3.3d, wind shear trends are displayed. In general, wind shear trends are weak and for the largest extent of the SH not statistically significant, however, over a region extending from the central Indian Ocean towards western Australia wind shear trends exceeding 0.6 m/s/100 hPa per decade are observed.

In Fig. 4.3.4 time series of annual zonal wind speed and vertical wind shear at 250 hPa are shown, for the period 1950–2021 and averaged over selected regions of interest. Concerning wind shear (Fig. 4.3.4a), there is a statistically significant increase in all regions (with an exception for Region A and C, in which although shear is increasing, it is not statistically significant), ranging from 1.56 to 5.69 m/s/100 hPa per decade. The largest wind shear increase (5.69 m/s/100 hPa per decade) is observed over the southern Indian Ocean, while statistically significant increasing trends are also identified over the southeastern Atlantic Ocean. In general, both the STJ (Region G) and PJ (Region F) have become more sheared during the last seven decades, however, vertical wind shear increase is more severe in the STJ (3.25 m/s/100 hPa per decade). Concerning wind speed (Fig. 4.3.4b), over almost all the subregions examined a decreasing trend is identified, which is statistically significant only over Region E (southern

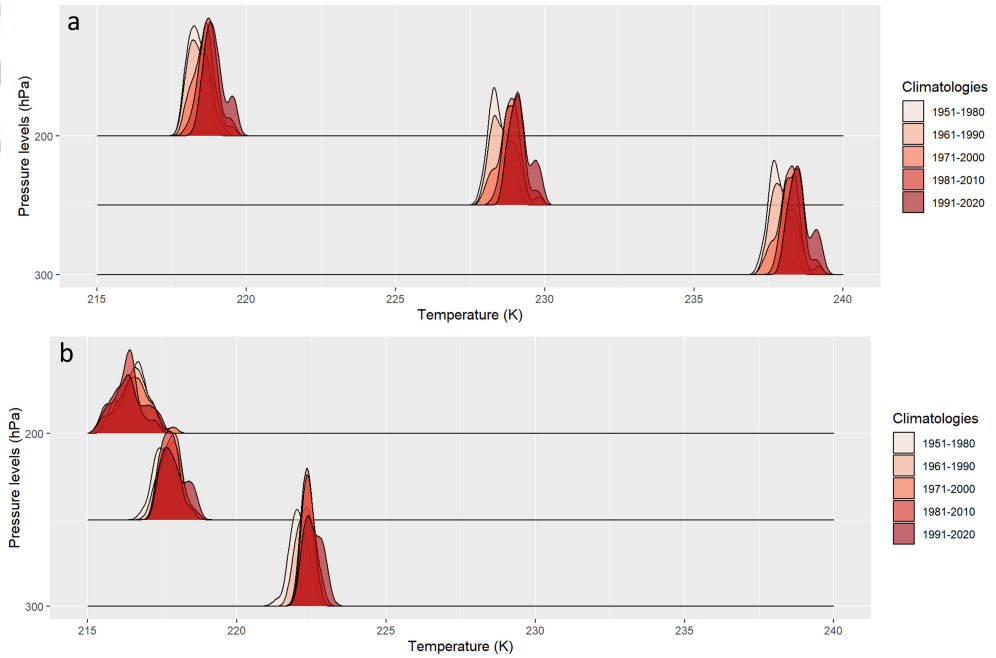

Figure 4.3.2: Density plots of annual temperature (K) for five climatological periods (1951-1980, 1961-1990, 1971-2000, 1981-2010, 1991-2020) in ERA5 and for three pressure levels: 200, 250 and 300 hPa. Spatial averages over a) from 1 to 40 °S and from 180 °E to 180 °W and b) from 40 to 80 °S and from 180 °E to 180 °W.

Indian Ocean). Overall, robust increasing wind speed is identified over Region F, implying that during the last seven decades the PJ has strengthened, with a rate 3.9 m/s per decade.

In Fig. 4.3.5 wind shear at 250 hPa calculated from the zonal wind fields at 200 and 300 hPa (Fig. 4.3.5a), along with wind shear calculated from thermal wind balance (Fig. 4.3.5c). As shown, wind shear calculated using the thermal wind balance displays very similar spatial patterns across the whole SH (compared to vertical wind shear calculated directly from observations at 200 and 300 hPa). More specifically, maximum vertical wind shear values are identified over latitudes ranging from 20 °S to 40 °S, indicating a strongly sheared STJ. Within this range of latitudes, local wind shear maxima are identified over the western Pacific, over a tilted region extending from central Pacific towards South America, and over the Indian Ocean and Australia. The spatial pattern of the trends of wind shear calculated from thermal wind balance (Fig. 4.3.5d) is very similar to the ones calculated from the zonal wind at 200 and 300 hPa.

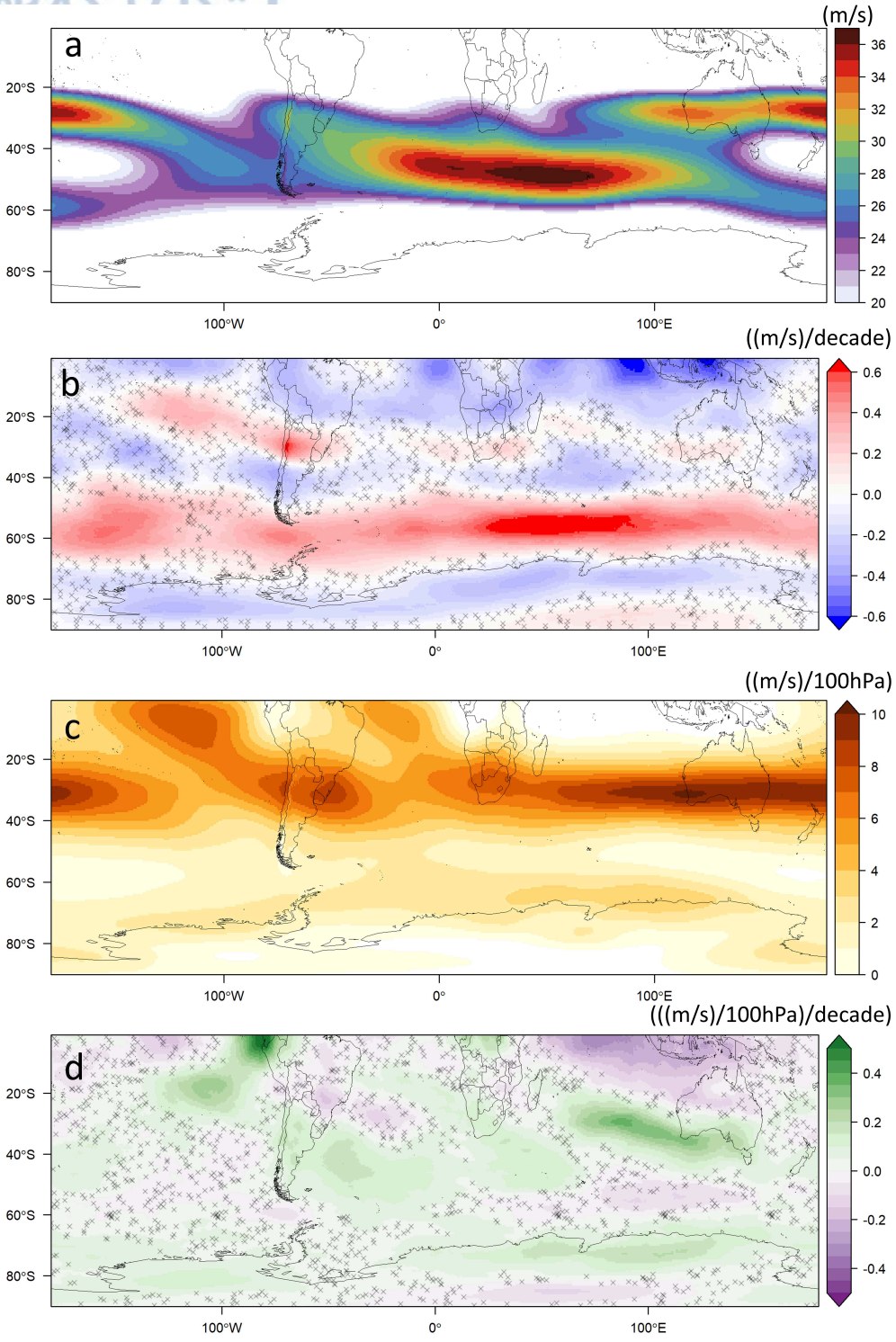

Figure 4.3.3: a) Mean annual zonal wind speed at 250 hPa (m/s), b) trend for mean annual zonal wind speed at 250 hPa (m/s per decade), c) mean annual wind shear of zonal wind at 250 hPa ((m/s)/100 hPa), d) trend for mean annual wind shear of the zonal wind at 250 hPa ((m/s)/100 hPa per decade). Data used: ERA5 for the period 1950 - 2021. Statistical significance is assessed using the Mann-Kendall test. Non-statistically significant trends are indicated by dots (a=0.05).

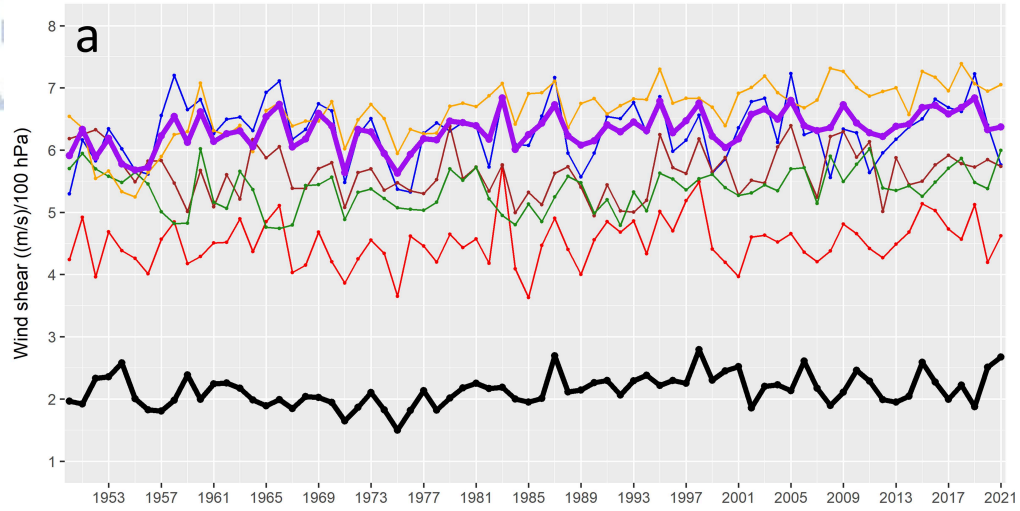

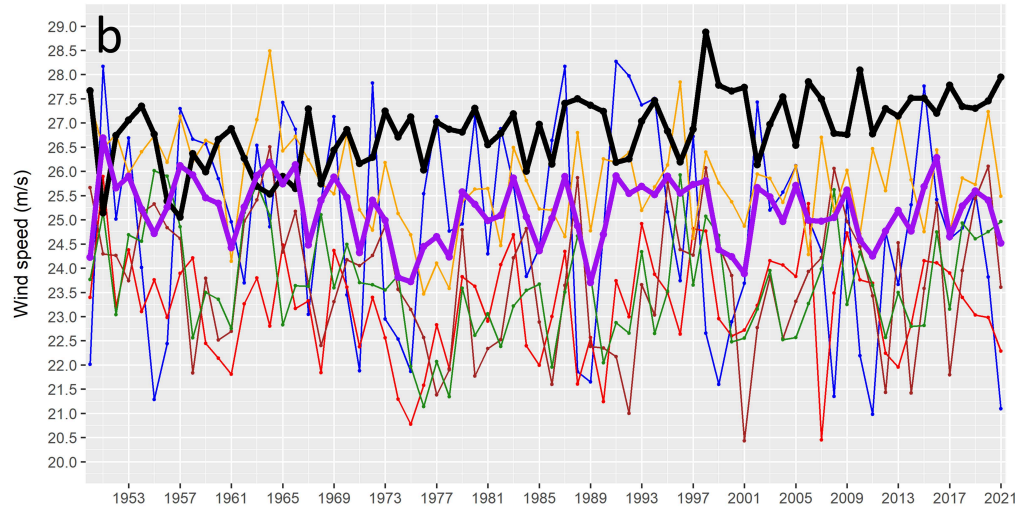

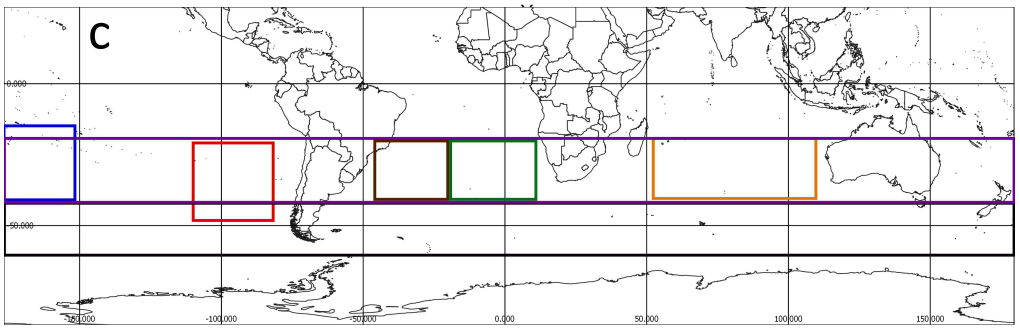

d

	RegionA	RegionB	RegionC	RegionD	RegionE	RegionF	RegionG
Wind Speed	-0.89	0.23	-0.65	-0.58	-1.61*	3.9*	-0.97
Wind Shear	0.65	1.59*	0.2	1.56*	5.69*	2.34*	3.25*

Figure 4.3.4: Time series of mean annual zonal wind attributes at 250 hPa in ERA5 for the period 1950-2021. a) Spatial average of vertical wind shear ((m/s)/100 hPa), b) spatial average of zonal wind speed (m/s). Spatial averaged are calculated the 6 boxes shown in panel c, d) Mann-Kendall tau per region asterisk indicates statistically significant trends (a=0.05).

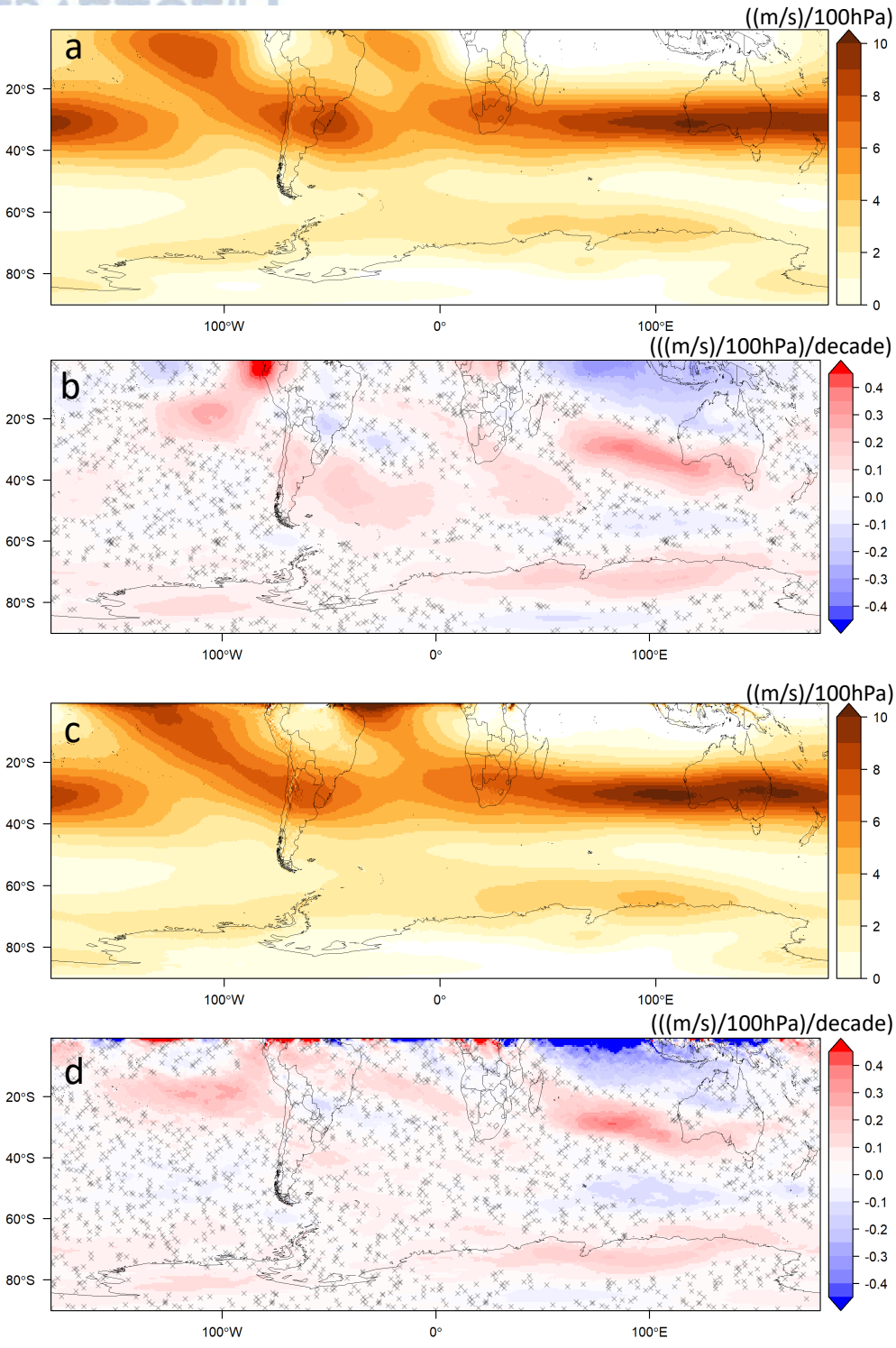

Figure 4.3.5: a) Mean annual wind shear of zonal wind at 250 hPa ((m/s)/100 hPa), b) trend for mean annual wind shear of the zonal wind at 250 hPa ((m/s)/100 hPa per decade), c) mean annual wind shear of zonal wind at 250 hPa ((m/s)/100 hPa) calculated from thermal wind balance, d) trend for mean annual wind shear of the zonal wind at 250 hPa ((m/s)/100 hPa per decade) calculated from thermal wind balance. Data used: ERA5 for the period 1950 - 2021. Statistical significance is assessed using the Mann-Kendall test. Non-statistically significant trends are indicated by dots (a=0.05).

4.4 Discussion

In this work the question in concern is whether wind shear over the SH in the upper-level jet stream has changed over the last seven decades, according to the ERA5 reanalysis product. Additionally, wind speed trends are also examined. It is found that the wind speed of the PJ is increasing with a rate of 3.9 m/s per decade. Maximum wind speed trends are identified over the southern Indian Ocean. Wind shear is increasing in both the STJ and the PJ, however, wind shear trends in the STJ are larger (3.25 m/s/100 hPa per decade). Wind shear can be attributed to the temperature gradient between the tropics and the pole, which is verified by the fact that when wind shear is calculated using the thermal wind balance, its spatial pattern and magnitude is very similar to when wind shear is calculated from the zonal wind fields at 200 and 300 hPa.

The robust declining temperature trends in the lower stratosphere - upper troposphere (200 hPa) over Antarctica are associated to the radiative cooling caused by ozone depletion (Bandoro et al. (2014)), while the near surface (700 – 1000 hPa) increasing trends are associated to a severe cyclonic anomaly over the western Pacific, in combination with a positive SAM phase (Clem et al. (2020)). Ozone depletion over Antarctica was found to exhibit a great impact on the circulation of the SH, mainly by favoring the occurrence of positive SAM events. Positive SAM was linked to warming over mainland regions of the SH, such as southern Africa (Manatsa et al. (2013)). Most notably, the enhancement of positive SAM was found to be correlated with the strengthening of a semi-permanent low-pressure system, the Angola Low pressure system (Munday and Washington (2017); Howard and Washington (2018)), which is a key atmospheric feature controlling the re-distribution of low-level moisture over SAF. Variability in strength, location and waviness of the STJ over the south-east Atlantic and south-west Indian Oceans severely affect the occurrence of tropical temperature troughs (TTTs) over southeastern SAF (Vigaud et al. (2012); Macron et al. (2014)). It is noted that precipitation over SAF is approximately to 40% attributed to the occurrence of TTTs (Macron et al. (2014)).

A further question to be tackled is how is the jet stream simulated in regional climate model simulations over Africa and how are their attributes associated to regional precipitation. This question is addressed in the following chapter.

5 Dynamical aspects of the rainy season climatology over southern Africa in the CORDEX-Africa ensemble

5.1 Introduction

Southern Africa (SAF) is a region whose societal and economic prosperity is highly coupled with precipitation variability (Hoell et al. (2021)). The timing of rainfall onset and cessation is a key attribute for successful agricultural yield (Sazib et al. (2020)), adequate hydropower supply (Conway et al. (2015)), and sufficient water for hygiene and sanitation (Winter et al. (2021)). In this context, access to "Clean Water and Sanitation" is indexed as the 6th Goal of the Sustainable Development Goals set by the United Nations (`https://sdgs.un.org/goals`). Therefore, precipitation is justifiably listed among the Essential Climatic Variables (ECVs), as defined by the Global Climate Observing System (GCOS) project (Bojinski et al. (2014)), operating under the auspices of the World Meteorological Organization (WMO). Nonetheless, accurate estimates of precipitation over SAF present a non-trivial challenge. Scarcity of observed precipitation data over the region, pose a severe difficulty in the construction process of homogeneous high-resolution rainfall products (Le Coz and van de Giesen (2020)).

Precipitation as simulated by the Global Climate Models (GCMs) participating in the Coupled Model Intercomparison Project Phase 5 (CMIP5) ensemble Taylor et al. (2012), displayed a systematic wet bias over SAF. This bias is caused by the excess moisture inflow towards mainland areas, originating primarily from the tropical Indian Ocean and entering SAF through Tanzania (Munday and Washington (2018)). Due to the coarse resolution of CMIP5 GCMs, high elevation areas over Tanzania are misrepresented and moisture flux from the tropical Indian Ocean enters central SAF unhindered. The same wet bias persists also in the CMIP6 ensemble (Tian and Dong (2020)). A substantial improvement with regards to precipitation was achieved by the Coordinated Regional Downscaling Experiment – Africa (CORDEX-Africa) set of simulations (Giorgi and Gutowski (2015); Jacob et al. (2020)), which was partly attributed to the increased spatial resolution of the Regional Climate Models (RCMs) involved (Karypidou et al. (2022a)). More specifically, it was diagnosed that in the CORDEX-Africa ensemble, low-level moisture fluxes entering SAF from the tropical Indian Ocean during December-January-February (DJF), are forced to recurve around northeast SAF and are navigated towards northern Madagascar. Still, a wet bias was nevertheless also present in the CORDEX-Africa ensemble, but it was of smaller magnitude than that observed in the CMIP5 ensemble.

Precipitation regimes over southern Africa are highly correlated with sea surface conditions both with the adjacent Atlantic and Indian Oceans and the more remote Pacific Ocean (Maidment et al. (2015); Pomposi et al. (2018)). The dominant mode of interannual precipitation variability over SAF is associated with the El Nino – Southern Oscillation (ENSO) (Reason and Jagadheesha (2005)), with the La Nina phase being associated with wet conditions over the subcontinent (Giannini et al. (2008)). Another significant mode of interannual variability is the Indian Ocean Dipole (IOD), associating SST differences between the east and the west Indian Ocean with the moisture that is advected towards SAF (Polonsky and Torbinsky (2021)). More specifically, when SSTs over the western Indian Ocean are warmer than those over its eastern counterpart, moisture fluxes towards eastern SAF are enhanced (Reason (2001)). A complimentary dipole between the south-west and the north-west Indian cean results to excess DJF precipitation over SAF, when SSTs over the south-west Indian Ocean are larger than SSTs over the north-west Indian Ocean (Washington and Preston (2006)).

Over the southern Atlantic Ocean, a semi-permanent high pressure (SAHP) system plays a significant role in navigating the cold ocean upwelling currents along SAF's western coast and inhibiting convection during DJF (Desbiolles et al. (2020)). Over the Indian Ocean, the Mascarene high (MH) pressure system is key for moisture transport towards SAF (Xulu et al. (2020)). Climatic conditions over the southeastern part of the subcontinent are significantly influenced by the Agulhas Current (AC), which is characterized as the strongest western boundary current of the southern hemisphere. The AC has been associated with a co-located rainband of precipitation, which is reinforced by enhanced latent heat fluxes, through the evaporation of sea water (Njouodo et al. (2018)). Over SAF, a dominant semi-permanent low-pressure system responsible for the distribution of moisture over the subcontinent is the Angola low (AL) pressure system (Munday and Washington (2017)), located over southeast Angola. The AL has solely heat low characteristics during the early rainy season (Oct-Nov: ON), while during DJF it is characterized as the climatological mean of transient low-pressure systems (Howard and Washington (2018)). The AL has been found to exert a significant impact on the severity of ENSO over SAF (Reason and Jagadheesha (2005)).

Although a significant number of studies has been performed within CORDEX-Africa with respect to evaluating key climatological variables (Nikulin et al. (2012); Kalognomou et al. (2013); Shongwe et al. (2014); Favre et al. (2016)) and assessing future projections (Maúre et al. (2018); Tang et al. (2019); Dosio et al. (2021)), there is still need to investigate the dynamical processes controlling precipitation climatology over SAF in more detail. One of the reasons hindering certain types of dynamical analysis within CORDEX-Africa is that variables available on vertical pressure levels are limited. In this work, the aim is to utilize the whole set of the CORDEX-Africa variables available on pressure levels, in order to get a more comprehensive overview of the simulated climate by each RCM for the historical simulations, and how the story each RCM narrates corresponds to the precipitation climatology during the rainy season of the period 1986-2005.

5.2 Data

In this work 26 RCM simulations are utilized, performed within CORDEX-Africa, with a 0.44° x 0.44° horizontal spatial resolution (Table 5.2.1). Historical runs for the period 1986-2005 are exploited and the

focus is placed on the rainy season over SAF, extending from October until March. All variables are analyzed for the early rainy season (ON) and for the core rainy season (DJF). The region in concern extends from 0 – 44 °S and from -24 to 59 °E, enclosing the southern hemisphere extent of the CORDEX-Africa domain. It is noted that more than half of the total grid points within the analyzed region are ocean grids points located over sea. Although CORDEX-Africa simulations are not coupled with ocean models, these grid points located over sea are preserved for visual inspection purposes. All simulations are retrieved from the Earth System Grid Federation (`https://esgf-data.dkrz.de/projects/esgf-dkrz/`). The downloaded files contain monthly values and the analyzed variables are the following: precipitation (pr), convective precipitation (prc), outgoing longwave radiation (OLR) at the top of the atmosphere (rlut), u and v wind components at 200 hPa, 500 hPa and 850 hPa (u200, u500, u850, v200, v500, v850), temperature at 200 hPa, 500 hPa and 850 hPa (ta200, ta500, ta850), sea level pressure (psl), specific humidity at 850 hPa (hus850), and geopotential height at 200 hPa and 500 hPa (zg200, zg500). Additionally, vertical velocity is retrieved from the ERA5 reanalysis dataset (Hersbach et al. (2020)), in order to identify regions with ascending motion over SAF. Moreover, the zonal wind component is obtained in order to investigate vertical zonal wind profiles. ERA5 data are retrieved from Copernicus Climate Data Store (`https://cds.climate.copernicus.eu/#!/home`). Vertical cross sections are plotted using data from the following pressure levels: 850, 800, 750, 700, 650, 600, 550, 500, 450, 400, 350, 300, 250, 200 and 150 hPa.

Table 5.2.1: Regional climate model simulations participating in the Coordinated Regional Climate Downscaling Experiment (CORDEX) Africa ensemble used in the current analysis, with a horizontal spatial resolution equal to 0.44° (CORDEX0.44). Data are retrieved from the Earth System Grid Federation (`https://esgf-data.dkrz.de/projects/esgf-dkrz/`).

RCM	Driving GCMs	Institute	References
CCLM4-8-17.v1	CNRM-CM5	CLMcom	
	EC-EARTH		
	HadGEM2-ES		
	MPI-ESM-LR	CNRM-CM5	COSMO (2020)
HIRHAM5.v2	EC-EARTH	DMI	Christensen et al. (2007)
RACMO22T.v1	EC-EARTH	KNMI	van Meijgaard et al. (2008)
	EC-EARTH		
	HadGEM2-ES		
RCA4.v1	CanESM2	SHMI	Samuelsson et al. (2015)
	CNRM-CM5		
	CSIRO-Mk3-6-0		
	EC-EARTH		
	IPSL-CM5A-MR		
	HadGEM2-ES		
	MPI-ESM-LR		
	NorESM1-M		
	GFDL-ESM2M		
REMO2009.v1	EC-EARTH	MPI - CSC	Jacob et al. (2012)
	MPI-ESM-LR	MPI - CSC	
	PSL-CM5A-MR	GERICS	
	MIROC5	GERICS	
	HadGEM2-ES	GERICS	
	GFDL-ESM2G	GERICS	
CRCM5.v1	CanESM2	CCCma	Scinocca et al. (2016)
	MPI-ESM-LR		

SHMI: Swedish Meteorological and Hydrological Institute, CLMcom: Climate Limited-area Modelling Community, DMI: Danish Meteorological Institute, KNMI: Royal Netherlands Meteorological Institute, MPI-CSC: Max Planck Institut and Climate Service Center Germany, Helmholtz-Zentrum Geesthacht, GERICS: Climate Service Center Germany, CCCma: Canadian Centre for Climate Modelling and Analysis

5.3 Methods

Starting from the large-scale atmospheric features influencing precipitation over SAF, the focus is placed on the position and intensity of the Subtropical Jet (STJ) identified at 200 hPa. STJ is seen as a current of fast-moving air circumnavigating the southern hemisphere (Gallego et al. (2005)), acquiring its maximum intensity (45 m/s) during winter months (June-July-August: JJA), while during summer months (December-January-February: DJF) it is observed to be at its weakest phase (Nakamura and Shimpo (2004)). The reason for that being that during winter months the temperature difference between tropical and polar regions is maximized, enhanced by the fact that convection in the tropics navigates the circulation through divergent outflow towards the southern pole (Gillett et al. (2021)). The mean latitude for STJ during JJA is 26 °S, while during DJF it migrates to higher latitudes (32 °S) (Gallego et al. (2005)). In this work, in order to identify STJ, the zonal component of wind at 200 hPa is used.

A lower-level jet (LLJ) that has received significant research attention for its influence on weather systems over western and eastern Africa is the African Easterly Jet (AEJ). Nonetheless, the southern branch of AEJ (AEJ-S) has been relatively neglected, despite its severe impact on precipitation over central and southern Africa (Kuete et al. (2020)). AEJ-S is particularly active during Sep-Oct-Nov (SON) and is identified at 500-600 hPa as an easterly flowing current of air ranging over latitudes between 5 – 15 °S (Nicholson and Grist (2003)). AEJ-S is a thermal wind (Nicholson and Grist (2003); Adebiyi and Zuidema (2016)) caused by the continental temperature gradient created between tropical Africa dominated by deep moist convective systems and the thermal heat low system residing over southern Angola and the Kalahari area (Munday and Washington (2017); Howard and Washington (2018)). Similarly to its northern counterpart (Wu et al. (2009)), AEJ-S is also characterized by strong vertical wind shear and therefore strong (weak) AEJ-S events are associated with decreased (increased) precipitation over southern Africa. In this work we identify AEJ-S using easterly moving zonal wind at 500 hPa.

Vorticity is a quantity describing the measure of spin of an air mass in the atmosphere and is a key variable in diagnosing cyclonic activity (in the southern hemisphere negative vorticity values indicate clockwise/cyclonic rotation) (Holton (2004)). When vorticity is examined as a sum of its shear and curvature components, is described by Equation 5.3 and is termed as relative vorticity. Here, the vertical component of vorticity is used and is calculated at 850 hPa, in order to identify the AL pressure system.

$$\zeta = \frac{\partial v}{\partial x} - \frac{\partial u}{\partial y}$$

For planetary vorticity in which the Coriolis parameter (f) is also considered, absolute vorticity is given in Equation 5.3. Absolute vorticity describes the spin of an air mass due to the rotation of the Earth, along with its shear and curvature components.

$$\xi = \frac{\partial v}{\partial x} - \frac{\partial u}{\partial y} + f$$

The advection of vorticity is used as a strong indication of areas of vertical motion (Holton (2004)). In the southern hemisphere, negative vorticity advection (NVA) intensifying with height, corresponds to regions of rising motion. Vorticity advection is usually examined at 500 hPa, since 500 hPa is considered to be the non-divergence level. Relative vorticity advection is given in Equation 5.3 and absolute vorticity advection is given in Equation 5.3. Both quantities are calculated at 500 hPa.

$$VA_\zeta = -\bar{u}\nabla\zeta$$

$$VA_\xi = -\bar{u}\nabla\xi$$

A significant process influencing climatic regimes over SAF is the inflow of moisture from the Atlantic and the Indian Oceans towards the mainland subcontinent. With the purpose to identify moisture fluxes, moisture flux divergence (MFD) is calculated at 850 hPa, which allows the investigation of low-level moisture circulation. For the calculation of MFD the u and v wind components and specific humidity (q) at 850 hPa are utilized. MFD is calculated using Equation 5.3. MFD at middle troposphere has been found to correlate strongly with precipitation (maximum correlation was identified at 700 hPa) and is a quantity that could be successfully used to constrain the results of climate models (Creese and Washington (2016)).

$$MFD = \frac{\partial(qu)}{\partial x} + \frac{\partial(qv)}{\partial y}$$

Potential temperature at 850 hPa is calculated using Poisson's equation, as given in Equation 5.3. T_0 is potential temperature, P_0 is the reference pressure level (1000 hPa) and P is the pressure surface in concern (850 hPa).

$$T_0 = T(\frac{P_0}{P})^{0.286}$$

5.4 Results

5.4.1 Precipitation climatology

October heralds the onset of the rainy season over SAF. In Fig. 5.4.1 the vertical velocity (Pa/s) profiles during ON from ERA5 are shown. As displayed in Fig. 5.4.1a, upward motion extending up to 200 hPa is observed in latitudes ranging from 5 to 15 °S. South of 30 °S, air is descending throughout the tropospheric column. Similarly, in Fig. 5.4.1b there is strong upward motion up to 15 °S, however, a secondary area of upward motion is also identified at 27 °S. The deep ascending cell is associated with the tropical rain band, which during October begins its southward migration (Nicholson (2009); Nicholson (2018)). The secondary area of rising air at 27 °S in Fig. 5.4.1b is associated with strong moisture convergence entering SAF from the southwest Indian Ocean (Munday and Washington (2018)). The area of intense upward motion is also identified in Fig. 5.4.1c, centered over longitudes at 20 °E. An intense circulation cell is seen at longitudes 30 – 35 °E, associated with local scale convection induced by lake Malawi (Nicholson et al. (2014); Koseki and Mooney (2019)). Rising motion seen in Fig. 5.4.1c is caused by strong surface convergence (Munday and Washington (2018)). In Fig. 5.4.2 vertical cross-sections of vertical velocity for DJF are displayed. As shown, ascending motions dominate the largest part of SAF and the rain band identified in Fig. 5.4.1a and Fig. 5.4.1b for ON, has migrated southwards during DJF (Fig. 5.4.2a and Fig. 5.4.2b).

Monthly precipitation climatology for ON during 1986-2005 is shown in Fig. 5.4.3, expressed in mm (monthly totals are averaged for ON). Overlayed on precipitation climatologies are contours of minimum

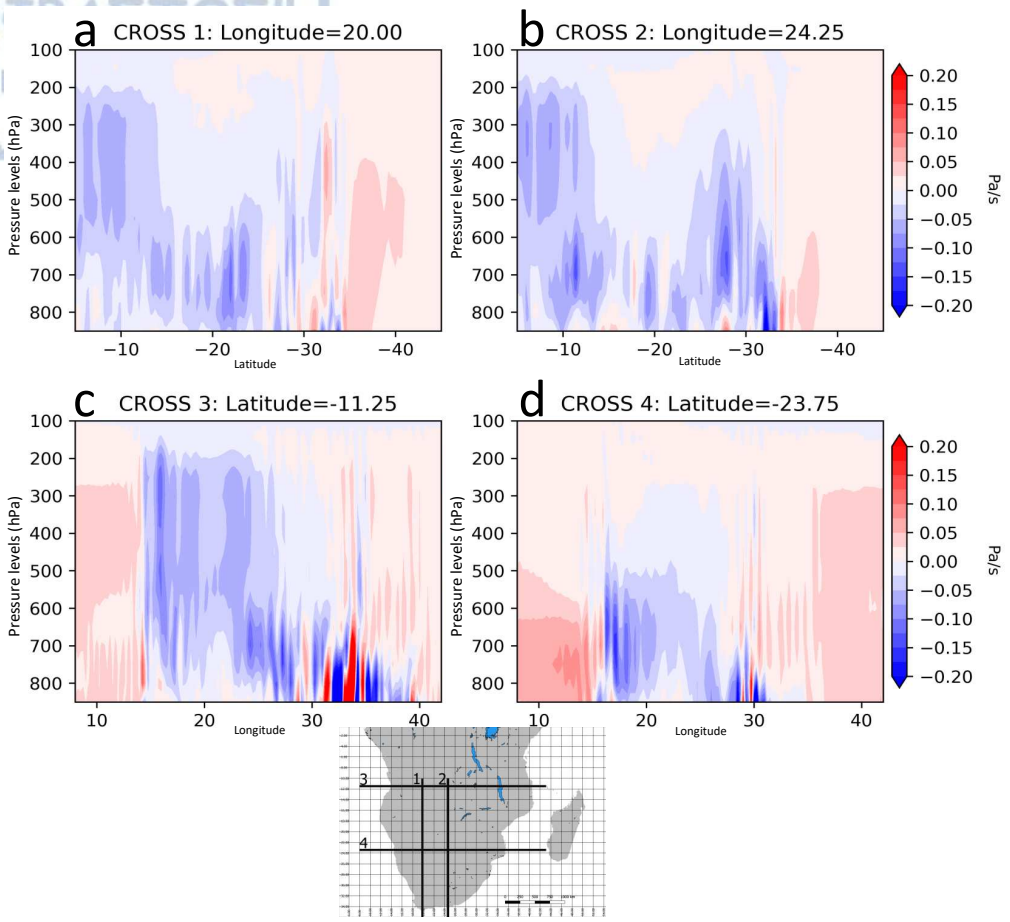

Figure 5.4.1: Vertical cross-sections of vertical velocity (Pa/s) in ERA5 over SAF for October-November during the period 1986-2005. Negative values indicate ascending upward motion.

values of OLR (rlut) in W/m^2. OLR has been used in satellite rainfall estimate algorithms as a predictor variable for rainfall (Xie and Arkin (1998);?) and is treated as a proxy for deep convection (Gu and Zhang (2002)). Minimum OLR contour is set at 160 W/m^2, maximum contour is set at 260 W/m^2 and an increment of 20 W/m^2 is used.

As seen in Fig. 5.4.3, during ON simulated precipitation amounts >180 mm are limited to the northwest part of SAF and do not extend to latitudes beyond 10 °S. In general, REMO2009 simulations yield the highest precipitation amounts (>350 mm), while RACMO22T simulations yield the lowest precipitation amounts. RCA precipitation climatologies differ based on the driving GCM. A feature that is present in all RCA simulations is that there is a very spatially heterogeneous distribution of precipitation, which over certain regions, appears to be pixelated. This issue has been ascribed to the abrupt elevation dataset employed by RCA simulations (Van Vooren et al. (2019)). In almost all RCMs, eastern Congo experiences little to no precipitation, a fact which is caused by the divergence of low-level moisture fluxes coming from the Indian ocean (Washington et al. (2013)). In general, it is observed that areas with high precipitation amounts are collocated with areas of low OLR, indicating that precipitation over SAF is mainly caused by mesoscale convective systems (Hartman (2021)). Monthly precipitation climatology for DJF during 1986-2005 is shown in Fig. 5.4.4 and displays a distinct southwards migration of the rain

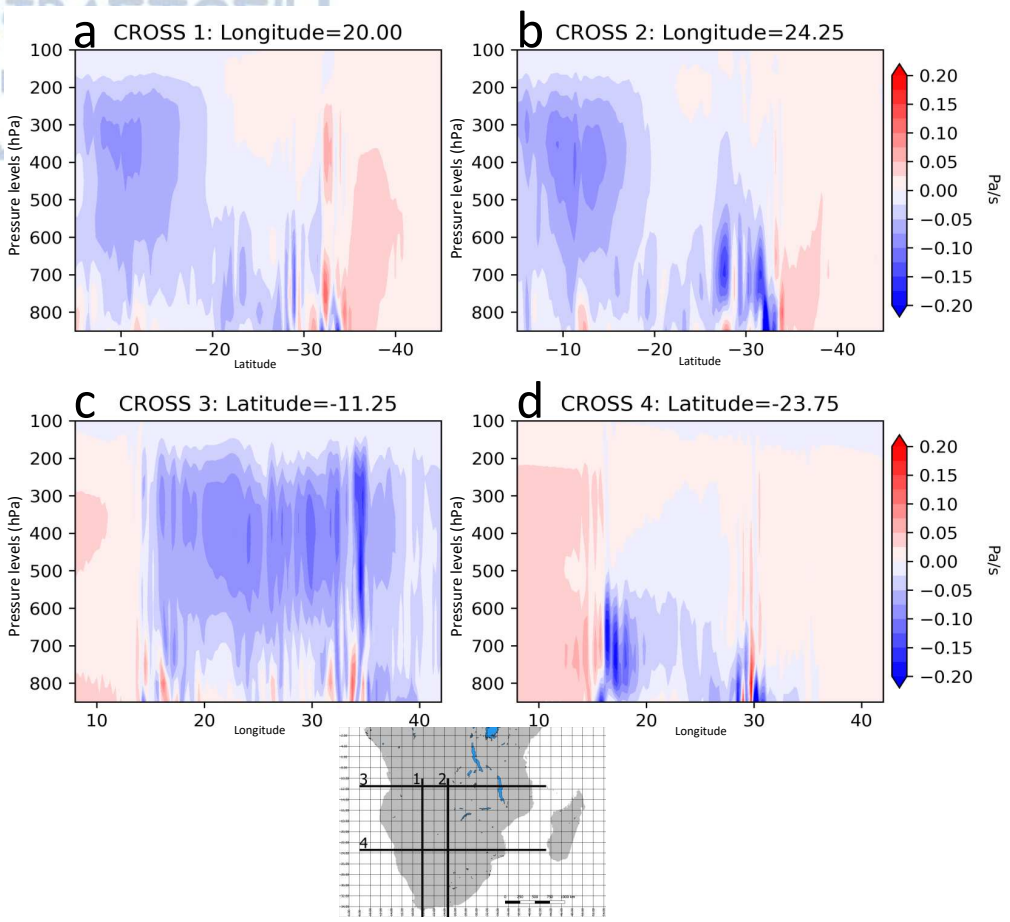

Figure 5.4.2: Vertical cross-sections of vertical velocity (Pa/s) in ERA5 over SAF for Dec-Jan-Feb during the period 1986-2005. Negative values indicate ascending upward motion.

band in all RCMs. RACMO22T still appears to be the driest among all models and the pixelated pattern in RCA enhances. As expected, high precipitation areas overlap with low OLR regions, indicating precipitation to originate from convective mechanisms.

5.4.2 Subtropical Jet at 200 hPa and African Easterly Jet at 500 hPa southern branch

Vertical cross sections for mean monthly zonal wind speed (u component) from ERA5 during 1986-2005 are shown in Fig. 5.4.5. During DJFM, the STJ and the Polar Jet (PJ) are almost merged. STJ is identified between 25 – 30 °S and the PJ core is identified between 45 – 50 °S. In April and May STJ migrates 5° northwards and the two jets become distinct. During JJA, STJ has its maximum intensity (37 m/s) and is distinct from the PJ, with its core being identified at 26 °S. During SON, STJ starts to weaken and as it moves southwards merges with the PJ. The AEJ-s is identified at 600 - 700 hPa between latitudes 5 – 10 °S and its climatological maximum intensity is observed during Sep - Oct. Nonetheless, during all months there is a considerable easterly wind present over these latitudes at middle troposphere.

Zonal wind speed fields at 200 hPa as simulated in each RCM of the CORDEX-Africa ensemble for ON during 1986-2005 is depicted in Fig. 5.4.6. As shown, high speeds (>20 m/s) indicative of STJ are

observed south of 20 °S and extend southwards over the whole CORDEX-Africa domain. It is noted that common zonal wind patterns exist between simulations driven by the same GCM. In general, CCLM4 produces very steep temperature meridional gradients of temperature between low and high latitude regions and therefore simulates the strongest wind speeds. RCA4 in general simulates very smooth temperature gradients and RACMO22T and REMO2009 simulate varying temperature gradients based on the driving GCM. Geopotential height at 200 hPa displays a smooth transition up to 25 °S and becomes more abrupt moving southwards. Zonal wind speed at 200 hPa for DJF is displayed in Fig. 5.4.7. During DJF, STJ has moved southwards and high wind speeds (>20 m/s) are identified below 30 °S. Circulation from 27 °S and below is almost entirely westerly, however, at 10 °S there is a systematic easterly flow that navigates southwards at 5°E and joins the STJ at 27 °S. The easterly flow is particularly strong in RCM simulations driven by HadGEM2-ES, MPI-ESM-LR and CNRM. CCLM4 persists in simulating steep temperature and geopotential height gradients at 200 hPa.

Zonal wind speed at 500 hPa for ON during 1986-2005 for the CORDEX-Africa ensemble is depicted in Fig. 5.4.8. Negative values indicate the easterly (westward) movement. As it is shown, easterly winds are observed from the Equator until 17 °S and this band of westwards moving air is considered to be indicative of the southern branch of the African Easterly Jet (AEJ-S). As shown, the spatial structure and wind speed magnitude of AEJ-S is dictated by the driving GCMs. Zonal wind speed at 500 hPa for DJF during 1986-2005 is displayed in Fig. 5.4.9. During DJF, the AEJ-S extends southwards (20 °S), its structure is less distinct and displays significant breaks, especially over the northeastern part of SAF. The structure of AEJ-S is relatively well maintained in RACMO22T simulations during DJF, a fact that may partly explain the decreased precipitation amounts in RACMO22T runs.

5.4.3 Absolute and relative vorticity advection at 500 hPa

Absolute vorticity advection at 500 hPa for ON during 1986-2004 is depicted in Fig. 5.4.10. A common feature identified in all RCMs is an elongated region of NVA starting from the west coast of southern Africa at 25 °S and extending towards southeast until 40 °S. These elongated regions of NVA can be associated with the formation of Tropical Temperate Troughs (TTTs) (Hart et al. (2010)), which are mainly identified as regions of ascending motion to the east of the large-scale trough. In general, the length of these elongated NVA regions depends on the driving GCM. West to these regions over the southeast Atlantic Ocean, there is a region of PVA, consistent in most RCMs. The southwest coast of SAF is a region of strong upwelling of the cold Benguela current, which generally inhibits convection over southwest SAF. In most RCA4 simulations a consistent region of strong NVA is identified at 5 °S and 15 °S. This region can be associated with the rising motion of atmospheric air observed over Malawi. A weaker NVA region is observed over the Angola region. Absolute vorticity advection at 500 hPa for DJF during 1986-2004 is depicted in Fig. 5.4.11. The elongated NVA region is reduced compared to ON, however, NVA regions are more widespread for all RCMs over the largest part of SAF.

Relative vorticity advection at 500 hPa for ON during 1986-2004 is depicted in Fig. 5.4.12. As in absolute vorticity advection, there is an elongated region of NVA, located over southwest SAF, followed by an intense region of PVA at southeast SAF at 40 °E. Vorticity advection over central SAF and over the Angola region is very weak, with a slight tendency for negative values over selected runs (those driven by CanESM2, CSIRO, MPI-ESM-LR and NorESM1). Relative vorticity advection at 500 hPa for DJF during

1986-2004 is depicted in Fig. 5.4.13. The two most prominent features remain NVA over South Africa and PVA at 40 °E, nonetheless weak NVA over the Angola region becomes more distinct, in almost all simulations.

5.4.4 Moisture flux divergence at 850 hPa

Moisture flux divergence at 850 hPa for ON during 1986-2005 is shown in Fig. 5.4.14, expressed in $kg\ kg^{-1}\ m\ s^{-1}$. Negative values indicate regions of moisture convergence. As shown, easterly winds from the Indian Ocean at 15 °S recurve systematically over northeast Madagascar, creating moisture divergence at the northeast coast of SAF. Recurvature is particularly strong for CRCM5 and in general for RCA4 runs, although deviations are observed based on the driving GCM. Strong convergence is identified over the Malawi region, with RACMO22T and CCLM4 displaying the strongest convergence values (>-1.5-e7 $kg\ kg^{-1}\ m\ s^{-1}$). Moisture fluxes entering SAF from northeast move inland and cause further moisture convergence over central SAF. At 25 °S, there is a weaker recurvature over southeast Madagascar. Fluxes weaken as they cross the Mozambique Channel but are enhanced over coastal Mozambique and eastern South Africa. More specifically, strong divergence is observed at the windward side of the Drakensberg mountains and strong convergence is observed at the leeward side. The same convergence-divergence pattern is systematically observed over eastern-to-western Madagascar. A distinct moisture convergence pattern is identified over the Angola region, stretching from 11 – 19 °S, and 10 – 22 °E. In general, CCLM4, REMO2009 and CRCM5 display the strongest convergence over the Angola region, indicating a strong AL system. RACMO22T which was identified as the driest model simulates the weakest AL during ON.

Moisture flux divergence at 850 hPa for DJF during 1986-2005 is shown in Fig. 5.4.15. During DJF circulation over northeast SAF is reversed, with moisture fluxes entering from the north and performing a recurvature towards the east of Madagascar. This is a systematic feature in all RCMs and is related to the moisture flux originating from the tropical Indian Ocean, that is directed towards SAF from the northeast. However, since the low-level atmospheric flow encounters the mountains of Tanzania, it is forced to recurve around north Madagascar. This is a feature attributed to the spatial resolution of the CORDEX-Africa ensemble and it was identified as a significant advancement of the CORDEX-Africa relative to CMIP5, resolving to a considerable degree the issue of wet bias seen in CMIP5 and CMIP6 ensembles (?). During DJF, moisture convergence over the Angola region is enhanced and substantial moisture fluxes enter SAF from the Atlantic Ocean at 10 °S. This specific area over the Atlantic Ocean is where the warm Angola ocean current converges with the cold Benguela current (Koseki and Mooney (2019)), which significantly affects the strength of the AL pressure system (Desbiolles et al. (2020)). For all RCMs and for both seasons (ON, DJF) moisture fluxes from the Congo Basin are particularly weak.

5.4.5 Relative vorticity climatology at 850 hPa

Cyclonic relative vorticity (ζ<0) at 850 hPa for ON during 1986-2005 is shown in Fig. 5.4.16 expressed in s^{-1}. In general, relative vorticity examined at the lower troposphere displays strong association with topography, due to the low-level drag effect and the gravity waves that are caused by high topographic features (Hartung et al. (2020)). Although ζ shows strong spatial heterogeneity across SAF, certain fea-

tures are common in all RCMs. For instance, southern Madagascar is a region of strong cyclonic vorticity, associated with the track of tropical low pressure systems moving towards continental SAF (Mavume et al. (2009); Nash et al. (2015)). In addition, the region between Lake Malawi and the Katanga Plateau is also a region of strong cyclonic vorticity, associated with low-level convergence. Another region of high cyclonic vorticity is identified along the mountain range located over southwest SAF and lastly, intense cyclonic motion is identified over eastern Angola, enclosed by the region between 11 – 19 °S, and 10 – 22 °E.

Cyclonic relative vorticity for DJF is shown in 5.4.17. During DJF the vorticity field is enhanced and continues to display strong association with elevation. The prominent region of strong and extended cyclonic vorticity over eastern Angola persists. Heat lows during the beginning of the rainy season (ON) tend to remain confined within the eastern Angola region and tropical lows during the core of the rainy season (DJF) tend to linger over the same region and to display a semi-stationary behavior that is unexpected for tropical low pressure systems (Ramsay (2017); Howard and Washington (2018)). Therefore, the vorticity field over the Angola region is of particularly interest, because of the anchoring process for both heat lows and for transient low-pressure systems (Howard and Washington (2018)).

In Fig. 5.4.18 the ensemble mean of cyclonic relative vorticity for the CORDEX-Africa ensemble is shown for ON (Fig. 5.4.18a) and for DJF (Fig. 5.4.18b) and is overlayed on the elevation map of the region. For both seasons (ON, DJF) there is a prominent area of cyclonic relative vorticity identified over Angola. From vorticity theory it is known that when a vortex stretches, its relative vorticity increases (Holton (2004)). Over the Angola region shown in Fig. 5.4.18, cyclonic vorticity increases over areas with steep terrain where high slopes are identified, implying that when a rotating air mass crosses a region of abrupt elevational change, topography imposes a "mechanical" stretch to the vortex, increasing its cyclonic vorticity. As shown in Howard and Washington (2018), the stretching term calculated from the vorticity budget equation is dominant over the region, explaining why tropical lows linger around the Angola region. The calculation of the stretching term was not possible for the CORDEX-Africa ensemble, since the vertical component of wind is not available.

5.4.6 Potential temperature at 850 hPa and sea level pressure

Potential temperature at 850 hPa (theta850 in K) and sea level pressure (slp in hPa) for ON are shown in Fig. 5.4.19. In all models a region of high theta850 values is observed between 15 – 20 °S and centered at 20 °E, corresponding to the region of maximum heating (Munday and Washington (2017)) and designating the region where the AL is mainly identified (Howard and Washington (2018)). The region of high theta850 values over Angola is collocated with minimum pressures, indicating the existence of a thermally induced low pressure system. Most RCMs place a closed contour of 1010 hPa over the maximum heating area. It is noted that RACMO22T which was identified as the least rainy RCM, simulates slightly higher pressures over the Angola region (1012 hPa), while CRCM5 driven by CanESM2 simulates the lowest pressure fields (1008 hPa) and highest potential temperature values (>316 K). REMO2009 which was identified as the wettest RCM, when driven by EC-EARTH (r12i1p1), HadGEM2-ES and IPSL-LR, simulated low pressures (1010 hPa) over a large part of the subcontinent, compared to the other RCMs in which 1010 hPa is a closed contour confined over Angola. It is also noted that in REMO2009 runs, the southern Atlantic Ocean high pressure (SAHP) system is simulated relatively weaker than in the rest of

the RCMs. In addition, we highlight the fact that common spatial patterns, especially for slp, are identified between simulations performed using the same RCM, regardless of the driving GCM, a fact that indicates that during ON, atmospheric processes are highly coupled to surface heating and therefore the impact of the RCM overcomes that of the driving GCM (?). For instance, all RCA4 simulations with an exception for two, locate the 1010 hPa closed contour between 10 – 20 °S, corresponding to a region of intense dry convection.

The same variables but for DJF are shown in Fig. 5.4.20. During DJF increased theta850 values are more widespread over the whole SAF, however, high values have migrated southwards to latitudes between 20 – 30 °S. Nonetheless, low slp values are identified approximately at their previous position (15 – 20 °S), indicating that low pressure systems over the Angola region are no longer of thermal cause, but that there is a dynamical driver at play (Munday and Washington (2017)). It is noted that the driest model identified (RACMO22T) simulates relatively higher pressures (1012 hPa) over the whole of SAF, compared to the other RCMs. Another consistent feature in most simulations is the low pressure region identified over the Mozambique channel, located between Madagascar and Mozambique. This closed contour, typically at 1008 hPa, corresponds to the climatological average of tropical low pressure systems moving from the southwest Indian Ocean and making landfall over continental SAF (Fitchett and Grab (2014)). In general, all RCMs simulate a weakened SAHP during DJF, relative to ON. Although RCMs are not coupled with an ocean model and therefore this feature is solely coming from the driving GCM, it indicates that the offshore southerly winds over southwest SAF are also weakened.

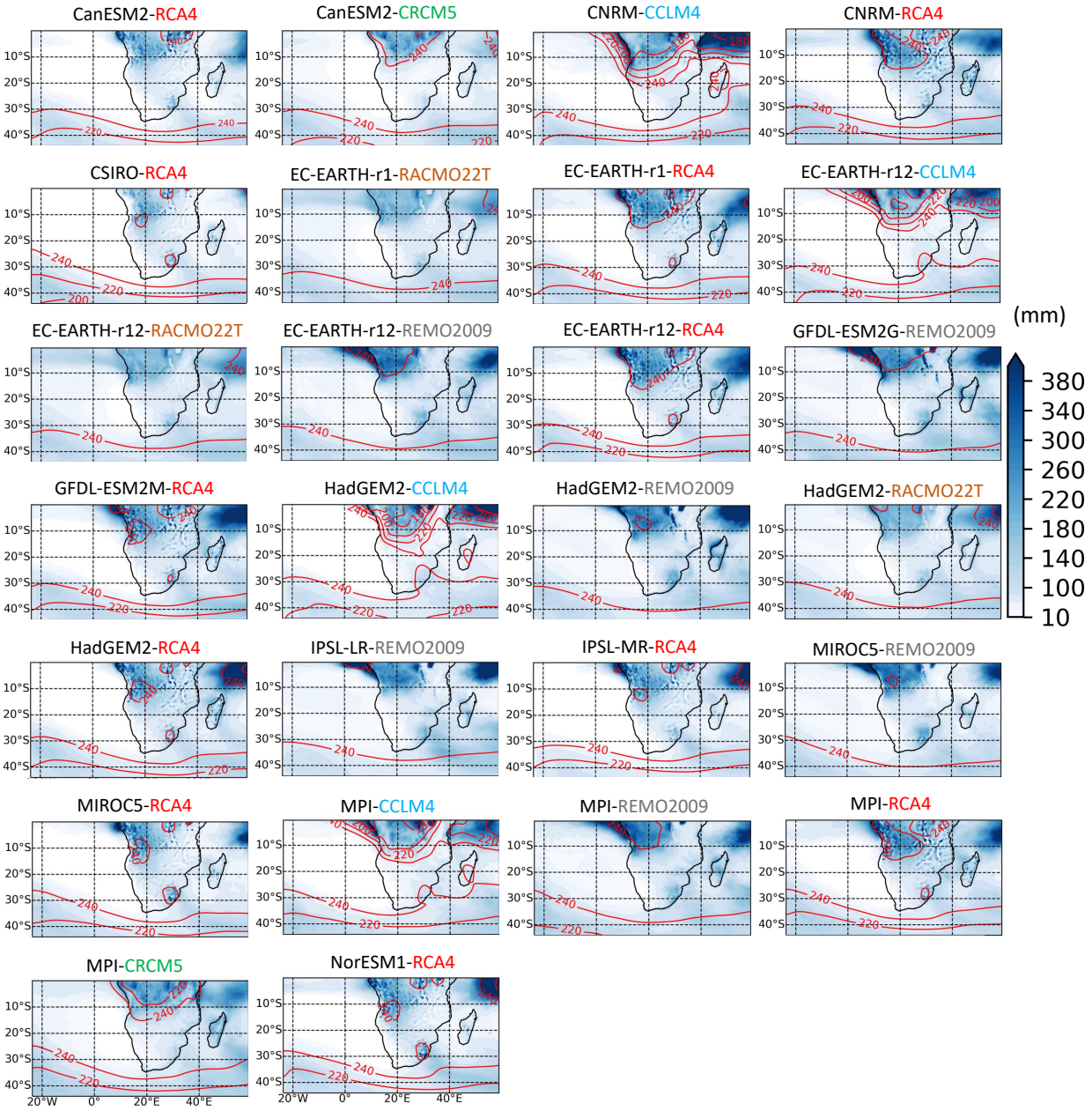

Figure 5.4.3: Monthly precipitation climatology for October-November during the period 1986-2005 (monthly totals are averaged for ON). Red contours indicate outgoing longwave radiation in W/m^2. Minimum OLR contour is set at 160 W/m^2, maximum contour is set at 260 W/m^2 and an increment of 20 W/m^2 is used.

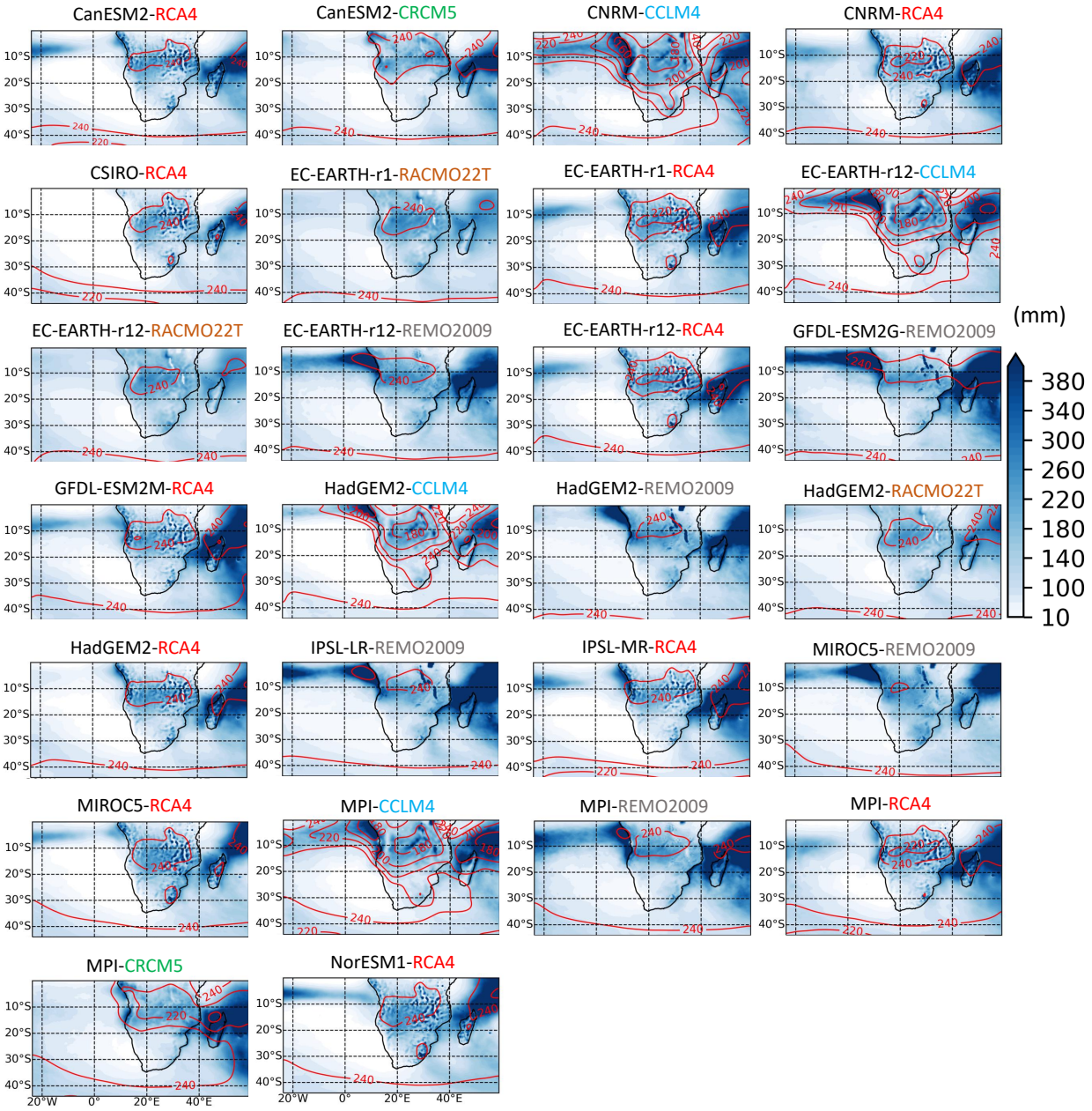

Figure 5.4.4: Monthly precipitation climatology for Dec-Jan-Feb during the period 1986-2005 (monthly totals are averaged for DJF). Red contours indicate outgoing longwave radiation in W/m^2. Minimum OLR contour is set at 160 W/m^2, maximum contour is set at 260 W/m^2 and an increment of 20 W/m^2 is used.

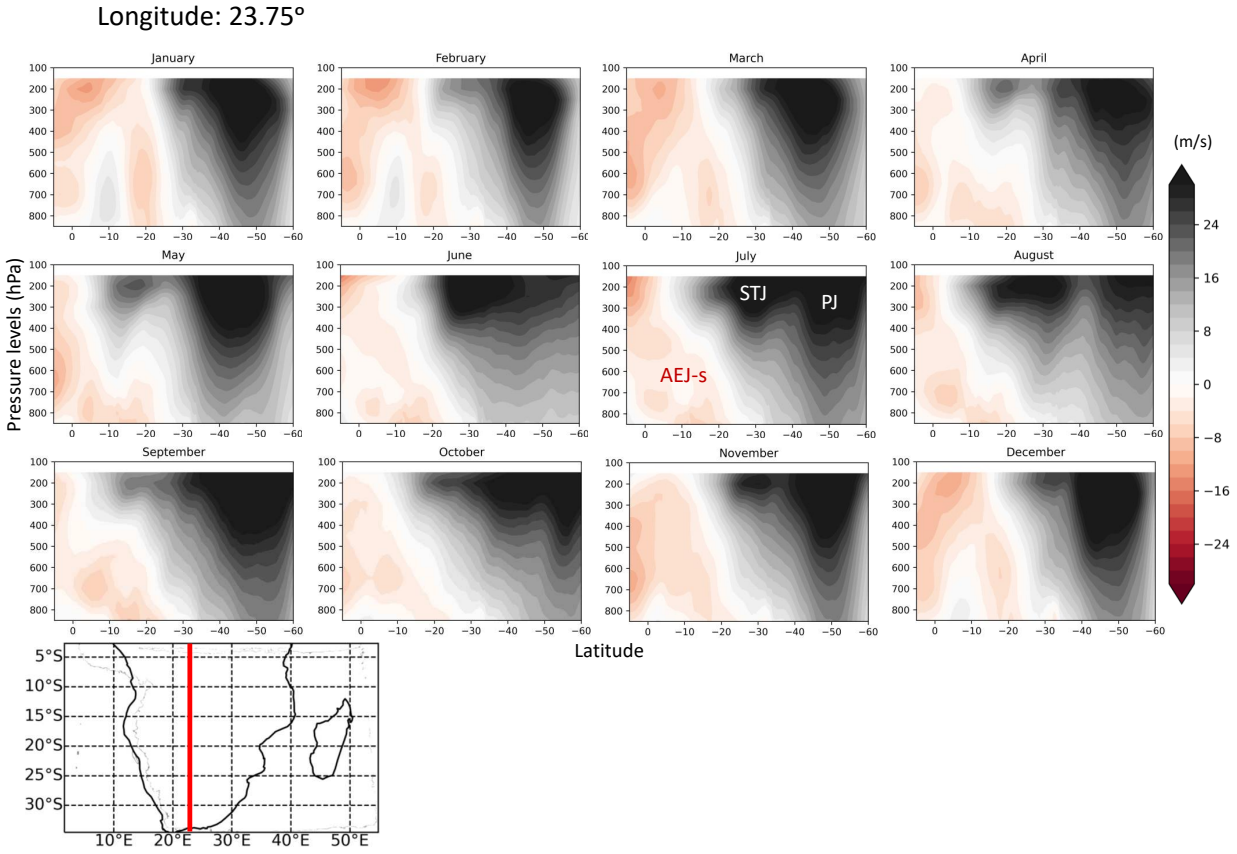

Figure 5.4.5: Vertical cross-sections of mean monthly zonal wind speed (u component) in ERA5 over SAF during the period 1986-2005. Positive values indicate eastward wind and negative values indicate westward wind. The cross section is taken for longitude 23.75°. STJ: Subtropical jet, PJ: Polar jet, AEJ-s: African easterly jet southern branch.

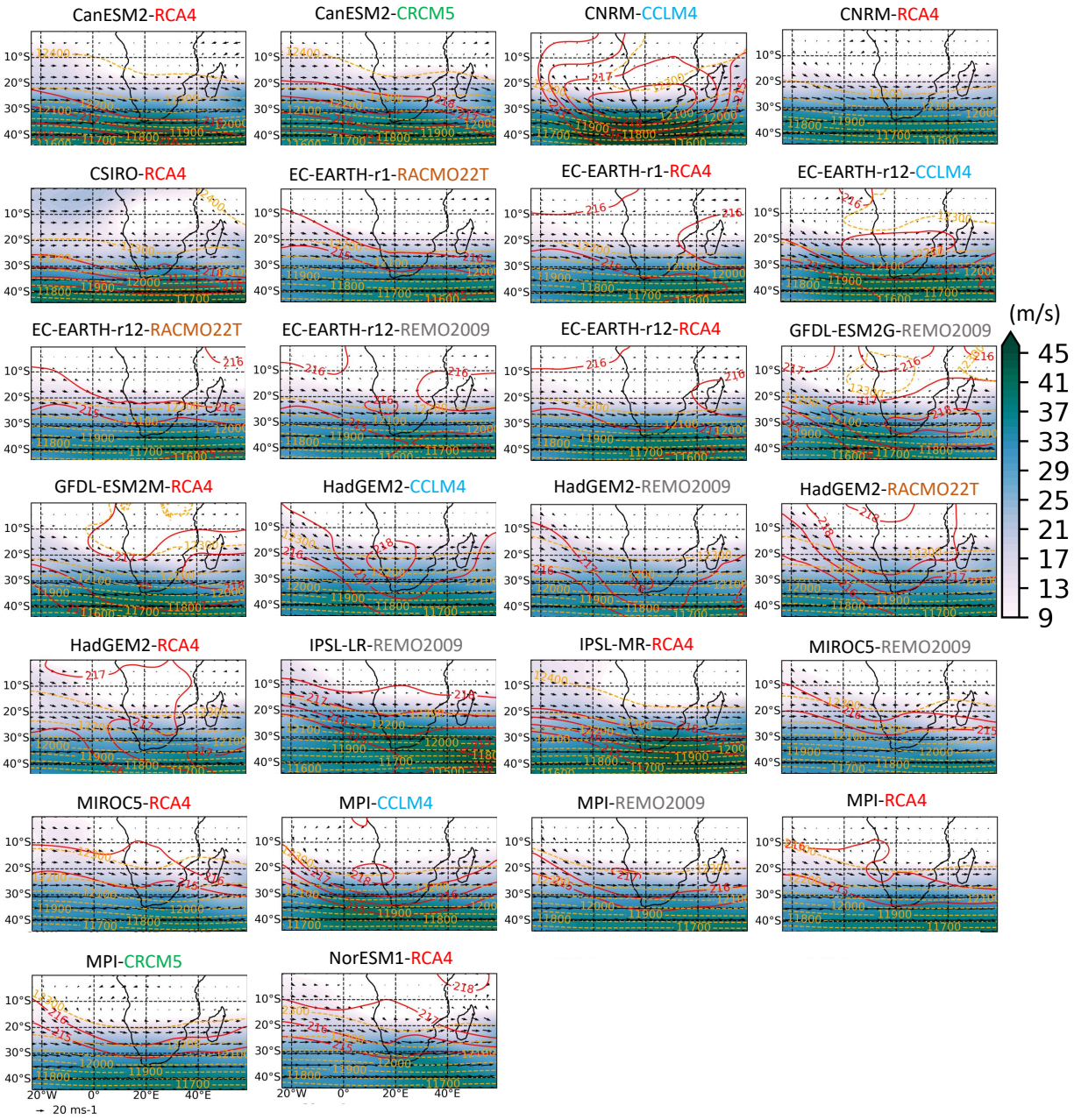

Figure 5.4.6: Filled colored contours indicate zonal wind (u component) at 200 hPa for October-November, which is indicative of the subtropical jet stream moving eastwards. Wind arrows are calculated using both u and v wind components. Units are m/s. Red isolines indicate temperature at 200 hPa in K. Yellow isolines indicate geopotential height at 200 hPa in m. Plotted fields are calculated using mean monthly values for the period 1986-2005 and were afterwards averaged for ON.

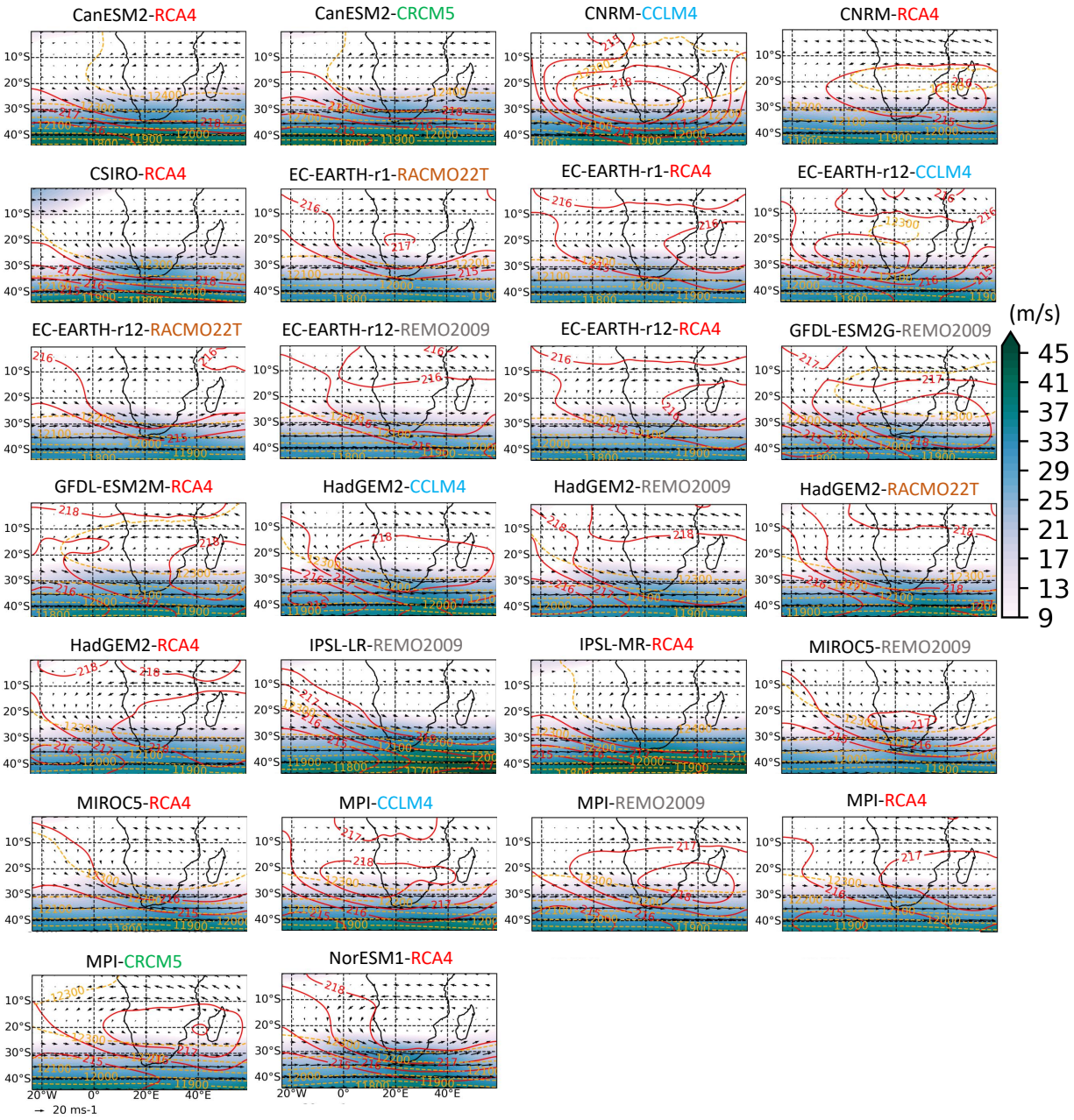

Figure 5.4.7: Filled colored contours indicate zonal wind (u component) at 200 hPa for December-January-February, which is indicative of the subtropical jet stream moving eastwards. Wind arrows are calculated using both u and v wind components. Units are m/s. Red isolines indicate temperature at 200 hPa in K. Yellow isolines indicate geopotential height at 200 hPa in m. Plotted fields are calculated using mean monthly values for the period 1986-2005 and were afterwards averaged for DJF.

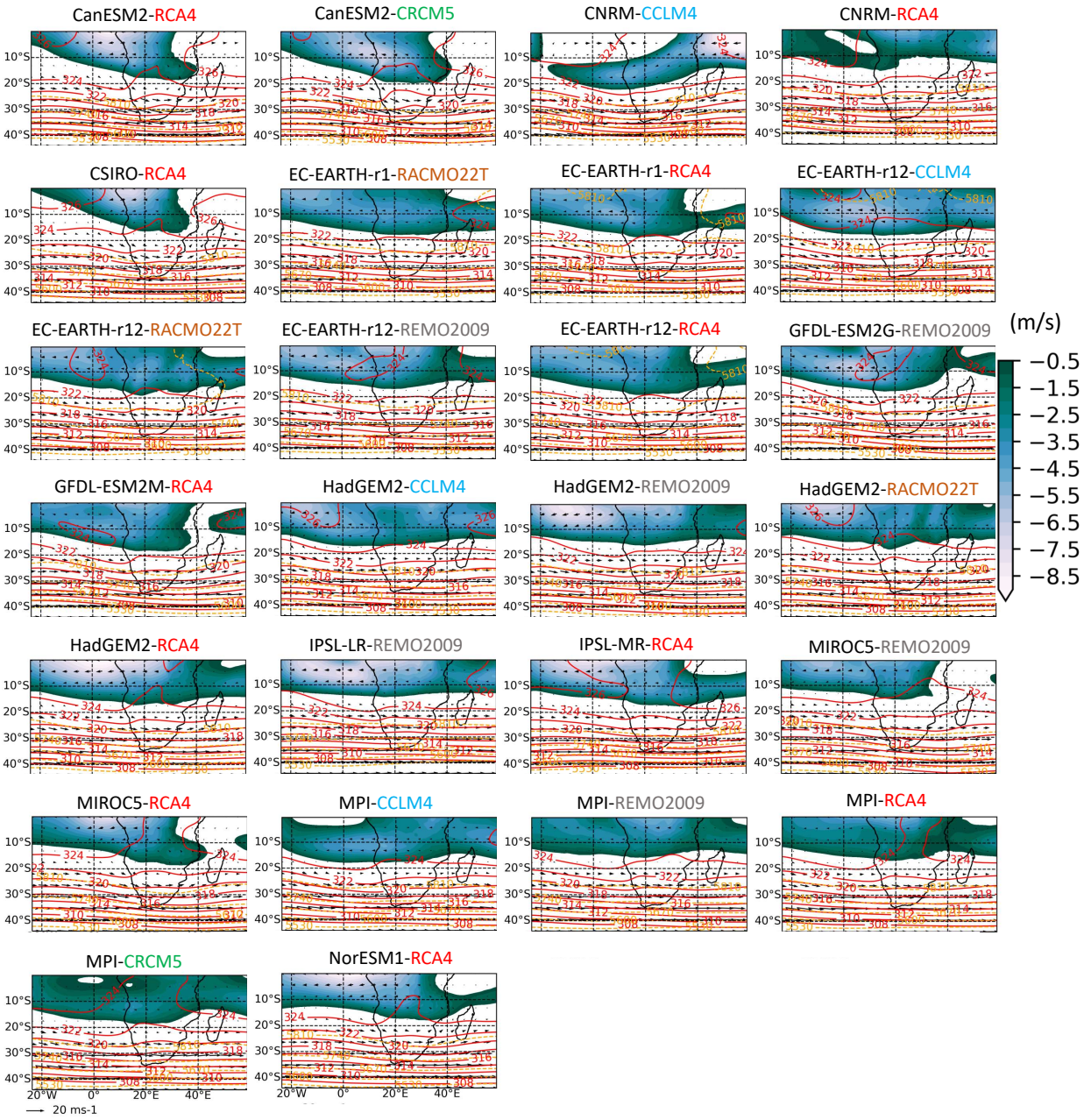

Figure 5.4.8: Filled colored contours indicate zonal wind (u component) at 500 hPa for October-November, which is indicative of the southern branch of the African Easterly Jet moving westwards. Wind arrows are calculated using both u and v wind components. Units are m/s. Red isolines indicate temperature at 500 hPa in K. Yellow isolines indicate geopotential height at 500 hPa in meters. Plotted fields are calculated using mean monthly values for the period 1986-2005 and are afterwards averaged for .

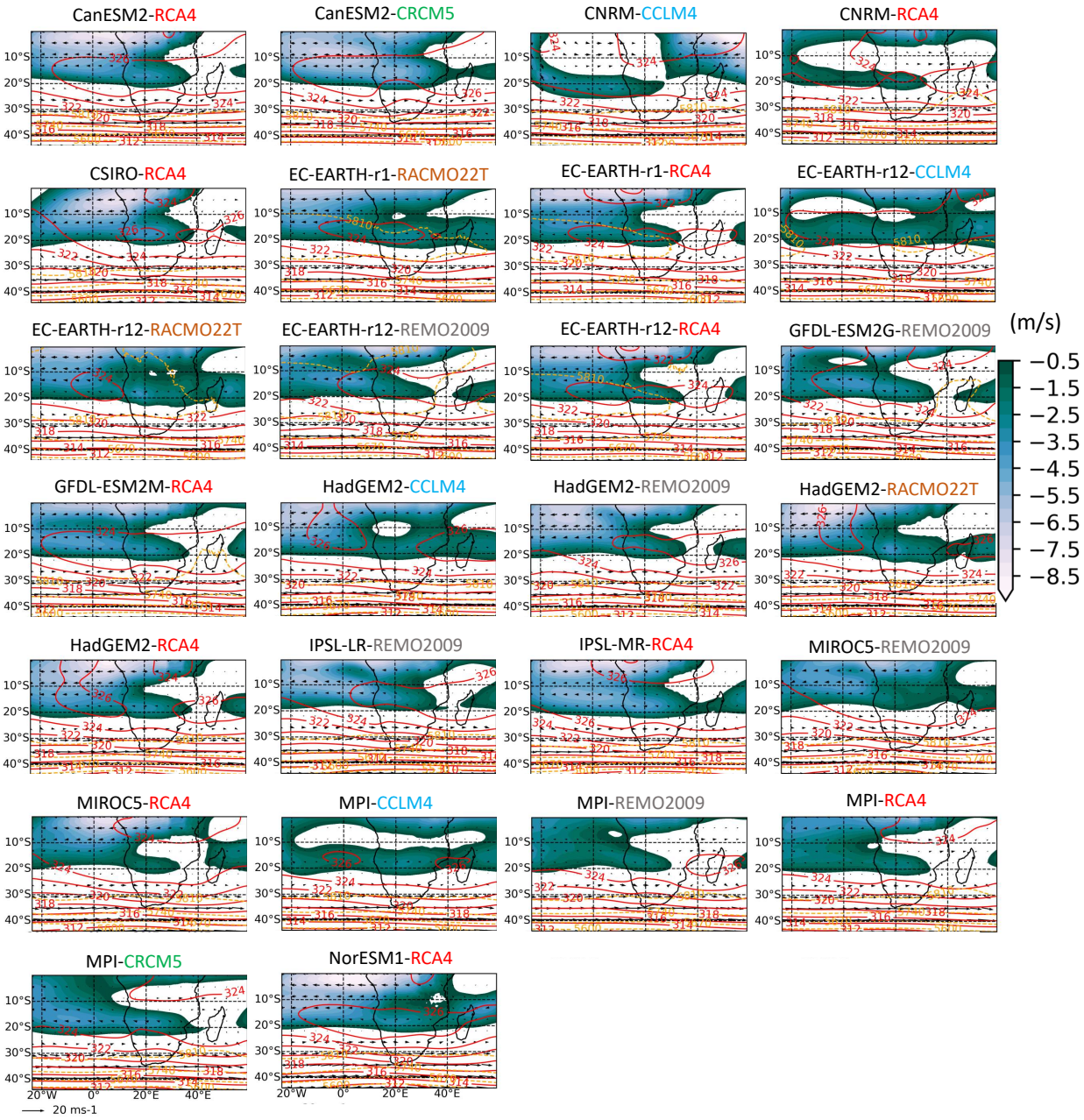

Figure 5.4.9: Filled colored contours indicate zonal wind (u component) at 500 hPa for December-January-February, which is indicative of the southern branch of the African Easterly Jet moving westwards. Wind arrows are calculated using both u and v wind components. Units are m/s. Red isolines indicate temperature at 500 hPa in K. Yellow isolines indicate geopotential height at 500 hPa in meters. Plotted fields are calculated using mean monthly values for the period 1986-2005 and are afterwards averaged for DJF.

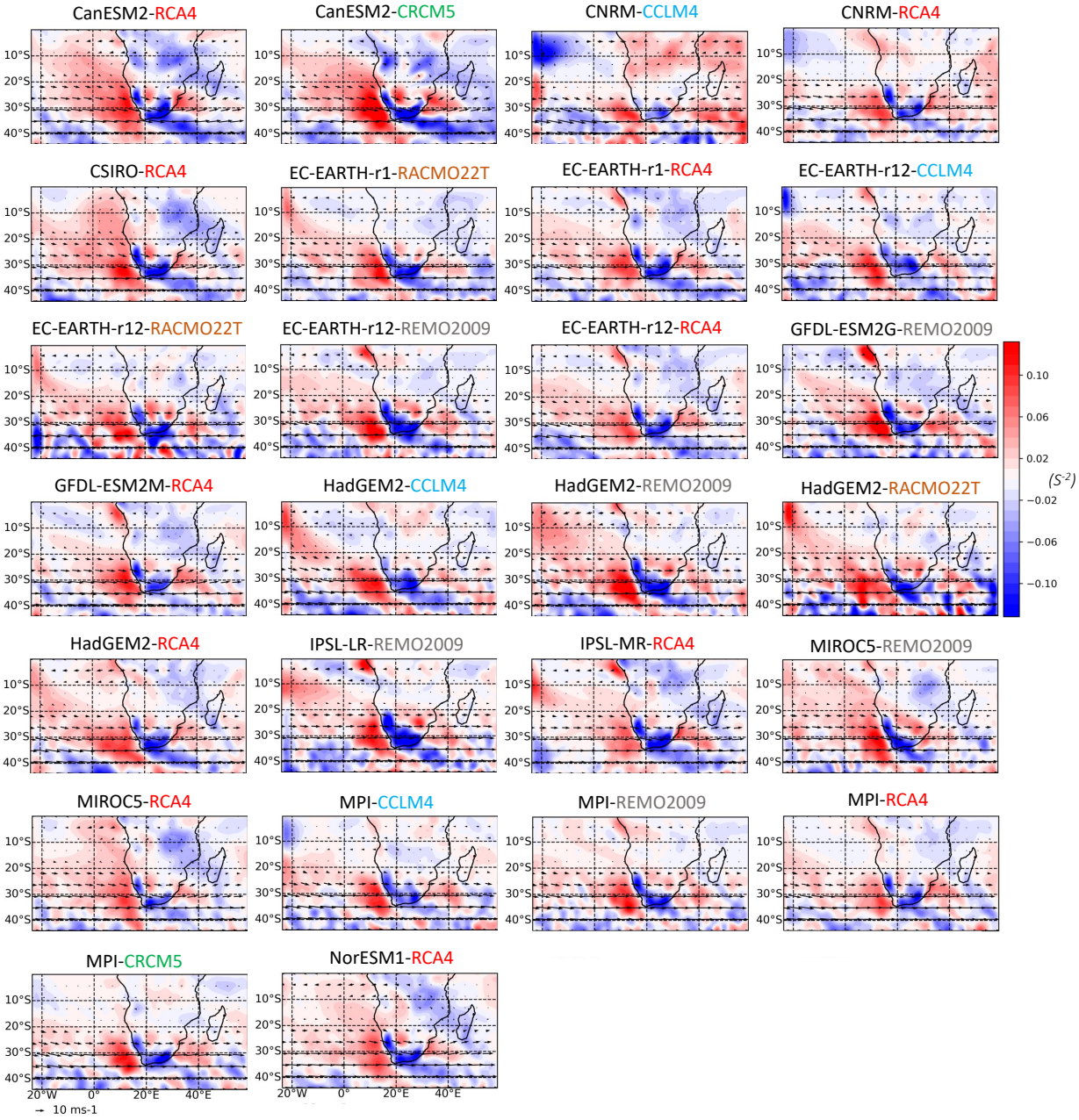

Figure 5.4.10: Absolute vorticity advection at 500 hPa in s^{-2} for October-November in colored contours. Arrows indicate wind direction at 500 hPa. Plotted fields are calculated using mean monthly values for the period 1986-2005.

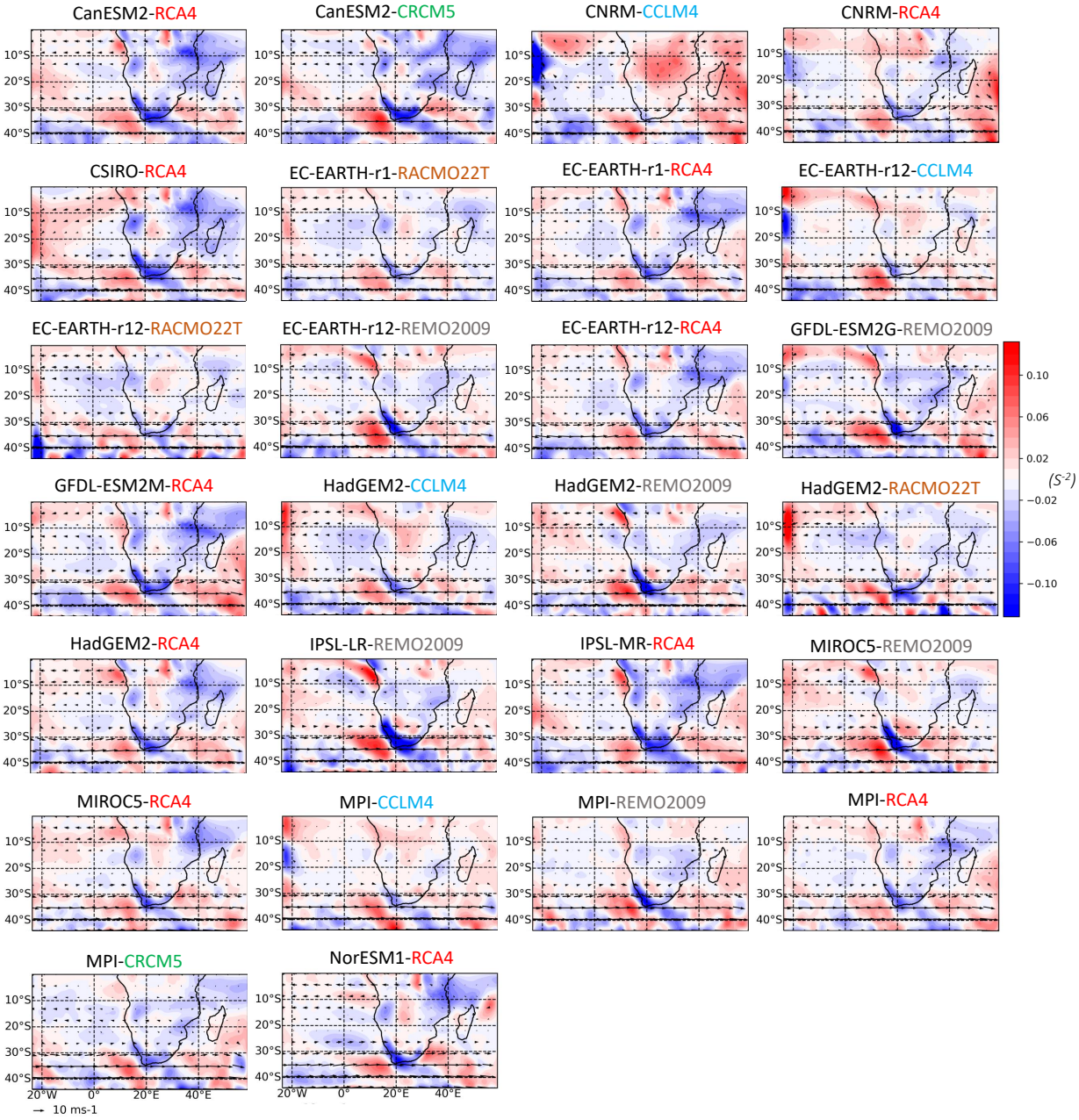

Figure 5.4.11: Absolute vorticity advection at 500 hPa in s^{-2} for December-January-February in colored contours. Arrows indicate wind direction at 500 hPa. Plotted fields are calculated using mean monthly values for the period 1986-2005.

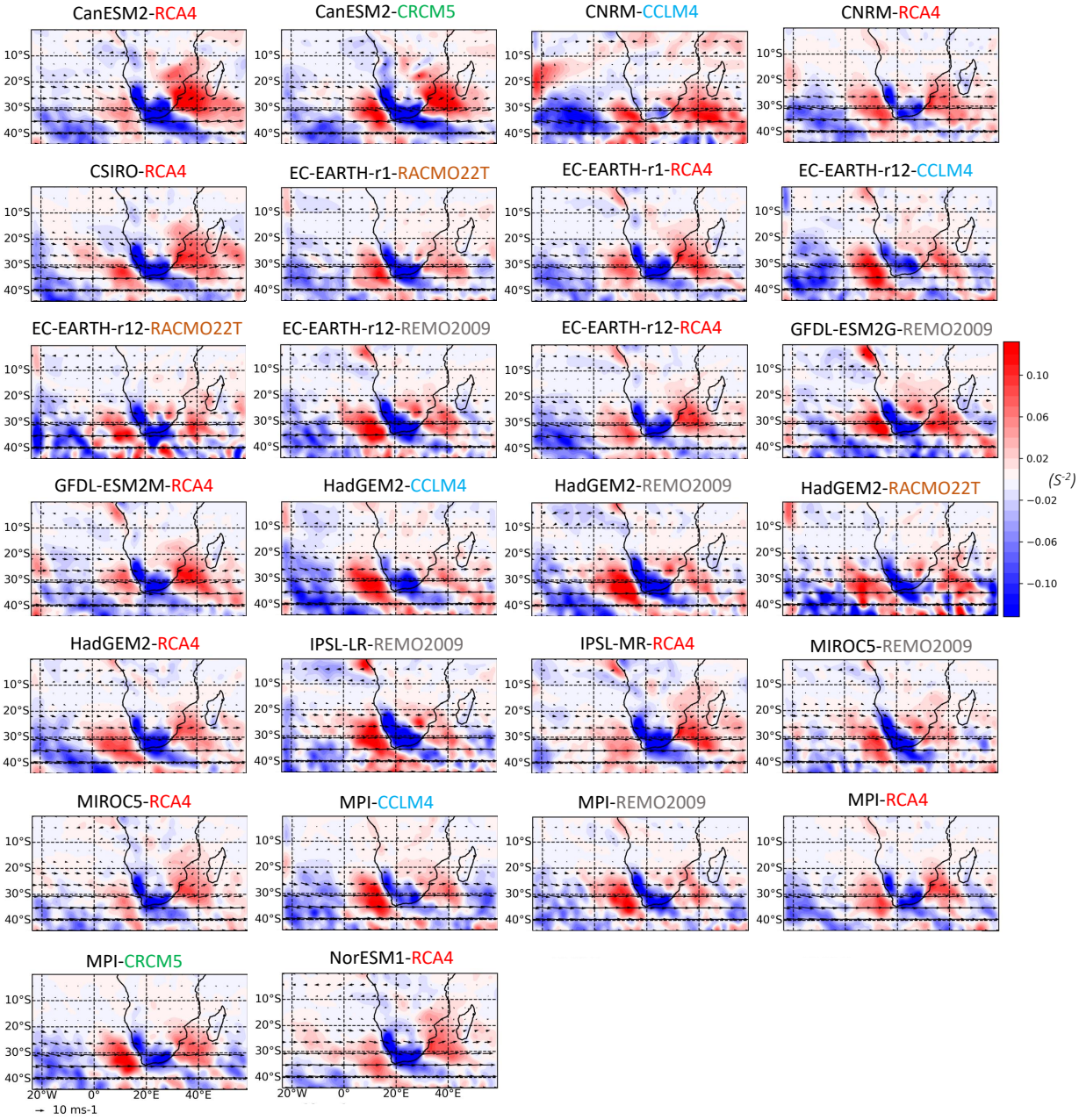

Figure 5.4.12: Relative vorticity advection at 500 hPa in s^2 for October-November in colored contours. Arrows indicate wind direction at 500 hPa. Plotted fields are calculated using mean monthly values for the period 1986-2005.

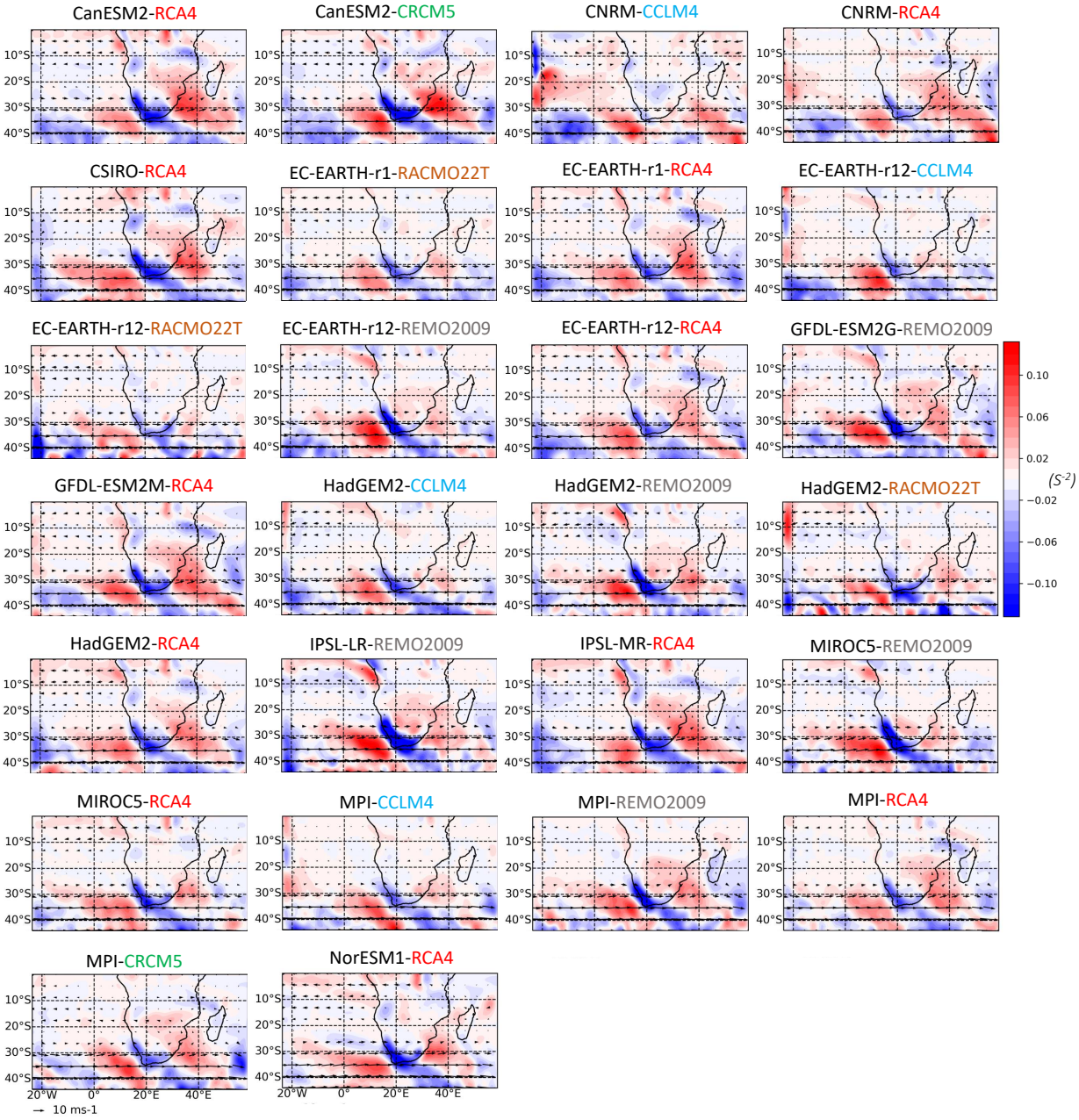

Figure 5.4.13: Relative vorticity advection at 500 hPa in s^2 for December-January-February in colored contours. Arrows indicate wind direction at 500 hPa. Plotted fields are calculated using mean monthly values for the period 1986-2005.

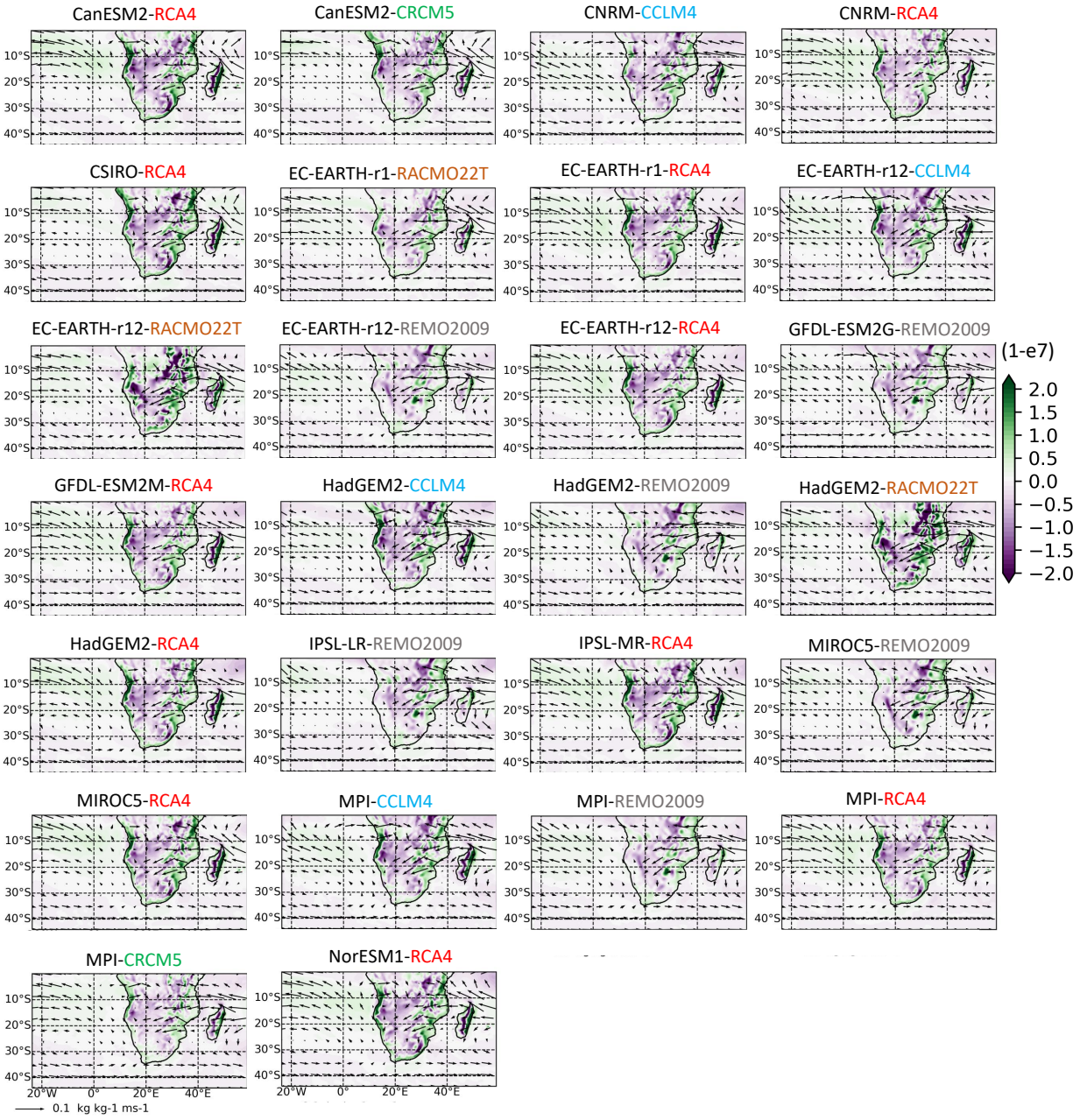

Figure 5.4.14: Moisture flux divergence at 850 hPa for October-November. Green areas indicate divergence, purple areas indicate convergence. Arrows are calculated as the product of u and v wind components and specific humidity at 850 hPa. Plotted fields are calculated using mean monthly values for the period 1986-2005 and are averaged for ON. Units are $kg\ kg^{-1}\ m\ s^{-1}$.

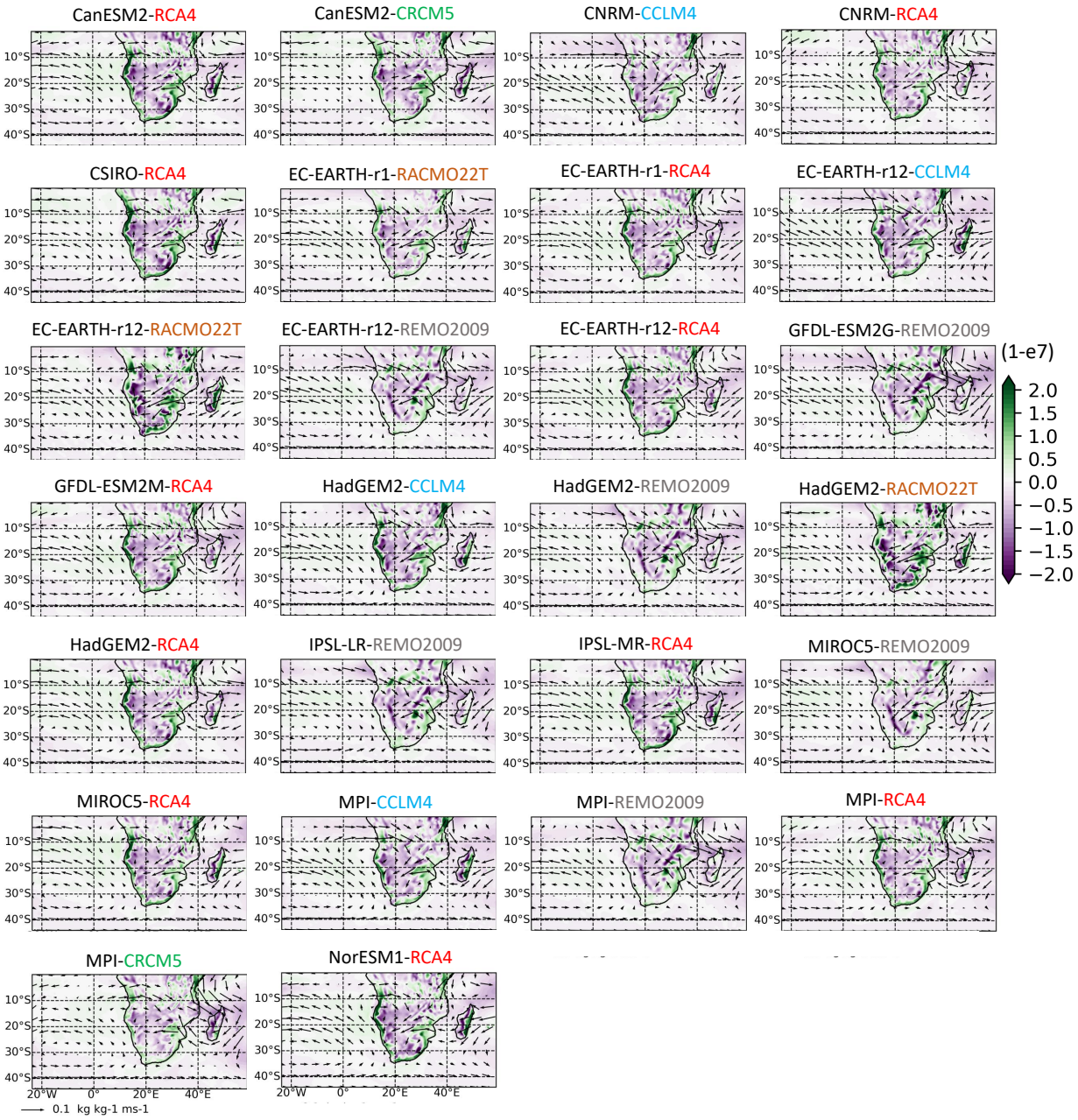

Figure 5.4.15: Moisture flux divergence at 850 hPa for December-January-February. Green areas indicate divergence, purple areas indicate convergence. Arrows are calculated as the product of u and v wind components and specific humidity at 850 hPa. Plotted fields are calculated using mean monthly values for the period 1986-2005 and are averaged for DJF. Units are $kg\ kg^{-1}\ m\ s^{-1}$.

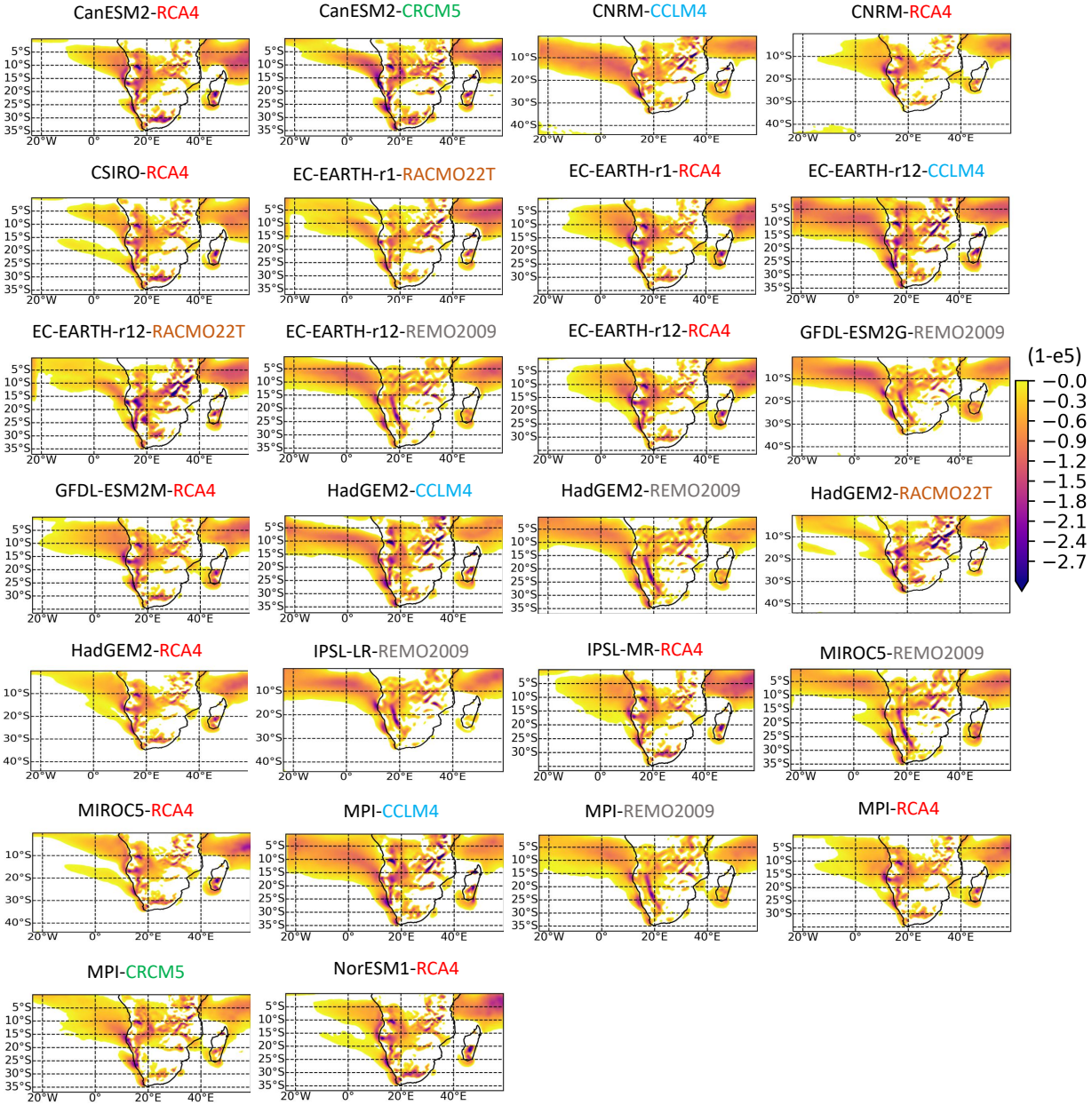

Figure 5.4.16: Mean relative vorticity for October-November during 1986-2005 in s^{-1}. Only negative vorticity values are plotted, which are indicative of cyclonic rotation.

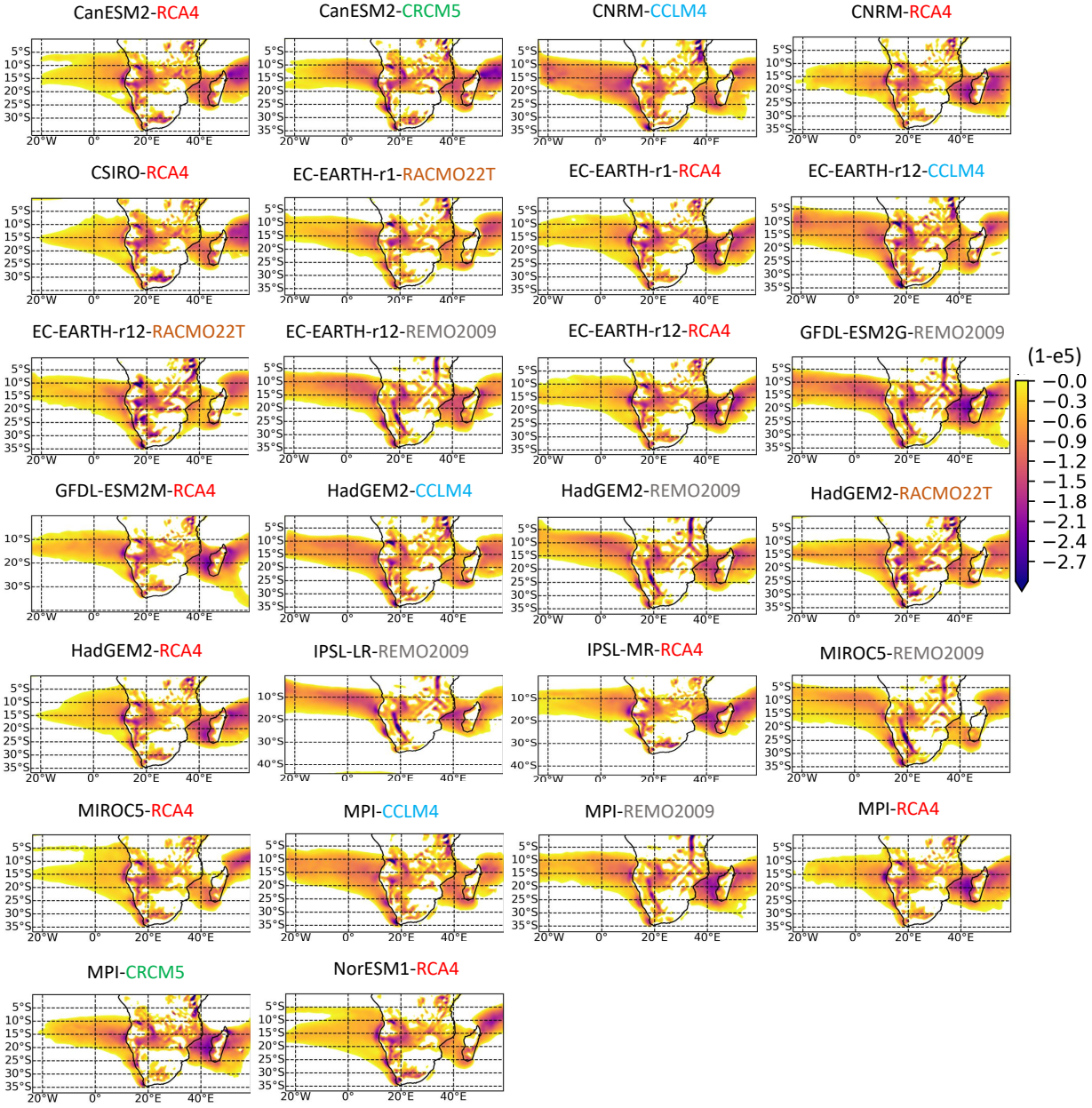

Figure 5.4.17: Mean relative vorticity for December-January-February during 1986-2005 in s^{-1}. Only negative vorticity values are plotted, which are indicative of cyclonic rotation.

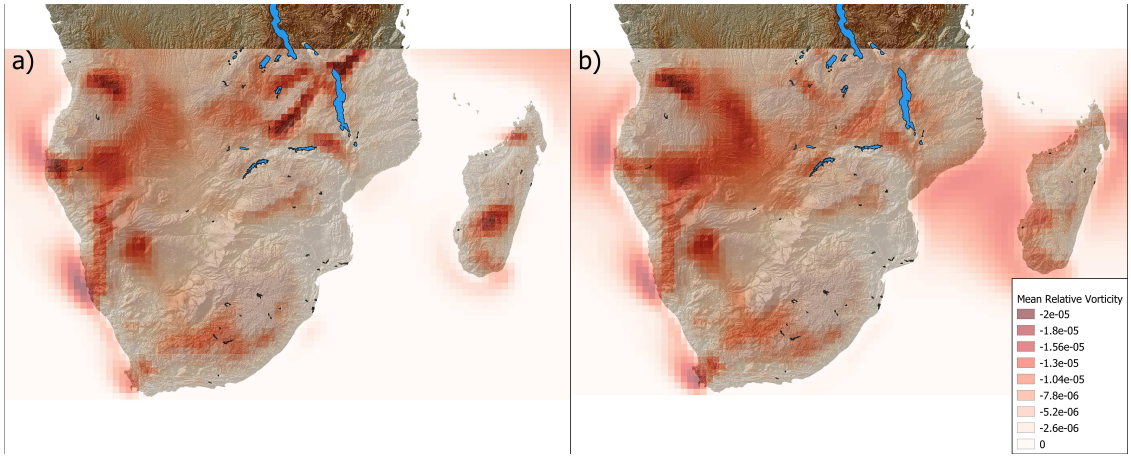

Figure 5.4.18: Ensemble mean cyclonic relative vorticity ($\zeta<0$) for all CORDEX-Africa ensemble models overlayed on the elevation map of southern Africa. A) October-November. B) December-January-February.

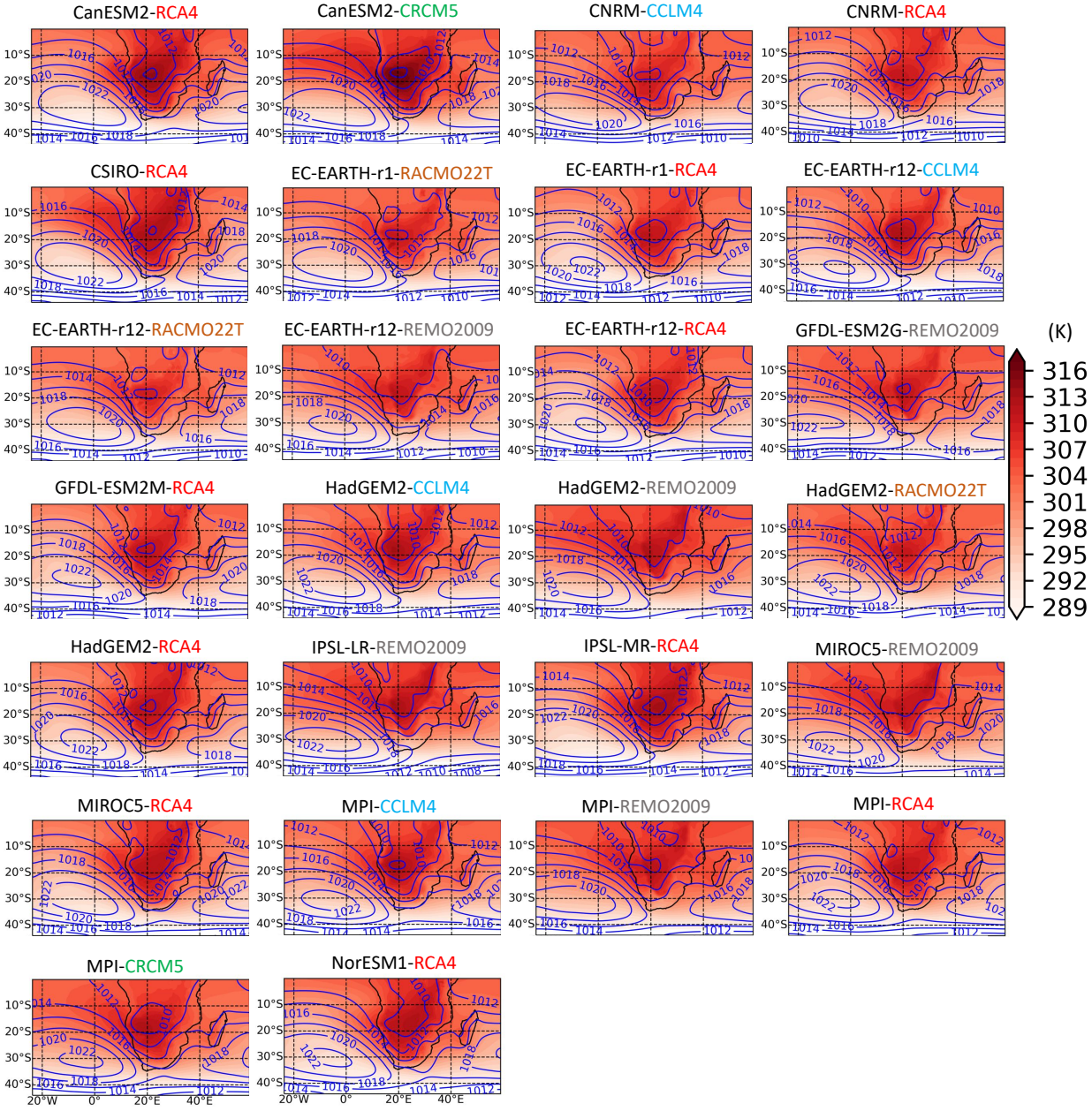

Figure 5.4.19: Potential temperature at 850 hPa for October-November (K). Blue isolines indicate sea level pressure (hPa).

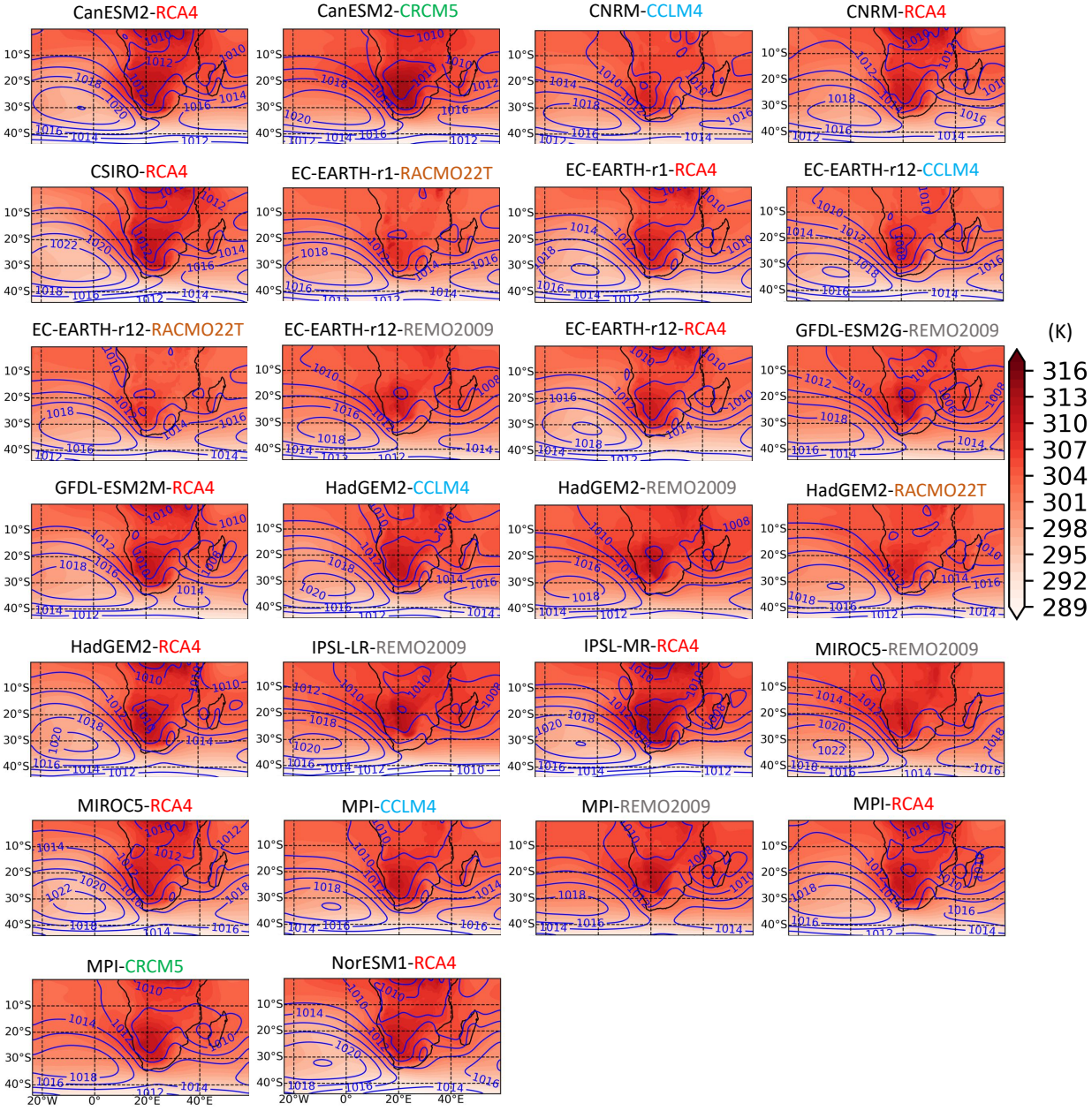

Figure 5.4.20: Potential temperature at 850 hPa for December-January-February (K). Blue isolines indicate sea level pressure (hPa).

5.5 Discussion

In this work certain key dynamical aspects of the observed precipitation climatology within the CORDEX-Africa domain are presented. Moreover, it is discussed how these features relate to the observed precipitation climatology for the early (ON) and for the core (DJF) rainy season. More specifically, it is concluded that the simulation of the STJ and of AEJ-S presents considerable challenges for the CORDEX-Africa ensemble. This observation was also found for the high resolution CORDEX-CORE set of simulations (Tamoffo et al. (2021)). Relative and absolute vorticity advection (negative values) are particularly strong over southern Africa. Over central SAF and over the Angola region, NVA is relatively weak. It is noted that a key variable providing insight to precipitation climatology over SAF is moisture flux divergence at 850 hPa. In general, models with strong moisture convergence yield more precipitation. Lastly, relative vorticity at 850 hPa, provides further insight with regards to convective regions over SAF.

Another key remark is that the topography over the Angola region is key for enhancing AL events, by imposing a mechanical stretch on the vortex of both heat lows (ON) and transient low-pressure systems (DJF). Taking into consideration the impact that topography exerts on the vorticity fields over the Angola region, it would be beneficial to conduct numerical model experiments and test this assumption. The impact that topography exerts over other parts of SAF, such as the Drakensberg mountains (Koseki and Demissie (2018)) or the mountains over South Africa (Abba Omar and Abiodun (2021)) has been examined using idealized experiments in which topographical features are either altered or removed. If the assumption that vorticity over the Angola region is enhanced due to topography is correct, then idealized simulations in which topography over Angola is completely removed would result to a decreasing depth of the climatological profile of the AL pressure system, making transient low pressure systems to no longer linger over the Angola region (Howard and Washington (2018)).

The famously known phrase from George E. P. Box, that "Essentially, all models are wrong, but some are useful" (Box (1979)), should function as a baseline navigator in the endeavors of the climate research community to improve state-of-the-art modeling systems. Currently, there are two main research directions with respect to the advancement of climate models, namely the increase in horizontal resolution (Haarsma et al. (2016); Giorgi (2019)) and the implementation of machine learning techniques, used instead or supplementary to parameterization schemes (Chantry et al. (2021); Watson-Parris (2021)). Increasing the horizontal spatial resolution is key for the furthering of the ability of climate models to accurately represent atmospheric processes and successful paradigms of such endeavors are ample (Feser et al. (2011); Giorgi and Gutowski (2015); Rummukainen (2016); Jacob et al. (2020)). Nonetheless, an increase in horizontal spatial resolution should be accompanied by an increase in understanding of scale-dependent mechanisms and processes. In addition, machine learning techniques have recently been used as an attempt to emulate parameterization schemes in climate models (O'Gorman and Dwyer (2018)) or to learn from big data and high resolution datasets, omitting the necessity for a theory or a process to be explicitly described in the model (Brenowitz and Bretherton (2019)). This fact has been simultaneously characterized as both an advantage and a disadvantage in machine learning techniques (Brenowitz et al. (2020); Watt-Meyer et al. (2021)). Nonetheless, the development of atmospheric sciences has traditionally relied on the balanced development of observations, theory and modeling (Emanuel (2020)). The unequivocal advancement of computing capabilities has significantly

catalyzed the improvement of climate models, still, a side effect of this advancement is that the other two counterparts, observations and theory, are not equally developed (Emanuel (2020)).

Further advancements for the improved modeling of the climate over SAF would require a holistic approach, in which observations, theory and modeling are equally developed. With regards to observations, coordinated endeavors with the purpose to perform field experiments have been made in the past for other African regions. Such initiatives as the HAPEX-Sahel project focusing over the Sahel region (Goutorbe et al. (1994); Goutorbe et al. (1997)), the DACCIWA (Knippertz et al. (2015)) and the AMMA projects (Redelsperger et al. (2006)) focusing over West Africa, and the FENNEC project focusing over the Sahara (Ryder et al. (2013); Ryder et al. (2015)) offered substantial insight with regards to specific processes and mechanisms. In this context we highlight that field experiments over southern Africa are necessary (Creese and Washington (2016); Ryoo et al. (2021)), so that key questions are resolved and the knowledge gained, would efficiently help to constrain model results. This need is especially timely, in light of the endeavor performed within CORDEX-CORE and the new generation of CORDEX-Africa simulations performed using CMIP6 GCMs.

6 Convection sensitivity during rainy season over southern Africa: an investigation of the impact of the cumulus scheme on precipitation using WRF

6.1 Introduction

Convection processes over southern Africa (SAF) involve the close interaction of local scale features with large/global scale forcing. Local scale atmospheric features over SAF are either directly caused or indirectly enhanced by the highly heterogeneous surface characteristics, such as the existence of high elevation and complex topography, the existence of lakes and open water bodies and a mosaic of multiple land uses and land covers. Therefore, the representative modeling of specific climatic features over SAF becomes a complex endeavor and the level of complexity varies based on the subregion examined, the length of the assessed period and the dynamic forcing that majorly contributes to the occurrence of a specific weather event or to a distinct climatic feature, depending on the temporal scale of the analysis. According to the literature, a key attribute affecting the accuracy of the simulated climate is the spatial horizontal resolution of the climate model employed (Nikulin et al. (2012); Dosio et al. (2019) Munday and Washington (2018)), with higher resolution – regional climate models presenting the capacity to alleviate systematic biases (Dosio et al. (2021); Karypidou et al. (2022b)) and improve the representation of specific processes (Pinto et al. (2018); Stratton et al. (2018)). The use of higher resolution models provides a valuable tool for a more in-depth study of convective processes and their impact on precipitation.

One of the first works involving the Weather Research and Forecasting (WRF) model (Skamarock et al. (2021)) over SAF that utilized a multi-member WRF ensemble, highlighted the fact that although specific large-scale rain-bearing atmospheric features were generally well reproduced, certain inconsistencies among ensemble members concerning specific morphological features at the margins of the large-scale forcing, resulted to large variations in precipitation amount among ensemble members (Crétat et al. (2011)). The strong effect of the cumulus scheme on seasonal rainfall amount was highlighted by (Crétat et al. (2012)), who found that although Kain-Fritsch and Betts-Miller-Janjic schemes overestimated precipitation, they should be preferred to Grell-Devenyi, which in combination to the Mellor-Yamada-Janjic planetary boundary layer, should be avoided when summer climatic conditions are simulated over SAF. Later WRF simulations highlighted the impact that sea surface temperate (SST)

exerts on climatic conditions over SAF (Ratnam et al. (2012)) and over the Angola Low (AL) pressure system in particular (Desbiolles et al. (2020)). SSTs and surface conditions over the Indian Ocean were also found to exert a strong impact on convection over SAF, mainly through their effect on tropical temperate troughs (Vigaud et al. (2012)), while coupling with a simple mixed layer ocean model with WRF was found to substantially improve the simulated precipitation over SAF (relative to using prescribed SSTs) (Ratnam et al. (2013)).

More specifically, convection processes over SAF are shown to be strongly influenced by the cumulus scheme used (Crétat et al. (2012); Meroni et al. (2021)). Some of the first WRF simulations over SAF (Boulard et al. (2013); Ratnam et al. (2012)) employed the Kain-Fritsch cumulus scheme (Kain (2004)), which has been reported to overestimate precipitation amounts and number of rainy days in convection sensitivity studies (Crétat et al. (2012); Pohl et al. (2014)). More recent studies using WRF over SAF (Moalafhi et al. (2017b); Moalafhi et al. (2017a); Koseki and Mooney (2019)) employ the Betts-Miller-Janjic (Janjić (1994)), which displays more accurately the spatial and temporal precipitation patterns. The WRF experiments over SAF using the New-Tiedtke (or over a region containing SAF) are rather limited (SUN and BI (2019); Bopape et al. (2021); Meroni et al. (2021); Mulovhedzi et al. (2021)). Although the existing literature provides some insight into which cumulus schemes could be considered optimal, it should be highlighted that simulation set-ups that would successfully replicate certain climatic features, do not necessarily replicate specific weather events (Meroni et al. (2021)), even over the same region.

An additional issue related to convection is the question regarding the absence of a cumulus parameterization scheme and the ability of very high-resolution models to numerically resolve convection. In RCM experiments diurnal cycle and the maximum convection intensity is simulated approximately 2-3 hours earlier than observed. This deficiency has been resolved by convection permitting simulations (CPS) for other parts of Africa (Parker et al. (2005); Pearson et al. (2014)), however CPS simulations have shown little to negligible improvement over SAF (Pohl et al. (2014)). More specifically, CPS experiments over a region in South Africa (Keat et al. (2019)) showed that CPS experiments at 1.5 km horizontal spatial resolution overestimated the number of large storms (compared to radar observations) and their associated rain rate and also, simulated a tendency for large storm cells to merge and therefore become long-lived in the atmospheric environment. In addition, CPS displayed a systematic tendency in the evolution of convective parcels according to which, storms reached their maximum intensity 15 minutes after their initiation, while the observed time in the radar data varied from 10 to 30 minutes (storm maximum intensity after initiation). Moreover, CPS displayed a systematic lack of small storms, a fact attributed to the inability of CPS to simulate small-scale storm triggering processes (e. g. cold pools). Overall, CPS simulated convection 2 hours prior to the observed time (according to radar). Based on Keat et al. (2019), the challenges of CPS simulations to provide an accurate estimation of the initiation time and life-cycle of convection, could be attributed to the fact that numerical models lack Convection Inhibition (CIN) profiles and that the contribution of subgrid mixing parameters may be more important than previously estimated. On the contrary, Stein et al. (2019) reported an improvement in the diurnal cycle and spatial pattern of precipitation over a region in southern Africa, however, they highlighted that further investigations on individual convective clouds should be performed, focusing on process-based evaluation, rather than space and time averaged statistics.

Individual extreme rainfall events assessed during the period 1981-2016 over the southeast part

of SAF identified a specific extreme precipitation event during January 2013 as the most severe event throughout the climatology (Rapolaki et al. (2019)). More specifically, during 11-21 January 2013 extreme precipitation occurred at the southeast part of SAF, with accumulated precipitation during the 10-day period exceeding 200 mm (Manhique et al. (2011)). According to Wiston and Mphale (2019), the excess precipitation amounts were caused by Mesoscale Convective Systems (MCS) that were more severe during the period 15-20 January 2013. This event claimed the lives of 100 people and caused the displacement of 200.000 (Manhique et al. (2011)). According to Rapolaki et al. (2021), the extreme event during 11-21 January 2013 had multiple moisture sources, with the most severe being the Mozambique Channel.

Considering that convection sensitivity studies using a high resolution domain and multiple cumulus schemes over SAF are limited and taking into consideration that the rainy season during 2012-2013 was dominated by transient tropical low pressure systems, it is deemed imperative to investigate how different cumulus parameterization schemes impact the October-November-December 2012 and January-February (2013) rainy season (henceforth: 2012-2013 rainy season). In addition, the extreme rain event during January 2013 is examined. The focus is placed during the period 15-20 January 2013, according to (Wiston and Mphale (2019)). Therefore, the goal of this work is to:

1. Use a regional climate model to simulate precipitation patterns over southern Africa, during the early rainy season (ON 2012) and core rainy season (Dec 2012 – Jan-Feb 2013) and during an extreme rain event (15-20 January 2013).
2. Validate the ability of the model to simulate accurately precipitation amounts and attribute potential model inconsistencies to processes.
3. Examine the sensitivity of model convective schemes, precipitation, and related dynamical processes.

6.2 Data and methods

6.2.1 Weather Research and Forecast (WRF) model

In this work, the WRF nonhydrostatic version 4.3.3 (Skamarock et al. (2021)) with the Advanced Research (ARW) dynamic solver is employed. The simulation domain shown as Fig. 6.2.1, extends from 2.66596 °S to 34.5717 °S (235 north - south grid points) and from 1.62366 °E to 54.7784 °E (356 west - east grid points), having a horizontal spatial resolution equal to 15 x 15 km (dx, dy = 15000). No nested domain is used and the map projection with the least distortion over the study domain is found to be Lambert. Lateral boundary conditions are obtained from ERA5 (Hersbach et al. (2020)) every six hours and they are provided at 38 vertical levels ($num\_metgrid\_levels$) and at four soil levels ($num\_metgrid\_soil\_levels$). In total 50 vertical levels are used (e_vert). The top level (p_top) is set at 20 hPa. SSTs are provided every six hours ($sst\_update1$, $sstskin1$). Based on its horizontal spatial resolution, the model is integrated every 90 seconds (6dx). The lateral boundary nudging is performed across 10 grid points and the relaxation zone employs nine grid points. The exponential multiplier for relaxation is set to 0.33. The spin-up time of the model starts at July 1st 2012 and lasts until September 30th 2012. In total four sensitivity experiments are performed.

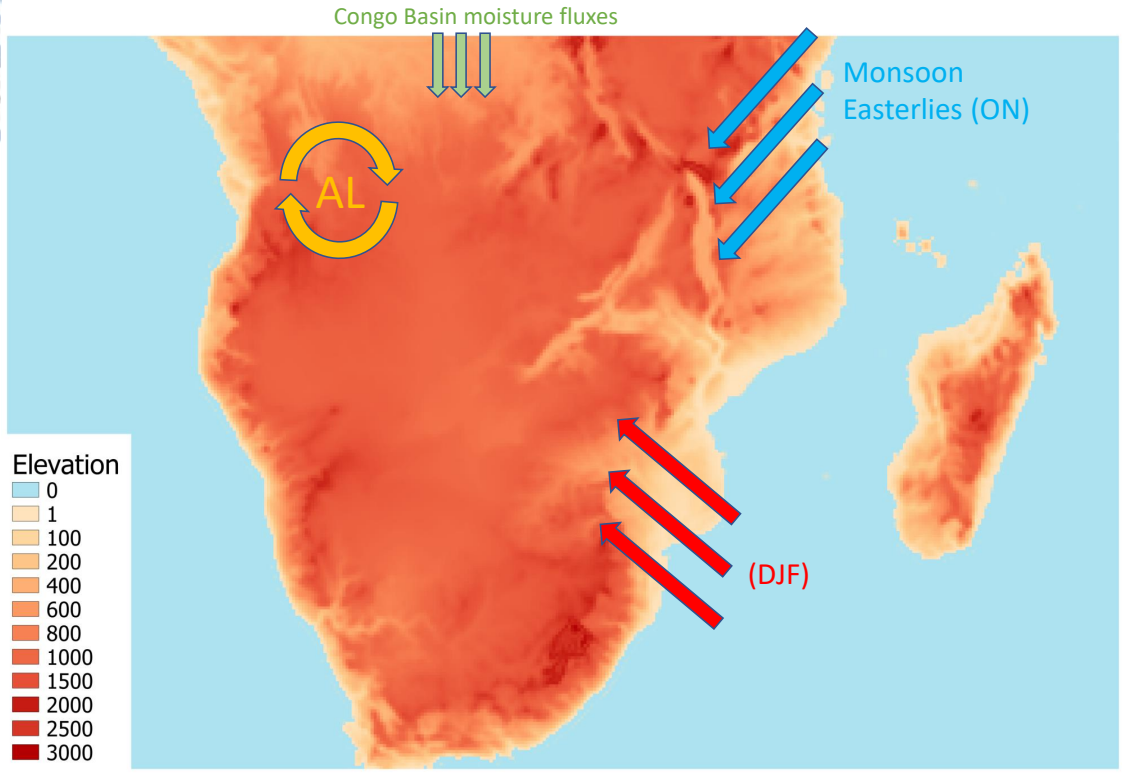

Figure 6.2.1: WRF domain and some of the key climatic features controlling precipitation climatology over southern Africa.

More specifically, all WRF runs parameterize short- and longwave radiation exploiting the RRTMG radiation scheme (Iacono et al. (2008)) which is called every 15 minutes. The aerosol option 2 ($aer\_opt = 2$) is used, which incorporates daily total atmospheric optical depth at 550 nm data. This information is retrieved from the Copernicus atmospheric Monitoring Service (). The MYNN surface layer option ($sf\_sfclay\_physics = 5$) and planetary boundary layer ($bl\_pbl\_physics5$) are used (Nakanishi and Niino (2006)) and the latter is called in every timestep. All WRF simulations are coupled with Noah-MP (Niu et al. (2011)) land surface model, employing four soil layers and the default USGS surface characteristics are used. Microphysical properties are parameterized using the Thompson scheme ($mp\_physics8$). The sensitivity experiments are conducted using the cumulus scheme for which four different cumulus parameterization options are employed. The schemes used are Kain-Fritsch (KF) (Kain (2004)), Betts-Miller-Janjic (Janjić (1994)), the New-Tiedtke (NT) (Zhang and Wang (2017)) and the Grell-Freitas (GF) (Grell and Freitas (2014)). All cumulus schemes are called in every timestep.

KF is a mass-flux scheme, based on the assumption that convection is a means of removing the convective available potential energy (CAPE) from an air parcel. In order for convection to be initiated, CAPE must be positive. The examination of CAPE is performed at each atmospheric level and also, entrainment (detrainment) of the environmental (updraft) air can occur at each atmospheric level. The BMJ scheme is based on reference atmospheric profiles that aim to simulate the atmospheric conditions

[0]https://atmosphere.copernicus.eu/

after a deep convective event. Convection initiation in the GF scheme also requires positive CAPE values, but in contrary to KF, GF handles the whole atmospheric column as a single deep convection region. Lastly, NT is also a mass-flux scheme and it also employs a CAPE closure in order to detect convection, but additionally, shallow convection is affected by surface evaporation.

6.2.2 Domain Selection

Before finalizing the region that would be used as the simulation domain for all WRF experiments, three types of domains are examined, shown in Fig. 6.2.2. "Domain 0" is the control domain, "Domain Minus" is defined as "Domain 0" reduced by five grid points on all sides and lastly, "Domain Plus" containing Madagascar is also examined. The grid attributes of each domain are given in Table 6.2.1. All three simulations are run for December 2012, using the same WRF configuration. After comparing all three domain simulations with ERA5 for a series of atmospheric variables, both at the surface and at specific pressure levels, "Domain Plus" is selected as the optimal domain. An additional sensitivity run is performed, in which "Domain Plus" is shifted to its east, in order to secure that the choice of its western - eastern boundaries are proper (not shown - ref_x parameter changed).

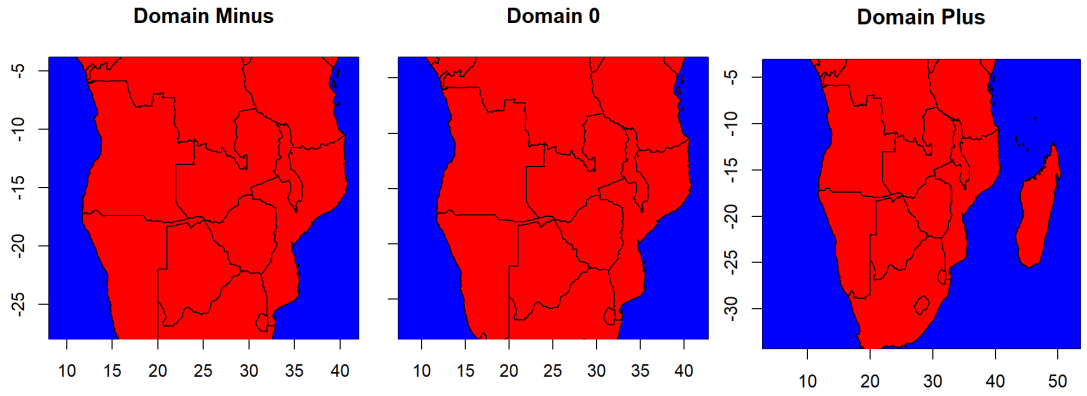

Figure 6.2.2: WRF domains examined over southern Africa.

Table 6.2.1: Grid attributes for the sensitivity runs on the domain.

Grid attributes	Domain Minus	Domain 0	Domain Plus
e_we	243	253	356
e_sn	181	191	235
dx	15000	15000	15000
dy	15000	15000	15000
ref_lat	-16.256	-16.256	-19.411
ref_lon	25.046	25.046	28.201
truelat1	-16.256	-16.256	-19.411
truelat2	0	0	0
stand_lon	25.046	25.046	28.201
ref_x	121.5	126.5	178.0
ref_y	90.5	95.5	117.5

6.2.3 Sensitivity on the Spin-up time and Noah-MP parameters

A major modeling choice affecting the accuracy of a simulation is the length of its spin-up time, that allows the RCM to reach an equilibrium state, especially with regards to soil parameters such as soil moisture and soil temperature. In this work, four spin-up time lengths are assessed with respect to soil temperature (TSLB) and soil moisture (SMOIS) observed in the four soil layers of the land surface model used (Noah-MP). The sensitivity runs employ four identical simulations, differing only in the length of their spin-up time. The first sensitivity has an one month spin-up time (Spinup-1) and starts on the 1st of September 2012. The second sensitivity has a three months spin-up time (Spinup-3) and starts on the 1st of July 2012. The third sensitivity has a six months spin-up time (Spinup-6) and starts on the 1st of April 2012. Lastly, the fourth sensitivity has a nine months spin-up time (Spinup-9) and starts on the 1st of January 2012. All runs last up until the 1st of January 2013 (Table 6.2.2).

Table 6.2.2: The spin-up sensitivity simulations performed.

Name	Spin-up	Start	End
Spinup-1	1 mn	1 Sep 2012	1 Jan 2013
Spinup-3	3 mn	1 Jul 2012	1 Jan 2013
Spinup-6	6 mn	1 Apr 2012	1 Jan 2013
Spinup-9	9 mn	1 Jan 2012	1 Jan 2013

In addition to the spin-up time sensitivity experiments, four more runs are performed, testing the sensitivity of the Noah-MP land surface model to certain parameters. The four additional Noah-MP sensitivity experiments are shown in Table 6.2.3. The results of both set of runs (Spin-up time and Noah-MP) are analysed over the whole SAF domain and over specific locations of interest (Fig. 6.2.3, Fig. 6.2.4). As a result, the three months spin-up time (Spinup-3) is selected as the optimal, starting on the 1st of July 2012. The one month spin-up time (Spinup-1) is found to be too short, not allowing WRF to reach an

equilibrium state with regards to soil temperature and soil moisture. On the contrary, the longer spin-up time lengths (Spinup-6 and Spinup-9) are found to be overly computationally expensive, being prone to accumulating unnecessary model errors. In addition, Noah-MP is selected using the "CONTROL" parameters, as shown in Table 6.2.3, as the altered parameters had a weak effect on soil temperature and soil moisture.

Table 6.2.3: Sensitivity simulations for NOAH-MP for the Spinup-9 runs.

Name	CONTROL	SAF1	SAF2	SAF3	SAF4
OPT_SFC	1	1	1	1	1
DVEG	4	4	4	4	4
OPT_CRS	1	1	1	1	1
OPT_BTR	1	1	1	1	2
OPT_RUN	2	1	1	2	2
OPT_FRZ	1	1	1	1	1
OPT_INF	1	1	2	1	1
OPT_RAD	3	3	3	3	3
OPT_ALB	2	2	2	2	2
OPT_SNF	1	1	1	1	1
OPT_TBOT	2	2	2	2	2
OPT_STC	1	1	1	1	1
OPT_GLA	1	1	1	1	1
OPT_RSF	1	1	1	1	1
OPT_SOIL		1	1	1	1
OPT_PEDO		1	1	1	1
OPT_CROP		0	0	0	0

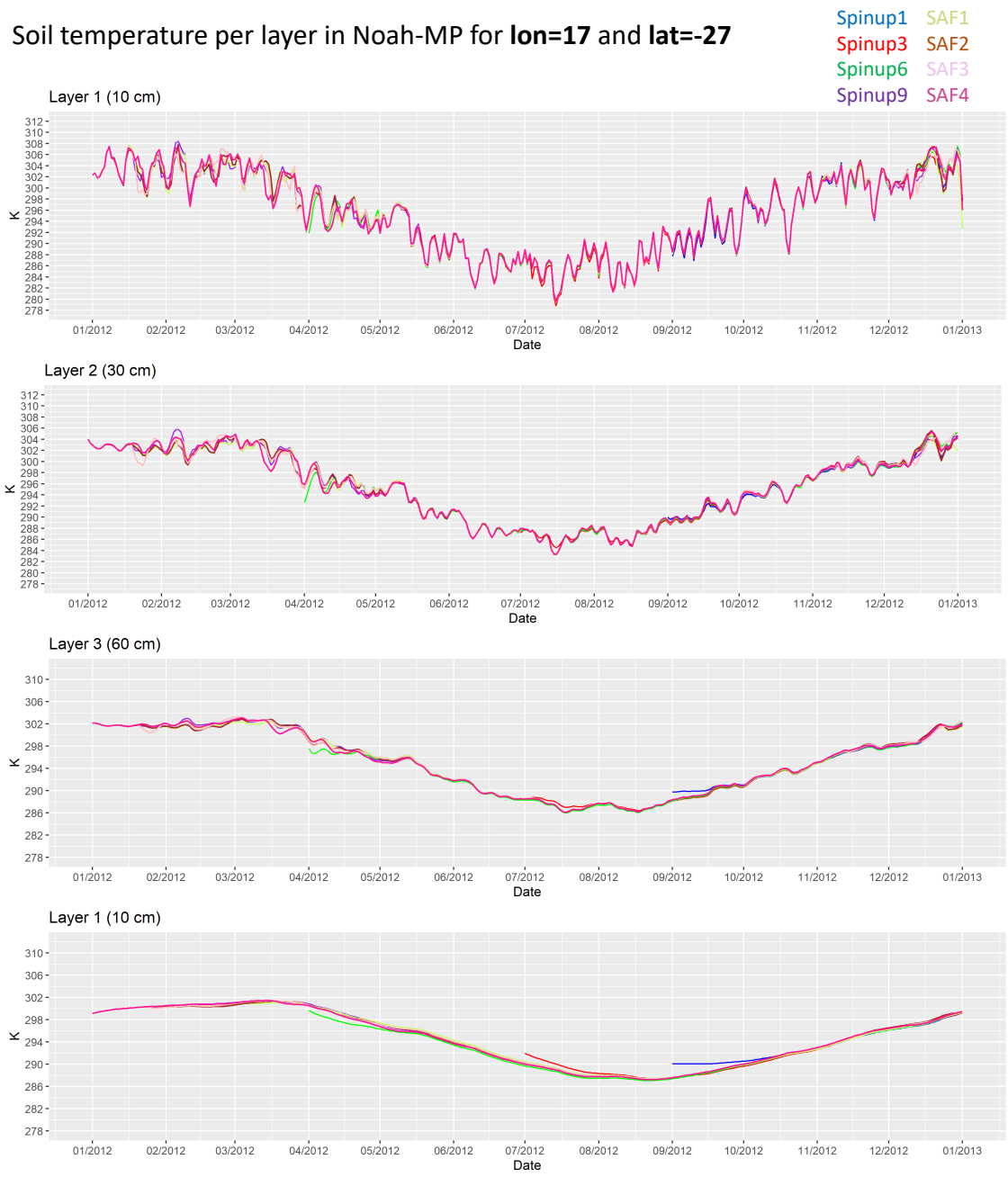

Figure 6.2.3: Soil temperature timeseries over DRY lon=20.33 and lat=-23.86.

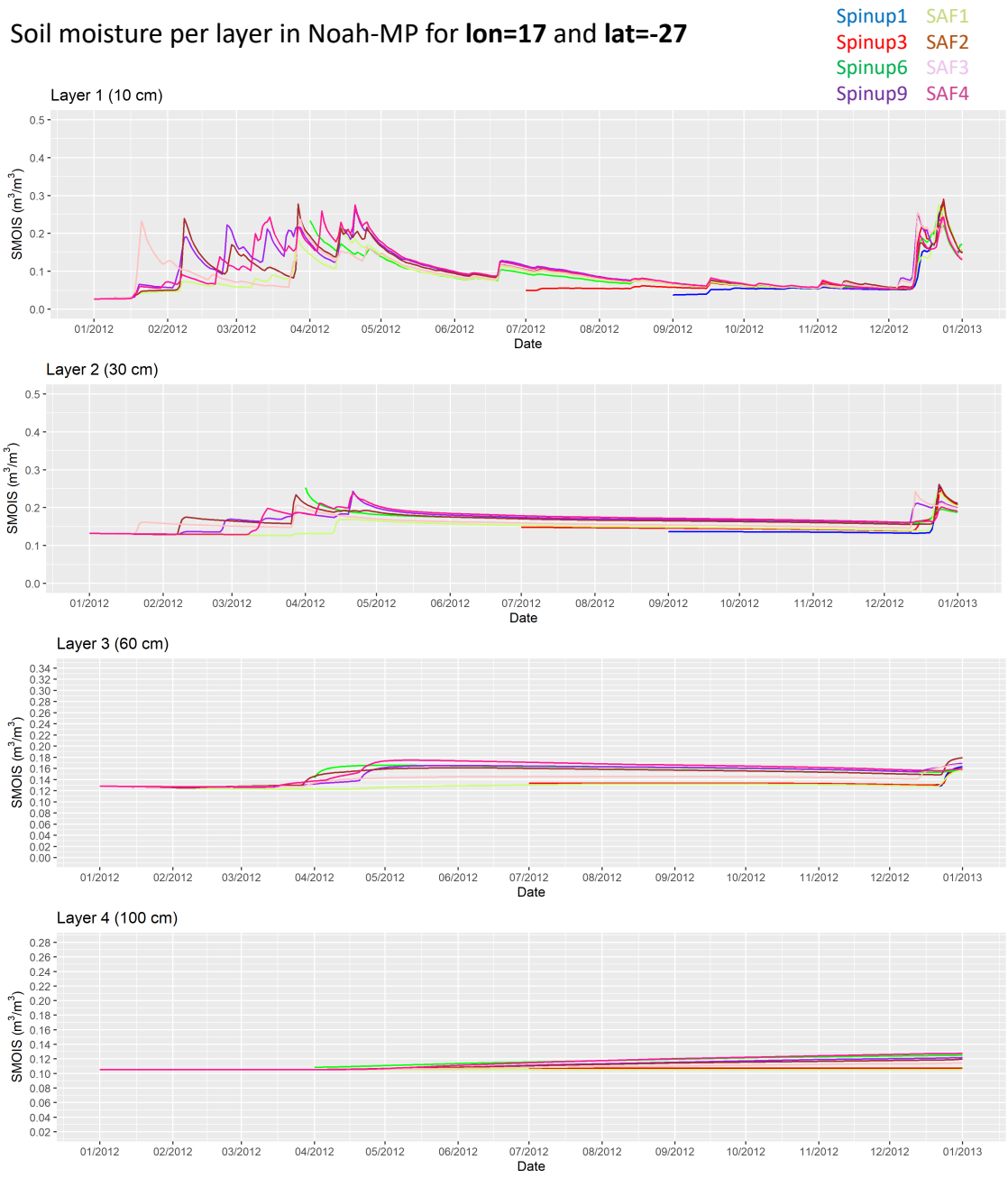

Figure 6.2.4: Soil moisture timeseries over DRY lon=20.33 and lat=-23.86.

6.2.4 Sensitivity of the model's performance in ARIS

Moreover, WRF.v4.2.2 is examined for its performance in ARIS HPC (`https://hpc.grnet.gr/`https://hpc.grnet.gr/), using 20 MPI tasks per compute node. The model is run for 24 hours (start: 2012-12-01:00:00:00 end: 2012-12-02:00:00:00). In all simulations "Domain Plus" over southern Africa is used (356 x 235 x 50). The variable "time" used is the "WRF execution time" shown in the .out file of the sbatch job script. All decomposition runs performed are shown in Table 6.2.4. Following the benchmarking analysis shown in Fig. 6.2.5, 12 nodes are used in all WRF experiments, using a 15 x 16 decomposition of the domain.

Table 6.2.4: Sensitivity of the model's performance in ARIS.

Nodes	Cores	Time	Decomposition
2	40	1139	5x8
4	80	858	8x10
6	120	709	10x12
8	160	606	10x16
10	200	560	10x20
12	240	564	15x16
14	280	532	14x20
16	320	519	16x20
18	360	503	18x20
20	400	498	20x20
22	440	493	20x22

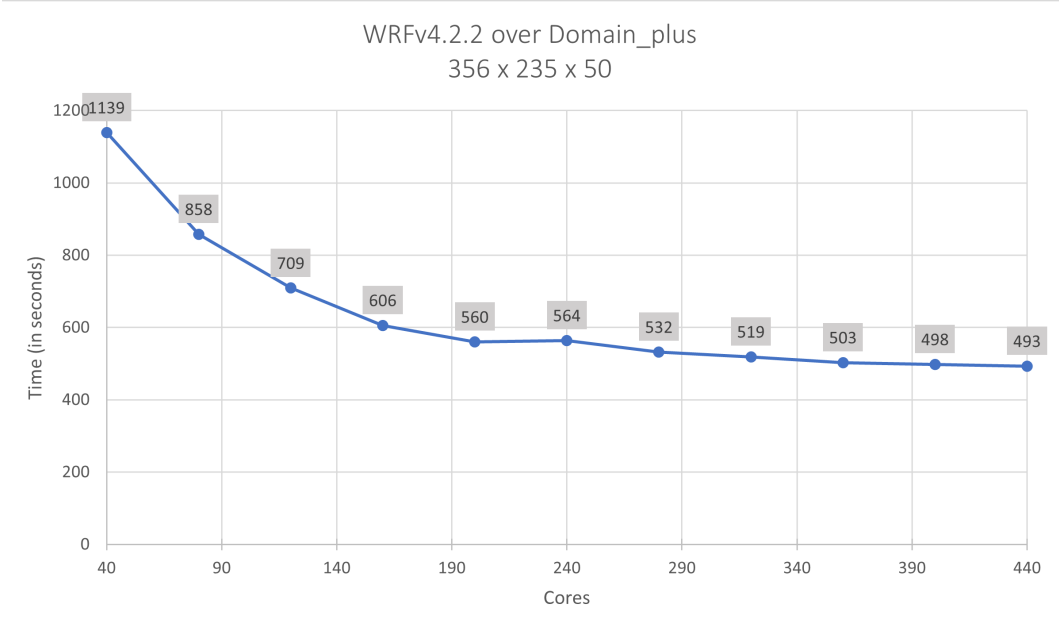

Figure 6.2.5: WRF execution time in ARIS for 1-day runs given in seconds (y-axis), per number of cores used.

6.2.5 Satellite and reanalysis data

The data used for comparison with the WRF simulations are listed in Table 6.2.5 below. The datasets were selected based on their spatial resolution.

Table 6.2.5: Satellite and reanalysis datasets used.

Dataset	Resolution	Type	Period	Reference
MSWEP	0.1°	Satellite	1979-present	(Beck et al. (2019))
TAMSAT.v3	0.0375°	Satellite	1983-present	(Tarnavsky et al. (2014))
CHIRPS.v2	0.05°	Satellite	1981-present	(Funk et al. (2015))
ERA5	0.28125°	Reanalysis	1979-present	(Hersbach et al. (2020))

6.3 Results

6.3.1 Rainy season analysis

Total precipitation amounts are shown in Fig. 6.3.1 for the early rainy season (ON – Fig. 6.3.1a) and for the core rainy season (DJF – Fig. 6.3.1b). During ON, the tropical rainband migrates southwards, as maximum solar heating and moisture advection from the surrounding Oceans and the Congo Basin, provide the necessary thermodynamic conditions for convection over northern SAF (Hart et al. (2013); Hart et al. (2019)). Tropical convection is largely dependent on the moist static energy available to an air parcel, hence, regions of high precipitation amounts coincide with high moist static energy (Nie et al. (2010); Hart et al. (2019)). As shown, high total precipitation amounts (>700 mm) during ON are observed at the northwest part of SAF, confined to the north of 15 °S and to the west of 30 °E, indicating the region to the northwest of the Congo Air Boundary (CAB) (Howard and Washington (2019)). This feature is identified in all WRF simulations and to a lesser degree in satellite products (CHIRPS, MSWEP, TAMSAT) and reanalysis (ERA5). Although all simulations identify the regional precipitation pattern, there are considerable differences between them. More specifically, the KF and GF experiments simulate larger total precipitation amounts, compared to the BMJ and NT simulations. In the satellite products, CHIRPS and MSWEP yield similar results, while TAMSAT yields considerably smaller precipitation amounts. ERA5 also, displays relatively smaller precipitation amounts, nonetheless there are regions of localized high precipitation amounts, mainly in the greater vicinity of lake Malawi. A secondary region of precipitation activity (<600 mm) is identified at the eastern part of South Africa. The main rain bearing mechanisms at that region involve the warm SSTs caused by the Agulhas Current (Njouodo et al. (2018)) and the existence of the Drakensberg mountains that function as a barrier to the moisture advection from the Indian Ocean and cause orographic lifting (Koseki and Demissie (2018)). As seen in Fig. 6.3.1a, the KF and the GF simulations yield the highest precipitation amounts over eastern South Africa (600 mm). From the satellite products, MSWEP also yields similar precipitation amounts.

Total precipitation amounts for DJF are displayed in Fig. 6.3.1b. As shown, large precipitation amounts extend on a northwest to southeast zone, north of 20 °S, which is indicative of the South Indian Ocean

Convergence Zone (SIOCZ) (Lazenby et al. (2016)). During DJF the CAB has broken (Howard and Washington (2019)), allowing moisture from the Congo Basin to enter SAF. As shown, high precipitation amounts are observed for KF (>2400 mm – cumulative precipitation for DJF), followed by GF. The BMJ and the NT simulations display results with a very similar spatial pattern, with NT yielding overall less precipitation than BMJ. From the satellite products, CHIRPS and MSWEP yield remarkably similar results, both from the aspect of precipitation magnitude, but also from the aspect of the spatial pattern of total precipitation. TAMSAT and ERA5 yield total precipitation <1400 mm. An observation with regards to the KF simulation consistent for both seasons (ON, DJF) is that precipitation follows very closely the spatial pattern of orography.

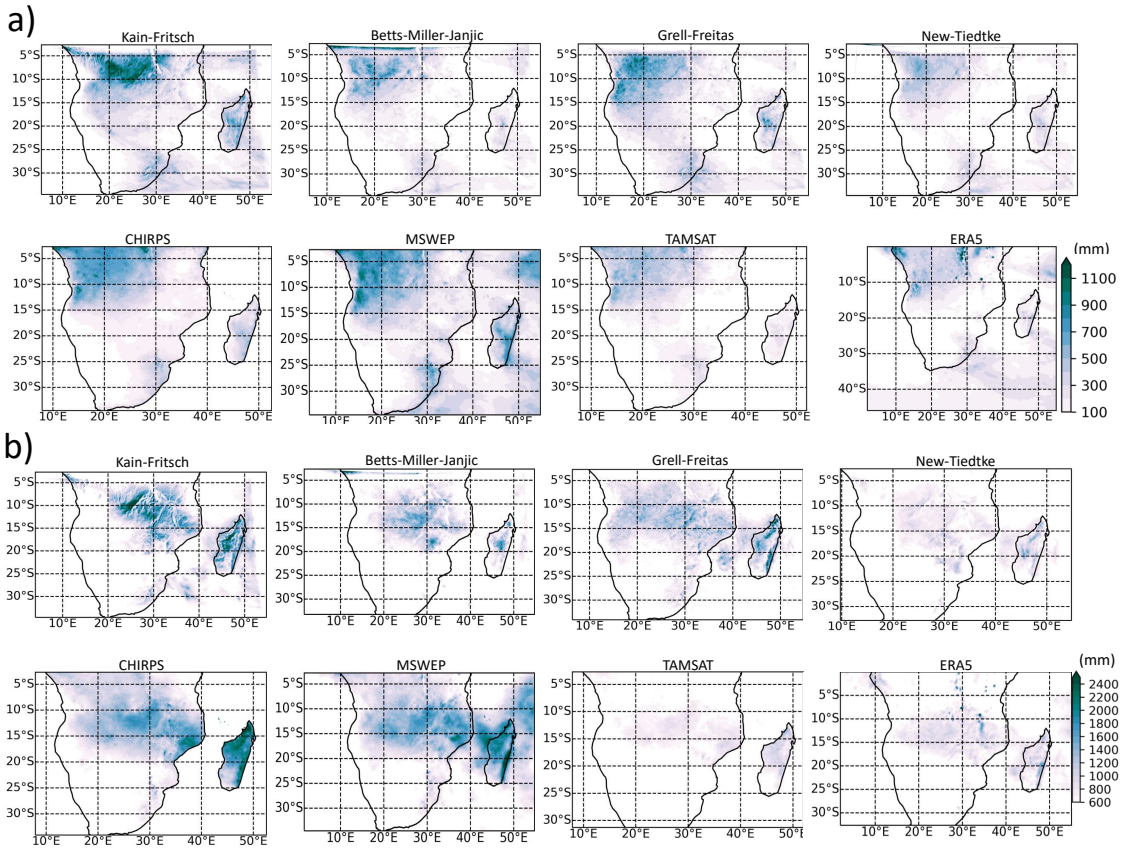

Figure 6.3.1: Total precipitation (mm) amounts. a) Cumulative precipitation for October-November 2012, b) Cumulative precipitation during December 2012 January-February 2013.

In Fig. 6.3.2 the spatial average of daily precipitation during the rainy season is shown, for the largest part of mainland SAF (Fig. 6.3.2a) and for the Angola region, which is the main area over which the Angola Low pressure system is identified (Fig. 6.3.2b). The regions over which the spatial averaging has taken place is shown at the bottom right of each panel. For the greater part of SAF (Fig. 6.3.2a) all simulations display a similar behavior for the most part of October, until the end of October during which the KF and GF simulations display almost double precipitation amounts, compared to the other WRF simulations and the satellite products. This behavior is seen also during the second half of November. From December and onward, the various spikes and peaks in the timeseries are mostly observed for

the KF and GF simulations. The BMJ and NT simulations are followed closely by the satellite products. In general, NT simulates the lowest precipitation amounts. The variability of daily precipitation is considerably larger when the Angola region is examined (Fig. 6.3.2 b). The spikes in the timeseries are also dominated by KF and GF simulations, nonetheless, the lowest precipitation amounts are seen for the KF simulation.

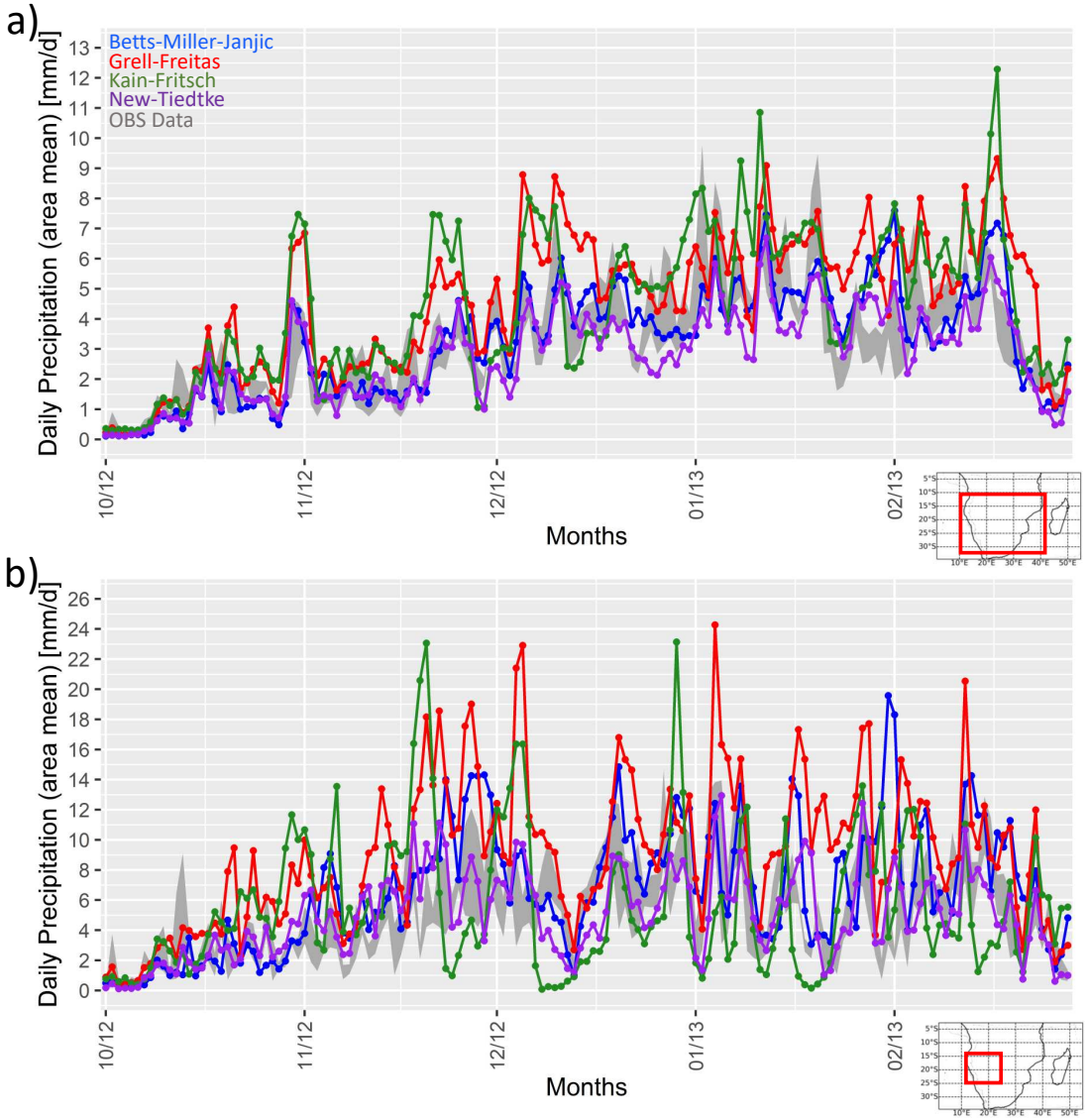

Figure 6.3.2: Spatial average of daily precipitation during the rainy season for the largest part of mainland SAF (a) and (b) for the Angola region. The regions over which the spatial averaging has taken place is shown at the bottom right of each panel.

The Pearson temporal correlations for the aforementioned timeseries are shown in Fig. 6.3.3. Correlations across SAF are shown in Fig. 6.3.3a. The smallest correlations identified (0.66 - 0.69) across SAF are between all WRF simulations and TAMSAT. The highest correlation (0.91) is identified for the NT simulation and ERA5, which is not surprising since ERA5 uses the NT scheme. However, a strong cor-

relation (0.9) is also identified between NT and MSWEP. In general, ERA5 and MSWEP display equally strong correlations with all WRF simulations, however, this is rather expected for ERA5, since it is used to provide lateral boundary conditions in all runs. CHIRPS displays moderately strong correlations (0.72 - 0.76) and TAMSAT follows last. In general, NT displays the strongest correlation with all datasets (0.67 – 0.91), the BMJ follows second (0.89 – 0.66) and the GF and KF simulations follow last. When the focus is placed over the Angola region (Fig. 6.3.3b), the correlations are more variable ranging from 0.12 to 0.73. More specifically, KF displays the lowest correlations (0.12 – 0.25) with all datasets. The highest correlations are identified for GF, with the NT following closely. The BMJ simulation displays moderately strong correlations (0.41 – 0.67). From the satellite rainfall products, the MSWEP displays the strongest correlations with all WRF runs.

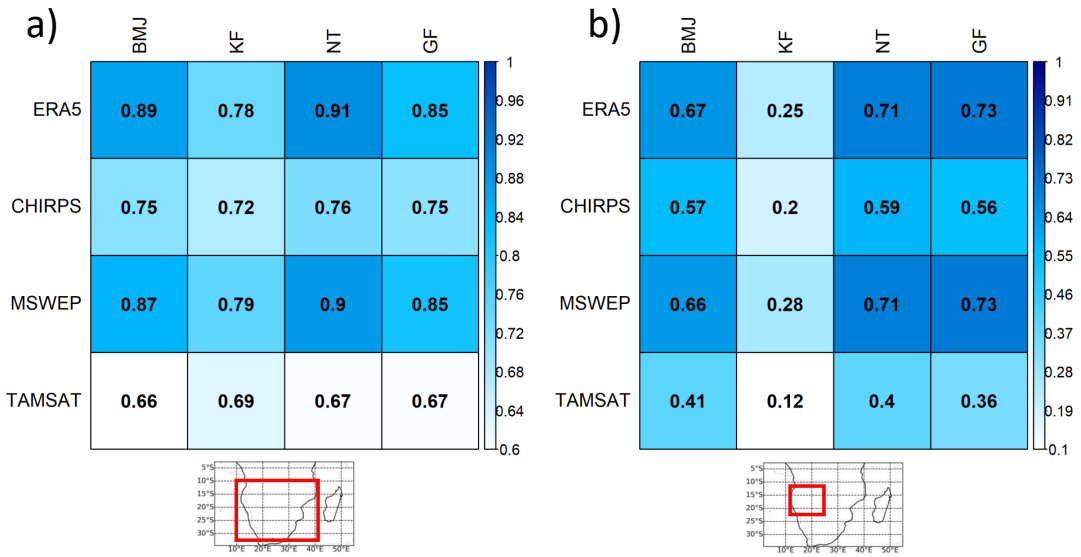

Figure 6.3.3: Pearson correlation of the spatial average of daily precipitation during the rainy season for the largest part of mainland SAF (a) and (b) for the Angola region. The regions over which the timeseries are correlated is shown at the bottom of each panel.

Specific humidity at 850 hPa (in kg/kg) over the study region is shown in Fig. 6.3.4, for ON (Fig. 6.3.4a) and for DJF (Fig. 6.3.4b). During the onset of the rainy season (ON) low-level atmospheric moisture is mostly confined to the northwest of SAF, confined within CAB (indicated in red in Fig. 6.3.4a). As shown, the KF and NT simulations display the largest amounts of specific humidity (>0.014 kg/kg) at the northwest part of SAF, which can be attributed either to excess moisture advection from the Congo Basin and the Atlantic Ocean though the circulation of the Angola Low pressure system, or to the existence of a very strong CAB that would prohibit the diffusion of moisture towards the southeast (or to the co-occurrence of both). Another distinct pattern identified in all simulations is the dry conditions observed at the southwest part of SAF, which is caused by the Benguela upwelling system, which is an eastern boundary system, invoking cool SST conditions (Lamont et al. (2018)) that generally favor the formation of shallow stratocumulus clouds and inhibit the development of deep convection. However, since the current WRF simulations do not exploit a coupled ocean model it would be problematic to

draw any further conclusions concerning the impact of oceanic conditions on mainland SAF. Specific humidity during DJF is shown in Fig. 6.3.4b. As displayed, moisture has migrated southwards, following the collapse of CAB, which during DJF has been replaced by SIOCZ. However, there are considerable differences in the spatial structure of high specific humidity patterns across the four simulations. More specifically, KF displays high specific humidity values (>0.014 kg/kg) over a region between 20 – 30 °E and 10 °S, extending towards the southeast, forming a clear tilt, indicative of the SIOCZ. The NT run displays a more extended region of high humidity values. The region of high humidity is placed more westwards in the GF run, while in BMJ, although located at the north - central part of SAF, high specific humidity is of smaller magnitude.

Moisture fluxes and moisture flux divergence (MFD) at 850 hPa is displayed in Fig. 6.3.5, for ON (Fig. 6.3.5a) and for DJF (Fig. 6.3.5b). As observed for ON, all simulations display a moisture inflow from the Atlantic Ocean and the Congo Basin, though the rotation of the AL pressure system and the influx of moisture from the monsoon region at the northeastern part of SAF. The air masses entering SAF converge forming CAB, which is essentially a discontinuity surface caused by the different thermodynamic characteristics of the converging air masses. These features are present in all simulations, however with variable intensity. More specifically, as seen in Fig. 6.3.5a, the KF simulation imports considerably larger amounts of moisture from the Atlantic Ocean and the Congo Basin, compared to the other experiments, causing strong convergence fields and a strong CAB. On the contrary, GF simulates weak moisture transport from the Atlantic Ocean and the Congo Basin. The BMJ and NT simulations show a more moderate behavior of moisture fluxes. During DJF (Fig. 6.3.5b) the moisture fluxes from the Atlantic Ocean and the Congo Basin are maintained, however, the northeastern monsoon is weakened and instead, there is an easterly flow entering SAF from the southeastern part, following the rotation of the South Indian Ocean High Pressure system (or Mascarene High) (Xulu et al. (2020)). Across all simulations, KF displays the strongest moisture flux convergence.

One of the primary characteristics of heat low pressure systems is that they are strongly coupled with land temperatures and their formation occurs over areas with increased surface heating. Over SAF and particularly over the greater Angola region, heat lows are present during Oct - Nov. As it is shown in Fig. 6.3.6a, maximum heating areas at 850 hPa in all simulations are identified at approximately 20 °S and are stronger in the KF and BMJ simulations (316 K), while in GF and NT maximum heating ranges between 312 - 314 K. In addition, maximum heating areas are collocated with minimum geopotential height at 850 hPa, indicating the presence of a thermally induced convective process. Geopotential height at 850 hPa is lowest (1490 m) in KF. The same variables but for DJF are shown in Fig. 6.3.6b. During DJF, all simulations display a southward migration of the maximum heating area to approximately 25 °S, with an exception for KF that displays a southward extension of the maximum heating area. Low geopotential heights for KF and BMJ have not migrated southwards but linger at 20 °S, indicating that during DJF there is convection over the Angola region, which nonetheless, in not wholly attributable to thermal heating. For DJF also, KF simulates the lowest geopotential height fields.

Static stability profiles for ON are displayed in Fig. 6.3.7. As shown, low stability values, indicating areas over which the dry air is prone to uplift, are usually identified up to 700 hPa and in some cases reach up to 500 hPa. The cross section across latitudes (at 20.00 and 24.25 °E – CROSS 1 and CROSS 2 respectively), display a region of low static stability between 10 and 30 °S. The cross section across

longitudes (at 11.25 and 23.75 °S – CROSS 3 and CROSS 4 respectively) identify also regions of low static stability, which are indicative of the AL pressure system, that during ON is at its heat low phase. The results for DJF are very similar (not shown), with the difference that they display a clear southward migration of the low static stability values, indicative of the southward migration of the maximum heating area over the Kalahari region. The vertical profiles of cyclonic relative vorticity are displayed in Fig. 6.3.8. As indicated, regions of high cyclonic vorticity correspond to areas over which the AL is active during DJF, with high negative vorticity being present up to 400 hPa.

6.3.2 Intense rain event: 15-20 January 2013

Total precipitation amount during the intense rain event in concern (15-20 January 2013) is shown in Fig. 6.3.9a. All satellite and reanalysis products display high precipitation amounts exceeding 300 mm (cumulative over the 6-day period) over a region extending from the south of Mozambique at approximately 25 °S towards mainland SAF. This elongated region of high precipitation amount appears more intensely in MSWEP and ERA5. The WRF simulations display rather diverse results, with an exception for simulation using the NT and BMJ schemes. The NT scheme displays high precipitation amounts over the region identified in the satellite and reanalysis products, however, precipitation amounts are of smaller magnitude and shifted by approximately 2° more mainland. The agreement of the NT scheme with ERA5 can be attributed to the fact that ERA5 also employs the NT scheme for its cumulus parameterization. KF also displays high precipitation amounts over southern Mozambique, nonetheless, the high precipitation zone is shifted southwards and extends on a west to east orientation. GF does not replicate any distinct precipitation activity over southern Mozambique. The distinction of convective (RAINC) and non-convective (RAINNC) precipitation for the WRF simulations is displayed in Fig. 6.3.9b and Fig. 6.3.9c, respectively. Starting from the NT simulation, it becomes evident that precipitation activity over the region in concern (red box in Fig. 6.3.9), is almost entirely classified as convective. For the rest of the simulations, over the regions that experienced the highest precipitation amounts, rainfall was mainly classified as large-scale non-convective, indicating that the atmospheric conditions for the convection trigger were not satisfied. This can partly explain the reason why they were not able to reproduce the spatial pattern of the high precipitation event, as yielded by the NT scheme and the satellite and reanalysis products. This is particularly evident in the BMJ simulation.

A more detailed aspect concerning the diurnal cycle of precipitation during the period 15-20 January 2013 is displayed in Fig. 6.3.10. Timeseries depict cumulative precipitation within the region 15 – 30 °S and 25 – 35 °E (area sum of all pixels), using hourly outputs from the four WRF sensitivity simulations. ERA5 is also used for comparison. The satellite products did not provide hourly outputs and therefore were not included. Data are used in their original grid resolution (Fig. 6.3.10a). As shown, all WRF runs overestimate hourly precipitation compared to ERA5. Of particular interest is the simulation employing KF, which after 17/1 produces extremely high precipitation amounts. Timeseries extracted from the remapped WRF simulations to the ERA5 grid are shown in (Fig. 6.3.10b). As displayed, when WRF simulations are remapped (using conservative remapping) to the coarser ERA5 grid, precipitation amounts display a considerably smaller divergence from ERA5. As shown, ERA5 displays more abrupt peaks, indicating precipitation maxima during the day, that precede maximum from WRF simulations by 2 or 3 hours (for 15/1 at 12:00 UTC, 16/1 at 12:00 UTC, 17/1 at 12:00 UTC). n 18/1 and at 12:00 UTC cu-

mulative precipitation amounts within the area of interest are almost double in ERA5, compared to the WRF simulations, with an exception for KF, which displays even higher precipitation amounts that keep increasing for the next 12 hours. During 19/1 there are two maxima observed in ERA5, the first occurring at 12 UTC and the second at 23:00 UTC. All WRF simulations display a considerable difference in replicating these two intense events during 19/1. After performing a temporal Pearson correlation between ERA5 and each WRF simulation separately (144 temporal entries resulting from hourly outputs for the 6-day period), the simulation which ranked first was BMJ (r=0.87), NT ranked second (r=0.81), GF ranked third (r=0.52) and KF ranked last (r=0.35).

Vertical velocity (omega) calculated for the intense rain event period (averaged during 15-20 January 2013) for a region dissecting the area in concern 15 – 30 °S and 25 – 35 °E is shown in Fig. 6.3.11. The region over which the cross-section is plotted is shown on the map at the bottom of Fig. 6.3.11. Omega values are given in Pa/s with negative (positive) values indicating upward (downward) motion. As shown, all simulations display overall prevailing upward motion over the region, however, negative omega values are more severe in the experiments employing the BMJ and NT schemes. In the latter, upward motion is even more intense. CAPE and CIN values averaged during the period 15-20 January 2013 are shown in Fig. 6.3.12 (values are given in J/kg). As shown, KF and NT display the highest CAPE values, exceeding 900 J/kg. BMJ displays substantially smaller CAPE values, especially over mainland SAF. CIN values are high at the south and south-west coast of SAF in all simulations.

The synoptic state during the intense rain event (15-20 January 2013) is depicted in Fig. 6.3.13. As shown, at 850 hPa there is a strong current of air moving from the southeast of Madagascar (at 25 °S), which at 30 °S curves eastwards, before crossing the Mozambique Channel. An exception to that is the simulation employing the KF scheme. At 500 hPa, there is a strong westerly flow south of 25 °S in all simulations. Nonetheless, in the simulation employing the KF scheme, at 20 °E the strong westerly flow moves equatorward forming a meander that reaches 20 °S and then moves again poleward. As observed for the KF simulation, the region over which the meandering occurs coincides with an extended region of warming (contour of 328 K). This region of localized warming is present in the BMJ and GF simulations also, however in KF it obtains a considerably larger extend. The strong wind current (9 m/s) at 500 hPa in the KF simulation moving southeast towards the southern coast of Mozambique can be considered as a cause of vertical wind shear, prohibiting the vertical development of convective systems. At 200 hPa there is a strong westerly flow located between 25-30 °S reaching 22 m/s, indicative of the subtropical jet stream. At 200 hPa also, KF displays the largest warming (in comparison to the rest of the simulations).

As shown in Fig. 6.3.14, the KF simulation is considerably wetter (compared to the rest of the simulations) over the lower troposphere (until 700 hPa) over the continental part of SAF. In addition, the westerly wind current at the upper troposphere (200 hPa) indicating the subtropical jet stream is more severe with regards to magnitude and extent in the BMJ and NT simulations and considerably weaker in the KF simulation, as shown in Fig. 6.3.15. The vertical profiles of potential temperature at 25 °S and across all longitudes are depicted in Fig. 6.3.16. As shown, all simulations (except of KF) display a distinct bend of the isotherms at 20 °E, which is indicative of the heat low phase of the Angola Low pressure system that during January has already migrated polewards.

In Fig. 6.3.17 the moisture flux divergence at 850 hPa for the intense rain event is displayed. As shown

there is a strong cyclonic activity over the Angola region, with moisture entering SAF from the northwest SAF at 5-10 °S, associated with transport from the Atlantic Ocean. The moisture follows a clockwise trajectory and converges with additional moisture entering SAF from the Indian Ocean. Strongest low-level convergence is identified in the NT simulation, coinciding with the region of high precipitation amounts observed during the intense rain event.

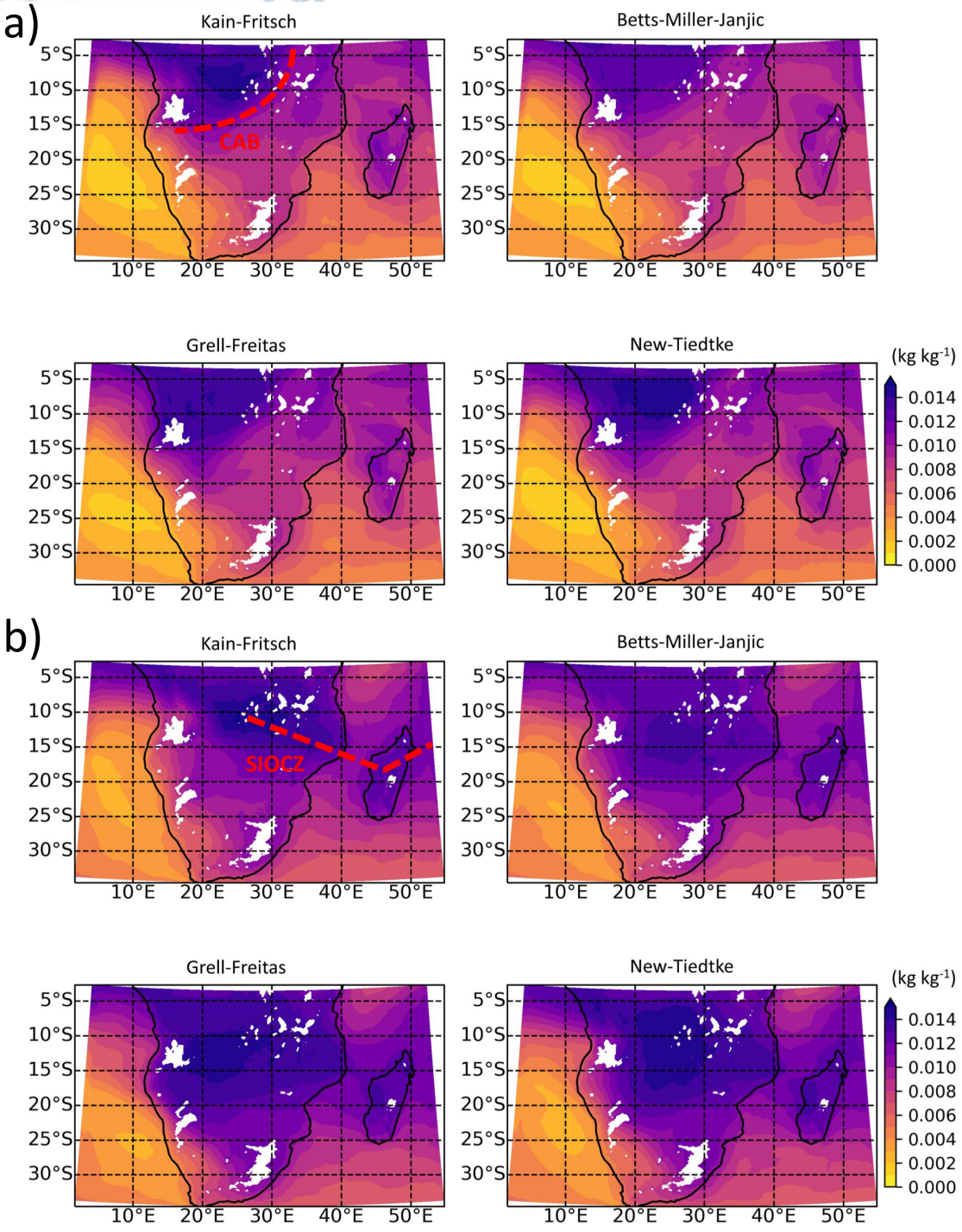

Figure 6.3.4: Specific humidity at 850 hPa (kg/kg) for ON (a) and for DJF (b).

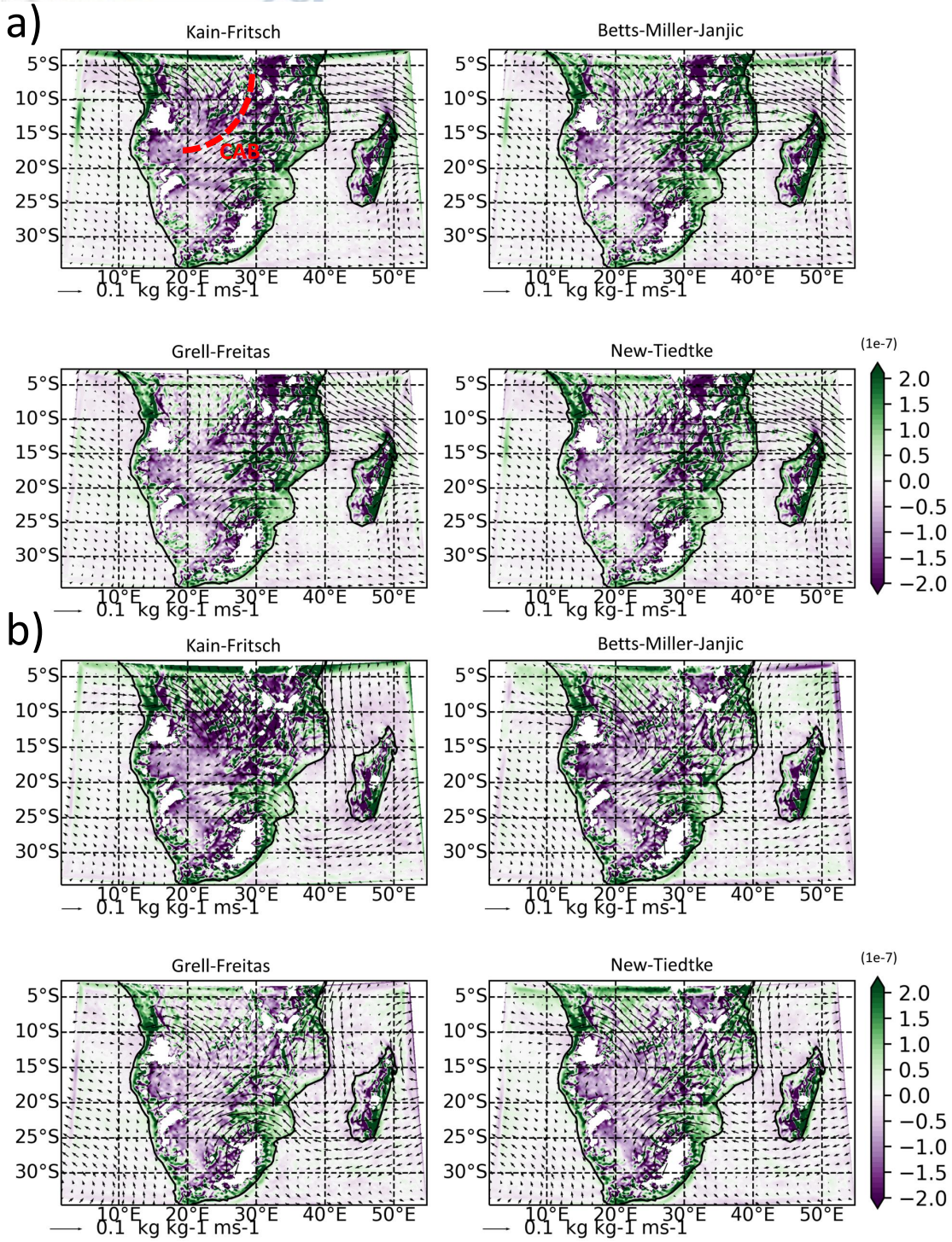

Figure 6.3.5: Moisture flux divergence at 850 hPa ($kg\ kg^{-1}\ m\ s^{-1}$) for ON (a) and for DJF (b).

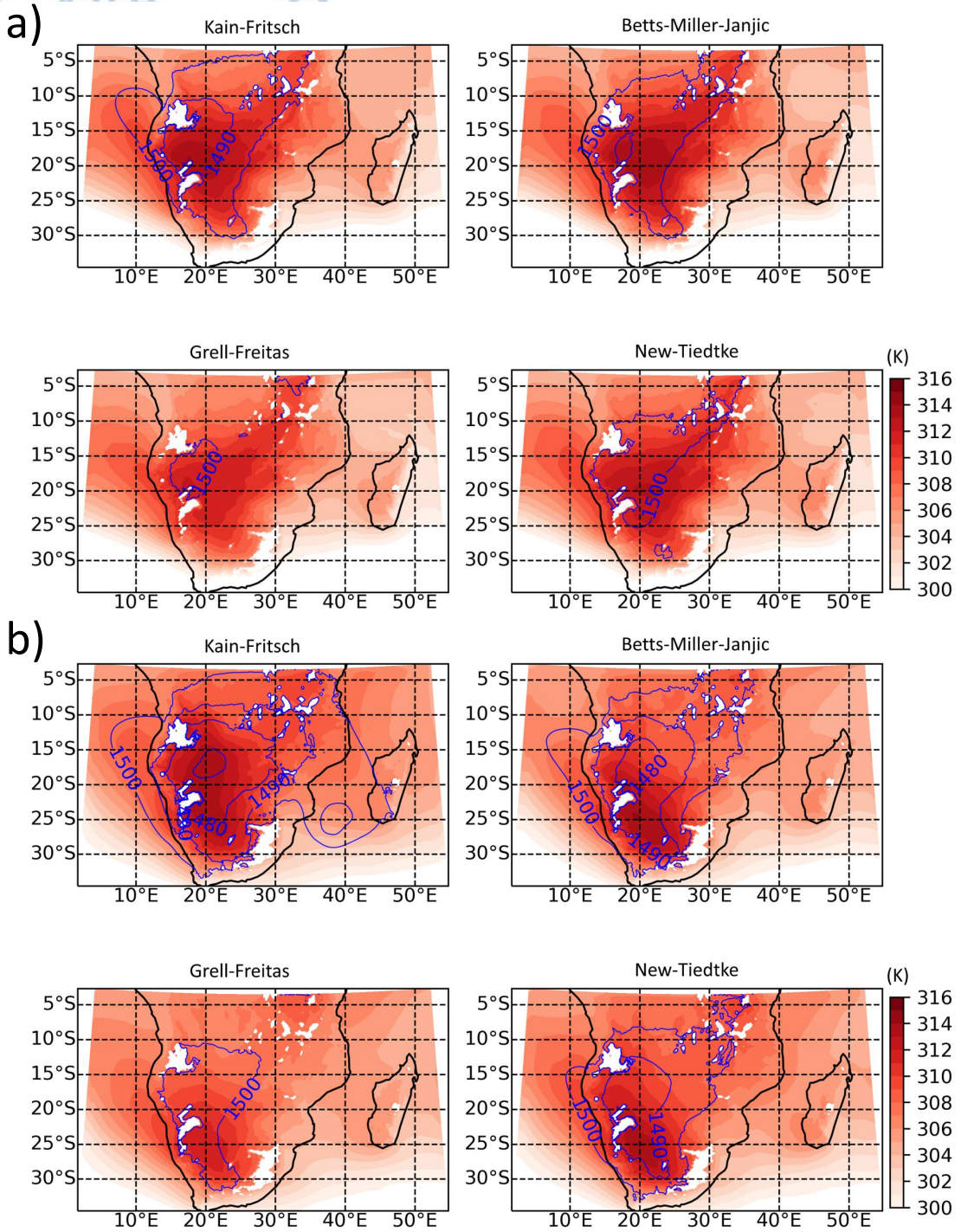

Figure 6.3.6: Potential temperature at 850 hPa (in K) shown with filled contours and geopotential height in contours (in m) for ON (a) and for DJF (b), for the four simulations performed.

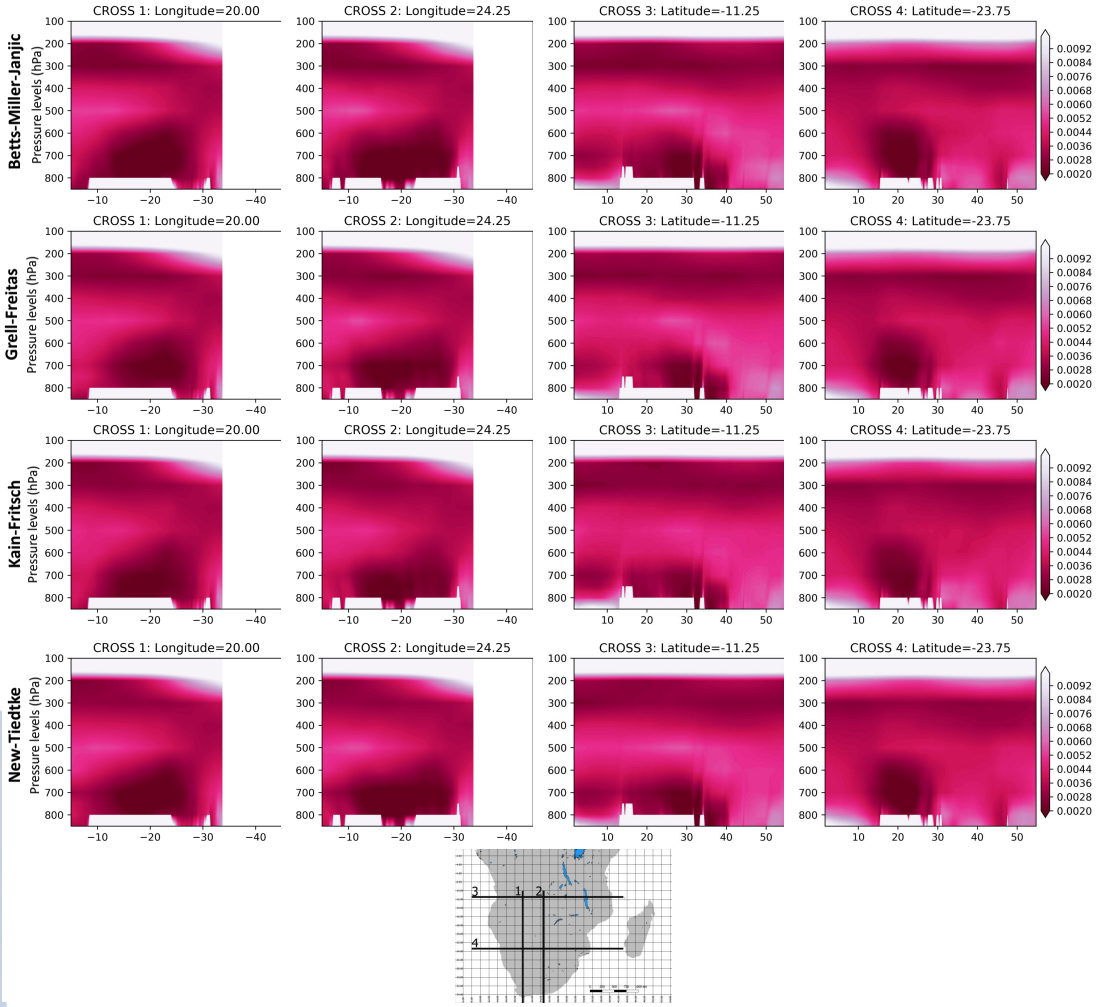

Figure 6.3.7: Static stability (/m) profiles for ON.

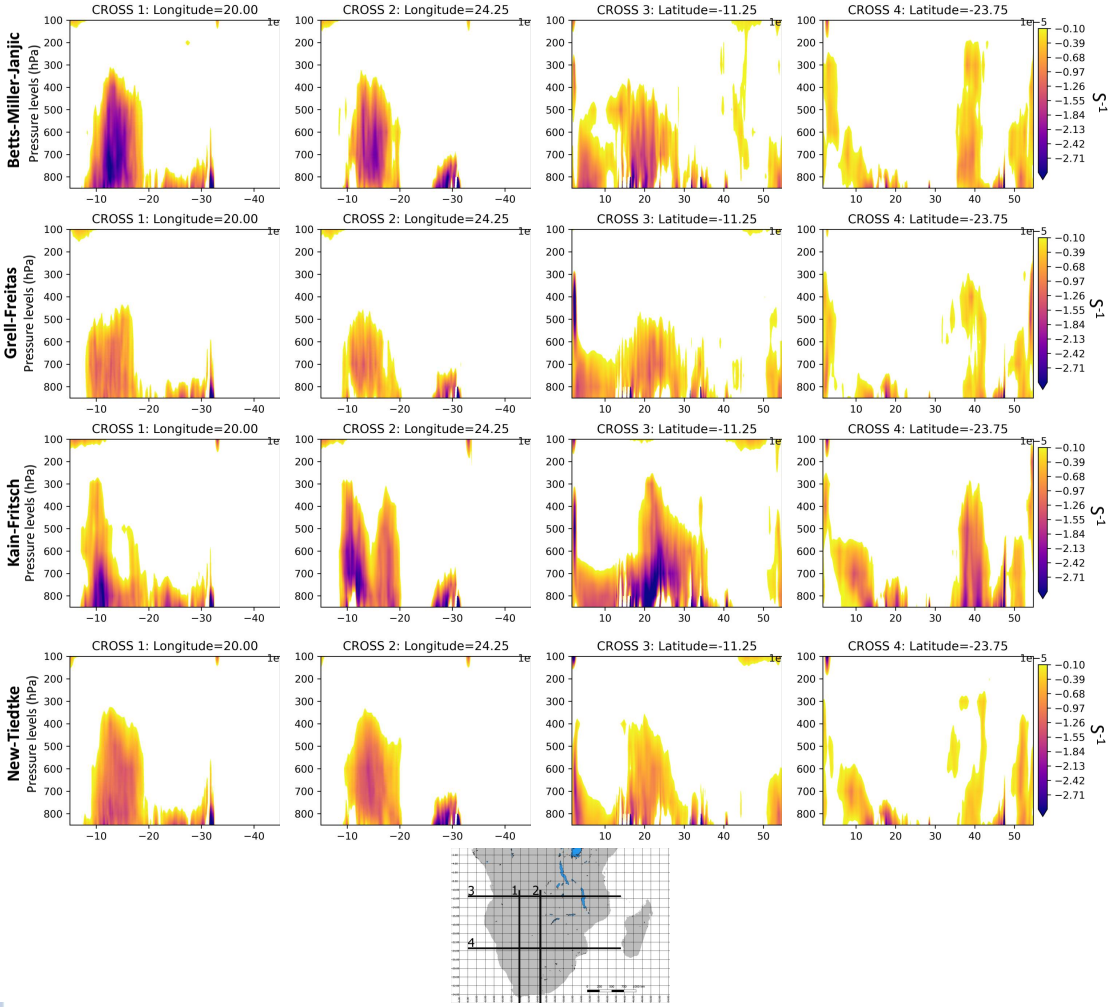

Figure 6.3.8: Cyclonic relative vorticity (s^{-1}) profiles for DJF.

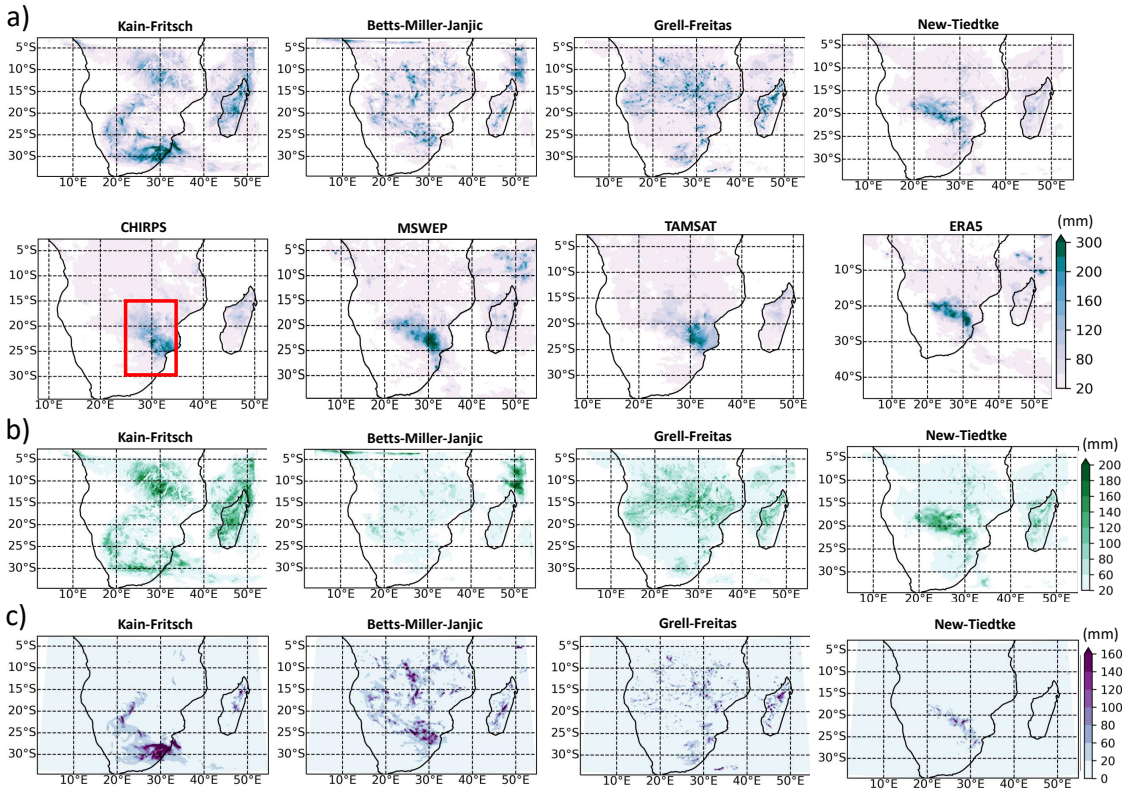

Figure 6.3.9: Total precipitation during the period 15-20 January 2013. a) Total precipitation in all simulations, satellite and reanalysis products, b) Convective precipitation (RAINC) in all WRF simulations, c) Large-scale non-convective precipitation (RAINNC) in all WRF simulations. All panels display cumulative precipitation in mm for the period 15-20 January 2013.

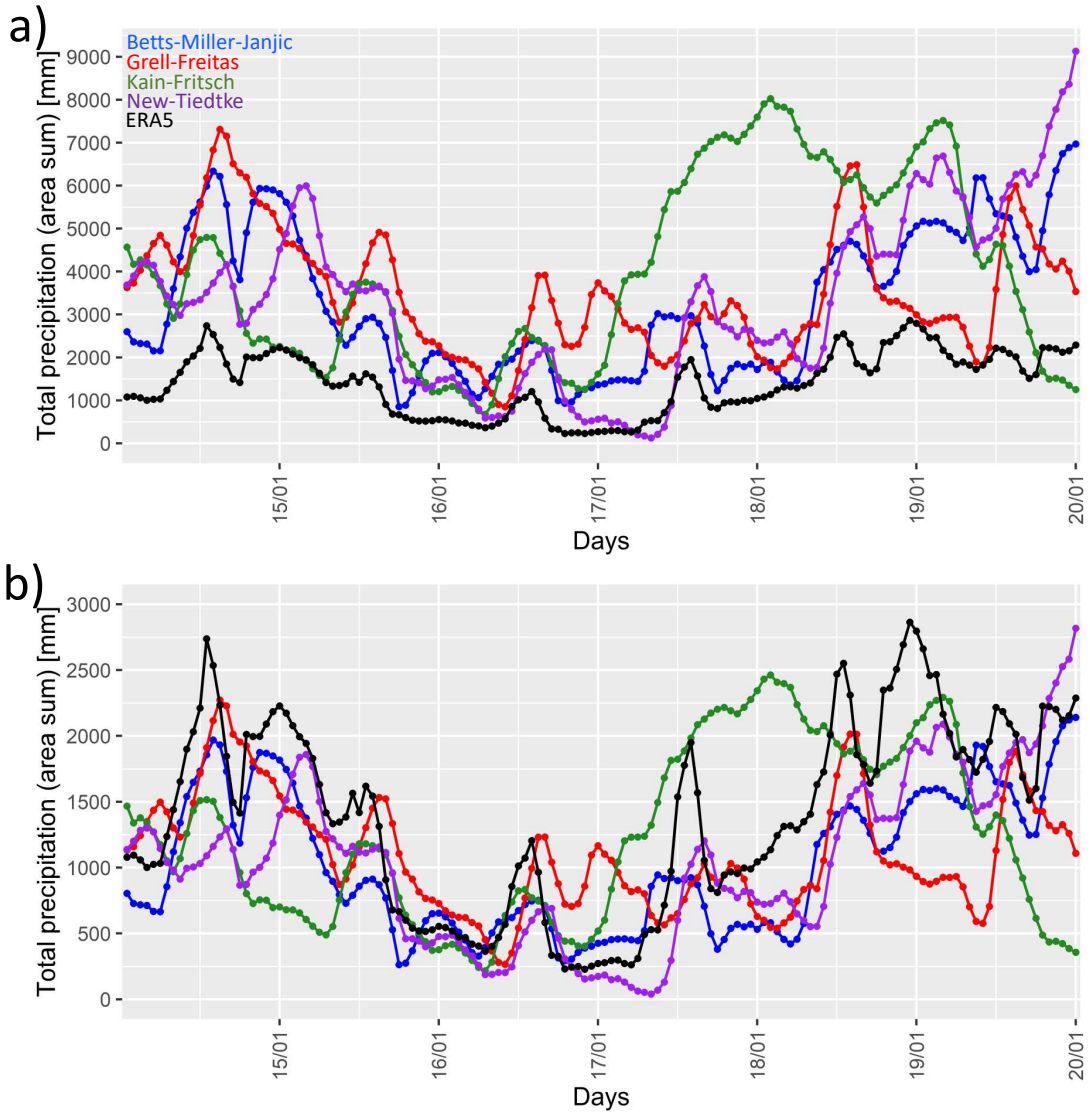

Figure 6.3.10: Hourly precipitation accumulated for all grid boxes defined within the area of interest 15 30 °S and 25 35 °E (area sum of all pixels) for the intense rain event during 15-20 January 2013. a) WRF simulation and ERA5 in their original grid, b) WRF simulations remapped to the grid of ERA5 (using conservative remapping).

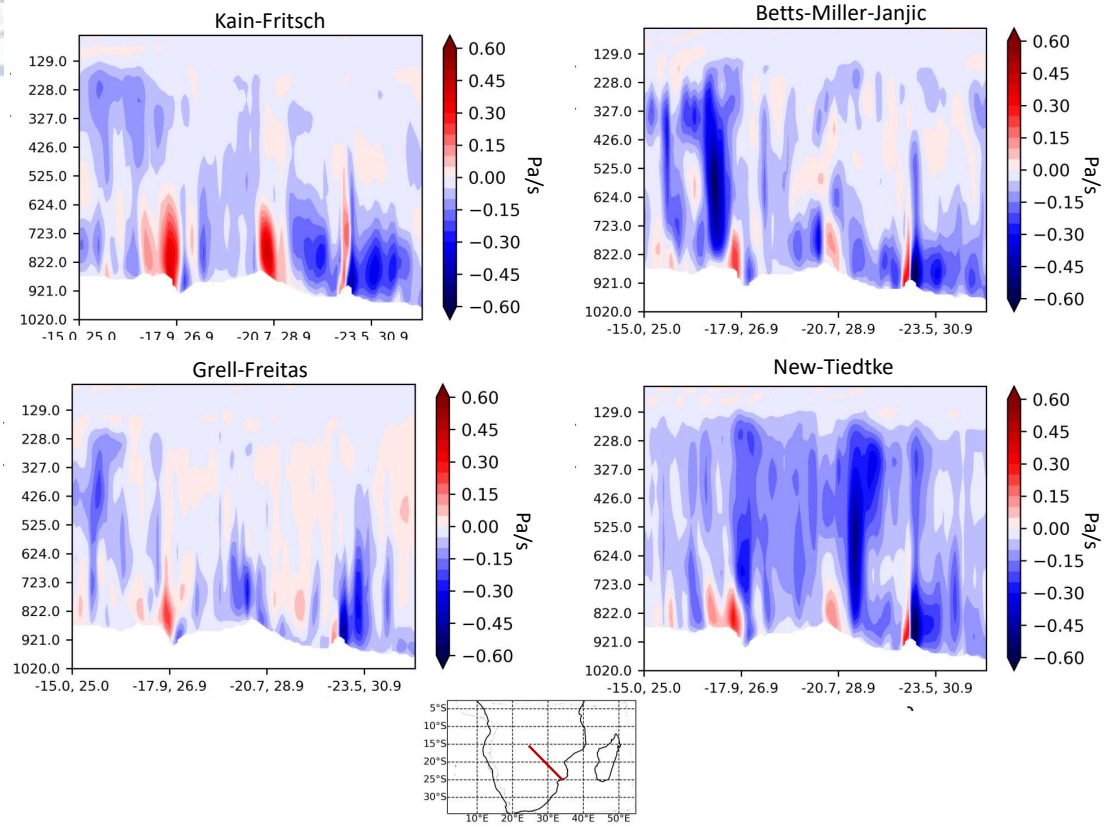

Figure 6.3.11: Hourly precipitation accumulated for all grid boxes defined within the area of interest 15 30 °S and 25 35 °E (area sum of all pixels) for the intense rain event during 15-20 January 2013. a) WRF simulation and ERA5 in their original grid, b) WRF simulations remapped to the grid of ERA5 (using conservative remapping).

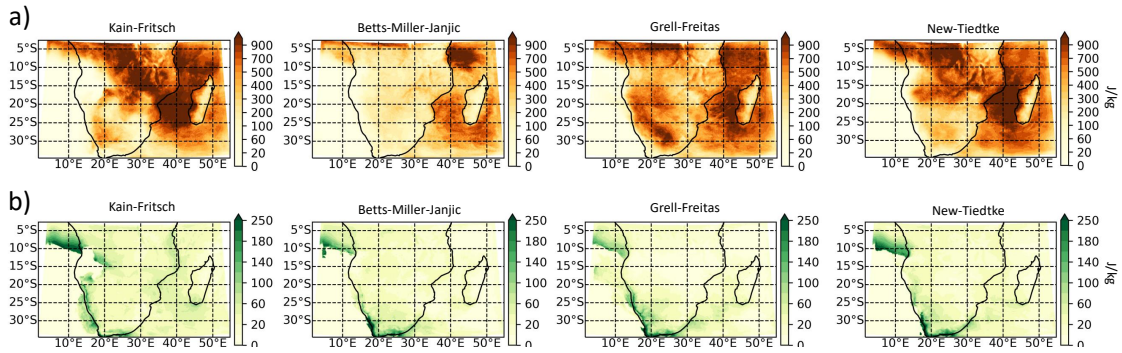

Figure 6.3.12: omega cross sections in Pa/s, averaged over the intense rain event period (15-20 January 2013).

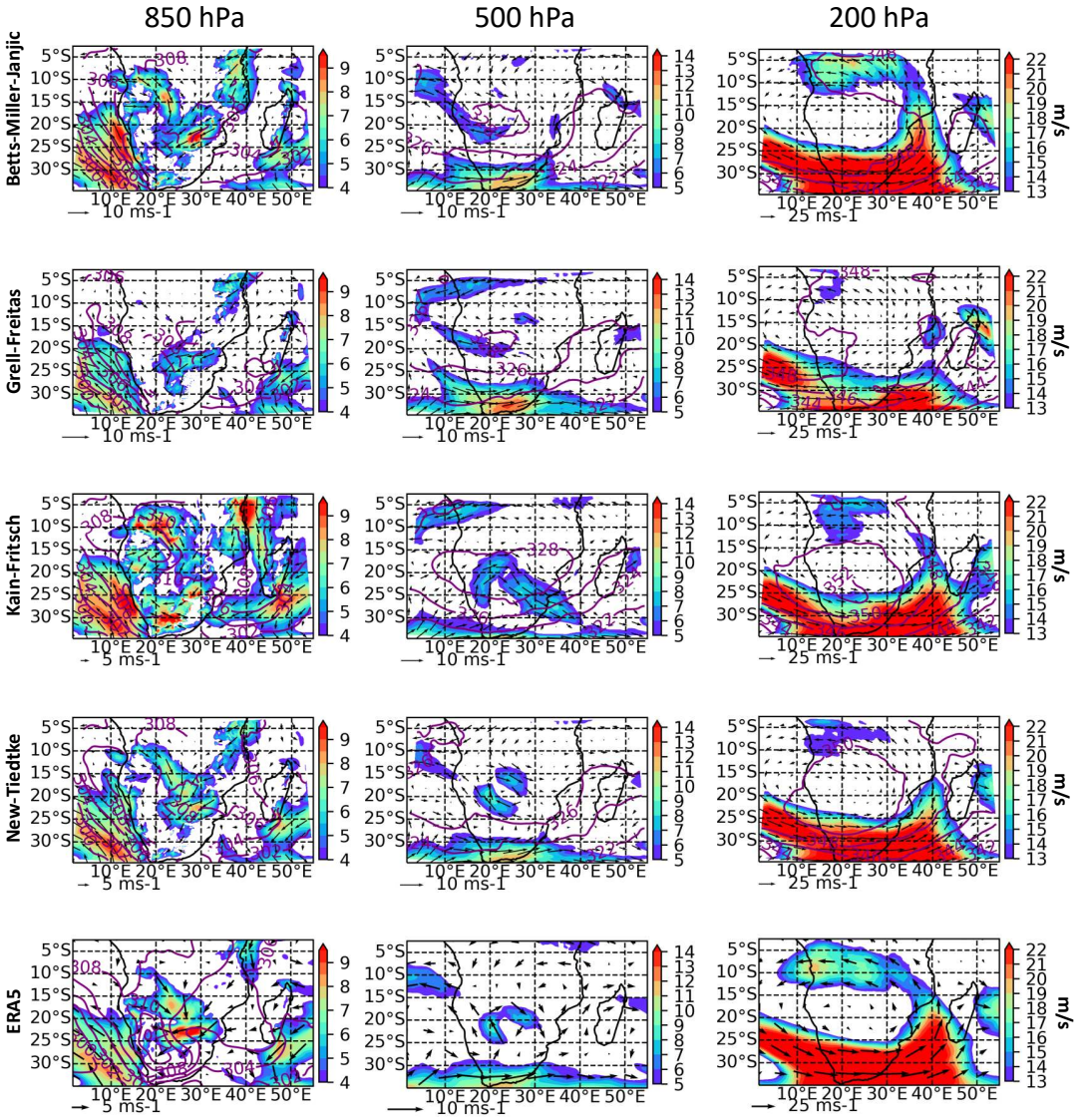

Figure 6.3.13: Wind speed (m/s) vectors and filled contours with potential temperature contours overlaid for the intense rain event (15-20 January 2013).

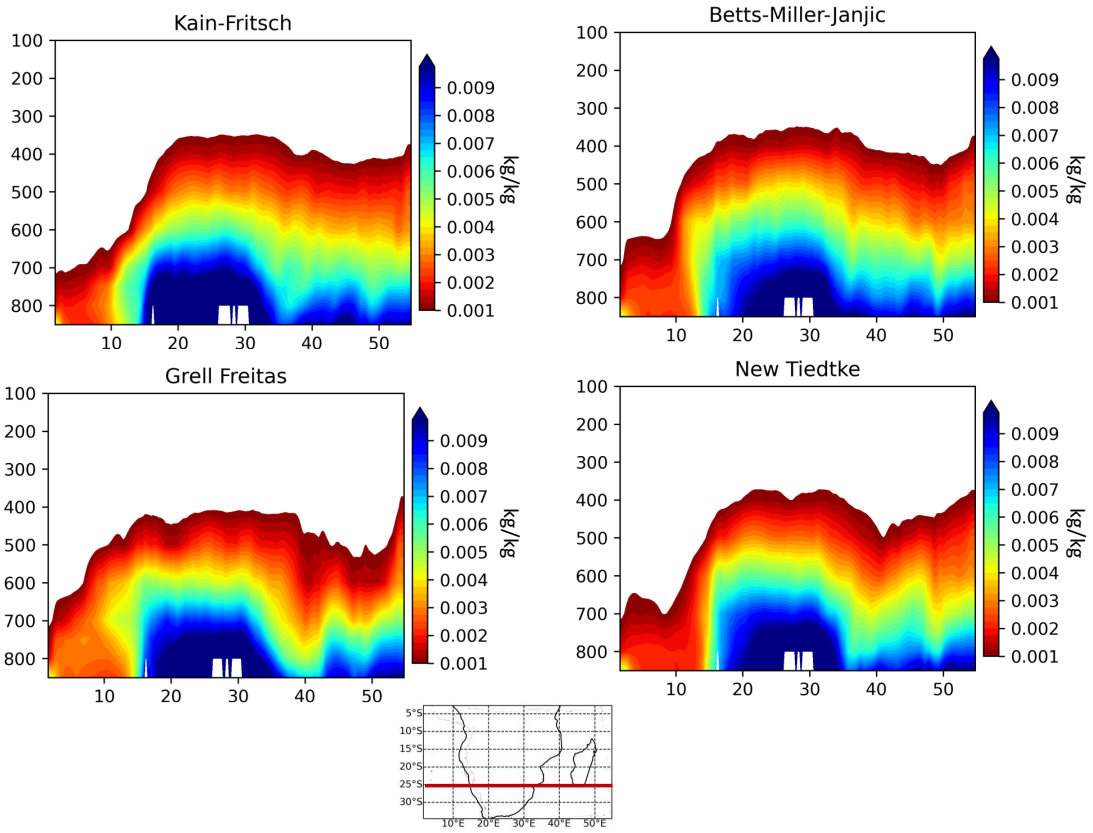

Figure 6.3.14: Specific humidity cross section (kg/kg) at 25 °S for the intense rain event (15-20 January 2013).

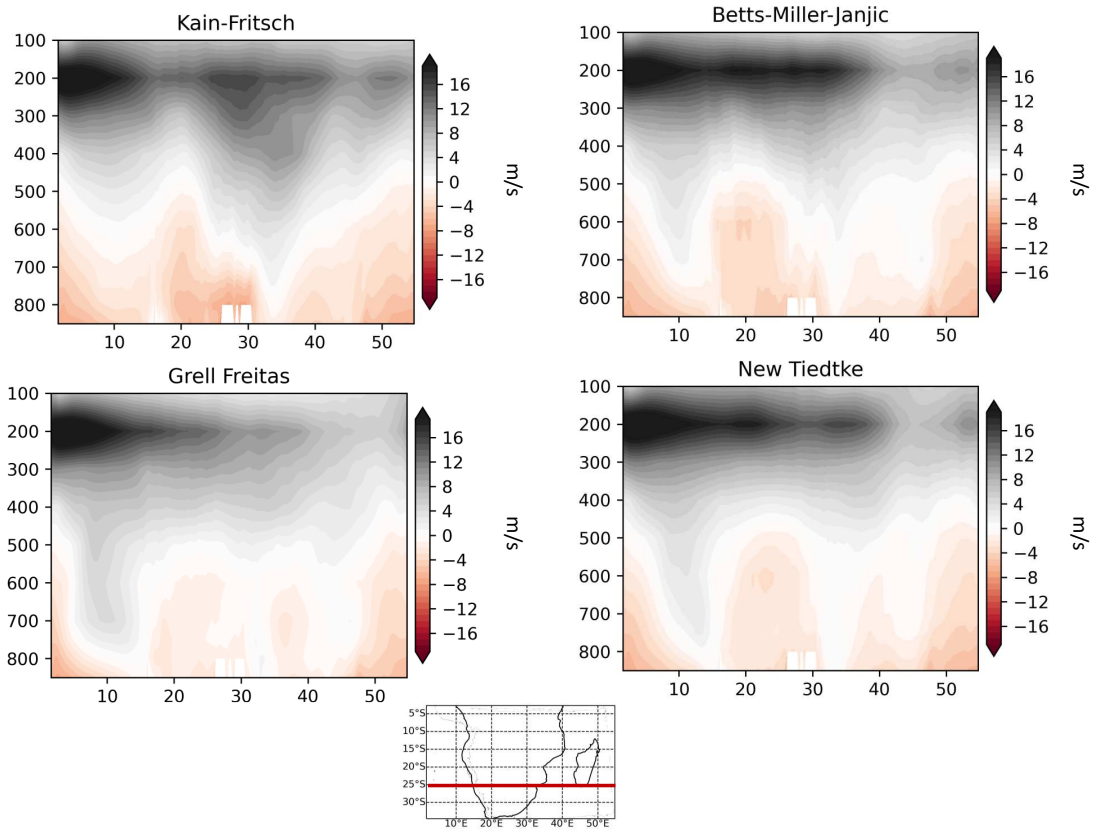

Figure 6.3.15: U wind cross section (m/s) at 25 °S for the intense rain event (15-20 January 2013).

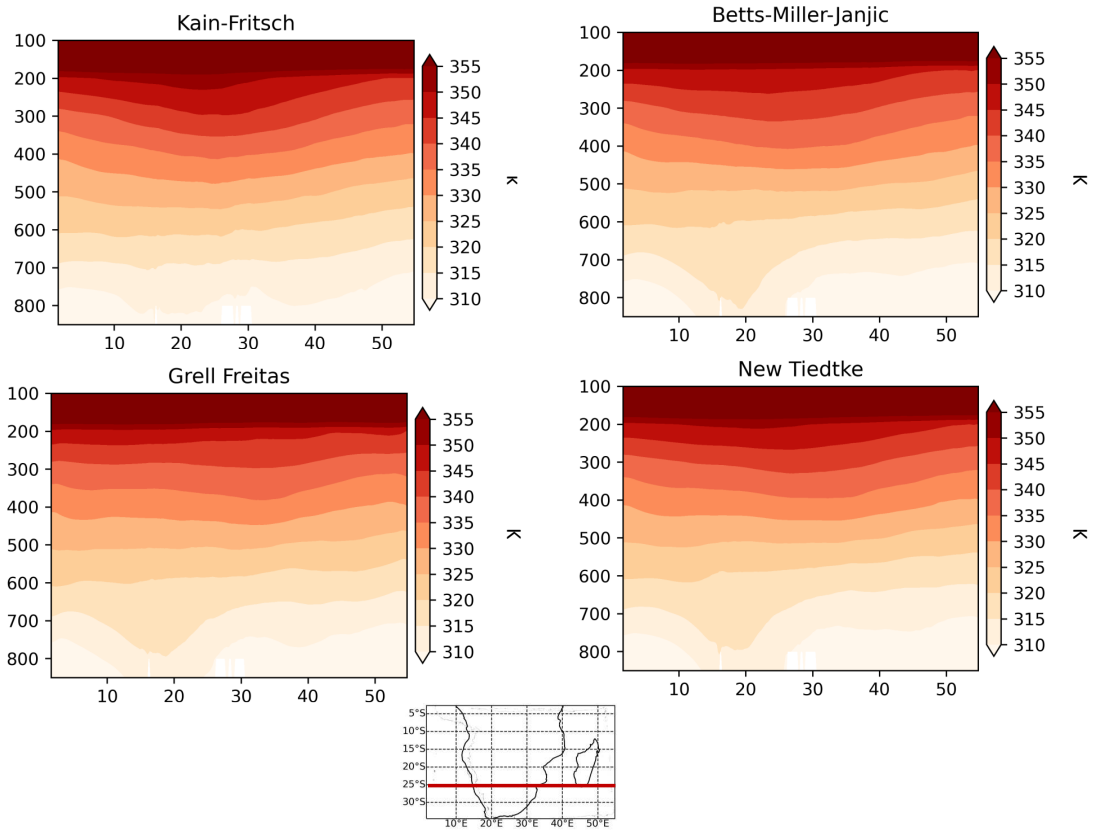

Figure 6.3.16: Potential temperature cross section at 25 °S for the intense rain event (15-20 January 2013).

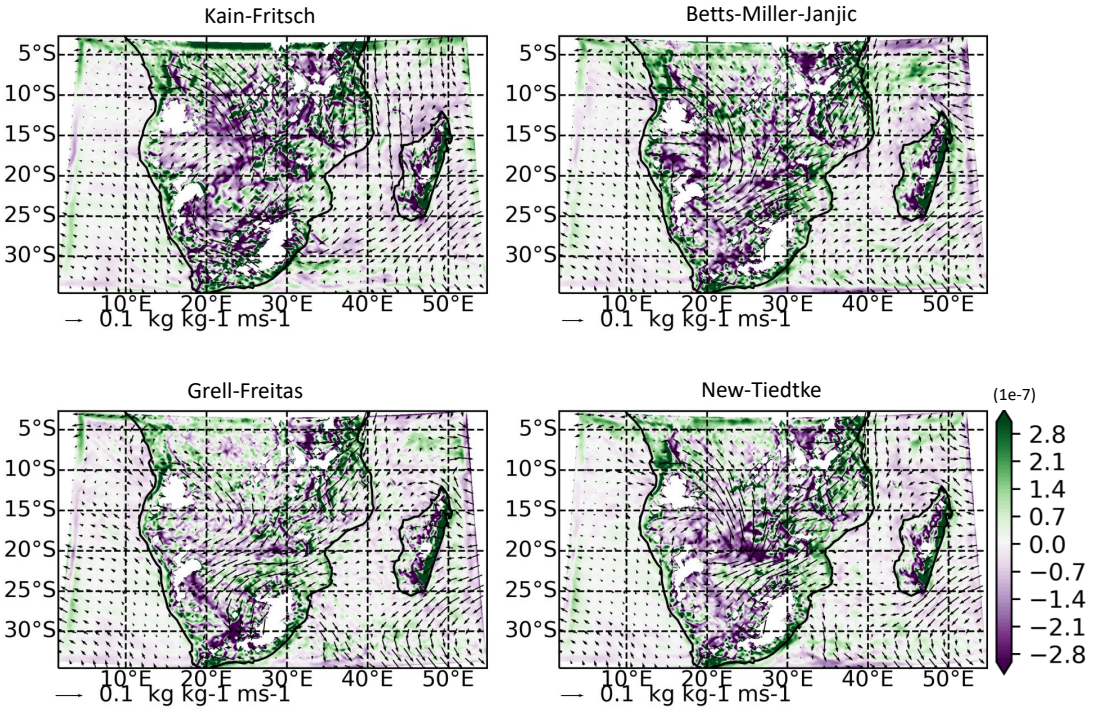

Figure 6.3.17: omega cross sections in Pa/s, averaged over the intense rain event period (15-20 January 2013).

6.4 Discussion

According to the literature, a cumulus scheme that may be suitable for climatic applications simulating conditions over a longer time period may not be optimal for short-time weather applications. In this work, the BMJ and NT schemes were found to more accurately simulate precipitation amounts during both the whole 2012-2013 rainy season and during the intense rain event (15-20 January 2013). More specifically during the whole rainy season, the daily timeseries of the BMJ and NT runs followed closely the satellite products and reanalysis, while KF and GF displayed systematic spikes, which were indicative of considerable overestimation in the daily precipitation amount. This was also consistent over the Angola region.

Also, when the intense rain event during 15-20 January 2013 was examined, simulations employing BMJ and NT schemes performed considerably close to ERA5 and the satellite products, while simulations using KF and GF displayed a different evolution in the total amount of precipitation that occurred within the area of interest, during the examined period (15-20 January 2013). However, it is noteworthy that this finding cannot be used as "evaluation" of the WRF simulations, since ERA5 was used as forcing field in all WRF experiments. It is also noteworthy, that although BMJ was the simulation performing closest to ERA5, when precipitation over the area in concern (15 – 30 °S and 25 – 35 °E – southern Mozambique) was classified into convective and non-convective for all WRF runs, BMJ was found to yield large-scale non-convective precipitation. BMJ and NT simulations displayed also the more intense and extended upward movement over the region in concern. In general, KF was found to produce excess rainfall and simulate strong low-level moisture converge over the Angola region. Also, the fact that overall BMJ performed satisfactorily, could be explained by the fact that the vertical atmospheric profiles on which the scheme is based, were calibrated over the tropical atmosphere, in order to optimally simulate deep convection.

Considering the fact that CPS have been shown to improve the simulation of convection in other parts of Africa, it is essential to investigate why such conclusions are not consistent with what has already been observed over regions of southern Africa (Keat et al. (2019)), over which the body of literature is considerably smaller compared to West Africa. Therefore, although higher resolution is shown to systematically provide more representative simulations of climatic conditions, it should not be used as a panacea on its own, but should be assessed on very local scales and focusing on specific phenomena.

7 Conclusions

7.1 Concluding remarks

In Chapter 2, precipitation climatology during the rainy season for the period 1986-2005 over southern African was examined, using the CORDEX-Africa, CMIP5 and CMIP6 ensembles. For the evaluation of all model ensembles, gridded observational data (CRU, UDEL, PREC/L, GPCC, CPC), reanalysis data (ERA5), and satellite data (ARC, CMAP, GPCP, CHIRPS, TAMSAT, PERSIANN) were used. In addition, an assessment of the uncertainty of the observational data was carried out. The results showed that regional climate simulations significantly improve monthly precipitation amounts in the southern African region (CORDEX-0.44), relative to global climate models from which they obtain lateral boundary conditions (CMIP5). Moreover, the higher spatial resolution of the CORDEX-Africa ensemble allows the more accurate representation of topography, compared to that in the coarse resolution global climate models. This results to the low-tropospheric moisture inflow from the tropical Indian Ocean being correctly blocked by the mountains in the Tanzania region and hindering it to progress towards the central southern African region, as is erroneously the case in the CMIP5 cluster ensemble. In addition, satellite estimates of rainfall over southern Africa (with an exception for the country of South Africa) were found to be highly uncertain, as they strongly depend on the network of rain gauges available.

In Chapter 3, an investigation was carried out concerning the impact of the lateral boundary conditions in the simulations of the CORDEX - Africa ensemble. The influence of the lateral boundary conditions on the regional simulations was relatively stronger during the months of Dec-Jan-Feb, when precipitation is mainly due to synoptic-scale systems entering the study region from the east and southeast. During DJF, synoptic-scale systems are steered by the mean atmospheric flow, while this effect was found to be weaker during Oct-Nov (early rainy season), as precipitation during these months is mainly due to thermal forcing. Convection due to thermal forcing is a result of land-atmosphere interactions that depend on the physical parameterization schemes of each respective regional model. In all months, and for the various subregions considered, the regional models systematically reduce the precipitation bias, relative to the driving global models.

In Chapter 4, the jet stream over the Southern Hemisphere was studied, with the aim to investigate the planetary-scale flow in the upper troposphere. Using annual data from reanalysis data (ERA5), the vertical wind shear of the jet stream was examined for the period 1950-2021, using zonal wind fields in the upper troposphere, and also using temperature data. The use of temperature data contributed to

the discussion of the effect of the thermal wind balance on the vertical wind shear of the jet stream. The study of the vertical wind shear of the jet stream, especially over the areas of maximum intensity (jet core), is performed because wind shear affects the surface atmospheric conditions in a manner opposite to that observed in the corresponding regions of the jet stream. Due to mass continuity, regions of the jet stream over which strong convergence (divergence) is observed, results in divergence (convergence) in the lower troposphere. The contribution of the thermal wind balance to the vertical wind shear of the jet stream over the Southern Hemisphere is considered important and in agreement to what has been shown in the literature for the Northern Hemisphere.

In Chapter 5, the analysis of the dynamical processes of the atmosphere in the CORDEX - Africa ensembles were discussed in relation to their effect on the simulated precipitation amounts during the rainy season. Moisture convergence at the surface significantly affects the amounts of precipitation in the wider Angola region, with the combination of moisture inflow from the southern Atlantic, from the southern Indian Ocean and the existence of cyclonic vorticity over the Angola region, co-formulating the conditions for the development of the Angola Low pressure system, which subsequently affects the amounts of precipitation observed in the region. The development of cyclonic vorticity in the Angola region is significantly influenced by the region's strong and sharply changing orography.

In Chapter 6, sensitivity experiments were performed using the WRF model, examining the impact of the cumulus parameterization scheme on several aspects of the southern Africa precipitation regime. The simulations showed that precipitation is significantly affected by the cumulus parameterization scheme and the results were consistent regardless of the study period (2012 - 2013 rainy season and intense rain event during the period 15-20 January 2013). More specifically, the Betts - Miller - Janjic and New - Tiedtke schemes produced the more realistic results (compared to satellite precipitation products and ERA5 reanalysis data) for the entire study period (rainy season 2012-2013), but also for the intense precipitation event, over south-eastern South Africa. The Kain - Fritsch scheme displayed an overestimation of precipitation throughout the study period.

7.2 Future Work

In Chapter 2, the CORDEX0.44 ensemble was found to substantially improve precipitation over southern Africa compared to the CMIP5 GCMs, however, this was not the case for the even higher resolution CORDEX0.22 ensemble (CORDEX-CORE). This observation testifies for the fact that higher resolution alone should not be considered as a panacea for the improvement of performance of an RCM. This may partly be caused by the fact that higher resolution simulations may reveal model deficiencies that were obscured in coarser resolution RCM simulations. Therefore, it would be necessary to examine in more detail all simulations participating CORDEX-CORE, before this ensemble is further populated by simulations from other Institutes and RCMs.

With respect to Chapter 4, it would be necessary to examine the sensitivity of the analysis to certain research choices, concerning the analysed timeseries, the input datasets, and their characteristics. More specifically, with regards to the Southern Hemisphere jet stream, it is imperative to consider in more detail the role that the ozone exerts on the stratospheric warming over Antarctica. Ozone depletion during the decades from 1960s to approximately the end of 1990s, resulted to the cooling of the

stratosphere over Antarctica. However, following the drastic regulations proposed through the Montreal Protocol in 1987, stratospheric ozone levels over Antarctica have been observed to gradually recover. Therefore, one important topic to consider, is that the analysis described in Chapter 4 is repeated using two timeseries, one employing data before 2000 and one by employing data after 2000. The year 2000 is used as an indicator year within the timeseries for ozone recovery. Moreover, an additional work that should be performed is related to the fact that the reanalysis datasets do not incorporate satellite data before the 1980s, which is very likely to reduce their accuracy. Here, the analysis described in Chapter 4 utilized annual data from 1950 to 2021. For this reason it would be necessary to further repeat the analysis using two timeseries, one for the period 1950-1980 (pre-satellite era) and one by employing data for the period 1980-2021 (post satellite era). In addition, the stratospheric warming as a result of ozone depletion displays a strong seasonal cycle. For this reason it would be imperative to repeat the analysis described in Chapter 4 using seasonal data, instead of annual. Moreover, the analysis should also be performed using other reanalysis products, besides ERA5, to account for the uncertainty introduced due to the dataset used. Additionally, the sensitivity of the calculation of the thermal wind balance should be examined with respect to the spatial resolution of the input dataset. This can be examined with a series of sensitivity tests in which ERA5 is remapped to coarser resolution grids. Lastly, it would be necessary to expand the analysis of Lee et al. (2019) for the whole Northern Hemisphere also (and not just the northern Atlantic sector). In this way, a fair comparison between findings concerning wind speed and wind shear trends between the two hemispheres could be performed.

In Chapter 5 and concerning the dynamical analysis in the CORDEX-Africa ensemble, certain conclusions are drawn about the impact of topography on relative vorticity over the Angola region. This statement could be experimentally verified or refuted using a series of sensitivity experiment in WRF. The sensitivity experiments would be concerned with removing or reducing elevation from over the Angola region and examine the impact of these changes on the relative vorticity field. Moreover, the analysis performed in Chapter 5 using the historical simulations of the CORDEX-Africa ensemble could be also performed for the future under RCP8.5, in order to investigate how the atmospheric dynamics will change over the study region, and how the changes in dynamics correspond to future changes in precipitation.

Concerning the work about the cumulus sensitivity experiments over SAF described in Chapter 6, future work towards understanding more aspects of convection processes over southern Africa, would involve the use of the New Simplified Arakawa Schubert (NSAS) scheme, whose convection trigger function is tied to the large-scale dynamics. Further insights could also be gained from an analysis of precipitation in terms of frequency of occurrence (testing the cumulus scheme's ability to trigger precipitation) and the intensity of precipitation when it does occur (testing the schemes ability to correctly determine the amount of moisture to remove from the atmosphere and deliver as precipitation). Lastly, convective processes over southern Africa could be more in depth analyzed through a Convection Permitting Simulation at very high resolution.

Bibliography

Sabina Abba Omar and Babatunde J. Abiodun. 2017. How well do CORDEX models simulate extreme rainfall events over the East Coast of South Africa? *Theoretical and Applied Climatology*, 128(1):453–464.

Sabina Abba Omar and Babatunde J. Abiodun. 2021. Simulating the influence of topography on cut-off lows over Southern Africa. *International Journal of Climatology*, 41(S1):E2231–E2243. _eprint: https://onlinelibrary.wiley.com/doi/pdf/10.1002/joc.6842.

Babatunde J. Abiodun, Nokwethaba Makhanya, Brilliant Petja, Abayomi A. Abatan, and Philip G. Oguntunde. 2019. Future projection of droughts over major river basins in Southern Africa at specific global warming levels. *Theoretical and Applied Climatology*, 137(3):1785–1799.

Babatunde J. Abiodun, Tlakale O. Mogebisa, Brilliant Petja, Abayomi A. Abatan, and Takong R. Roland. 2020. Potential impacts of specific global warming levels on extreme rainfall events over southern Africa in CORDEX and NEX-GDDP ensembles. *International Journal of Climatology*, 40(6):3118–3141. _eprint: https://onlinelibrary.wiley.com/doi/pdf/10.1002/joc.6386.

Adeyemi A. Adebiyi and Paquita Zuidema. 2016. The role of the southern African easterly jet in modifying the southeast Atlantic aerosol and cloud environments. *Quarterly Journal of the Royal Meteorological Society*, 142(697):1574–1589.

Robert F. Adler, Guojun Gu, and George J. Huffman. 2012. Estimating Climatological Bias Errors for the Global Precipitation Climatology Project (GPCP). *Journal of Applied Meteorology and Climatology*, 51(1):84–99. Publisher: American Meteorological Society.

AFDB. 2019. Southern Africa Economic Outlook 2019. Technical report, African Development Bank.

Lisa V. Alexander, Margot Bador, Rémy Roca, Steefan Contractor, Markus G. Donat, and Phuong Loan Nguyen. 2020. Intercomparison of annual precipitation indices and extremes over global land areas from in situ, space-based and reanalysis products. *Environmental Research Letters*, 15(5):055002. Publisher: IOP Publishing.

Hamed Ashouri, Kuo-Lin Hsu, Soroosh Sorooshian, Dan K. Braithwaite, Kenneth R. Knapp, L. Dewayne Cecil, Brian R. Nelson, and Olivier P. Prat. 2015. PERSIANN-CDR: Daily Precipitation Climate Data Record from Multisatellite Observations for Hydrological and Climate Studies. *Bulletin of the American Meteorological Society*, 96(1):69–83. Publisher: American Meteorological Society.

Getachew Tesfaye Ayehu, Tsegaye Tadesse, Berhan Gessesse, and Tufa Dinku. 2018. Validation of new satellite rainfall products over the Upper Blue Nile Basin, Ethiopia. *Atmospheric Measurement Techniques*, 11(4):1921–1936. Publisher: Copernicus GmbH.

Carlo Azzarri and Sara Signorelli. 2020. Climate and poverty in Africa South of the Sahara. *World Development*, 125:104691.

Nikolina Ban, Cecile Caillaud, Erika Coppola, Emanuela Pichelli, Stefan Sobolowski, Marianna Adinolfi, Bodo Ahrens, Antoinette Alias, Ivonne Anders, Sophie Bastin, Danijel Belusic, Segolene Berthou, Erwan Brisson, Rita M. Cardoso, Steven Chan, Ole Bossing Christensen, Jesus Fernandez, Lluis Fita, Thomas Frisius, Goran Gasparac, Filippo Giorgi, Klaus Goergen, Jan Erik Haugen, Oivind Hodnebrog, Stergios Kartsios, Eleni Katragkou, Elizabeth J. Kendon, Klaus Keuler, Alvaro Lavin-Gullon, Geert Lenderink, David Leutwyler, Torge Lorenz, Douglas Maraun, Paola Mercogliano, Josipa Milovac, Hans-Juergen Panitz, Mario Raffa, Armelle Reca Remedio, Christoph Schar, Pedro M.M Soares, Lidija Srnec, Birthe Marie Steensen, Paolo Stocchi, Merja H. Tolle, Heimo Truhetz, Jesus Vergara-Temprado, Hylke de Vries, Kirsten Warrach-Sagi, Volker Wulfmeyer, and Marjanne Zander. 2021. The first multi-model ensemble of regional climate simulations at the kilometer-scale resolution, Part I: Evaluation of precipitation.

Justin Bandoro, Susan Solomon, Aaron Donohoe, David W. J. Thompson, and Benjamin D. Santer. 2014. Influences of the Antarctic Ozone Hole on Southern Hemispheric Summer Climate Change. *Journal of Climate*, 27(16):6245–6264. Publisher: American Meteorological Society Section: Journal of Climate.

Elizabeth A Barnes and James A Screen. 2015. The impact of Arctic warming on the midlatitude jet-stream: Can it? Has it? Will it? *WIREs Climate Change*, 6(3):277–286. _eprint: https://onlinelibrary.wiley.com/doi/pdf/10.1002/wcc.337.

Elizabeth A. Barnes and Isla R. Simpson. 2017. Seasonal Sensitivity of the Northern Hemisphere Jet Streams to Arctic Temperatures on Subseasonal Time Scales. *Journal of Climate*, 30(24):10117–10137. Publisher: American Meteorological Society Section: Journal of Climate.

Hylke E. Beck, Eric F. Wood, Ming Pan, Colby K. Fisher, Diego G. Miralles, Albert I. J. M. van Dijk, Tim R. McVicar, and Robert F. Adler. 2019. MSWEP V2 Global 3-Hourly 0.1° Precipitation: Methodology and Quantitative Assessment. *Bulletin of the American Meteorological Society*, 100(3):473–500. Publisher: American Meteorological Society Section: Bulletin of the American Meteorological Society.

M. Bentsen, I. Bethke, J. B. Debernard, T. Iversen, A. Kirkevåg, Ø Seland, H. Drange, C. Roelandt, I. A. Seierstad, C. Hoose, and J. E. Kristjánsson. 2013. The Norwegian Earth System Model, NorESM1-M – Part 1: Description and basic evaluation of the physical climate. *Geoscientific Model Development*, 6(3):687–720. Publisher: Copernicus GmbH.

Fredrik Boberg and Jens H. Christensen. 2012. Overestimation of Mediterranean summer temperature projections due to model deficiencies. *Nature Climate Change*, 2(6):433–436. Number: 6 Publisher: Nature Publishing Group.

Stephan Bojinski, Michel Verstraete, Thomas C. Peterson, Carolin Richter, Adrian Simmons, and Michael Zemp. 2014. The Concept of Essential Climate Variables in Support of Climate Research, Applications, and Policy. *Bulletin of the American Meteorological Society*, 95(9):1431–1443. Publisher: American Meteorological Society Section: Bulletin of the American Meteorological Society.

Mary-Jane M. Bopape, Hipolito Cardoso, Robert S. Plant, Elelwani Phaduli, Hector Chikoore, Thando Ndarana, Lino Khalau, and Edward Rakate. 2021. Sensitivity of Tropical Cyclone Idai Simulations to Cumulus Parametrization Schemes. *Atmosphere*, 12(8):932. Number: 8 Publisher: Multidisciplinary Digital Publishing Institute.

Damien Boulard, Benjamin Pohl, Julien Crétat, Nicolas Vigaud, and Thanh Pham-Xuan. 2013. Downscaling large-scale climate variability using a regional climate model: the case of ENSO over Southern Africa. *Climate Dynamics*, 40(5):1141–1168.

G. E. P. Box. 1979. Robustness in the Strategy of Scientific Model Building. In ROBERT L. Launer and GRAHAM N. Wilkinson, editors, *Robustness in Statistics*, pages 201–236. Academic Press.

Noah D. Brenowitz, Tom Beucler, Michael Pritchard, and Christopher S. Bretherton. 2020. Interpreting and Stabilizing Machine-Learning Parametrizations of Convection. *Journal of the Atmospheric Sciences*, 77(12):4357–4375. Publisher: American Meteorological Society Section: Journal of the Atmospheric Sciences.

Noah D. Brenowitz and Christopher S. Bretherton. 2019. Spatially Extended Tests of a Neural Network Parametrization Trained by Coarse-Graining. *Journal of Advances in Modeling Earth Systems*, 11(8):2728–2744. _eprint: https://onlinelibrary.wiley.com/doi/pdf/10.1029/2019MS001711.

Marisa Casale, Scott Drimie, Timothy Quinlan, and Gina Ziervogel. 2010. Understanding vulnerability in southern Africa: comparative findings using a multiple-stressor approach in South Africa and Malawi. *Regional Environmental Change*, 10(2):157–168.

CCCma. 2017. Environment and Climate Change Canada - Climate Change - CanESM2. Last Modified: 2017-05-31 Library Catalog: www.ec.gc.ca.

Matthew Chantry, Hannah Christensen, Peter Dueben, and Tim Palmer. 2021. Opportunities and challenges for machine learning in weather and climate modelling: hard, medium and soft AI. *Philosophical Transactions of the Royal Society A: Mathematical, Physical and Engineering Sciences*, 379(2194):20200083. Publisher: Royal Society.

Mingyue Chen, Wei Shi, Pingping Xie, Viviane B. S. Silva, Vernon E. Kousky, R. Wayne Higgins, and John E. Janowiak. 2008. Assessing objective techniques for gauge-based analyses of global daily precipitation. *Journal of Geophysical Research: Atmospheres*, 113(D4). _eprint: https://agupubs.onlinelibrary.wiley.com/doi/pdf/10.1029/2007JD009132.

Mingyue Chen, Pingping Xie, John E. Janowiak, and Phillip A. Arkin. 2002. Global Land Precipitation: A 50-yr Monthly Analysis Based on Gauge Observations. *Journal of Hydrometeorology*, 3(3):249–266. Publisher: American Meteorological Society.

Paul S. Chinowsky, Amy E. Schweikert, Niko L. Strzepek, and Ken Strzepek. 2015. Infrastructure and climate change: a study of impacts and adaptations in Malawi, Mozambique, and Zambia. *Climatic Change*, 130(1):49–62.

Ole B. Christensen and Erik Kjellström. 2020. Partitioning uncertainty components of mean climate and climate change in a large ensemble of European regional climate model projections. *Climate Dynamics*, 54(9):4293–4308.

Ole Bøssing Christensen, Martin Drews, Jens Hesselbjerg Christensen, Klaus Dethloff, Klaus Ketelsen, Ines Hebestadt, and Anette Rinke. 2007. The HIRHAM Regional Climate Model Version 5. Technical report 06-17, Danish Meteorological Institute, Copenhagen.

Kyle R. Clem, Ryan L. Fogt, John Turner, Benjamin R. Lintner, Gareth J. Marshall, James R. Miller, and James A. Renwick. 2020. Record warming at the South Pole during the past three decades. *Nature Climate Change*, 10(8):762–770. Number: 8 Publisher: Nature Publishing Group.

Judah Cohen, James A. Screen, Jason C. Furtado, Mathew Barlow, David Whittleston, Dim Coumou, Jennifer Francis, Klaus Dethloff, Dara Entekhabi, James Overland, and Justin Jones. 2014. Recent Arctic amplification and extreme mid-latitude weather. *Nature Geoscience*, 7(9):627–637. Number: 9 Publisher: Nature Publishing Group.

W. J. Collins, N. Bellouin, M. Doutriaux-Boucher, N. Gedney, P. Halloran, T. Hinton, J. Hughes, C. D. Jones, M. Joshi, S. Liddicoat, G. Martin, F. O'Connor, J. Rae, C. Senior, S. Sitch, I. Totterdell, A. Wiltshire, and S. Woodward. 2011. Development and evaluation of an Earth-System model – HadGEM2. *Geoscientific Model Development*, 4(4):1051–1075. Publisher: Copernicus GmbH.

Declan Conway, Emma Archer van Garderen, Delphine Deryng, Steve Dorling, Tobias Krueger, Willem Landman, Bruce Lankford, Karen Lebek, Tim Osborn, Claudia Ringler, James Thurlow, Tingju Zhu, and Carole Dalin. 2015. Climate and southern Africa's water–energy–food nexus. *Nature Climate Change*, 5(9):837–846. Number: 9 Publisher: Nature Publishing Group.

Erika Coppola, Francesca Raffaele, Filippo Giorgi, Graziano Giuliani, Gao Xuejie, James M. Ciarlo, Taleena Rae Sines, José Abraham Torres-Alavez, Sushant Das, Fabio di Sante, Emanuela Pichelli, Russell Glazer, Sebastian Karl Müller, Sabina Abba Omar, Moetasim Ashfaq, Melissa Bukovsky, E.-S. Im, Daniela Jacob, Claas Teichmann, Armelle Remedio, Thomas Remke, Arne Kriegsmann, Katharina Bülow, Torsten Weber, Lars Buntemeyer, Kevin Sieck, and Diana Rechid. 2021. Climate hazard indices projections based on CORDEX-CORE, CMIP5 and CMIP6 ensemble. *Climate Dynamics*, 57(5):1293–1383.

COSMO. 2020. COSMO core documentation.

A. Creese and R. Washington. 2016. Using qflux to constrain modeled Congo Basin rainfall in the CMIP5 ensemble. *Journal of Geophysical Research: Atmospheres*, 121(22):13,415–13,442. _eprint: https://onlinelibrary.wiley.com/doi/pdf/10.1002/2016JD025596.

Julien Crétat, Clémence Macron, Benjamin Pohl, and Yves Richard. 2011. Quantifying internal variability in a regional climate model: a case study for Southern Africa. *Climate Dynamics*, 37(7):1335–1356.

Julien Crétat, Benjamin Pohl, Bastien Dieppois, Ségolène Berthou, and Julien Pergaud. 2019. The Angola Low: relationship with southern African rainfall and ENSO. *Climate Dynamics*, 52(3):1783–1803.

Julien Crétat, Benjamin Pohl, Yves Richard, and Philippe Drobinski. 2012. Uncertainties in simulating regional climate of Southern Africa: sensitivity to physical parameterizations using WRF. *Climate Dynamics*, 38(3):613–634.

Joseph Daron, Laura Burgin, Tamara Janes, Richard G. Jones, and Christopher Jack. 2019. Climate process chains: Examples from southern Africa. *International Journal of Climatology*, 39(12):4784–4797. _eprint: https://rmets.onlinelibrary.wiley.com/doi/pdf/10.1002/joc.6106.

Claire L. Davis and K. Vincent. 2017. *Climate risk and vulnerability: A handbook for Southern Africa*. CSIR. Accepted: 2018-02-26T13:08:32Z.

B. Denis, R. Laprise, and D. Caya. 2003. Sensitivity of a regional climate model to the resolution of the lateral boundary conditions. *Climate Dynamics*, 20(2-3):107–126.

Fabien Desbiolles, Emma Howard, Ross C. Blamey, Rondrotiana Barimalala, Neil C. G. Hart, and Chris J. C. Reason. 2020. Role of ocean mesoscale structures in shaping the Angola-Low pressure system and the southern Africa rainfall. *Climate Dynamics*, 54(7):3685–3704.

S. S. Dhomse, W. Feng, S. A. Montzka, R. Hossaini, J. Keeble, J. A. Pyle, J. S. Daniel, and M. P. Chipperfield. 2019. Delay in recovery of the Antarctic ozone hole from unexpected CFC-11 emissions. *Nature Communications*, 10(1):5781. Number: 1 Publisher: Nature Publishing Group.

Alejandro Di Luca, Ramón de Elía, and René Laprise. 2013. Potential for added value in temperature simulated by high-resolution nested RCMs in present climate and in the climate change signal. *Climate Dynamics*, 40(1):443–464.

Bastien Dieppois, Benjamin Pohl, Julien Crétat, Jonathan Eden, Moussa Sidibe, Mark New, Mathieu Rouault, and Damian Lawler. 2019. Southern African summer-rainfall variability, and its teleconnections, on interannual to interdecadal timescales in CMIP5 models. *Climate Dynamics*, 53(5):3505–3527.

Noah S. Diffenbaugh and Filippo Giorgi. 2012. Climate change hotspots in the CMIP5 global climate model ensemble. *Climatic Change*, 114(3):813–822.

Tufa Dinku, Chris Funk, Pete Peterson, Ross Maidment, Tsegaye Tadesse, Hussein Gadain, and Pietro Ceccato. 2018. Validation of the CHIRPS satellite rainfall estimates over eastern Africa. *Quarterly Journal of the Royal Meteorological Society*, 144(S1):292–312. _eprint: https://onlinelibrary.wiley.com/doi/pdf/10.1002/qj.3244.

Alessandro Dosio, Richard G. Jones, Christopher Jack, Christopher Lennard, Grigory Nikulin, and Bruce Hewitson. 2019. What can we know about future precipitation in Africa? Robustness, significance and added value of projections from a large ensemble of regional climate models. *Climate Dynamics*, 53(9):5833–5858.

Alessandro Dosio, Martin W. Jury, Mansour Almazroui, Moetasim Ashfaq, Ismaila Diallo, Francois A. Engelbrecht, Nana A. B. Klutse, Christopher Lennard, Izidine Pinto, Mouhamadou B. Sylla, and Alain T.

Tamoffo. 2021. Projected future daily characteristics of African precipitation based on global (CMIP5, CMIP6) and regional (CORDEX, CORDEX-CORE) climate models. *Climate Dynamics*, 57(11):3135–3158.

Alessandro Dosio and Hans-Jürgen Panitz. 2016. Climate change projections for CORDEX-Africa with COSMO-CLM regional climate model and differences with the driving global climate models. *Climate Dynamics*, 46(5):1599–1625.

Alessandro Dosio, Hans-Jürgen Panitz, Martina Schubert-Frisius, and Daniel Lüthi. 2015. Dynamical downscaling of CMIP5 global circulation models over CORDEX-Africa with COSMO-CLM: evaluation over the present climate and analysis of the added value. *Climate Dynamics*, 44(9):2637–2661.

Hongbo Duan, Gupeng Zhang, Shouyang Wang, and Ying Fan. 2019. Robust climate change research: a review on multi-model analysis. *Environmental Research Letters*, 14(3):033001. Publisher: IOP Publishing.

J.-L. Dufresne, M.-A. Foujols, S. Denvil, A. Caubel, O. Marti, O. Aumont, Y. Balkanski, S. Bekki, H. Bellenger, R. Benshila, S. Bony, L. Bopp, P. Braconnot, P. Brockmann, P. Cadule, F. Cheruy, F. Codron, A. Cozic, D. Cugnet, N. de Noblet, J.-P. Duvel, C. Ethé, L. Fairhead, T. Fichefet, S. Flavoni, P. Friedlingstein, J.-Y. Grandpeix, L. Guez, E. Guilyardi, D. Hauglustaine, F. Hourdin, A. Idelkadi, J. Ghattas, S. Joussaume, M. Kageyama, G. Krinner, S. Labetoulle, A. Lahellec, M.-P. Lefebvre, F. Lefevre, C. Levy, Z. X. Li, J. Lloyd, F. Lott, G. Madec, M. Mancip, M. Marchand, S. Masson, Y. Meurdesoif, J. Mignot, I. Musat, S. Parouty, J. Polcher, C. Rio, M. Schulz, D. Swingedouw, S. Szopa, C. Talandier, P. Terray, N. Viovy, and N. Vuichard. 2013. Climate change projections using the IPSL-CM5 Earth System Model: from CMIP3 to CMIP5. *Climate Dynamics*, 40(9):2123–2165.

John P. Dunne, Jasmin G. John, Alistair J. Adcroft, Stephen M. Griffies, Robert W. Hallberg, Elena Shevliakova, Ronald J. Stouffer, William Cooke, Krista A. Dunne, Matthew J. Harrison, John P. Krasting, Sergey L. Malyshev, P. C. D. Milly, Peter J. Phillipps, Lori T. Sentman, Bonita L. Samuels, Michael J. Spelman, Michael Winton, Andrew T. Wittenberg, and Niki Zadeh. 2012. GFDL's ESM2 Global Coupled Climate–Carbon Earth System Models. Part I: Physical Formulation and Baseline Simulation Characteristics. *Journal of Climate*, 25(19):6646–6665. Publisher: American Meteorological Society.

Caroline M. Dunning, Emily Black, and Richard P. Allan. 2018. Later Wet Seasons with More Intense Rainfall over Africa under Future Climate Change. *Journal of Climate*, 31(23):9719–9738. Publisher: American Meteorological Society Section: Journal of Climate.

M. Déqué, D. P. Rowell, D. Lüthi, F. Giorgi, J. H. Christensen, B. Rockel, D. Jacob, E. Kjellström, M. de Castro, and B. van den Hurk. 2007. An intercomparison of regional climate simulations for Europe: assessing uncertainties in model projections. *Climatic Change*, 81(1):53–70.

M. Déqué, S. Somot, E. Sanchez-Gomez, C. M. Goodess, D. Jacob, G. Lenderink, and O. B. Christensen. 2012. The spread amongst ENSEMBLES regional scenarios: regional climate models, driving general circulation models and interannual variability. *Climate Dynamics*, 38(5):951–964.

Kerry Emanuel. 2020. The Relevance of Theory for Contemporary Research in Atmospheres, Oceans, and Climate. *AGU Advances*, 1(2):e2019AV000129. _eprint: https://onlinelibrary.wiley.com/doi/pdf/10.1029/2019AV000129.

Veronika Eyring, Sandrine Bony, Gerald A. Meehl, Catherine A. Senior, Bjorn Stevens, Ronald J. Stouffer, and Karl E. Taylor. 2016. Overview of the Coupled Model Intercomparison Project Phase 6 (CMIP6) experimental design and organization. *Geoscientific Model Development*, 9(5):1937–1958. Publisher: Copernicus GmbH.

Tom G. Farr, Paul A. Rosen, Edward Caro, Robert Crippen, Riley Duren, Scott Hensley, Michael Kobrick, Mimi Paller, Ernesto Rodriguez, Ladislav Roth, David Seal, Scott Shaffer, Joanne Shimada, Jeffrey Umland, Marian Werner, Michael Oskin, Douglas Burbank, and Douglas Alsdorf. 2007. The Shuttle Radar Topography Mission. *Reviews of Geophysics*, 45(2). _eprint: https://agupubs.onlinelibrary.wiley.com/doi/pdf/10.1029/2005RG000183.

Alice Favre, Nathalie Philippon, Benjamin Pohl, Evangelia-Anna Kalognomou, Christopher Lennard, Bruce Hewitson, Grigori Nikulin, Alessandro Dosio, Hans-Juergen Panitz, and Ruth Cerezo-Mota. 2016. Spatial distribution of precipitation annual cycles over South Africa in 10 CORDEX regional climate model present-day simulations. *Climate Dynamics*, 46(5):1799–1818.

Frauke Feser, Burkhardt Rockel, Hans von Storch, Jörg Winterfeldt, and Matthias Zahn. 2011. Regional Climate Models Add Value to Global Model Data: A Review and Selected Examples. *Bulletin of the American Meteorological Society*, 92(9):1181–1192. Publisher: American Meteorological Society Section: Bulletin of the American Meteorological Society.

Jennifer M. Fitchett and Stefan W. Grab. 2014. A 66-year tropical cyclone record for south-east Africa: temporal trends in a global context. *International Journal of Climatology*, 34(13):3604–3615. _eprint: https://onlinelibrary.wiley.com/doi/pdf/10.1002/joc.3932.

Chris Funk, Pete Peterson, Martin Landsfeld, Diego Pedreros, James Verdin, Shraddhanand Shukla, Gregory Husak, James Rowland, Laura Harrison, Andrew Hoell, and Joel Michaelsen. 2015. The climate hazards infrared precipitation with stations—a new environmental record for monitoring extremes. *Scientific Data*, 2(1):150066. Number: 1 Publisher: Nature Publishing Group.

David Gallego, Pedro Ribera, Ricardo Garcia-Herrera, Emiliano Hernandez, and Luis Gimeno. 2005. A new look for the Southern Hemisphere jet stream. *Climate Dynamics*, 24(6):607–621.

Alessandra Giannini, Michela Biasutti, Isaac M. Held, and Adam H. Sobel. 2008. A global perspective on African climate. *Climatic Change*, 90(4):359–383.

Nick van de Giesen, Rolf Hut, and John Selker. 2014. The Trans-African Hydro-Meteorological Observatory (TAHMO). *WIREs Water*, 1(4):341–348. _eprint: https://onlinelibrary.wiley.com/doi/pdf/10.1002/wat2.1034.

Z. E. Gillett, H. H. Hendon, J. M. Arblaster, and E.-P. Lim. 2021. Tropical and Extratropical Influences on the Variability of the Southern Hemisphere Wintertime Subtropical Jet. *Journal of Climate*, 34(10):4009–4022. Publisher: American Meteorological Society Section: Journal of Climate.

Marco A. Giorgetta, Johann Jungclaus, Christian H. Reick, Stephanie Legutke, Jürgen Bader, Michael Böttinger, Victor Brovkin, Traute Crueger, Monika Esch, Kerstin Fieg, Ksenia Glushak, Veronika Gayler, Helmuth Haak, Heinz-Dieter Hollweg, Tatiana Ilyina, Stefan Kinne, Luis Kornblueh, Daniela Matei,

Thorsten Mauritsen, Uwe Mikolajewicz, Wolfgang Mueller, Dirk Notz, Felix Pithan, Thomas Raddatz, Sebastian Rast, Rene Redler, Erich Roeckner, Hauke Schmidt, Reiner Schnur, Joachim Segschneider, Katharina D. Six, Martina Stockhause, Claudia Timmreck, Jörg Wegner, Heinrich Widmann, Karl-H. Wieners, Martin Claussen, Jochem Marotzke, and Bjorn Stevens. 2013. Climate and carbon cycle changes from 1850 to 2100 in MPI-ESM simulations for the Coupled Model Intercomparison Project phase 5. *Journal of Advances in Modeling Earth Systems*, 5(3):572–597. _eprint: https://onlinelibrary.wiley.com/doi/pdf/10.1002/jame.20038.

Filippo Giorgi. 2019. Thirty Years of Regional Climate Modeling: Where Are We and Where Are We Going next? *Journal of Geophysical Research: Atmospheres*, 124(11):5696–5723. _eprint: https://onlinelibrary.wiley.com/doi/pdf/10.1029/2018JD030094.

Filippo Giorgi, Erika Coppola, Francesca Raffaele, Gulilat Tefera Diro, Ramon Fuentes-Franco, Graziano Giuliani, Ashu Mamgain, Marta Pereira Llopart, Laura Mariotti, and Csaba Torma. 2014. Changes in extremes and hydroclimatic regimes in the CREMA ensemble projections. *Climatic Change*, 125(1):39–51.

Filippo Giorgi and William J. Gutowski. 2015. Regional Dynamical Downscaling and the CORDEX Initiative. *Annual Review of Environment and Resources*, 40(1):467–490.

J. P. Goutorbe, T. Lebel, A. J. Dolman, J. H. C. Gash, P. Kabat, Y. H. Kerr, B. Monteny, S. D. Prince, J. N. M. Stricker, A. Tinga, and J. S. Wallace. 1997. An overview of HAPEX-Sahel: a study in climate and desertification. *Journal of Hydrology*, 188-189:4–17.

J.-P. Goutorbe, T. Lebel, A. Tinga, P. Bessemoulin, J. Brouwer, A. J. Dolman, E. T. Engman, J. H. C. Gash, M. Hoepffner, P. Kabat, Y. H. Kerr, B. Monteny, S. Prince, F. Said, P. Sellers, and J. S. Wallace. 1994. HAPEX-Sahel: a large-scale study of land-atmosphere interactions in the semi-arid tropics. *Annales Geophysicae*, 12(1):53–64. Publisher: Copernicus GmbH.

G. A. Grell and S. R. Freitas. 2014. A scale and aerosol aware stochastic convective parameterization for weather and air quality modeling. *Atmospheric Chemistry and Physics*, 14(10):5233–5250. Publisher: Copernicus GmbH.

Guojun Gu and Chidong Zhang. 2002. Cloud components of the Intertropical Convergence Zone. *Journal of Geophysical Research: Atmospheres*, 107(D21):ACL 4–1–ACL 4–12. _eprint: https://onlinelibrary.wiley.com/doi/pdf/10.1029/2002JD002089.

Reindert J. Haarsma, Malcolm J. Roberts, Pier Luigi Vidale, Catherine A. Senior, Alessio Bellucci, Qing Bao, Ping Chang, Susanna Corti, Neven S. Fučkar, Virginie Guemas, Jost von Hardenberg, Wilco Hazeleger, Chihiro Kodama, Torben Koenigk, L. Ruby Leung, Jian Lu, Jing-Jia Luo, Jiafu Mao, Matthew S. Mizielinski, Ryo Mizuta, Paulo Nobre, Masaki Satoh, Enrico Scoccimarro, Tido Semmler, Justin Small, and Jin-Song von Storch. 2016. High Resolution Model Intercomparison Project (HighResMIP v1.0) for CMIP6. *Geoscientific Model Development*, 9(11):4185–4208. Publisher: Copernicus GmbH.

I. Harris, P. D. Jones, T. J. Osborn, and D. H. Lister. 2014. Updated high-resolution grids of monthly climatic observations – the CRU TS3.10 Dataset. *International Journal of Climatology*, 34(3):623–642. _eprint: https://rmets.onlinelibrary.wiley.com/doi/pdf/10.1002/joc.3711.

Laura Harrison, Chris Funk, and Pete Peterson. 2019. Identifying changing precipitation extremes in Sub-Saharan Africa with gauge and satellite products. *Environmental Research Letters*, 14(8):085007. Publisher: IOP Publishing.

N. C. G. Hart, C. J. C. Reason, and N. Fauchereau. 2010. Tropical–Extratropical Interactions over Southern Africa: Three Cases of Heavy Summer Season Rainfall. *Monthly Weather Review*, 138(7):2608–2623. Publisher: American Meteorological Society Section: Monthly Weather Review.

Neil C. G. Hart, Chris J. C. Reason, and Nicolas Fauchereau. 2013. Cloud bands over southern Africa: seasonality, contribution to rainfall variability and modulation by the MJO. *Climate Dynamics*, 41(5):1199–1212.

Neil C. G. Hart, Richard Washington, and Ross I. Maidment. 2019. Deep Convection over Africa: Annual Cycle, ENSO, and Trends in the Hotspots. *Journal of Climate*, 32(24):8791–8811. Publisher: American Meteorological Society Section: Journal of Climate.

Adam T. Hartman. 2021. Tracking mesoscale convective systems in central equatorial Africa. *International Journal of Climatology*, 41(1):469–482. _eprint: https://onlinelibrary.wiley.com/doi/pdf/10.1002/joc.6632.

Kerstin Hartung, Theodore G. Shepherd, Brian J. Hoskins, John Methven, and Gunilla Svensson. 2020. Diagnosing topographic forcing in an atmospheric dataset: The case of the North American Cordillera. *Quarterly Journal of the Royal Meteorological Society*, 146(726):314–326. _eprint: https://onlinelibrary.wiley.com/doi/pdf/10.1002/qj.3677.

Wilco Hazeleger, Camiel Severijns, Tido Semmler, Simona Ştefănescu, Shuting Yang, Xueli Wang, Klaus Wyser, Emanuel Dutra, José M. Baldasano, Richard Bintanja, Philippe Bougeault, Rodrigo Caballero, Annica M. L. Ekman, Jens H. Christensen, Bart van den Hurk, Pedro Jimenez, Colin Jones, Per Kållberg, Torben Koenigk, Ray McGrath, Pedro Miranda, Twan van Noije, Tim Palmer, José A. Parodi, Torben Schmith, Frank Selten, Trude Storelvmo, Andreas Sterl, Honoré Tapamo, Martin Vancoppenolle, Pedro Viterbo, and Ulrika Willén. 2010. EC-EarthA Seamless Earth-System Prediction Approach in Action. *Bulletin of the American Meteorological Society*, 91(10):1357–1364. Publisher: American Meteorological Society.

I. M. Held, H. Guo, A. Adcroft, J. P. Dunne, L. W. Horowitz, J. Krasting, E. Shevliakova, M. Winton, M. Zhao, M. Bushuk, A. T. Wittenberg, B. Wyman, B. Xiang, R. Zhang, W. Anderson, V. Balaji, L. Donner, K. Dunne, J. Durachta, P. P. G. Gauthier, P. Ginoux, J.-C. Golaz, S. M. Griffies, R. Hallberg, L. Harris, M. Harrison, W. Hurlin, J. John, P. Lin, S.-J. Lin, S. Malyshev, R. Menzel, P. C. D. Milly, Y. Ming, V. Naik, D. Paynter, F. Paulot, V. Rammaswamy, B. Reichl, T. Robinson, A. Rosati, C. Seman, L. G. Silvers, S. Underwood, and N. Zadeh. 2019. Structure and Performance of GFDL's CM4.0 Climate Model. *Journal of Advances in Modeling Earth Systems*, 11(11):3691–3727. _eprint: https://agupubs.onlinelibrary.wiley.com/doi/pdf/10.1029/2019MS001829.

Younggu Her, Seung-Hwan Yoo, Jaepil Cho, Syewoon Hwang, Jaehak Jeong, and Chounghyun Seong. 2019. Uncertainty in hydrological analysis of climate change: multi-parameter vs. multi-GCM ensemble predictions. *Scientific Reports*, 9(1):4974. Bandiera_abtest: a Cc_license_type: cc_by Cg_type: Nature Research Journals Number: 1 Primary_atype: Research Publisher: Nature Publishing Group Subject_term: Hydrology;Projection and prediction Subject_term_id: hydrology;projection-and-prediction.

Hans Hersbach, Bill Bell, Paul Berrisford, Shoji Hirahara, András Horányi, Joaquín MuñozSabater, Julien Nicolas, Carole Peubey, Raluca Radu, Dinand Schepers, Adrian Simmons, Cornel Soci, Saleh Abdalla, Xavier Abellan, Gianpaolo Balsamo, Peter Bechtold, Gionata Biavati, Jean Bidlot, Massimo Bonavita, Giovanna De Chiara, Per Dahlgren, Dick Dee, Michail Diamantakis, Rossana Dragani, Johannes Flemming, Richard Forbes, Manuel Fuentes, Alan Geer, Leo Haimberger, Sean Healy, Robin J. Hogan, Elías Hólm, Marta Janisková, Sarah Keeley, Patrick Laloyaux, Philippe Lopez, Cristina Lupu, Gabor Radnoti, Patricia de Rosnay, Iryna Rozum, Freja Vamborg, Sebastien Villaume, and Jean-Noël Thépaut. 2020. The ERA5 global reanalysis. *Quarterly Journal of the Royal Meteorological Society*, 146(730):1999–2049. _eprint: https://rmets.onlinelibrary.wiley.com/doi/pdf/10.1002/qj.3803.

Andrew Hoell, Andrea E. Gaughan, Tamuka Magadzire, and Laura Harrison. 2021. The Modulation of Daily Southern Africa Precipitation by El Niño–Southern Oscillation across the Summertime Wet Season. *Journal of Climate*, 34(3):1115–1134. Publisher: American Meteorological Society Section: Journal of Climate.

James R. Holton. 2004. *An Introduction to Dynamic Meteorology*. Academic Press. Google-Books-ID: fhW50Dv3EPsC.

Robert A. Houze Jr. 2012. Orographic effects on precipitating clouds. *Reviews of Geophysics*, 50(1). _eprint: https://onlinelibrary.wiley.com/doi/pdf/10.1029/2011RG000365.

Emma Howard and Richard Washington. 2018. Characterizing the Synoptic Expression of the Angola Low. *Journal of Climate*, 31(17):7147–7165. Publisher: American Meteorological Society.

Emma Howard and Richard Washington. 2019. Drylines in Southern Africa: Rediscovering the Congo Air Boundary. *Journal of Climate*, 32(23):8223–8242. Publisher: American Meteorological Society.

Michael J. Iacono, Jennifer S. Delamere, Eli J. Mlawer, Mark W. Shephard, Shepard A. Clough, and William D. Collins. 2008. Radiative forcing by long-lived greenhouse gases: Calculations with the AER radiative transfer models. *Journal of Geophysical Research: Atmospheres*, 113(D13). _eprint: https://onlinelibrary.wiley.com/doi/pdf/10.1029/2008JD009944.

IPCC and T.F. Stocker. 2013. *Climate Change 2013: The Physical Science Basis*. Cambridge University Press.

Daniela Jacob, Alberto Elizalde, Andreas Haensler, Stefan Hagemann, Pankaj Kumar, Ralf Podzun, Diana Rechid, Armelle Reca Remedio, Fahad Saeed, Kevin Sieck, Claas Teichmann, and Christof Wilhelm. 2012. Assessing the Transferability of the Regional Climate Model REMO to Different COordinated Regional Climate Downscaling EXperiment (CORDEX) Regions. *Atmosphere*, 3(1):181–199. Number: 1 Publisher: Molecular Diversity Preservation International.

Daniela Jacob, Claas Teichmann, Stefan Sobolowski, Eleni Katragkou, Ivonne Anders, Michal Belda, Rasmus Benestad, Fredrik Boberg, Erasmo Buonomo, Rita M. Cardoso, Ana Casanueva, Ole B. Christensen, Jens Hesselbjerg Christensen, Erika Coppola, Lesley De Cruz, Edouard L. Davin, Andreas Dobler, Marta Domínguez, Rowan Fealy, Jesus Fernandez, Miguel Angel Gaertner, Markel García-Díez, Filippo Giorgi, Andreas Gobiet, Klaus Goergen, Juan José Gómez-Navarro, Juan Jesús González Alemán, Claudia Gutiérrez, José M. Gutiérrez, Ivan Güttler, Andreas Haensler, Tomáš Halenka, Sonia Jerez, Pedro Jiménez-Guerrero, Richard G. Jones, Klaus Keuler, Erik Kjellström, Sebastian Knist, Sven Kotlarski, Douglas Maraun, Erik van Meijgaard, Paola Mercogliano, Juan Pedro Montávez, Antonio Navarra, Grigory Nikulin, Nathalie de Noblet-Ducoudré, Hans-Juergen Panitz, Susanne Pfeifer, Marie Piazza, Emanuela Pichelli, Joni-Pekka Pietikäinen, Andreas F. Prein, Swantje Preuschmann, Diana Rechid, Burkhardt Rockel, Raquel Romera, Enrique Sánchez, Kevin Sieck, Pedro M. M. Soares, Samuel Somot, Lidija Srnec, Silje Lund Sørland, Piet Termonia, Heimo Truhetz, Robert Vautard, Kirsten Warrach-Sagi, and Volker Wulfmeyer. 2020. Regional climate downscaling over Europe: perspectives from the EURO-CORDEX community. *Regional Environmental Change*, 20(2):51.

Zaviša I. Janjić. 1994. The Step-Mountain Eta Coordinate Model: Further Developments of the Convection, Viscous Sublayer, and Turbulence Closure Schemes. *Monthly Weather Review*, 122(5):927–945. Publisher: American Meteorological Society Section: Monthly Weather Review.

John E. Janowiak. 1988. An Investigation of Interannual Rainfall Variability in Africa. *Journal of Climate*, 1(3):240–255. Publisher: American Meteorological Society.

Stephen Jeffrey, Leon D. Rotstayn, Mark Collier, Stacey Maree Dravitzki, Carlo Hamalainen, Chris Moeseneder, Kenneth Wong, and Jozef Syktus. 2013. Australia ' s CMIP 5 submission using the CSIRO-Mk 3 . 6 model.

John S. Kain. 2004. The Kain–Fritsch Convective Parameterization: An Update. *Journal of Applied Meteorology and Climatology*, 43(1):170–181. Publisher: American Meteorological Society Section: Journal of Applied Meteorology and Climatology.

Evangelia-Anna Kalognomou, Christopher Lennard, Mxolisi Shongwe, Izidine Pinto, Alice Favre, Michael Kent, Bruce Hewitson, Alessandro Dosio, Grigory Nikulin, Hans-Jürgen Panitz, and Matthias Büchner. 2013. A Diagnostic Evaluation of Precipitation in CORDEX Models over Southern Africa. *Journal of Climate*, 26(23):9477–9506.

Alexey Yu Karpechko. 2020. International regulations have paused a jet-stream shift in the Southern Hemisphere. *Nature*, 579(7800):500–501. Bandiera_abtest: a Cg_type: News And Views Number: 7800 Publisher: Nature Publishing Group Subject_term: Atmospheric science, Climate sciences.

Maria Chara Karypidou, Eleni Katragkou, and Stefan Pieter Sobolowski. 2022a. Precipitation over southern Africa: is there consensus among global climate models (GCMs), regional climate models (RCMs) and observational data? *Geoscientific Model Development*, 15(8):3387–3404. Publisher: Copernicus GmbH.

Maria Chara Karypidou, Stefan Pieter Sobolowski, Eleni Katragkou, Lorenzo Sangelantoni, and Grigory Nikulin. 2022b. The impact of lateral boundary forcing in the CORDEX-Africa ensemble over southern Africa. *Geoscientific Model Development Discussions*, pages 1–36. Publisher: Copernicus GmbH.

William J. Keat, Thorwald H. M. Stein, Elelwani Phaduli, Stephanie Landman, Erik Becker, Mary-Jane M. Bopape, Kirsty E. Hanley, Humphrey W. Lean, and Stuart Webster. 2019. Convective initiation and storm life cycles in convection-permitting simulations of the Met Office Unified Model over South Africa. *Quarterly Journal of the Royal Meteorological Society*, 145(721):1323–1336. _eprint: https://onlinelibrary.wiley.com/doi/pdf/10.1002/qj.3487.

M.G. Kendall. 1948. *Rank correlation methods*. Rank correlation methods. Griffin, Oxford, England.

Christian Kerkhoff, Hans R. Künsch, and Christoph Schär. 2015. A Bayesian Hierarchical Model for Heterogeneous RCM–GCM Multimodel Ensembles. *Journal of Climate*, 28(15):6249–6266. Publisher: American Meteorological Society Section: Journal of Climate.

J. Kim, Duane E. Waliser, Chris A. Mattmann, Cameron E. Goodale, Andrew F. Hart, Paul A. Zimdars, Daniel J. Crichton, Colin Jones, Grigory Nikulin, Bruce Hewitson, Chris Jack, Christopher Lennard, and Alice Favre. 2014. Evaluation of the CORDEX-Africa multi-RCM hindcast: systematic model errors. *Climate Dynamics*, 42(5):1189–1202.

Yeon-Hee Kim, Seung-Ki Min, Xuebin Zhang, Jana Sillmann, and Marit Sandstad. 2020. Evaluation of the CMIP6 multi-model ensemble for climate extreme indices. *Weather and Climate Extremes*, 29:100269.

Peter Knippertz, Hugh Coe, J. Christine Chiu, Mat J. Evans, Andreas H. Fink, Norbert Kalthoff, Catherine Liousse, Celine Mari, Richard P. Allan, Barbara Brooks, Sylvester Danour, Cyrille Flamant, Oluwagbemiga O. Jegede, Fabienne Lohou, and John H. Marsham. 2015. The DACCIWA Project: Dynamics–Aerosol–Chemistry–Cloud Interactions in West Africa. *Bulletin of the American Meteorological Society*, 96(9):1451–1460. Publisher: American Meteorological Society Section: Bulletin of the American Meteorological Society.

Shunya Koseki and Teferi Demissie. 2018. Does the Drakensberg dehydrate southwestern Africa? *Journal of Arid Environments*, 158:35–42.

Shunya Koseki and Priscilla A. Mooney. 2019. Influences of Lake Malawi on the spatial and diurnal variability of local precipitation. *Hydrology and Earth System Sciences*, 23(7):2795–2812. Publisher: Copernicus GmbH.

Giresse Kuete, Wilfried Pokam Mba, and Richard Washington. 2020. African Easterly Jet South: control, maintenance mechanisms and link with Southern subtropical waves. *Climate Dynamics*, 54(3):1539–1552.

Nothemba Kula, Andy Haines, and Robert Fryatt. 2013. Reducing Vulnerability to Climate Change in Sub-Saharan Africa: The Need for Better Evidence. *PLoS Medicine*, 10(1).

Paul J. Kushner, Isaac M. Held, and Thomas L. Delworth. 2001. Southern Hemisphere Atmospheric Circulation Response to Global Warming. *Journal of Climate*, 14(10):2238–2249. Publisher: American Meteorological Society Section: Journal of Climate.

T. Lamont, M. García-Reyes, S. J. Bograd, C. D. van der Lingen, and W. J. Sydeman. 2018. Upwelling indices for comparative ecosystem studies: Variability in the Benguela Upwelling System. *Journal of Marine Systems*, 188:3–16.

R. Laprise, R. de Elía, D. Caya, S. Biner, P. Lucas-Picher, E. Diaconescu, M. Leduc, A. Alexandru, L. Separovic, and Canadian Network for Regional Climate Modelling and Diagnostics. 2008. Challenging some tenets of Regional Climate Modelling. *Meteorology and Atmospheric Physics*, 100(1):3–22.

Melissa J. Lazenby, Martin C. Todd, and Yi Wang. 2016. Climate model simulation of the South Indian Ocean Convergence Zone: mean state and variability. *Climate Research*, 68(1):59–71.

Camille Le Coz and Nick van de Giesen. 2020. Comparison of Rainfall Products over Sub-Saharan Africa. *Journal of Hydrometeorology*, 21(4):553–596. Publisher: American Meteorological Society.

Simon H. Lee, Paul D. Williams, and Thomas H. A. Frame. 2019. Increased shear in the North Atlantic upper-level jet stream over the past four decades. *Nature*, 572(7771):639–642. Number: 7771 Publisher: Nature Publishing Group.

Camille Li and Justin J. Wettstein. 2012. Thermally Driven and Eddy-Driven Jet Variability in Reanalysis. *Journal of Climate*, 25(5):1587–1596. Publisher: American Meteorological Society Section: Journal of Climate.

Daniela C. A. Lima, Pedro M. M. Soares, Alvaro Semedo, Rita M. Cardoso, William Cabos, and Dmitry V. Sein. 2019. How Will a Warming Climate Affect the Benguela Coastal Low-Level Wind Jet? *Journal of Geophysical Research: Atmospheres*, 124(9):5010–5028. _eprint: https://agupubs.onlinelibrary.wiley.com/doi/pdf/10.1029/2018JD029574.

Elisabeth A. Lloyd, Melissa Bukovsky, and Linda O. Mearns. 2020. An analysis of the disagreement about added value by regional climate models. *Synthese*.

Christof Lorenz and Harald Kunstmann. 2012. The Hydrological Cycle in Three State-of-the-Art Reanalyses: Intercomparison and Performance Analysis. *Journal of Hydrometeorology*, 13(5):1397–1420. Publisher: American Meteorological Society.

Yibo Luan, Xuefeng Cui, and Marion Ferrat. 2013. Historical trends of food self-sufficiency in Africa. *Food Security*, 5(3):393–405.

Alejandro Di Luca, Daniel Argüeso, Jason P. Evans, Ramón de Elía, and René Laprise. 2016. Quantifying the overall added value of dynamical downscaling and the contribution from different spatial scales. *Journal of Geophysical Research: Atmospheres*, 121(4):1575–1590. _eprint: https://agupubs.onlinelibrary.wiley.com/doi/pdf/10.1002/2015JD024009.

Bradfield Lyon and Simon J. Mason. 2007. The 1997–98 Summer Rainfall Season in Southern Africa. Part I: Observations. *Journal of Climate*, 20(20):5134–5148.

Bradfield Lyon and Simon J. Mason. 2009. The 1997/98 Summer Rainfall Season in Southern Africa. Part II: Model Simulations and Coupled Model Forecasts. *Journal of Climate*, 22(13):3802–3818.

Michelle L. L'Heureux, Sukyoung Lee, and Bradfield Lyon. 2013. Recent multidecadal strengthening of the Walker circulation across the tropical Pacific. *Nature Climate Change*, 3(6):571–576. Number: 6 Publisher: Nature Publishing Group.

Tafadzwanashe Mabhaudhi, Sylvester Mpandeli, Luxon Nhamo, Vimbayi G. P. Chimonyo, Charles Nhemachena, Aidan Senzanje, Dhesigen Naidoo, and Albert T. Modi. 2018. Prospects for Improving Irrigated Agriculture in Southern Africa: Linking Water, Energy and Food. *Water*, 10(12):1881. Number: 12 Publisher: Multidisciplinary Digital Publishing Institute.

Clémence Macron, Benjamin Pohl, Yves Richard, and Miloud Bessafi. 2014. How do Tropical Temperate Troughs Form and Develop over Southern Africa? *Journal of Climate*, 27(4):1633–1647. Publisher: American Meteorological Society Section: Journal of Climate.

Penelope Maher, Michael E. Kelleher, Philip G. Sansom, and John Methven. 2020. Is the subtropical jet shifting poleward? *Climate Dynamics*, 54(3):1741–1759.

Ross I. Maidment, Richard P. Allan, and Emily Black. 2015. Recent observed and simulated changes in precipitation over Africa. *Geophysical Research Letters*, 42(19):8155–8164. _eprint: https://agupubs.onlinelibrary.wiley.com/doi/pdf/10.1002/2015GL065765.

Ross I. Maidment, David Grimes, Richard P. Allan, Elena Tarnavsky, Marc Stringer, Tim Hewison, Rob Roebeling, and Emily Black. 2014. The 30 year TAMSAT African Rainfall Climatology And Time series (TARCAT) data set. *Journal of Geophysical Research: Atmospheres*, 119(18):10,619–10,644. _eprint: https://agupubs.onlinelibrary.wiley.com/doi/pdf/10.1002/2014JD021927.

Desmond Manatsa, Yushi Morioka, Swadhin K. Behera, Toshi Yamagata, and Caxton H. Matarira. 2013. Link between Antarctic ozone depletion and summer warming over southern Africa. *Nature Geoscience*, 6(11):934–939.

A. J. Manhique, C. J. C. Reason, L. Rydberg, and N. Fauchereau. 2011. ENSO and Indian Ocean sea surface temperatures and their relationships with tropical temperate troughs over Mozambique and the Southwest Indian Ocean. *International Journal of Climatology*, 31(1):1–13.

Henry B. Mann. 1945. Nonparametric Tests Against Trend. *Econometrica*, 13(3):245–259. Publisher: [Wiley, Econometric Society].

Gloria L. Manney and Michaela I. Hegglin. 2018. Seasonal and Regional Variations of Long-Term Changes in Upper-Tropospheric Jets from Reanalyses. *Journal of Climate*, 31(1):423–448. Publisher: American Meteorological Society Section: Journal of Climate.

Tshepo S. Masipa. 2017. The impact of climate change on food security in South Africa: Current realities and challenges ahead. *Jàmbá : Journal of Disaster Risk Studies*, 9(1).

François Massonnet, Martin Ménégoz, Mario Acosta, Xavier Yepes-Arbós, Eleftheria Exarchou, and Francisco J. Doblas-Reyes. 2020. Replicability of the EC-Earth3 Earth system model under a change in computing environment. *Geoscientific Model Development*, 13(3):1165–1178. Publisher: Copernicus GmbH.

Thorsten Mauritsen, Jürgen Bader, Tobias Becker, Jörg Behrens, Matthias Bittner, Renate Brokopf, Victor Brovkin, Martin Claussen, Traute Crueger, Monika Esch, Irina Fast, Stephanie Fiedler, Dagmar Fläschner, Veronika Gayler, Marco Giorgetta, Daniel S. Goll, Helmuth Haak, Stefan Hagemann, Christopher Hedemann, Cathy Hohenegger, Tatiana Ilyina, Thomas Jahns, Diego JimenézdelaCuesta, Johann Jungclaus, Thomas Kleinen, Silvia Kloster, Daniela Kracher, Stefan Kinne, Deike Kleberg, Gitta Lasslop, Luis Kornblueh, Jochem Marotzke, Daniela Matei, Katharina Meraner, Uwe Mikolajewicz, Kameswarrao Modali, Benjamin Möbis, Wolfgang A. Müller, Julia E. M. S. Nabel, Christine C. W. Nam, Dirk Notz, Sarah-Sylvia Nyawira, Hanna Paulsen, Karsten Peters, Robert Pincus, Holger Pohlmann, Julia Pongratz, Max Popp, Thomas Jürgen Raddatz, Sebastian Rast, Rene Redler, Christian H. Reick, Tim Rohrschneider, Vera Schemann, Hauke Schmidt, Reiner Schnur, Uwe Schulzweida, Katharina D. Six, Lukas Stein, Irene Stemmler, Bjorn Stevens, Jin-Song von Storch, Fangxing Tian, Aiko Voigt, Philipp Vrese, Karl-Hermann Wieners, Stiig Wilkenskjeld, Alexander Winkler, and Erich Roeckner. 2019. Developments in the MPI-M Earth System Model version 1.2 (MPI-ESM1.2) and Its Response to Increasing CO2. *Journal of Advances in Modeling Earth Systems*, 11(4):998–1038. _eprint: https://agupubs.onlinelibrary.wiley.com/doi/pdf/10.1029/2018MS001400.

A. F. Mavume, L. Rydberg, M. Rouault, and J. R. E. Lutjeharms. 2009. Climatology and Landfall of Tropical Cyclones in the South- West Indian Ocean. *Western Indian Ocean Journal of Marine Science*, 8(1). Number: 1.

G. Maúre, I. Pinto, M. Ndebele-Murisa, M. Muthige, C. Lennard, G. Nikulin, A. Dosio, and A. Meque. 2018. The southern African climate under 1.5\hspace0.167em°C and 2\hspace0.167em°C of global warming as simulated by CORDEX regional climate models. *Environmental Research Letters*, 13(6):065002. Publisher: IOP Publishing.

Arlindo Meque and Babatunde J. Abiodun. 2015. Simulating the link between ENSO and summer drought in Southern Africa using regional climate models. *Climate Dynamics*, 44(7):1881–1900.

Agostino N. Meroni, Kizito A. Oundo, Richard Muita, Mary-Jane Bopape, Thizwilondi R. Maisha, Martina Lagasio, Antonio Parodi, and Giovanna Venuti. 2021. Sensitivity of some African heavy rainfall events to microphysics and planetary boundary layer schemes: Impacts on localised storms. *Quarterly Journal of the Royal Meteorological Society*, 147(737):2448–2468. _eprint: https://onlinelibrary.wiley.com/doi/pdf/10.1002/qj.4033.

Alison Misselhorn and Sheryl L. Hendriks. 2017. A systematic review of sub-national food insecurity research in South Africa: Missed opportunities for policy insights. *PLOS ONE*, 12(8):e0182399. Publisher: Public Library of Science.

Ditiro B. Moalafhi, Jason P. Evans, and Ashish Sharma. 2017a. Influence of reanalysis datasets on dynamically downscaling the recent past. *Climate Dynamics*, 49(4):1239–1255.

Ditiro Benson Moalafhi, Ashish Sharma, Jason Peter Evans, Rajeshwar Mehrotra, and Eytan Rocheta. 2017b. Impact of bias-corrected reanalysis-derived lateral boundary conditions on WRF simulations. *Journal of Advances in Modeling Earth Systems*, 9(4):1828–1846. _eprint: https://onlinelibrary.wiley.com/doi/pdf/10.1002/2017MS001003.

Patience T. Mulovhedzi, Gift T. Rambuwani, Mary-Jane Bopape, Robert Maisha, and Nkwe Monama. 2021. Model inter-comparison for short-range forecasts over the southern African domain. *South African Journal of Science*, 117(9/10). Number: 9/10.

C. Munday and R. Washington. 2018. Systematic Climate Model Rainfall Biases over Southern Africa: Links to Moisture Circulation and Topography. *Journal of Climate*, 31(18):7533–7548. Publisher: American Meteorological Society Section: Journal of Climate.

Callum Munday and Richard Washington. 2017. Circulation controls on southern African precipitation in coupled models: The role of the Angola Low. *Journal of Geophysical Research: Atmospheres*, 122(2):861–877.

M. S. Muthige, J. Malherbe, F. A. Englebrecht, S. Grab, A. Beraki, T. R. Maisha, and J. Van der Merwe. 2018. Projected changes in tropical cyclones over the South West Indian Ocean under different extents of global warming. *Environmental Research Letters*, 13(6):065019. Publisher: IOP Publishing.

Hisashi Nakamura and Akihiko Shimpo. 2004. Seasonal Variations in the Southern Hemisphere Storm Tracks and Jet Streams as Revealed in a Reanalysis Dataset. *Journal of Climate*, 17(9):1828–1844. Publisher: American Meteorological Society Section: Journal of Climate.

Mikio Nakanishi and Hiroshi Niino. 2006. An Improved Mellor–Yamada Level-3 Model: Its Numerical Stability and Application to a Regional Prediction of Advection Fog. *Boundary-Layer Meteorology*, 119(2):397–407.

David J. Nash, Kathleen Pribyl, Jørgen Klein, Georgina H. Endfield, Dominic R. Kniveton, and George C. D. Adamson. 2015. Tropical cyclone activity over Madagascar during the late nineteenth century. *International Journal of Climatology*, 35(11):3249–3261. _eprint: https://onlinelibrary.wiley.com/doi/pdf/10.1002/joc.4204.

S. E. Nicholson, D. Klotter, and G. Chavula. 2014. A detailed rainfall climatology for Malawi, Southern Africa. *International Journal of Climatology*, 34(2):315–325.

Sharon E. Nicholson. 2009. A revised picture of the structure of the "monsoon" and land ITCZ over West Africa. *Climate Dynamics*, 32(7):1155–1171.

Sharon E. Nicholson. 2018. The ITCZ and the Seasonal Cycle over Equatorial Africa. *Bulletin of the American Meteorological Society*, 99(2):337–348. Publisher: American Meteorological Society Section: Bulletin of the American Meteorological Society.

Sharon E. Nicholson and Jeremy P. Grist. 2003. The Seasonal Evolution of the Atmospheric Circulation over West Africa and Equatorial Africa. *Journal of Climate*, 16(7):1013–1030. Publisher: American Meteorological Society Section: Journal of Climate.

Ji Nie, William R. Boos, and Zhiming Kuang. 2010. Observational Evaluation of a Convective Quasi-Equilibrium View of Monsoons. *Journal of Climate*, 23(16):4416–4428. Publisher: American Meteorological Society Section: Journal of Climate.

Grigory Nikulin, Colin Jones, Filippo Giorgi, Ghassem Asrar, Matthias Büchner, Ruth Cerezo-Mota, Ole Bøssing Christensen, Michel Déqué, Jesus Fernandez, Andreas Hänsler, Erik van Meijgaard, Patrick Samuelsson, Mouhamadou Bamba Sylla, and Laxmi Sushama. 2012. Precipitation Climatology in an Ensemble of CORDEX-Africa Regional Climate Simulations. *Journal of Climate*, 25(18):6057–6078. Publisher: American Meteorological Society Section: Journal of Climate.

Guo-Yue Niu, Zong-Liang Yang, Kenneth E. Mitchell, Fei Chen, Michael B. Ek, Michael Barlage, Anil Kumar, Kevin Manning, Dev Niyogi, Enrique Rosero, Mukul Tewari, and Youlong Xia. 2011. The community Noah land surface model with multiparameterization options (Noah-MP): 1. Model description and evaluation with local-scale measurements. *Journal of Geophysical Research: Atmospheres*, 116(D12). _eprint: https://onlinelibrary.wiley.com/doi/pdf/10.1029/2010JD015139.

Arielle Stela Nkwinkwa Njouodo, Shunya Koseki, Noel Keenlyside, and Mathieu Rouault. 2018. Atmospheric Signature of the Agulhas Current. *Geophysical Research Letters*, 45(10):5185–5193. _eprint: https://onlinelibrary.wiley.com/doi/pdf/10.1029/2018GL077042.

Nicholas S. Novella and Wassila M. Thiaw. 2013. African Rainfall Climatology Version 2 for Famine Early Warning Systems. *Journal of Applied Meteorology and Climatology*, 52(3):588–606. Publisher: American Meteorological Society.

Paul A. O'Gorman and John G. Dwyer. 2018. Using Machine Learning to Parameterize Moist Convection: Potential for Modeling of Climate, Climate Change, and Extreme Events. *Journal of Advances in Modeling Earth Systems*, 10(10):2548–2563. _eprint: https://onlinelibrary.wiley.com/doi/pdf/10.1029/2018MS001351.

Charles Onyutha. 2018. Trends and variability in African long-term precipitation. *Stochastic Environmental Research and Risk Assessment*, 32(9):2721–2739.

D. J. Parker, R. R. Burton, A. Diongue-Niang, R. J. Ellis, M. Felton, C. M. Taylor, C. D. Thorncroft, P. Bessemoulin, and A. M. Tompkins. 2005. The diurnal cycle of the West African monsoon circulation. *Quarterly Journal of the Royal Meteorological Society*, 131(611):2839–2860. _eprint: https://onlinelibrary.wiley.com/doi/pdf/10.1256/qj.04.52.

K. J. Pearson, G. M. S. Lister, C. E. Birch, R. P. Allan, R. J. Hogan, and S. J. Woolnough. 2014. Modelling the diurnal cycle of tropical convection across the 'grey zone'. *Quarterly Journal of the Royal Meteorological Society*, 140(679):491–499. _eprint: https://onlinelibrary.wiley.com/doi/pdf/10.1002/qj.2145.

Cristina Pena-Ortiz, David Gallego, Pedro Ribera, Paulina Ordonez, and Maria Del Carmen Alvarez-Castro. 2013. Observed trends in the global jet stream characteristics during the second half of the 20th century. *Journal of Geophysical Research: Atmospheres*, 118(7):2702–2713. _eprint: https://onlinelibrary.wiley.com/doi/pdf/10.1002/jgrd.50305.

Thomas C. Peterson and Michael J. Manton. 2008. Monitoring Changes in Climate Extremes: A Tale of International Collaboration. *Bulletin of the American Meteorological Society*, 89(9):1266–1271. Publisher: American Meteorological Society.

Emanuela Pichelli, Erika Coppola, Stefan Sobolowski, Nikolina Ban, Filippo Giorgi, Paolo Stocchi, Antoinette Alias, Danijel Belušić, Segolene Berthou, Cecile Caillaud, Rita M. Cardoso, Steven Chan, Ole Bøssing Christensen, Andreas Dobler, Hylke de Vries, Klaus Goergen, Elizabeth J. Kendon, Klaus Keuler, Geert Lenderink, Torge Lorenz, Aditya N. Mishra, Hans-Juergen Panitz, Christoph Schär, Pedro M. M. Soares, Heimo Truhetz, and Jesus Vergara-Temprado. 2021. The first multi-model ensemble of regional climate simulations at kilometer-scale resolution part 2: historical and future simulations of precipitation. *Climate Dynamics*.

David W. Pierce, Tim P. Barnett, Benjamin D. Santer, and Peter J. Gleckler. 2009. Selecting global climate models for regional climate change studies. *Proceedings of the National Academy of Sciences*, 106(21):8441–8446. Publisher: National Academy of Sciences Section: Physical Sciences.

Izidine Pinto, Chris Jack, and Bruce Hewitson. 2018. Process-based model evaluation and projections over southern Africa from Coordinated Regional Climate Downscaling Experiment and Coupled Model Intercomparison Project Phase 5 models. *International Journal of Climatology*, 38(11):4251–4261. _eprint: https://rmets.onlinelibrary.wiley.com/doi/pdf/10.1002/joc.5666.

Izidine Pinto, Christopher Lennard, Mark Tadross, Bruce Hewitson, Alessandro Dosio, Grigory Nikulin, Hans-Juergen Panitz, and Mxolisi E. Shongwe. 2016. Evaluation and projections of extreme precipitation over southern Africa from two CORDEX models. *Climatic Change*, 135(3):655–668.

Benjamin Pohl, Mathieu Rouault, and Shouraseni Sen Roy. 2014. Simulation of the annual and diurnal cycles of rainfall over South Africa by a regional climate model. *Climate Dynamics*, 43(7):2207–2226.

Alexander Polonsky and Anton Torbinsky. 2021. The IOD–ENSO Interaction: The Role of the Indian Ocean Current's System. *Atmosphere*, 12(12):1662. Number: 12 Publisher: Multidisciplinary Digital Publishing Institute.

Catherine Pomposi, Chris Funk, Shraddhanand Shukla, Laura Harrison, and Tamuka Magadzire. 2018. Distinguishing southern Africa precipitation response by strength of El Niño events and implications for decision-making. *Environmental Research Letters*, 13(7):074015.

Michael Previdi, Karen L. Smith, and Lorenzo M. Polvani. 2021. Arctic amplification of climate change: a review of underlying mechanisms. *Environmental Research Letters*, 16(9):093003. Publisher: IOP Publishing.

Komaragiri Srinivasa Raju and Dasika Nagesh Kumar. 2020. Review of approaches for selection and ensembling of GCMs. *Journal of Water and Climate Change*, 11(3):577–599.

Hamish Ramsay. 2017. The Global Climatology of Tropical Cyclones. ISBN: 9780199389407.

Arun Rana, Grigory Nikulin, Erik Kjellström, Gustav Strandberg, Marco Kupiainen, Ulf Hansson, and Michael Kolax. 2020. Contrasting regional and global climate simulations over South Asia. *Climate Dynamics*, 54(5):2883–2901.

Mika Rantanen, Alexey Yu Karpechko, Antti Lipponen, Kalle Nordling, Otto Hyvärinen, Kimmo Ruosteenoja, Timo Vihma, and Ari Laaksonen. 2022. The Arctic has warmed nearly four times faster than

the globe since 1979. *Communications Earth & Environment*, 3(1):1–10. Number: 1 Publisher: Nature Publishing Group.

R. S. Rapolaki, R. C. Blamey, J. C. Hermes, and C. J. C. Reason. 2021. Moisture sources and transport during an extreme rainfall event over the Limpopo River Basin, southern Africa. *Atmospheric Research*, 264:105849.

Ramontsheng S. Rapolaki, Ross C. Blamey, Juliet C. Hermes, and Chris J. C. Reason. 2019. A classification of synoptic weather patterns linked to extreme rainfall over the Limpopo River Basin in southern Africa. *Climate Dynamics*, 53(3):2265–2279.

Satyaban B. Ratna, Swadhin Behera, J. Venkata Ratnam, Keiko Takahashi, and Toshio Yamagata. 2013. An index for tropical temperate troughs over southern Africa. *Climate Dynamics*, 41(2):421–441.

J. V. Ratnam, S. K. Behera, Y. Masumoto, K. Takahashi, and T. Yamagata. 2012. A simple regional coupled model experiment for summer-time climate simulation over southern Africa. *Climate Dynamics*, 39(9):2207–2217.

J. V. Ratnam, S. K. Behera, S. B. Ratna, C. J. de W. Rautenbach, C. Lennard, J.-J. Luo, Y. Masumoto, K. Takahashi, and T. Yamagata. 2013. Dynamical Downscaling of Austral Summer Climate Forecasts over Southern Africa Using a Regional Coupled Model. *Journal of Climate*, 26(16):6015–6032. Publisher: American Meteorological Society Section: Journal of Climate.

C. J. C. Reason. 2001. Subtropical Indian Ocean SST dipole events and southern African rainfall. *Geophysical Research Letters*, 28(11):2225–2227. _eprint: https://onlinelibrary.wiley.com/doi/pdf/10.1029/2000GL012735.

C. J. C. Reason and D. Jagadheesha. 2005. A model investigation of recent ENSO impacts over southern Africa. *Meteorology and Atmospheric Physics*, 89(1):181–205.

Michelle Simões Reboita, Tércio Ambrizzi, Bruna Andrelina Silva, Raniele Fátima Pinheiro, and Rosmeri Porfírio da Rocha. 2019. The South Atlantic Subtropical Anticyclone: Present and Future Climate. *Frontiers in Earth Science*, 0. Publisher: Frontiers.

Jean-Luc Redelsperger, Chris D. Thorncroft, Arona Diedhiou, Thierry Lebel, Douglas J. Parker, and Jan Polcher. 2006. African Monsoon Multidisciplinary Analysis: An International Research Project and Field Campaign. *Bulletin of the American Meteorological Society*, 87(12):1739–1746. Publisher: American Meteorological Society Section: Bulletin of the American Meteorological Society.

Gwendal Rivière. 2011. A Dynamical Interpretation of the Poleward Shift of the Jet Streams in Global Warming Scenarios. *Journal of the Atmospheric Sciences*, 68(6):1253–1272. Publisher: American Meteorological Society Section: Journal of the Atmospheric Sciences.

Joacim Rocklöv and Robert Dubrow. 2020. Climate change: an enduring challenge for vector-borne disease prevention and control. *Nature Immunology*, 21(5):479–483. Number: 5 Publisher: Nature Publishing Group.

L. D. Rotstayn, M. A. Collier, S. J. Jeffrey, J. Kidston, J. I. Syktus, and K. K. Wong. 2013. Anthropogenic effects on the subtropical jet in the Southern Hemisphere: aerosols versus long-lived greenhouse gases. *Environmental Research Letters*, 8(1):014030. Publisher: IOP Publishing.

Markku Rummukainen. 2016. Added value in regional climate modeling. *WIREs Climate Change*, 7(1):145–159. _eprint: https://wires.onlinelibrary.wiley.com/doi/pdf/10.1002/wcc.378.

C. L. Ryder, E. J. Highwood, P. D. Rosenberg, J. Trembath, J. K. Brooke, M. Bart, A. Dean, J. Crosier, J. Dorsey, H. Brindley, J. Banks, J. H. Marsham, J. B. McQuaid, H. Sodemann, and R. Washington. 2013. Optical properties of Saharan dust aerosol and contribution from the coarse mode as measured during the Fennec 2011 aircraft campaign. *Atmospheric Chemistry and Physics*, 13(1):303–325. Publisher: Copernicus GmbH.

C. L. Ryder, J. B. McQuaid, C. Flamant, P. D. Rosenberg, R. Washington, H. E. Brindley, E. J. Highwood, J. H. Marsham, D. J. Parker, M. C. Todd, J. R. Banks, J. K. Brooke, S. Engelstaedter, V. Estelles, P. Formenti, L. Garcia-Carreras, C. Kocha, F. Marenco, H. Sodemann, C. J. T. Allen, A. Bourdon, M. Bart, C. Cavazos-Guerra, S. Chevaillier, J. Crosier, E. Darbyshire, A. R. Dean, J. R. Dorsey, J. Kent, D. O'Sullivan, K. Schepanski, K. Szpek, J. Trembath, and A. Woolley. 2015. Advances in understanding mineral dust and boundary layer processes over the Sahara from Fennec aircraft observations. *Atmospheric Chemistry and Physics*, 15(14):8479–8520. Publisher: Copernicus GmbH.

Ju-Mee Ryoo, Leonhard Pfister, Rei Ueyama, Paquita Zuidema, Robert Wood, Ian Chang, and Jens Redemann. 2021. A meteorological overview of the ORACLES (ObseRvations of Aerosols above CLouds and their intEractionS) campaign over the southeastern Atlantic during 2016–2018: Part 1 – Climatology. *Atmospheric Chemistry and Physics*, 21(22):16689–16707. Publisher: Copernicus GmbH.

Patrick Samuelsson, Stefan Gollvik, Christer Jansson, Marco Kupiainen, Ekaterina Kourzeneva, and Willem Jan van de Berg. 2015. The surface processes of the Rossby Centre regional atmospheric climate model (RCA4).

Nazmus Sazib, Iliana E. Mladenova, and John D. Bolten. 2020. Assessing the Impact of ENSO on Agriculture Over Africa Using Earth Observation Data. *Frontiers in Sustainable Food Systems*, 4.

Udo Schneider, Andreas Becker, Peter Finger, Anja Meyer-Christoffer, Bruno Rudolf, and Markus Ziese. 2015. GPCC Full Data Reanalysis Version 7.0 at 0.5°: Monthly Land-Surface Precipitation from Rain-Gauges built on GTS-based and Historic Data.

J. F. Scinocca, V. V. Kharin, Y. Jiao, M. W. Qian, M. Lazare, L. Solheim, G. M. Flato, S. Biner, M. Desgagne, and B. Dugas. 2016. Coordinated Global and Regional Climate Modeling. *Journal of Climate*, 29(1):17–35. Publisher: American Meteorological Society Section: Journal of Climate.

Øyvind Seland, Mats Bentsen, Dirk Olivié, Thomas Toniazzo, Ada Gjermundsen, Lise Seland Graff, Jens Boldingh Debernard, Alok Kumar Gupta, Yan-Chun He, Alf Kirkevåg, Jörg Schwinger, Jerry Tjiputra, Kjetil Schanke Aas, Ingo Bethke, Yuanchao Fan, Jan Griesfeller, Alf Grini, Chuncheng Guo, Mehmet Ilicak, Inger Helene Hafsahl Karset, Oskar Landgren, Johan Liakka, Kine Onsum Moseid, Aleksi Nummelin, Clemens Spensberger, Hui Tang, Zhongshi Zhang, Christoph Heinze, Trond Iversen,

and Michael Schulz. 2020. Overview of the Norwegian Earth System Model (NorESM2) and key climate response of CMIP6 DECK, historical, and scenario simulations. *Geoscientific Model Development*, 13(12):6165–6200. Publisher: Copernicus GmbH.

Pranab Kumar Sen. 1968. Estimates of the Regression Coefficient Based on Kendall's Tau. *Journal of the American Statistical Association*, 63(324):1379–1389. Publisher: Taylor & Francis _eprint: https://www.tandfonline.com/doi/pdf/10.1080/01621459.1968.10480934.

Olivia Serdeczny, Sophie Adams, Florent Baarsch, Dim Coumou, Alexander Robinson, William Hare, Michiel Schaeffer, Mahé Perrette, and Julia Reinhardt. 2017. Climate change impacts in Sub-Saharan Africa: from physical changes to their social repercussions. *Regional Environmental Change*, 17(6):1585–1600.

Aaron M. Shew, Jesse B. Tack, Lawton L. Nalley, and Petronella Chaminuka. 2020. Yield reduction under climate warming varies among wheat cultivars in South Africa. *Nature Communications*, 11(1):4408. Number: 1 Publisher: Nature Publishing Group.

Mxolisi E. Shongwe, Chris Lennard, Brant Liebmann, Evangelia-Anna Kalognomou, Lucky Ntsangwane, and Izidine Pinto. 2014. An evaluation of CORDEX regional climate models in simulating precipitation over Southern Africa. *Atmospheric Science Letters*, 16(3):199–207.

J. Sillmann, V. V. Kharin, F. W. Zwiers, X. Zhang, and D. Bronaugh. 2013. Climate extremes indices in the CMIP5 multimodel ensemble: Part 2. Future climate projections. *Journal of Geophysical Research: Atmospheres*, 118(6):2473–2493. _eprint: https://agupubs.onlinelibrary.wiley.com/doi/pdf/10.1002/jgrd.50188.

W. C. Skamarock, J. B. Klemp, J. Dudhia, D. O. Gill, Z. Liu, J. Berner, and X. Huang. 2021. A Description of the Advanced Research WRF Model Version 4.3. ((No. NCAR/TN-556+STR)).

Paul W. Staten, Jian Lu, Kevin M. Grise, Sean M. Davis, and Thomas Birner. 2018. Re-examining tropical expansion. *Nature Climate Change*, 8(9):768–775. Number: 9 Publisher: Nature Publishing Group.

T. H. M. Stein, W. Keat, R. I. Maidment, S. Landman, E. Becker, D. F. A. Boyd, A. Bodas-Salcedo, G. Pankiewicz, and S. Webster. 2019. An Evaluation of Clouds and Precipitation in Convection-Permitting Forecasts for South Africa. *Weather and Forecasting*, 34(1):233–254. Publisher: American Meteorological Society Section: Weather and Forecasting.

A. K. Steiner, F. Ladstädter, W. J. Randel, A. C. Maycock, Q. Fu, C. Claud, H. Gleisner, L. Haimberger, S.-P. Ho, P. Keckhut, T. Leblanc, C. Mears, L. M. Polvani, B. D. Santer, T. Schmidt, V. Sofieva, R. Wing, and C.-Z. Zou. 2020. Observed Temperature Changes in the Troposphere and Stratosphere from 1979 to 2018. *Journal of Climate*, 33(19):8165–8194. Publisher: American Meteorological Society Section: Journal of Climate.

Rachel A. Stratton, Catherine A. Senior, Simon B. Vosper, Sonja S. Folwell, Ian A. Boutle, Paul D. Earnshaw, Elizabeth Kendon, Adrian P. Lock, Andrew Malcolm, James Manners, Cyril J. Morcrette, Christopher

Short, Alison J. Stirling, Christopher M. Taylor, Simon Tucker, Stuart Webster, and Jonathan M. Wilkinson. 2018. A Pan-African Convection-Permitting Regional Climate Simulation with the Met Office Unified Model: CP4-Africa. *Journal of Climate*, 31(9):3485–3508. Publisher: American Meteorological Society Section: Journal of Climate.

Bi-Yun SUN and Xun-Qiang BI. 2019. Validation for a tropical belt version of WRF: sensitivity tests on radiation and cumulus convection parameterizations. *Atmospheric and Oceanic Science Letters*, 12(3):192–200. Publisher: Taylor & Francis _eprint: https://doi.org/10.1080/16742834.2019.1590118.

Neil C. Swart, Jason N. S. Cole, Viatcheslav V. Kharin, Mike Lazare, John F. Scinocca, Nathan P. Gillett, James Anstey, Vivek Arora, James R. Christian, Sarah Hanna, Yanjun Jiao, Warren G. Lee, Fouad Majaess, Oleg A. Saenko, Christian Seiler, Clint Seinen, Andrew Shao, Michael Sigmond, Larry Solheim, Knut von Salzen, Duo Yang, and Barbara Winter. 2019. The Canadian Earth System Model version 5 (CanESM5.0.3). *Geoscientific Model Development*, 12(11):4823–4873. Publisher: Copernicus GmbH.

Neil C. Swart, John C. Fyfe, Nathan Gillett, and Gareth J. Marshall. 2015. Comparing Trends in the Southern Annular Mode and Surface Westerly Jet. *Journal of Climate*, 28(22):8840–8859. Publisher: American Meteorological Society Section: Journal of Climate.

Silje Lund Sørland, Christoph Schär, Daniel Lüthi, and Erik Kjellström. 2018. Bias patterns and climate change signals in GCM-RCM model chains. *Environmental Research Letters*, 13(7):074017. Publisher: IOP Publishing.

Alain T. Tamoffo, Leonard K. Amekudzi, Torsten Weber, Derbetini A. Vondou, Edmund I. Yamba, and Daniela Jacob. 2021. Mechanisms of Rainfall Biases in Two CORDEX-CORE Regional Climate Models at Rainfall Peaks over Central Equatorial Africa. *Journal of Climate*, 35(2):639–668. Publisher: American Meteorological Society Section: Journal of Climate.

Chao Tang, Béatrice Morel, Martin Wild, Benjamin Pohl, Babatunde Abiodun, Chris Lennard, and Miloud Bessafi. 2019. Numerical simulation of surface solar radiation over Southern Africa. Part 2: projections of regional and global climate models. *Climate Dynamics*, 53(3):2197–2227.

Elena Tarnavsky, David Grimes, Ross Maidment, Emily Black, Richard P. Allan, Marc Stringer, Robin Chadwick, and Francois Kayitakire. 2014. Extension of the TAMSAT Satellite-Based Rainfall Monitoring over Africa and from 1983 to Present. *Journal of Applied Meteorology and Climatology*, 53(12):2805–2822. Publisher: American Meteorological Society.

Hiroaki Tatebe, Tomoo Ogura, Tomoko Nitta, Yoshiki Komuro, Koji Ogochi, Toshihiko Takemura, Kengo Sudo, Miho Sekiguchi, Manabu Abe, Fuyuki Saito, Minoru Chikira, Shingo Watanabe, Masato Mori, Nagio Hirota, Yoshio Kawatani, Takashi Mochizuki, Kei Yoshimura, Kumiko Takata, Ryouta O'ishi, Dai Yamazaki, Tatsuo Suzuki, Masao Kurogi, Takahito Kataoka, Masahiro Watanabe, and Masahide Kimoto. 2019. Description and basic evaluation of simulated mean state, internal variability, and climate sensitivity in MIROC6. *Geoscientific Model Development*, 12(7):2727–2765. Publisher: Copernicus GmbH.

Karl E. Taylor, Ronald J. Stouffer, and Gerald A. Meehl. 2012. An Overview of CMIP5 and the Experiment Design. *Bulletin of the American Meteorological Society*, 93(4):485–498. Publisher: American Meteorological Society.

Claudia Tebaldi and Reto Knutti. 2007. The use of the multi-model ensemble in probabilistic climate projections. *Philosophical Transactions of the Royal Society A: Mathematical, Physical and Engineering Sciences*, 365(1857):2053–2075. Publisher: Royal Society.

Henri Theil. 1992. A Rank-Invariant Method of Linear and Polynomial Regression Analysis. In Baldev Raj and Johan Koerts, editors, *Henri Theil's Contributions to Economics and Econometrics: Econometric Theory and Methodology*, Advanced Studies in Theoretical and Applied Econometrics, pages 345–381. Springer Netherlands, Dordrecht.

David W. J. Thompson, Susan Solomon, Paul J. Kushner, Matthew H. England, Kevin M. Grise, and David J. Karoly. 2011. Signatures of the Antarctic ozone hole in Southern Hemisphere surface climate change. *Nature Geoscience*, 4(11):741–749. Number: 11 Publisher: Nature Publishing Group.

David W. J. Thompson and John M. Wallace. 2000. Annular Modes in the Extratropical Circulation. Part I: Month-to-Month Variability. *Journal of Climate*, 13(5):1000–1016. Publisher: American Meteorological Society Section: Journal of Climate.

David W. J. Thompson and Jonathan D. Woodworth. 2014. Barotropic and Baroclinic Annular Variability in the Southern Hemisphere. *Journal of the Atmospheric Sciences*, 71(4):1480–1493. Publisher: American Meteorological Society Section: Journal of the Atmospheric Sciences.

Baijun Tian and Xinyu Dong. 2020. The Double-ITCZ Bias in CMIP3, CMIP5, and CMIP6 Models Based on Annual Mean Precipitation. *Geophysical Research Letters*, 47(8):e2020GL087232. _eprint: https://onlinelibrary.wiley.com/doi/pdf/10.1029/2020GL087232.

M. C. Tirado, D. Hunnes, M. J. Cohen, and A. Lartey. 2015. Climate Change and Nutrition in Africa. *Journal of Hunger & Environmental Nutrition*, 10(1):22–46. Publisher: Taylor & Francis _eprint: https://doi.org/10.1080/19320248.2014.908447.

Carolien Toté, Domingos Patricio, Hendrik Boogaard, Raymond Van der Wijngaart, Elena Tarnavsky, and Chris Funk. 2015. Evaluation of Satellite Rainfall Estimates for Drought and Flood Monitoring in Mozambique. *Remote Sensing*, 7(2):1758–1776.

Anna M. Ukkola, Martin G. De Kauwe, Michael L. Roderick, Gab Abramowitz, and Andrew J. Pitman. 2020. Robust Future Changes in Meteorological Drought in CMIP6 Projections Despite Uncertainty in Precipitation. *Geophysical Research Letters*, 47(11):e2020GL087820. _eprint: https://agupubs.onlinelibrary.wiley.com/doi/pdf/10.1029/2020GL087820.

E. van Meijgaard, L. H. van Ulft, W. J. van de Berg, F. C. Bosveld, B. J. J. M. van den Hurk, G. Lenderink, and A. P. Siebesma. 2008. The KNMI regional atmospheric climate model RACMO version 2.1. TR - 302, KNMI, The Netherland.

Sander Van Vooren, Bert Van Schaeybroeck, Jan Nyssen, Michiel Van Ginderachter, and Piet Termonia. 2019. Evaluation of CORDEX rainfall in northwest Ethiopia: Sensitivity to the model representation of the orography. *International Journal of Climatology*, 39(5):2569–2586. _eprint: https://onlinelibrary.wiley.com/doi/pdf/10.1002/joc.5971.

Robert Vautard, Nikolay Kadygrov, Carley Iles, Fredrik Boberg, Erasmo Buonomo, Katharina Bülow, Erika Coppola, Lola Corre, Erik van Meijgaard, Rita Nogherotto, Marit Sandstad, Clemens Schwingshackl, Samuel Somot, Emma Aalbers, Ole B. Christensen, James M. Ciarlò, Marie-Estelle Demory, Filippo Giorgi, Daniela Jacob, Richard G. Jones, Klaus Keuler, Erik Kjellström, Geert Lenderink, Guillaume Levavasseur, Grigory Nikulin, Jana Sillmann, Cosimo Solidoro, Silje Lund Sørland, Christian Steger, Claas Teichmann, Kirsten WarrachSagi, and Volker Wulfmeyer. 2020. Evaluation of the large EURO-CORDEX regional climate model ensemble. *Journal of Geophysical Research: Atmospheres*, n/a(n/a):e2019JD032344. _eprint: https://agupubs.onlinelibrary.wiley.com/doi/pdf/10.1029/2019JD032344.

N. Vigaud, B. Pohl, and J. Crétat. 2012. Tropical-temperate interactions over southern Africa simulated by a regional climate model. *Climate Dynamics*, 39(12):2895–2916.

A. Voldoire, D. SaintMartin, S. Sénési, B. Decharme, A. Alias, M. Chevallier, J. Colin, J.-F. Guérémy, M. Michou, M.-P. Moine, P. Nabat, R. Roehrig, D. Salas y Mélia, R. Séférian, S. Valcke, I. Beau, S. Belamari, S. Berthet, C. Cassou, J. Cattiaux, J. Deshayes, H. Douville, C. Ethé, L. Franchistéguy, O. Geoffroy, C. Lévy, G. Madec, Y. Meurdesoif, R. Msadek, A. Ribes, E. SanchezGomez, L. Terray, and R. Waldman. 2019. Evaluation of CMIP6 DECK Experiments With CNRM-CM6-1. *Journal of Advances in Modeling Earth Systems*, 11(7):2177–2213. _eprint: https://agupubs.onlinelibrary.wiley.com/doi/pdf/10.1029/2019MS001683.

A. Voldoire, E. Sanchez-Gomez, D. Salas y Mélia, B. Decharme, C. Cassou, S. Sénési, S. Valcke, I. Beau, A. Alias, M. Chevallier, M. Déqué, J. Deshayes, H. Douville, E. Fernandez, G. Madec, E. Maisonnave, M.-P. Moine, S. Planton, D. Saint-Martin, S. Szopa, S. Tyteca, R. Alkama, S. Belamari, A. Braun, L. Coquart, and F. Chauvin. 2013. The CNRM-CM5.1 global climate model: description and basic evaluation. *Climate Dynamics*, 40(9):2091–2121.

John M. Wallace and Peter V. Hobbs. 2006. *Atmospheric Science, Second Edition: An Introductory Survey*, 2nd edition edition. Academic Press, Amsterdam ; Boston.

Erika A. Warnatzsch and David S. Reay. 2019. Temperature and precipitation change in Malawi: Evaluation of CORDEX-Africa climate simulations for climate change impact assessments and adaptation planning. *Science of The Total Environment*, 654:378–392.

Richard Washington, Rachel James, Helen Pearce, Wilfried M. Pokam, and Wilfran Moufouma-Okia. 2013. Congo Basin rainfall climatology: can we believe the climate models? *Philosophical Transactions of the Royal Society B: Biological Sciences*, 368(1625):20120296. Publisher: Royal Society.

Richard Washington and Anthony Preston. 2006. Extreme wet years over southern Africa: Role of Indian Ocean sea surface temperatures. *Journal of Geophysical Research: Atmospheres*, 111(D15). _eprint: https://onlinelibrary.wiley.com/doi/pdf/10.1029/2005JD006724.

Masahiro Watanabe, Tatsuo Suzuki, Ryouta O'ishi, Yoshiki Komuro, Shingo Watanabe, Seita Emori, Toshihiko Takemura, Minoru Chikira, Tomoo Ogura, Miho Sekiguchi, Kumiko Takata, Dai Yamazaki, Tokuta Yokohata, Toru Nozawa, Hiroyasu Hasumi, Hiroaki Tatebe, and Masahide Kimoto. 2010. Improved

Climate Simulation by MIROC5: Mean States, Variability, and Climate Sensitivity. *Journal of Climate*, 23(23):6312–6335. Publisher: American Meteorological Society.

D. Watson-Parris. 2021. Machine learning for weather and climate are worlds apart. *Philosophical Transactions of the Royal Society A: Mathematical, Physical and Engineering Sciences*, 379(2194):20200098. Publisher: Royal Society.

Oliver Watt-Meyer, Noah Domino Brenowitz, Spencer Koncius Clark, Brian Henn, Anna Kwa, Jeremy J. McGibbon, Walter A. Perkins, and Christopher S. Bretherton. 2021. Correcting weather and climate models by machine learning nudged historical simulations. Archive Location: world Publisher: Earth and Space Science Open Archive Section: Atmospheric Sciences.

C. J. Willmott and K Matsuura. 2001. Global Air Temperature and Precipitation Archive.

James C. Winter, Gary L. Darmstadt, Alexandria B. Boehm, and Jennifer Davis. 2021. The impact of on-premises piped water supply on fecal contamination pathways in rural Zambia. *npj Clean Water*, 4(1):1–8. Number: 1 Publisher: Nature Publishing Group.

Modise Wiston and Kgakgamatso Marvel Mphale. 2019. Mesoscale Convective Systems: A Case Scenario of the 'Heavy Rainfall' Event of 15–20 January 2013 over Southern Africa. *Climate*, 7(6):73. Number: 6 Publisher: Multidisciplinary Digital Publishing Institute.

Piotr Wolski, David Lobell, Dáithí Stone, Izidine Pinto, Olivier Crespo, and Peter Johnston. 2020. On the role of anthropogenic climate change in the emerging food crisis in southern Africa in the 2019–2020 growing season. *Global Change Biology*, 26(5):2729–2730. _eprint: https://onlinelibrary.wiley.com/doi/pdf/10.1111/gcb.15047.

Tim Woollings and Mike Blackburn. 2012. The North Atlantic Jet Stream under Climate Change and Its Relation to the NAO and EA Patterns. *Journal of Climate*, 25(3):886–902. Publisher: American Meteorological Society.

Jia Wu and Xuejie Gao. 2020. Present day bias and future change signal of temperature over China in a series of multi-GCM driven RCM simulations. *Climate Dynamics*, 54(1):1113–1130.

Man-Li C. Wu, Oreste Reale, Siegfried D. Schubert, Max J. Suarez, Randy D. Koster, and Philip J. Pegion. 2009. African Easterly Jet: Structure and Maintenance. *Journal of Climate*, 22(17):4459–4480.

Klaus Wyser, Twan van Noije, Shuting Yang, Jost von Hardenberg, Declan O'Donnell, and Ralf Döscher. 2020. On the increased climate sensitivity in the EC-Earth model from CMIP5 to CMIP6. *Geoscientific Model Development*, 13(8):3465–3474. Publisher: Copernicus GmbH.

Pingping Xie and Phillip A. Arkin. 1997. Global Precipitation: A 17-Year Monthly Analysis Based on Gauge Observations, Satellite Estimates, and Numerical Model Outputs. *Bulletin of the American Meteorological Society*, 78(11):2539–2558. Publisher: American Meteorological Society.

Pingping Xie and Phillip A. Arkin. 1998. Global Monthly Precipitation Estimates from Satellite-Observed Outgoing Longwave Radiation. *Journal of Climate*, 11(2):137–164. Publisher: American Meteorological Society Section: Journal of Climate.

Nkosinathi G. Xulu, Hector Chikoore, Mary-Jane M. Bopape, and Nthaduleni S. Nethengwe. 2020. Climatology of the Mascarene High and Its Influence on Weather and Climate over Southern Africa. *Climate*, 8(7):86. Number: 7 Publisher: Multidisciplinary Digital Publishing Institute.

Hu Yang, Gerrit Lohmann, Jian Lu, Evan J. Gowan, Xiaoxu Shi, Jiping Liu, and Qiang Wang. 2020. Tropical Expansion Driven by Poleward Advancing Midlatitude Meridional Temperature Gradients. *Journal of Geophysical Research: Atmospheres*, 125(16):e2020JD033158. _eprint: https://onlinelibrary.wiley.com/doi/pdf/10.1029/2020JD033158.

Bo Young Yim, Sang-Wook Yeh, and Byung-Ju Sohn. 2016. ENSO-Related Precipitation and Its Statistical Relationship with the Walker Circulation Trend in CMIP5 AMIP Models. *Atmosphere*, 7(2):19. Number: 2 Publisher: Multidisciplinary Digital Publishing Institute.

Chunxi Zhang and Yuqing Wang. 2017. Projected Future Changes of Tropical Cyclone Activity over the Western North and South Pacific in a 20-km-Mesh Regional Climate Model. *Journal of Climate*, 30(15):5923–5941. Publisher: American Meteorological Society Section: Journal of Climate.